Informatics Control Measurement
in Economy and Environment Protection

4/2020

Informatyka Automatyka Pomiary

www.e-IAPGOS.pl

w gospodarce i ochronie środowiska

ISSN 2083-0157

Kwartalnik Naukowo-Techniczny

fot. arch. uczelni

State University of Telecommunications
(Kyiv, Ukraine)

4/2020

październik – grudzień

Wydanie pod redakcją naukową
prof. dr hab. inż. Waldemara Wójcika

INFORMATYKA
AUTOMATYKA
POMIARY
W GOSPODARCE i OCHRONIE ŚRODOWISKA
Informatics Control Measurement in Economy and Environment Protection

p-ISSN 2083-0157, e-ISSN 2391-6761, www.e-iapgos.pl

EDITORIAL OFFICE
REDAKCJA

Redakcja czasopisma
Informatyka, Automatyka, Pomiary w Gospodarce i Ochronie Środowiska
Katedra Elektroniki i Technik Informacyjnych
Politechnika Lubelska
ul. Nadbystrzycka 38A, 20-618 Lublin
tel. +48 81 53 84 309,
fax: +48 81 53 84 312
iapgos@pollub.pl
www.e-iapgos.pl
iapgos.pollub.pl
ph.pollub.pl/index.php/iapgos

PUBLISHER
WYDAWCA

Politechnika Lubelska
ul. Nadbystrzycka 38D
20-618 Lublin
tel. +48 81 53 84 100
www.pollub.pl
ph.pollub.pl

PRINTING HOUSE – DRUKARNIA

DjaF – Naświetlarnia B1+
ul. Kmietowicza 1/1
30-092 Kraków
http://www.djaf.pl
nakład: 100 egzemplarzy

OTHER INFORMATION – INNE INFORMACJE

Czasopismo jest indeksowane w bazach:

DOAJ:	doaj.org
BazTech:	baztech.icm.edu.pl
IC Journals Master List:	www.journals.indexcopernicus.com
Google Scholar	scholar.google.pl
POL-index	pbn.nauka.gov.pl

Czasopismo *Informatyka, Automatyka, Pomiary w Gospodarce i Ochronie Środowiska* zostało objęte finansowaniem przez Ministerstwo Nauki i Szkolnictwa Wyższego w ramach programu *Wsparcie dla czasopism naukowych* w latach 2019-2020.

Czasopismo znajduje się w wykazie czasopism naukowych opublikowanym w Komunikacie Ministra Nauki i Szkolnictwa Wyższego z dnia 31 lipca 2019 r., pozycja 27864 – z przypisaną liczbą punktów przyznawanych za publikację równą 20.

Zasady publikowania artykułów, przygotowania tekstów, zasady etyczne, procedura recenzowania, wykazy recenzentów oraz pełne teksty artykułów dostępne są na stronie internetowej czasopisma:

www.e-iapgos.pl

W celu zwiększenia oddziaływania czasopisma w środowisku naukowym redakcja zaleca:

- w artykułach publikowanych w IAPGOS cytować artykuły z renomowanych czasopism międzynarodowych (szczególnie indeksowanych w bazach Web of Science oraz Scopus) używając oficjalnych skrótów nazw czasopism,
- w artykułach publikowanych w innych czasopismach (zwłaszcza indeksowanych w bazach Web of Science oraz Scopus) cytować prace publikowane w IAPGOS – zwłaszcza posługując się numerami DOI, np.:
  Kluszczyński K. *Modelowanie – umiejętność czy sztuka?* Informatyka, Automatyka, Pomiary w Gospodarce i Ochronie Środowiska – IAPGOS, 1/2016, 4–15, DOI: 10.5604/20830157.1193833.

CONTENTS – SPIS TREŚCI

http://doi.org/10.35784/iapgos.2383

MODELING ELECTROMAGNETIC NANOSTRUCTURES AND EXPERIMENTING WITH NANOELECTRIC ELEMENTS TO FORM PERIODIC STRUCTURES

Miloslav Steinbauer[1], Roman Pernica[1], Jiri Zukal[1], Radim Kadlec[1], Tibor Bachorec[1], Pavel Fiala[2]
[1]Brno University of Technology, Department of Theoretical and Experimental Electrical Engineering, Brno, Czech Republic
[2]Brno University of Technology, SIX Research Center, Brno, Czech Republic

Abstract. *We discuss the numerical modeling of electromagnetic, carbon-based periodic structures, including graphene, graphane, graphite, and graphyne. The materials are suitable for sub-micron sensors, electric lines, and other applications, such as those within biomedicine, photonics, nano- and optoelectronics; in addition to these domains and branches, the applicability extends into, for example, microscopic solutions for modern SMART elements. The proposed classic and hybrid numerical models are based on analyzing a periodic structure with a high repeatability, and they exploit the concept of a carbon structure having its fundamental dimension in nanometers. The models can simulate harmonic and transient processes; are capable of evaluating the actual random motion of an electric charge as a source of spurious signals; and consider the parameters of harmonic signal propagation along the structure. The results obtained from the analysis are utilizable for the design of sensing devices based on carbon periodic structures and were employed in experiments with a plasma generator. The aim is to provide a broader overview of specialized nanostructural modeling, or, more concretely, to outline a model utilizable in evaluating the propagation of a signal along a structure's surface.*

Keywords: nanomaterial, graphene, graphite, experimental modeling, hydrogen bond, periodic structure

MODELOWANIE NANOSTRUKTUR ELEKTROMAGNETYCZNYCH I EKSPERYMENTY Z ELEMENTAMI NANOELEKTRYCZNYMI W CELU TWORZENIA STRUKTUR OKRESOWYCH

Streszczenie. *W artykule omówiony został proces numerycznego modelowania elektromagnetycznych, węglowych struktur okresowych, w tym grafenu, grafanu, grafitu i grafinu. Materiały te nadają się do czujników submikronowych, przewodów elektrycznych i innych zastosowań, takich jak biomedycyna, fotonika, nano- i optoelektronika. Oprócz tych dziedzin i gałęzi przemysłu, zastosowanie materiałów pokrywa się także na przykład z mikroskopijnymi rozwiązaniami dla nowoczesnych elementów SMART. Proponowane klasyczne i hybrydowe modele numeryczne opierają się na analizie okresowej struktury o wysokiej powtarzalności i wykorzystują koncepcję struktury węglowej o podstawowym wymiarze w nanometrach. Modele mogą symulować procesy harmoniczne i przejściowe, potrafią ocenić rzeczywisty losowy ruch ładunku elektrycznego jako źródła fałszywych sygnałów i uwzględniają parametry propagacji sygnału harmonicznego wzdłuż konstrukcji. Rezultaty uzyskane w wyniku analizy można wykorzystać do projektowania czujników opartych na węglowych strukturach okresowych oraz do eksperymentów z generatorem plazmy. Celem jest zapewnienie szerszego przeglądu specjalistycznego modelowania nanostrukturalnego lub, bardziej konkretnie, zarysu modelu nadającego się do oceny propagacji sygnału wzdłuż powierzchni struktury.*

Słowa kluczowe: nanomateriał, grafen, grafit, modelowanie eksperymentalne, wiązanie wodorowe, struktura okresowa

Introduction

The current decade has witnessed a major rise of interest in graphene [4, 5], Fig. 1, a carbon-based, single-layer periodic material. However, one-atom layered systems were investigated previously, with attempts made at estimating their mechanical and electrical properties via macroscopic experiments [24, 38] or theoretical considerations [40]. Graphene has been successfully manufactured from graphite, which essentially comprises periodically bonded carbon atoms arranged in multiple layers (Fig. 2). A further monolayered carbon periodic system, with bonds to hydrogen or other atomic nuclei, is commonly referred to as graphane (Fig. 3). Even though the polymer (with a benzene core or graphane base element) has not become a subject of mainstream research or found practical application to date, it shows significant potential for electronics and nanoelectronics. It has been identified through theoretical modeling as an advantageous material to facilitate the manufacturing of nanoelectric signal transmission lines [20]. Within the present investigation of single-atom carbon substances [4, 5, 20, 24, 30, 38, 40, 50], however, only few laboratories produce deterministic models of carbon-based nanomaterials. Another periodically structured form of carbon, graphyne (Fig. 4), exhibits interatomic bonding different from that of related carbon systems and can be shaped into pre-selected patterns or periodic motifs.

This paper compares several structural models of graphite, graphene, and graphane samples, focusing on an analysis and evaluation of the electromagnetic wave propagation along such systems. Earlier research and modeling [8, 12, 13, 16, 32, 46] point to the influence exerted by the actual oscillation of a periodically arranged carbon structure on a transmitted signal; such an impact is parametrically expressed as S/N. Moreover, in connection with the relevant numerical models, the question of how large a signal (electric current) can be smoothly carried along a nanoelectric line. Some authors consider graphene usable for logic or memory circuits in microelectronics [30, 44, 50]. In the above context, our study is intended to outline the possibilities of stochastic and deterministic methods [22, 23, 49] in numerical modeling and to examine the modeled sample periodic carbon structures in terms of the electromagnetic properties that may support the designing of a system to transmit a signal; the signal is describable by both the relevant electric power P and its density expressed via the Poynting vector $\boldsymbol{\Pi}$. We also refer to various options of characterizing other properties and parameters (such as the S/N ratio) which appear to be indispensable in forming a nanoelectric element. The resulting information and data are utilizable especially in photonics, nanoelectronics, and associated subdomains of nanoelectronic system engineering. An interesting aspect lies in the analysis and evaluation of an electromagnetic wave and its propagation at the visible (in the order of hundreds of 100 THz), infrared (units to tens of THz), or lower (units to hundreds of GHz) spectral frequencies. The spectra are of particular interest for the given branch of engineering, as they offer broad application potential [9, 31, 41]. To set up the geometrical dimensions of the periodic system models at the atomic level and to design or analyze the structures in a stochastic model, we followed several relevant papers, including [26, 27, 45].

According to the research presented in [8, 12, 13, 16, 20, 22, 23, 32, 44, 46, 49], the periodic structure of graphene exhibits certain interesting electrical and electromagnetic properties regarding the propagation of an electromagnetic wave. The referenced articles nevertheless do not provide a clear conclusion as to prospective application of periodic structures with exact properties in the field of EMG wave propagation; these structures can be based on either natural or artificial materials.

The concept of our study involved assembling several numerical models and performing their analyses to evaluate parameters such as the S/N ratio of the actual structure carrying the useful signal and to determine the maximum current density that may load the system without destructive effects. Figure 5 displays some of the carbon-based periodic structures tested within the investigation outlined herein.

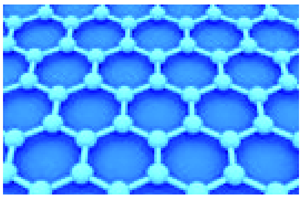

Fig. 1. Arrangement of carbon periodic structures: a graphene layer

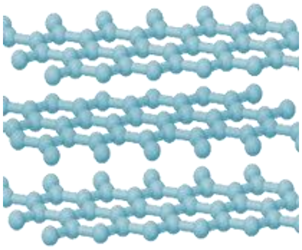

Fig. 2. Arrangement of carbon periodic structures: a graphite layer

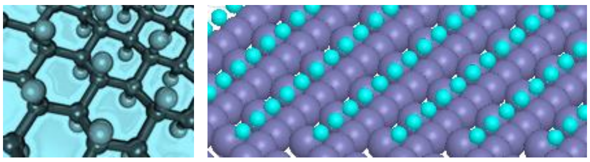

Fig. 3. Arrangement of carbon periodic structures: a layer of graphane, and its bonds to hydrogen

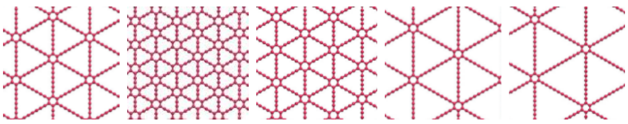

Fig. 4. Arrangement of carbon periodic structures: a graphyne layer at various levels

In evaluating these structures and their frequency responses to incident electromagnetic waves, it is necessary to employ convenient tools to facilitate a combined theoretical and experimental analysis. Such a process then has to be built on a specific geometrical and numerical model, and this model should respect the character of the probabilistic mathematical model; the uncertainty of the occurrence of an electric charge q; and the frequency of the transmitted signal f_t compared to the first harmonic frequency f_{a1} [22, 23, 49], which is defined by the motion of the elementary charged parts of an atom with a diameter d_{a1}. We have:

$$f_t \ll \frac{c}{d_{a1}} \qquad (1)$$

where c is the speed of light in vacuum, and $f_{a1} = c/d_{a1}$. The model embodies an application of the quantum-mechanical model of matter and the stochastic distribution of electric charges in individual elements of the structure. Although the structure is large, it exhibits a significant degree of periodicity; thus, it is possible to utilize, up to a certain level of complexity, the known finite methods (the finite and boundary element techniques or the finite volume method combined with a deterministic stochastic model). An example is provided in Fig. 5, via the design of a single conductor being a structure with a non-conductive space around each atom; more concretely, we can refer to Figs. 5d, 5e and the model of a coaxial, symmetric electric line comprising two polymer systems formed on a graphane basis.

In any such geometrical arrangement of a periodic nanostructure, it is suitable to analyze the EMG field at the level of structure elements with respect to the evaluation of known macroscopic quantities, including the surface power flux density and the electric and magnetic field intensities and specific fluxes for the harmonic behavior of signal propagation along the structure or for transient states of signal propagation along similar structures. As regards the proposed frequency-dependent EMG field analysis, the field comprises two basic domains: A) $f_t \in \langle 1\cdot 10^6; 500\cdot 10^9\rangle$ [Hz], $f_{a1} \approx 2\cdot 10^{13}$ [Hz], which satisfies the above precondition (1), and B) $f_t \in \langle 20\cdot 10^{13}; 40\cdot 10^{13}\rangle$ [Hz], $f_{a1} \approx 2\cdot 10^{13}$ [Hz], which does not satisfy precondition (1). In the former domain, A), the numerical analysis is then carried out via the classic approach, simulating the propagation of an electromagnetic wave in a harmonic model formulated by using reduced Maxwell's equations, [1, 34, 39, 43, 48]; in the latter region, B), the hybrid technique is employed to evaluate the propagation of an electromagnetic wave in a transient model formulated by means of reduced Maxwell's equations, [1, 20, 34, 39, 43, 48].

In model analyses where the electromagnetic field quantities are not evaluated at comparable magnitudes and sizes of the wavelength and the geometric structure [30, 31, 32, 33, 34, 35, 36, 37, 38, 39, 40, 41, 42, 43, 44, 45], the mathematical model does not necessarily have to be formed with respect to the quality criterion. Thus, the most convenient approach is selected according to the type of analysis planned and the numerical model designed. If an analysis of signals on a nano- or microstructure is to be performed, we can set up the numerical model based on the condition (1) – ad A) $f_t \in \langle 1\cdot 10^6; 500\cdot 10^9\rangle$ [Hz], $f_{a1} \approx 2\cdot 10^{13}$ [Hz], facilitating:

1) evaluation of both the transient processes which capture the motion of the electrically charged objects (electrons) and the electromagnetic couplings known from physico-chemical descriptions of inorganic and organic material structures [10, 20, 23], and
2) harmonic analysis and evaluation of the S and Z parameters, with represented distribution of the electromagnetic field in the time and frequency domains [6, 10, 17, 19].

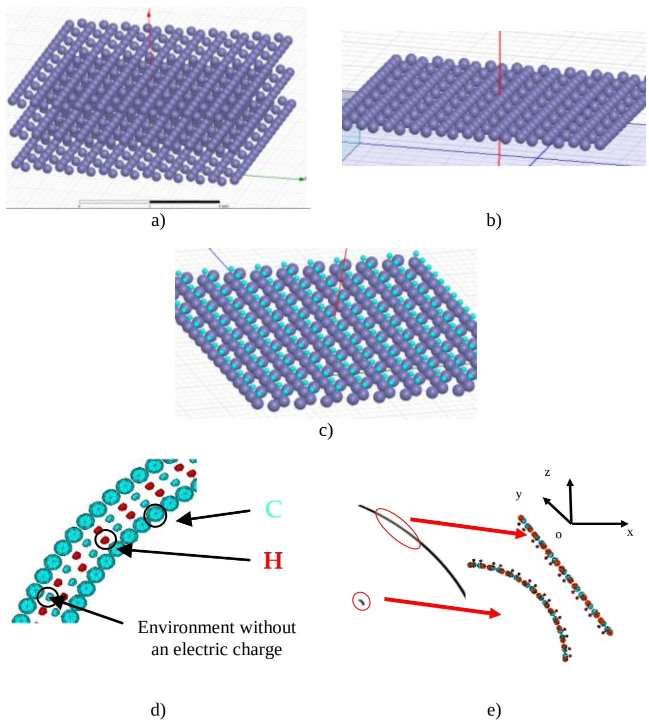

Fig. 5. Model of various geometrical structures of carbon nanomaterials: a) graphite; b) graphene; c) graphane; d) a graphane-based coaxial line model having the radius ratio of 1.4; e) a graphane-based coaxial line with the radius ratio of 30

If the desired task is to analyze and evaluate the distribution of the electromagnetic field at the level of the nanostructure elements (nanometric objects; condition (1), ad B) $f_t \in \langle 20{\cdot}10^{13};\ 40{\cdot}10^{13}\rangle$ [Hz], $f_{a1} \approx 2{\cdot}10^{13}$ [Hz]), the model should include:

1) a harmonic analysis and evaluation of the S parameters, with a swept frequency for the expected band, and
2) a different, ring theory-based design [22, 23, 49] to evaluate the electromagnetic field and to carry out an analysis with a swept frequency spectrum.

A periodic structure (single layered)

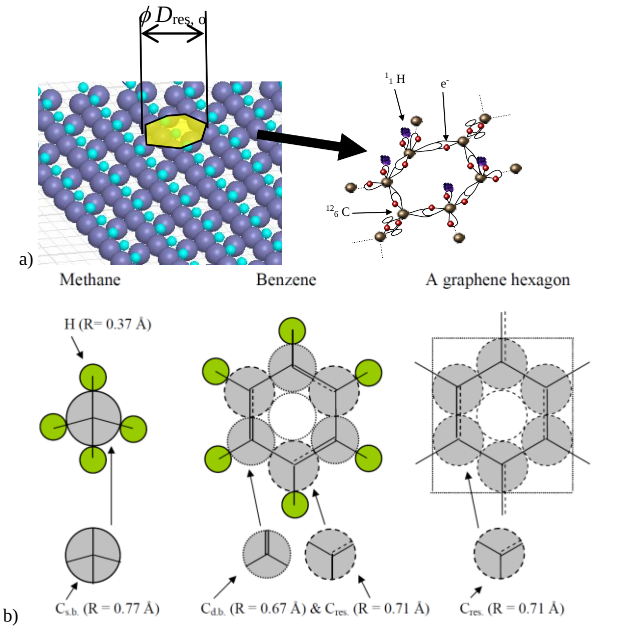

Fig. 6. Model of the geometrical structures of selected carbon nanomaterials: a) graphane; b) the dimensions of the basic element of graphene

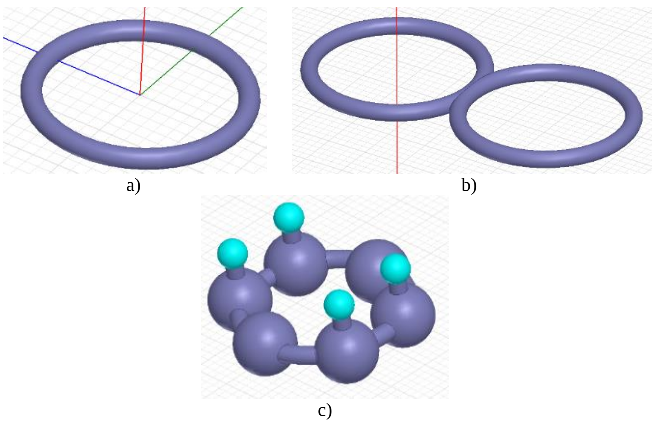

Fig. 7. Simplified geometrical model of the basic "benzene core" elements for carbon nanomaterial structures: a) benzene; b) double benzene; c) benzene core of a graphane structure

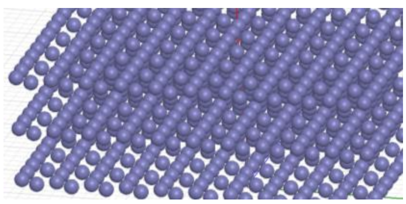

Fig. 8. Geometrical model of the three-layered structure of a graphene nanomaterial (graphite)

In the numerical analyses and their evaluation, we assume the basic forms of an excited (index 1) and a generated (index 2) electromagnetic wave, each having a forward and a backward component (whose electric intensities are denoted by E_f and E_b, respectively).

The vectors of the electric field of the electromagnetic wave are expressed as:

$$\begin{aligned} \boldsymbol{E}_1(t,x,y,z) &= \\ &= \boldsymbol{E}_{1f}(x,y,z)\cdot e^{-j\omega_1 t+\varphi}\cdot e^{\underline{k}_1 \mathbf{n}_1\cdot \boldsymbol{r}_1} + \\ &+ \boldsymbol{E}_{1b}(x,y,z)\cdot e^{+j\omega_1 t+\varphi}\cdot e^{\underline{k}_1 \mathbf{n}_1\cdot \boldsymbol{r}_1} \end{aligned} \tag{2}$$

$$\begin{aligned} \boldsymbol{E}_2(t,x,y,z) &= \\ &= \boldsymbol{E}_{2f}(x,y,z)\cdot e^{-j\omega_2 t+\varphi}\cdot e^{\underline{k}_2 \mathbf{n}_2\cdot \boldsymbol{r}_2} + \\ &+ \boldsymbol{E}_{2b}(x,y,z)\cdot e^{+j\omega_2 t+\varphi}\cdot e^{\underline{k}_2 \mathbf{n}_2\cdot \boldsymbol{r}_2} \end{aligned} \tag{3}$$

where x, y, z are the coordinates of a point in the Cartesian coordinate system; t denotes the time; ω represents the angular frequency; $\boldsymbol{n}$ is the normal vector of the direction of the electromagnetic wave propagation; $\underline{k}$ stands for the comprehensive notation of the wave number; $\boldsymbol{r}$ represents the position vector of the source of the electromagnetic wave and, if related to the origin, denotes the coordinates of the point at which a component is evaluated; index 1 expresses the classification of an excited electromagnetic wave; and index 2 specifies the actual oscillation system (such as a modeled structure, atom, and molecule). These procedural instruments and approaches are known from quantum mechanical models, including, for example, that proposed by Bina [3] for the Rabi oscillation, Fig. 9; in this context, the referenced paper [3] presents an example of the interference between an incident electromagnetic wave and the oscillation of the actual system, Fig. 10.

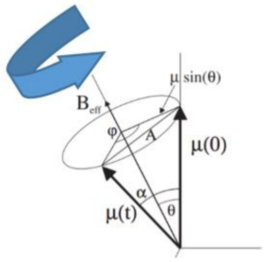

Fig. 9. Model of the atom and the magnetic moment $\mu(t)$

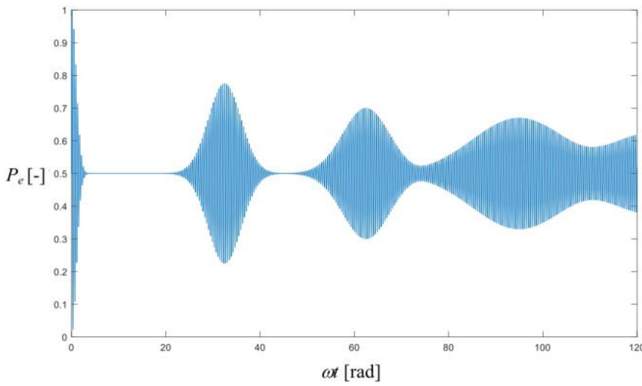

Fig. 10. Resulting shape of the "Rabi oscillations" relating to an external source of an electromagnetic wave

Principally, the interference process thus consists in identifying the relationships between two oscillating systems, namely, an oscillator and an electromagnetic wave generated by an oscillating object exhibiting a physical similarity known in Rabi oscillations [3]. The ratio of frequencies, $m_{M,}$ can then be employed to evaluate the parameters and types of models that will enable the analysis (ad 1–4, formulas (2), (3)):

$$m_{M,abs} = \frac{|\omega_1 - \omega_2|}{\omega_2}, \tag{4}$$

$$m_M = \frac{(\omega_1 - \omega_2)}{\omega_2}. \tag{5}$$

The proportional relationships characterized in (4), (5) for the frequencies m_{M} yield:

$$\omega_1 \ll \omega_2\,, \tag{6}$$

$$\omega_1 \leq \omega_2\,, \tag{7}$$

$$\omega_1 \cong \omega_2 \vee \omega_1 = m\omega_2\,,\; m = 2,3,..,N^\circ\,. \tag{8}$$

The distribution of the effects and frequency bands defining the electromagnetic waves' interference (9) $\boldsymbol{E}_{\mathrm{coupl}}$ can be written for two coupled waves as:

$$\begin{aligned} \boldsymbol{E}_{coupl}(t) &= \boldsymbol{E}_{1f}(x,y,z)\cdot e^{-j\omega_1 t+\varphi_1}\cdot e^{k_1\mathbf{n}_1\cdot\boldsymbol{r}_1} + \\ &\boldsymbol{E}_{1b}(x,y,z)\cdot e^{+j\omega_1 t+\varphi_1}\cdot e^{k_1\mathbf{n}_1\cdot\boldsymbol{r}_1} + \\ &\boldsymbol{E}_{2f}(x,y,z)\cdot e^{-j\omega_2 t+\varphi_2}\cdot e^{k_2\mathbf{n}_2\cdot\boldsymbol{r}_2} + \\ &\boldsymbol{E}_{2b}(x,y,z)\cdot e^{+j\omega_2 t+\varphi_2}\cdot e^{k_2\mathbf{n}_2\cdot\boldsymbol{r}_2} \end{aligned} \tag{9}$$

where $\boldsymbol{E}_{\mathrm{f}}$, $\boldsymbol{E}_{\mathrm{b}}$ are the forward and backward vector components of the intensity of the electric field of an electromagnetic wave in the assumed system (the periodic system of the structure), and $\boldsymbol{E}_1$ denotes the component of the external source of the incident electromagnetic wave's intensity vector; such a description allows us to characterize the known interference effects. For conditions (6), (7), and (8), we then have the interference and, if the waves are coherent, also the resonance effects.

When characterizing the two basic, mutually interfering electromagnetic waves (2), (3) according to their impact on the measured structure, we can categorize them into the impinging ($\boldsymbol{E}_{\mathrm{f}}$) and the reflected groups, enabling us to evaluate the structural properties via the parameters of the impedance matrix ($\boldsymbol{Z}$) or the scattering matrix ($\boldsymbol{S}$). These parameters will then allow the tested model to be analyzed within the frequency spectrum in relation to the preset number of ports. For two ports, the scattering parameters are:

$$\boldsymbol{E}_{1\mathrm{b}} = s_{11}\cdot\boldsymbol{E}_{1\mathrm{f}} + s_{12}\cdot\boldsymbol{E}_{2\mathrm{f}}, \tag{10}$$

$$\boldsymbol{E}_{2\mathrm{b}} = s_{21}\cdot\boldsymbol{E}_{1\mathrm{f}} + s_{22}\cdot\boldsymbol{E}_{2\mathrm{f}}. \tag{11}$$

Based on the formulas, it is then possible to define the individual S parameters, as follows:

$s_{11} = \boldsymbol{E}_{1\mathrm{b}}\boldsymbol{E}_{1\mathrm{f}}^{-1}\mid \boldsymbol{E}_{2\mathrm{f}} = \mathbf{0}$	the input reflection coefficient;	(12)
$s_{12} = \boldsymbol{E}_{1\mathrm{b}}\boldsymbol{E}_{2\mathrm{f}}^{-1}\mid \boldsymbol{E}_{1\mathrm{f}} = \mathbf{0}$	the backward transmission coefficient;	(13)
$s_{21} = \boldsymbol{E}_{2\mathrm{b}}\boldsymbol{E}_{1\mathrm{f}}^{-1}\mid \boldsymbol{E}_{2\mathrm{f}} = \mathbf{0}$	the transmission coefficient;	(14)
$s_{22} = \boldsymbol{E}_{2\mathrm{b}}\boldsymbol{E}_{2\mathrm{f}}^{-1}\mid \boldsymbol{E}_{1\mathrm{f}} = \mathbf{0}$	and the output reflection coefficient.	(15)

In terms of the impedance parameters, we have:

$z_{11} = \boldsymbol{E}_{1\mathrm{b}}\boldsymbol{H}_{1\mathrm{f}}^{-1}\mid \boldsymbol{H}_{2\mathrm{f}} = \mathbf{0}$	the input reflection coefficient;	(16)
$z_{12} = \boldsymbol{E}_{1\mathrm{b}}\boldsymbol{H}_{2\mathrm{f}}^{-1}\mid \boldsymbol{H}_{1\mathrm{f}} = \mathbf{0}$	the backward transmission coefficient;	(17)
$z_{21} = \boldsymbol{E}_{2\mathrm{b}}\boldsymbol{H}_{1\mathrm{f}}^{-1}\mid \boldsymbol{H}_{2\mathrm{f}} = \mathbf{0}$	the transmission coefficient;	(18)
$z_{22} = \boldsymbol{E}_{2\mathrm{b}}\boldsymbol{H}_{2\mathrm{f}}^{-1}\mid \boldsymbol{H}_{1\mathrm{f}} = \mathbf{0}$	and the output reflection coefficient.	(19)

1. Modeling the parameters of a periodic structure

In order to design the geometries of the models capturing the investigated carbon-based periodic structures (Fig. 5), it is necessary to define the initial and boundary conditions of the given model and the sources of the electromagnetic field. The basic formation of a stochastic model to represent an element of a periodic structure consists in describing the atomic bonds and the region where an atom may occur; the motion of the valence electrons is displayed in Fig. 6 (extreme left). Another step in setting the conditions of the model requires us to evaluate the components of the electric field E intensity vector in the basic geometrical element E_{r}. To facilitate simple estimation of the order of magnitude of the intensities, we can – for the hydrogen atom H bound to carbon C and one binding electron in the middle electrodes of the coaxial arrangement of the internal structure (Fig. 6, Fig. 11) – evaluate the radial potential electric field intensity from the single C–H bond as:

$$\begin{gathered} E_{r,a} = \frac{1}{4\pi\varepsilon_0}\cdot\frac{q_e}{\left|R_1\right|^2}\,, \\ E_{r,a} = \frac{1}{4\pi\cdot 8.856\cdot 10^{-12}}\cdot\frac{1.602\cdot 10^{-19}}{\left(0.71\cdot 10^{-10}\right)^2} = \\ 2.937\cdot 10^{11}\ V/m\ \left(2.937\cdot 10^{2}\ V/nm\right) \end{gathered} \tag{20}$$

where R_1 is the radius of the modeled elements. Similarly to the approach adopted in [6] and [30], the analysis of the structure was based on models for solving the telegrapher's equations [6, 11, 19].

2. Relativity effect in the carbon structure models

The known models [6, 11, 15, 25] allow us to express changes of the electromagnetic field in dependence on the motion of the system A relative to its counterpart A′. Let us assume that an external electromagnetic wave in the system A and the modeled structure together constitute the systems A and A′; the analysis of the models classified via ad A) $f_{\mathrm{t}} \in \langle 1\cdot 10^6;\ 500\cdot 10^9\rangle$ [Hz], $f_{\mathrm{a}1} \approx 2\cdot 10^{13}$ [Hz] then depends on the modified current density $\boldsymbol{J}$ and the intensities of the electric and magnetic fields, $\boldsymbol{E}$ and $\boldsymbol{H}$ [6, 11]. For the unabbreviated expression, respecting the element motion at a velocity v in all directions, the current density in relation to the moving system A-A′ can be subsequently written as:

$$\begin{aligned} \boldsymbol{J}_{S\square} = &\frac{J'_{\mathrm{x}} - v_x div\left(\dfrac{\varepsilon'}{\gamma'}\boldsymbol{J}'_{\Delta}\right)}{\sqrt{1-\left(\dfrac{v}{c}\right)^2}}\boldsymbol{u}_x + \\ &+\frac{J'_{\mathrm{y}} - v_y div\left(\dfrac{\varepsilon'}{\gamma'}\boldsymbol{J}'_{\Delta}\right)}{\sqrt{1-\left(\dfrac{v}{c}\right)^2}}\boldsymbol{u}_y + \frac{J'_{\mathrm{z}} - v_z div\left(\dfrac{\varepsilon'}{\gamma'}\boldsymbol{J}'_{\Delta}\right)}{\sqrt{1-\left(\dfrac{v}{c}\right)^2}}\boldsymbol{u}_z + \\ &+j\frac{c\,div\left(\dfrac{\varepsilon'}{\gamma'}\boldsymbol{J}'_{\Delta}\right) - \dfrac{v_x}{c}J'_x - \dfrac{v_y}{c}J'_y - \dfrac{v_z}{c}J'_z}{\sqrt{1-\left(\dfrac{v}{c}\right)^2}}\boldsymbol{u}_t \end{aligned} \tag{21}$$

The formula for the value of the electric volume charge density ρ reads:

$$\rho = \frac{\rho' - \dfrac{\boldsymbol{v}_{\Delta}}{c^2}\boldsymbol{J}'_{S\Delta}}{\sqrt{1-\left(\dfrac{v}{c}\right)^2}} \tag{22}$$

In (21) and (22), $\boldsymbol{v}$ represents the relative motion with an instantaneous velocity of the moving system A, $\boldsymbol{v}_{\Delta}$ is the relative motion vector with components v_{x}, v_{y}, v_{z} in the Cartesian coordinate system A, $\boldsymbol{u}_{\mathrm{x}}$, $\boldsymbol{u}_{\mathrm{y}}$, $\boldsymbol{u}_{\mathrm{z}}$ are its base vectors, $\boldsymbol{J}'_{\Delta}$ is the current density vector in system A′ with components J_{x}', J_{y}', J_{z}', c represents the speed of light in a vacuum, ρ, ρ', are the volume densities of the electric charge in the system A and A′, respectively, $\boldsymbol{J}_{\mathrm{S}}$, is the total current density vector in system A, $\boldsymbol{J}'_{\mathrm{S}\Delta}$ is the current density vector in system A′, γ' is the specific electrical conductivity of an environment from the macroscopic view in system A′, and ε' is the electric permittivity from the point of view of the system A′.

As regards electrical engineering, relativistic effects are known especially in signal transmission within radar technology [21, 29, 47, 51]. According to the above example, [25], the effects manifest themselves in electromagnetic fields of dynamic systems from speeds in the order of 1 m/s [11, 15].

In precise nanometric analyses, such effects have to be individually considered and respected, through the perspective of the above conditions (1) ad A), ad B).

3. Relativity limit parameters of the electromagnetic model of a carbon-based periodic structure

The standard approach to modeling structures with a probabilistic distribution of the electric charge in atomic parts is usable in analyses centered on the evaluation of the frequency spectrum of the parameters S and Z; this procedure can also be employed to evaluate, as outlined in formulas (9–20), models of chemical elements and compounds, including that of the benzene nucleus (Figs. 11–13). Within such models, it is possible to consider the impact exerted on the parameters of the spectrum by the geometrical configuration of the "motion" of the electric charge q in the structure of the modeled elements. The modeling-based results may then be compared with those of the experiments to determine the overall match. This classic approach to numerical model creation has been widely employed [2, 6, 11, 14, 15, 18, 21, 25, 29, 33, 35, 36, 42, 47, 51, 52], as also shown through the relevant criterion (1) ad A). To perform the associated qualitative analysis, it is convenient to use the classification embodied in the above precondition (1), ad B), which covers the behavior of the dynamic system inside the modeled structure; for cases of strong coupling between the internal and the external electromagnetic fields, some basic aspects of the modeled object are comprised, too. The geometry of the models, Fig. 11, Fig. 12, Fig. 13, and their dimensions were chosen according to the work of R. Heyrovska [26, 27, 28].

The design of the geometrical model for the frequency range B) can be characterized in greater detail as suggested in Fig. 14. The fundamental element of the graphene-based periodic structure is a hexagonal carbon nucleus [50]; from the perspective of the stochastic distribution of the instantaneous position and arrangement of carbon C valence electrons, the fundamental element and bonds can be schematically described as shown in Fig. 15.

The applicability of the designed nanometer structures in electrical signal transmission is strongly dependent on both the structures' ability to transmit high-quality signals (parametrically expressed via indicators such as the S/N ratio, [2, 7, 17, 18, 52]) along the system's surface and the limit properties of the input electric current $i_s(t)$. We have:

$$i_s(t) = \frac{d(q \cdot n_q)}{dt}, \; i_s(t) = \frac{q \cdot n_q}{\Delta\ell} \cdot v_{ok} \cdot e^{-\frac{q}{kT} u_{r,u}}, \qquad (23)$$

where q is the electric charge of an elementary object, n_q is the number of elementary objects in the observed volume, $i_s(t)$ is the instantaneous value of the electric current, $\Delta\ell$ is the element of length, Fig. 15a, v_{ok} is the mean speed of movement of an electrically charged object, $u_{r,u}$ is the voltage on the elementary path of an electric charge q, k is the Boltzmann constant, and T is the temperature.

In the periodic structure [8, 12, 13, 16, 20, 32, 35, 46] composed of basic elements according to Figs. 1, 2, 3, and 4 and schematically illustrated in Fig. 14, it is possible to estimate the electric current $i_{s,max}(t)$ from the motion (at speed v_{ok}) of the bonding electron's electric charge q_e and binding particles n_q (in accordance with the Bohr–Sommerfeld Theory [36]). We thus have:

$$i_{s,max}(t) = \frac{q_e \cdot n_q}{\Delta\ell} \cdot v_{ok}, \; i_{s,max}(t) = 0.364 \cdot 10^{-9} \text{ [A]}, \qquad (24)$$

$$J_{s,max} = \frac{i_{s,max}}{S} = \frac{0.364 \cdot 10^{-9}}{1.539 \cdot 10^{-20}} = 23.66 \cdot 10^{9} \; [A/m^2] \; \left(23.66 \; [nA/nm^2]\right) \qquad (25)$$

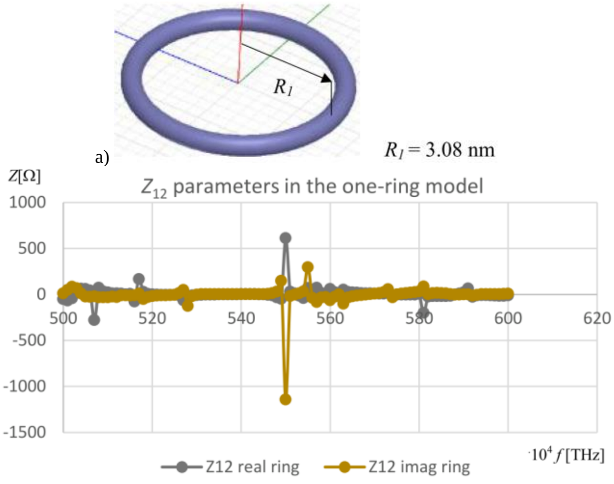

Fig. 11. Simplified geometrical model of the basic "benzene core" elements for carbon nanomaterial structures: a) benzene; b) spectral analysis of the Z parameters

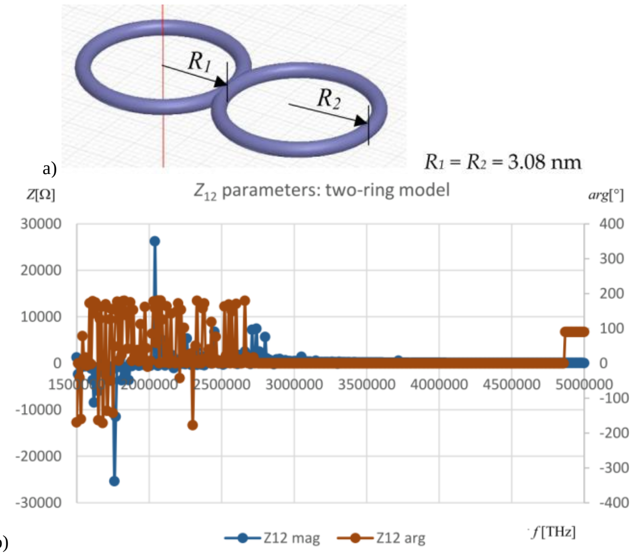

Fig. 12. Simplified geometrical model of the basic "benzene core" elements for carbon nanomaterial structures: a) double benzene; b) spectral analysis of the Z parameters

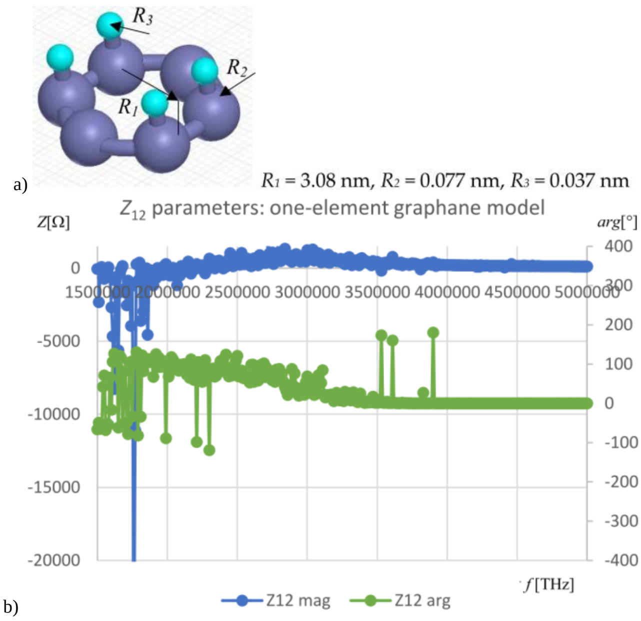

Fig. 13. Simplified geometrical model of the basic "benzene core" elements for carbon nanomaterial structures: a) double benzene; b) spectral analysis of the Z parameters

From this current, we can then express the current density $\boldsymbol{J}$ caused by the given bonds (Fig. 15). If the density is known, models exploiting the solution of Maxwell's equations allow establishing, via stochastic simulation of a periodic element (Fig. 15b), the hypothetical current density $\boldsymbol{J}_{ext}$ of an external electromagnetic field; this density originates from, for example, the transmission of an EMG wave along a periodic structure. The condition when a temporary or permanent alteration (rearrangement) may occur in the basic element of the structure, Fig. 15b, then embodies a critical stage for the model. The formula for the potential condition expressed by the intensity $E_{r,a}$ enables us to express, from the known electric current magnitude (30) and density (31), the actual intensity of the electric field of the modeled and analyzed periodic structure; such intensity is generated by the propagation of a longitudinal electromagnetic wave. We have:

$$E_t=\frac{1}{4\pi\varepsilon_0}\cdot\frac{dq_e}{|d\ell|^2},\quad E_t=\frac{1}{4\pi\cdot\varepsilon_0}\frac{dq_e}{d\ell}\frac{1}{d\ell},$$

$$E_t=\frac{1}{4\pi\cdot\varepsilon_0}\frac{i_s}{v_{ok}}\frac{1}{d\ell},\quad E_t=2.937\cdot10^2\,[V/nm] \qquad (26)$$

where E_t is the tangential component of the electric intensity along the considered bound, Fig. 15b. The quantities thus expressed then facilitate determining the macroscopic quantity, or the specific electrical conductivity, of the periodic structure:

$$\gamma=\frac{J_{s,max}}{E_t},\quad \gamma=\frac{i_{s,max}}{S}\frac{4\pi\varepsilon_0 v_{ok}d\ell}{i_{s,max}},$$

$$\gamma=\frac{4\pi\varepsilon_0 v_{ok}}{\pi d\ell^2}d\ell,\quad \gamma=\frac{4\pi\varepsilon_0 n_q q^e\left(\frac{1}{4\pi\varepsilon_0 m_0 d\ell}\right)^{\frac{1}{2}}}{\pi d\ell}, \qquad (27)$$

$$\gamma=2n_q q^e\frac{\left(\frac{\varepsilon_0}{\pi m_0}\right)^{\frac{1}{2}}}{d\ell^{\frac{3}{2}}},\quad \gamma=9.623\ [S/nm]$$

Further steps within the procedure are aimed at finding an external electromagnetic field having an intensity $E_{ext,c}$ at which the periodic structure of the designed system and its electromagnetic properties change temporarily. A temporary rearrangement of the element's bonds facilitates restoring or resetting the properties of the structure; a permanent change (when the value of $E_{ext,c}$ is exceeded), however, will not enable such restoration. The value of the electric intensity $E_{ext,c}$ is related to the permissible maximum current density at which the nanostructure can be stressed without permanent damage. Therefore, this parameter is related to the lifetime of the target application using a periodic nanostructure. In the discussed case, the monitored parameter can be obtained through an experimental measurement of the speed $\boldsymbol{v}_w$ of the electromagnetic wave propagation along the periodic structure (Fig. 5a, b, c, d, Fig. 8); the relevant propagation behavior is shown in Fig. 16.

Using the above-presented specifications, it is then possible to perform a numerical analysis and to evaluate the parameters of the periodic system from the perspective of the properties of an electromagnetic field having anticipated limit parameters, which, generally, are desirable in nanoelectric systems designed to transmit or process signals along carbon-based structures. The parameters embody a fundamental prerequisite for planning the service life of a periodic structure [20] and the superior nano- or microelectronic element. The numerical model was solved with ANSYS-HFSS for the frequency range A) (for $\boldsymbol{E}_{1f}$ = 1 V/m) and ANSYS-EMAG [1], the APDL language, in the frequency range B), [1, 8, 12, 13, 16, 20, 21, 22, 23, 46, 49].

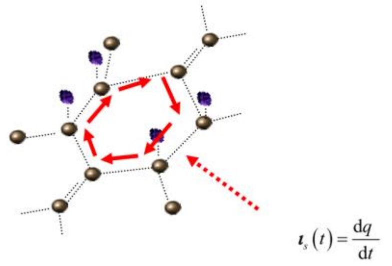

Fig. 14. Simplified expression of the electric currents in an element of the periodic structure

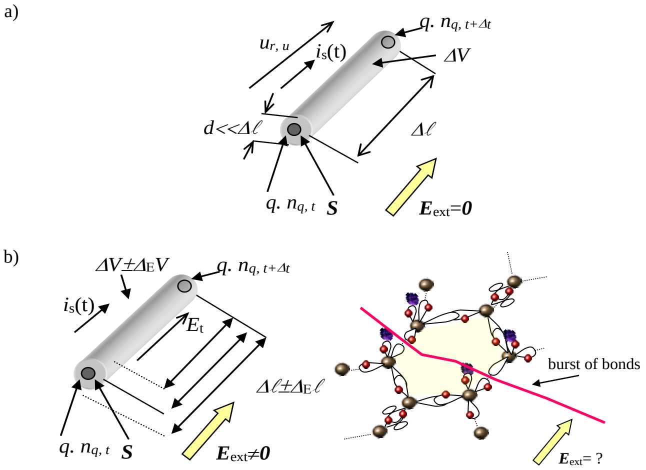

Fig. 15. Bonding details: a) model of an electron moving in the basic element of a carbon structure; b) changes due to an external electromagnetic field

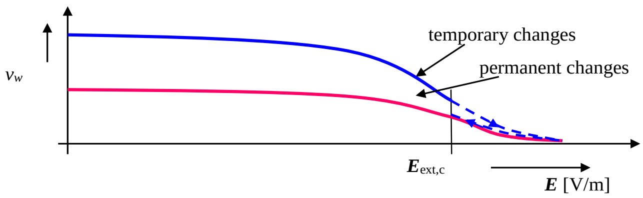

Fig. 16. Anticipated speeds of a surface electromagnetic wave propagation along a carbon-based periodic structure

The relative permittivity ε_r, a macroscopic parameter to facilitate the modeling of electromagnetic quantities outside the model of the atom and its vicinity, is obtainable via a simple assumption: In two neighboring atoms bound by electrostatic forces, the mutual force from Coulomb's law can be evaluated for the condition $r_a \ll R_{12}$ (Fig. 17) as:

$$\boldsymbol{F}_{12}=\frac{1}{4\pi\cdot\varepsilon_0}\frac{q_{1e}q_{2e}}{\|\boldsymbol{R}_{12}\|}\boldsymbol{u}_r, \qquad (28)$$

where q_{1e}, q_{2e}, are the electric charges (electrons) in the "benzene core" nanostructure;; $\boldsymbol{R}_{12}$ represents the vector of the distance between the atomic centers; and $\boldsymbol{F}_{12}$ denotes the vector of the electromagnetic force acting between atoms 1 and 2, Fig. 17; in which they are $\boldsymbol{E}_1$, $\boldsymbol{E}_2$, the intensity vectors of the electric fields of atoms 1 and 2; and r_{a1}, r_{a2} stand for the radii of atoms 1 and 2. After satisfying the conditions $r_{a1} \ll R_{12}$, $r_{a2} \ll R_{12}$, we can interpret the effects in Fig. 17 as forces between the point charges represented by atoms 1 and 2, considering, for example, the case where q_{1e} elementary charge 1 is defined by n_{e1} = 1, the electric charge of atom 2 (carbon, C) is defined by q_{2e} and n_{e2} = 4; we then have:

$$\boldsymbol{F}_{12}=\frac{1}{4\pi\cdot\varepsilon_0}\frac{q_{1e}n_{e1}q_e n_{e2}}{\|\boldsymbol{R}_{12}\|}\boldsymbol{u}_r. \qquad (29)$$

where n_{e1}, n_{e2} denote the amounts of electrons in the shells of atoms 1 and 2, Fig. 17. Upon comparing the formulas (29), (30), and based on Gauss's theorem, the relative permittivity of atom 2 is expressed via:

$$\Phi_{e2} = \oint\limits_{S(r_{a2})} \frac{1}{4\pi \cdot \varepsilon_0} \frac{q_{2e} n_{e2}}{\|\boldsymbol{r}_{a2}\|^2} \boldsymbol{u}_r \cdot d\,\boldsymbol{S}_{a2}\,, \tag{30}$$

$$\Phi_{e2} = \int\limits_{S(r)} \frac{1}{4\pi \cdot \varepsilon_0} \frac{n_{e2} q_{2e}}{\|\boldsymbol{r}_{a2}\|^2} \boldsymbol{u}_r \cdot d\,\boldsymbol{S}\,,$$

$$\Phi_{e2} = \int\limits_{S(r)} \varepsilon_r E_r\, \boldsymbol{u}_r \cdot d\,\boldsymbol{S}\,, \tag{31}$$

$$\varepsilon_r = n_{e2}\,,$$

where E_r is the radial component of the electric intensity, ε_r is the relative permittivity, $\boldsymbol{u}_r$ is the base vector of a spherical coordinate system, and $S(r)$ is the surface of the sphere depending on the radius r.

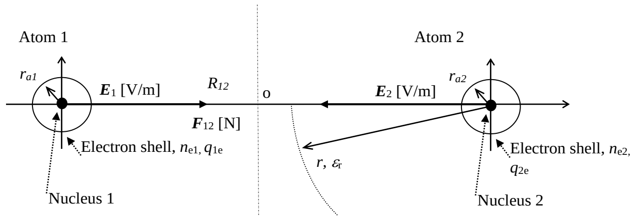

Fig. 17. Scheme of the atomic forces to facilitate relative permittivity evaluation

4. Modeling, analyzing, evaluating, and experimenting with the organic structures

As indicated above, the basic model is built by exploiting a FEM-based system, namely, ANSYS [1], and enables us to find the geometry and parameters of the target structure with respect to its chemical survivability.

We conducted diverse numerical analyses of periodic system models, assuming precondition (1); relevant outcomes are illustrated in Fig. 5a–c and Fig. 5d–e for the frequency domains A) and B), respectively.

The elementary structure according to Figs. 5, 6, and 14 was chosen and solved (Figs. 18–20) as the basis of the numerical model introduced in the above formulas (5–9) for the frequency range A) and (14) for the frequency range B); the model analysis was processed in the batch mode. In order to design the geometry of the models of the carbon-based periodic structures (Figs. 5 and 6), it is necessary to define the corresponding initial and boundary conditions and the sources of the electromagnetic field. The basic formation (an element of the periodic structure) can be simply described by the atomic bonds, namely, the motion of the valence electrons (Fig. 6 and Fig. 14). In the case of using the periodic nanostructure as the electric line material [7, 17, 20], the movement of electrons is taken into account as a source of unwanted signal, i.e., noise. Therefore, it is necessary to evaluate the components of the electromagnetic field caused by the motion of the electric charges of the nanostructure with respect to the components of the transmitted EMG waves.

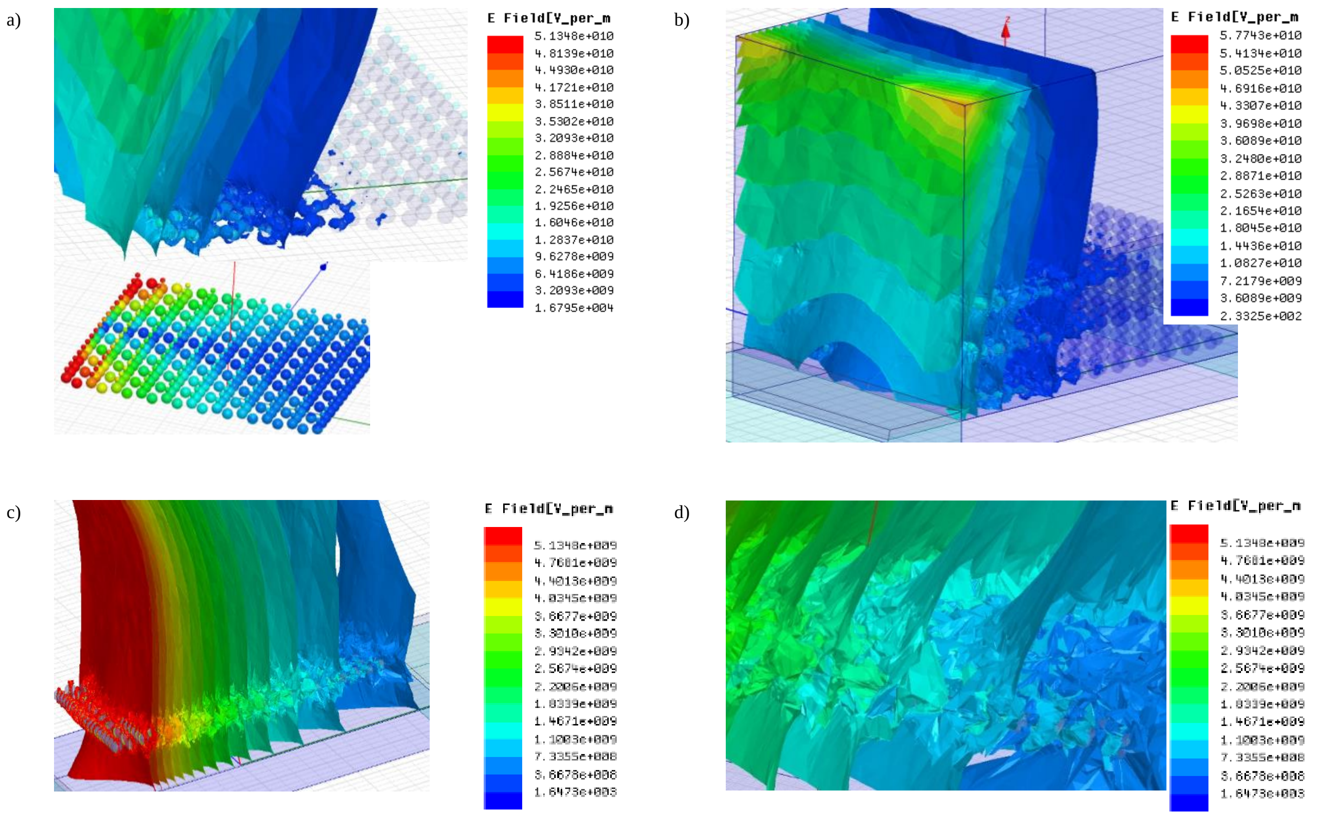

Fig. 18. Distribution of the intensities of an incident electromagnetic wave's electric component E in: a) graphane; b) graphite; c) graphene; d) the close vicinity of the graphene structure

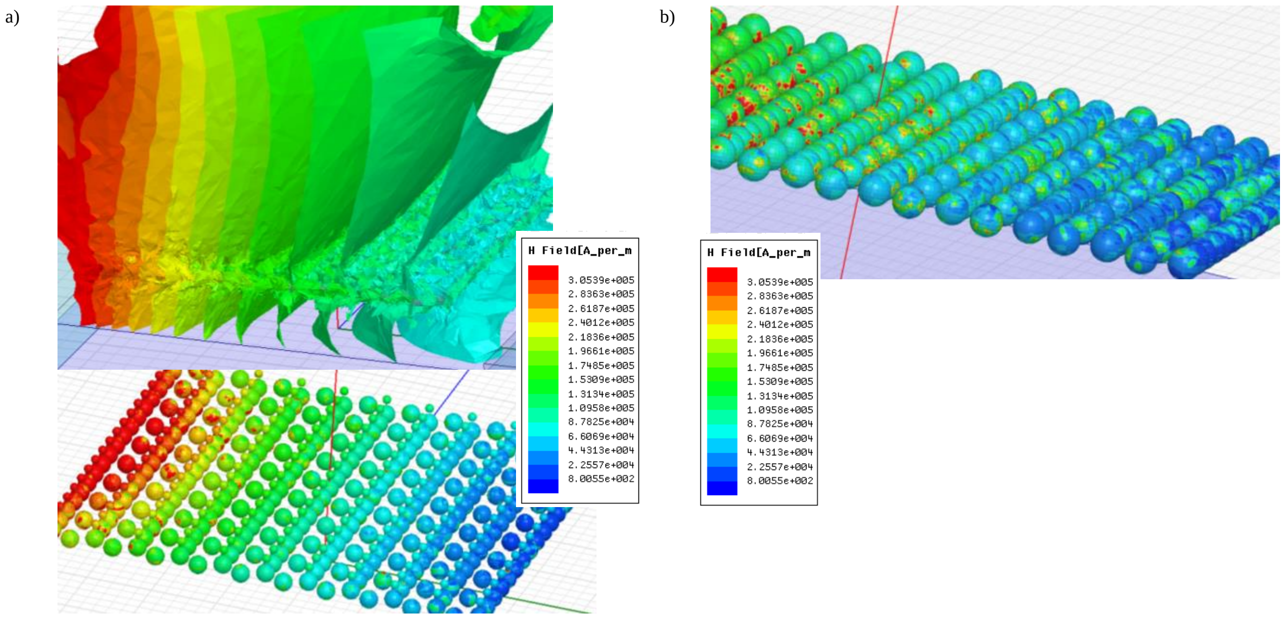

Fig. 19. The distribution of the intensities of an incident electromagnetic wave's magnetic field H in a) the close vicinity of graphane; b) graphene atoms

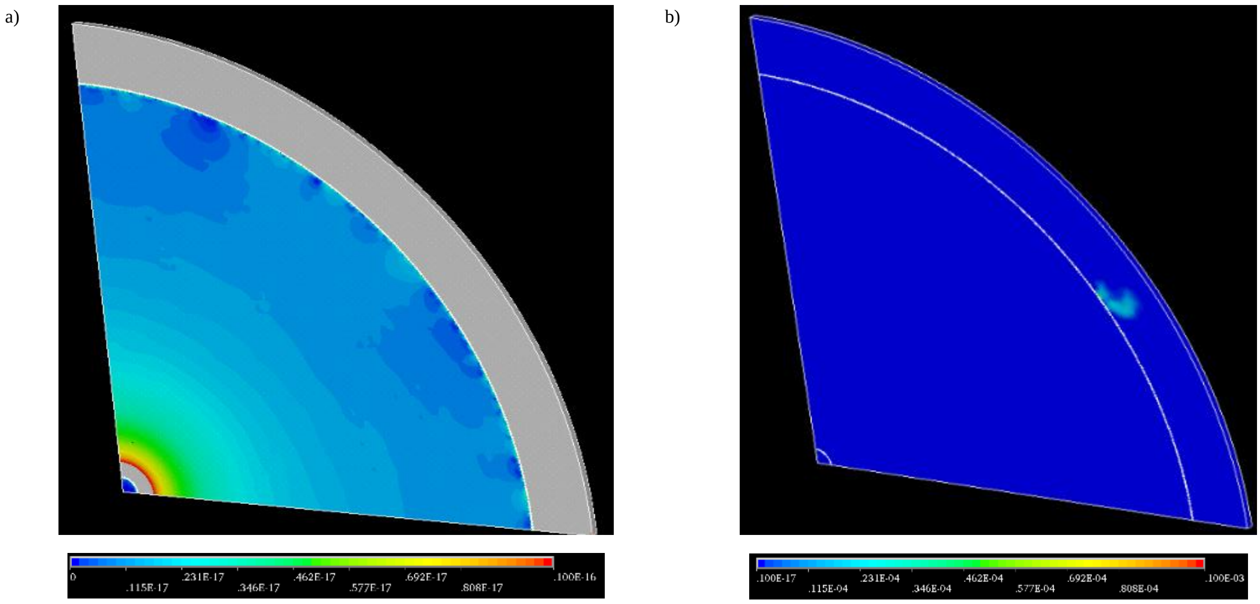

Fig. 20. Distribution of a) the electric intensity E [V/m] in coaxially arranged graphane electrodes; b) the magnetic flux density B [T] in signal transmission at current i = 1 μA

Within the macroscopic model, both the maximum signal transmitted by the designed graphene-based polymer structure and the tangential electric strength are estimable by utilizing formula (30); the electric field intensity as the limit parameter $E_{\max}$ is set according to Eq. (2) and can be, in the vicinity of an atom of the structure, considered identical for both the radial and the tangential components (2).

To experimentally develop the formation and application technologies suitable for the above-modeled, benzene core-based organic structures, we designed and tested a plasma jet, performing a specific analysis [37] to ensure highly efficient modification of the plasma discharge precursor. In this context, we also investigated diverse methods for optimizing the argon discharge with respect to the frequency required to set the optimal power output transmission (resonance; lossless power output transmission along the path of the plasma discharge). Using the numerical approaches described above, we parametrically investigated the conditions for maintaining the plasma discharge. The discharge very effectively shaped the organic precursors in the frequency band and its multiples (Eqs. 2, 3, Fig. 10). Such modified precursors, when applied to the surface of the material, form the desired "polymeric" nanostructures, with a basic elements of the benzene core type.

We measured the HF parameters along the plasma discharge (Fig. 21a–b) and carried out the relevant basic experiments to ensure the conditions shown in Fig. 21c, d. The indicated setting is expected to facilitate, via the above-presented numerical models, effective formation of organic periodic structures on the desired sample material surface.

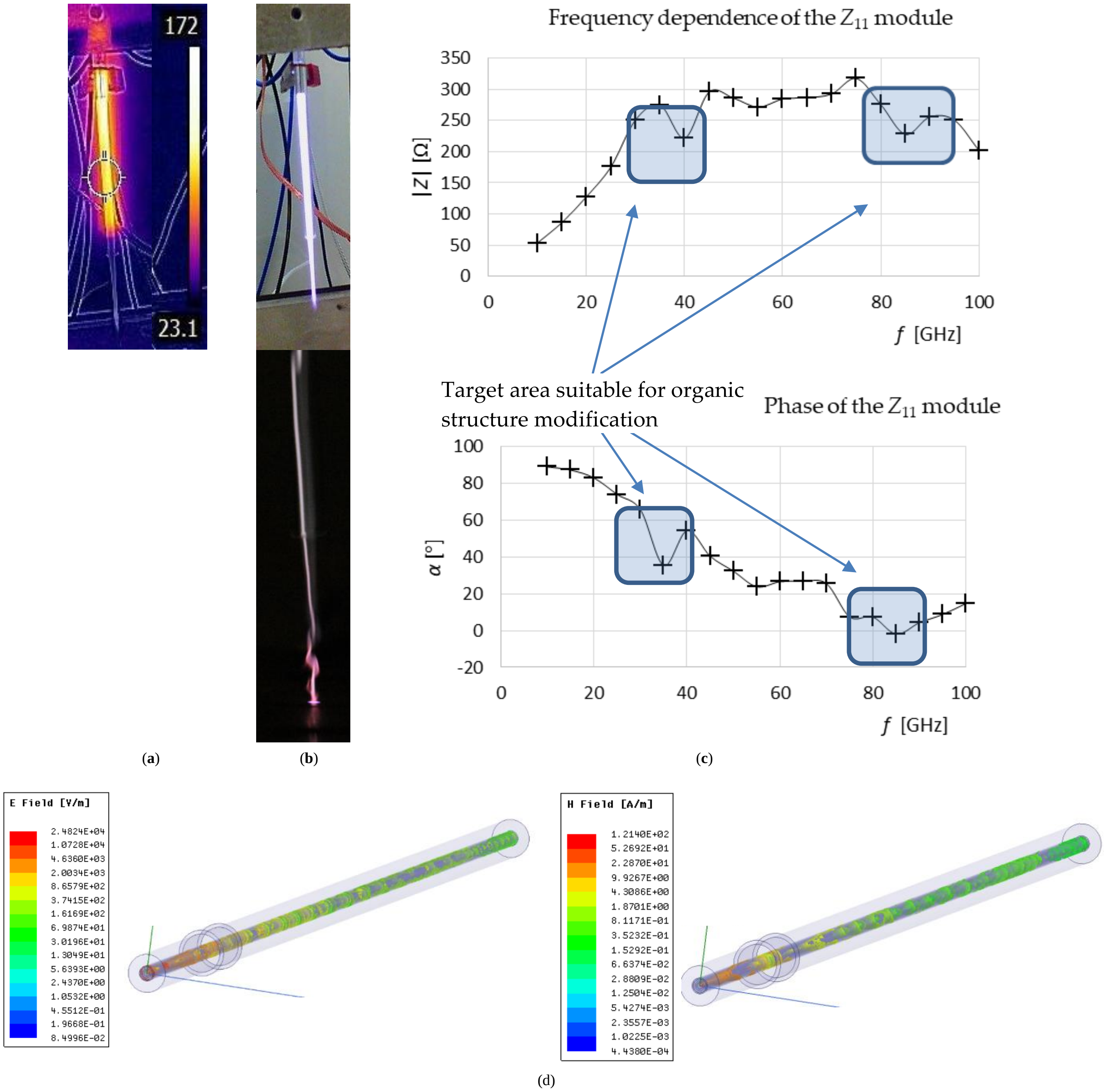

Fig. 21. Model of the channel plasma jet (EMG generator output P_{out} = 10 W): a) argon discharge in the IR spectrum; b) argon discharge in the visible spectrum; c) spectral analysis of the parameter z_{11}; d) electric field intensity E [V/m] and magnetic field intensity H [A/m], f = 40 GHz

5. Results of the numerical modeling

The analyses of the numerical models exploiting the precondition (1) for the frequency region A), Fig. 18a, show that the electric and magnetic components (having the intensities E and H, Figs. 18 and 19a) of an electromagnetic wave in close vicinity of the carbon atoms of the modeled periodic systems are distributed unevenly. Such a distribution then implies, in the time domain, a spurious signal added to the transmitted signal of the excitation electromagnetic wave and also degraded S/N parameters in the given space of the modeled structure. These effects manifest themselves as additive noise in the transmission of the useful signal, as already determined through similar tasks previously (although with geometries in the order of mm to m), [7, 19, 20].

The evaluated numerical model of the designed coaxial line for the frequency region B, Fig. 5e, displays uneven distribution of the electric and the magnetic fields having electric intensities E and magnetic flux densities B, respectively (Fig. 20a, b).

For the purposes of the modeling procedure, we set the following specifications: the anticipated limit values of the current density $J_{s,max}$ as the source of a structure's electromagnetic field (31); the limit intensity of the electric field E_t of the designed model of a given structure; and the macroscopic parameter of the electrical conductivity γ calculated from the Bohr-Sommerfeld model [36]. These parameters are indispensable for the evaluation of the electromagnetic fields and possible comparison with the experimental measurements centered on the A) and B) frequency domains.

The models calibrated in this manner, for the above conditions (1) ad A) and ad B), allow us to consider the expected results of the analyses, such as that of the DNA [28]; these models can then be formed by using not only implicit approaches and experiments, but also explicit description and evaluation of the electromagnetic field and its quantities. In application terms, nanotechnology may exploit models and analyses published previously, including those comprised in sources [6, 7, 10, 11, 14, 17, 19, 28, 33].

6. Conclusion

We designed geometrical models of graphene-, graphite-, and graphane-based nanostructures exhibiting high periodicity. In this context, a modeling approach was proposed that simulates the electromagnetic parameters of the selected periodic systems with respect to the frequency bands of the transmitted signals and electromagnetic wave propagation. We then formed a simple model to capture the propagation of an electromagnetic wave and created a hybrid numerical model for solving the simulated structures, whose element dimensions approach the wavelengths of the transmitted signal; the models include the dynamics and effects of the relative motion of parts of the system in relation to one another and an external environment, namely, an electromagnetic field.

From the perspective of numerical model design, we defined the key limit parameters (the current density, electric field intensity, and electrical conductivity) enabling us to identify, during the evaluation of the numerical analyses, the conditions that determine the temporary or permanent character of changes in a designed or fabricated structure.

In accordance with the underlying concept, basic experiments were performed to verify in the structures those properties that accompany the plasma discharge.

The experimental approach to modeling nanostructures centered on signal transmission was presented with respect to the basic parameters required for such an arranged electric line; the described model is narrowly oriented towards this purpose. We outlined the results of the basic experiments with material deposition via plasma technology. In the given context, the proposed procedures and models bring items of knowledge that are seldom discussed in relation to the propagation of EMG waves along periodic (and with not always 100% periodicity) nanomaterials. Moreover, the presented work opens the path to wholly or partially novel interpretations and options in this subdomain of quantitative structural evaluation; relevant points and activities then include calculating the maximum current load of the nanostructure and a discussion of selecting the numerical analysis technique with respect to the considered frequency spectrum.

Author Contributions: Pavel Fiala and Tibor Bachorec contributed to the theoretical part, numerical modeling, and design of the experiments, and they also co-wrote the paper; Miloslav Steinbauer and Roman Pernica conceived and designed the experiments that allowed partial verification of the effects; and Jiri Zukal with Radim Kadlec modified the manuscript graphically and participated in evaluating the experiments.

Funding: This research was funded by a grant of Czech Science Foundation (GA-20-14105S).

Acknowledgments: The research was funded and supported within a grant of Czech Science Foundation (GA-20-14105S). For the actual analyses and experiments, the infrastructure of the SIX Center was used.

References

[1] ANSYS, Ansys Multiphysics Manuals, 2020, https://www.ansys.com/.
[2] Bartusek K., Drexler P., Fiala P., et al.: Magnetoinductive Lens for Experimental Mid-field MR Tomograph. Progress in Electromagnetics Research Symposium Proceedings 1&2, 2010, 1047–1050.
[3] Bina M.: The coherent interaction between matter and radiation. The European Physical Journal Special Topics 203(1), 2012, 163–183.
[4] Castro Neto A.H., Guinea F., Novoselov K.S., Geim A.K.: The electronic properties of graphene. Reviews of modern physics 81, 2009, 109.
[5] Chao Yan, Kwang-Seop Kim, Seoung-Ki Lee, Sang-Hoon Bae, Byung Hee Hong, Jae-Hyun Kim, Hak-Joo Lee, Jong-Hyun Ahn: Mechanical and Environmental Stability of Polymer Thin-Film-Coated Graphene. ACS Nano 6(3), 2012, 2096–2103.
[6] Drexler P., Fiala P., Dohnal P., Marcon P.: The Electromagnetic Properties of a Multilayered Resonant Structure Formed from Inorganic Elements. Progress in Electromagnetics Research Symposium 2018, 2176–2183 [https://doi.org/10.23919/PIERS.2018.8597705].
[7] Drexler P., Fiala P., Dohnal P., Marcoň P.: The electromagnetic properties of a resonant structure formed from inorganic or organic elements. Progress in Electromagnetics Research Symposium 2017, 970–974 [https://doi.org/10.1109/PIERS-FALL.2017.8293274].
[8] Drexler P., Nespor D., Kadlec R., Cap M.: Numerical Analysis of Metallic Periodic Structures in THz Region. Progress in Electromagnetics Research Symposium, 2016, 2730–2733.
[9] Farhana Faisal T., Islam A., Jouini M. S., Devarapalli R. S., Jouiad M., Sassi M.: Numerical prediction of carbonate elastic properties based on multi-scale imaging. Geomechanics for Energy and the Environment 20, 2019, 100125 [https://doi.org/10.1016/j.gete.2019.100125].
[10] Fiala P., Bartušek K., Bachorec T., Dohnal P.: An Interference EMG Model of Selected Water Samples. Progress in Electromagnetics Research Symposium 2018, 775–781 [https://doi.org/10.23919/PIERS.2018.8597958].
[11] Fiala P., Bartušek K., Dědková J., Dohnal P.: EMG field analysis in dynamic microscopic/nanoscopic models of matter. Informatyka, Automatyka, Pomiary w Gospodarce i Ochronie Środowiska 9(1), 2019, 4–10.
[12] Fiala P., Drexler P., Nespor D.: A resonance-based solar element: a numerical model and micro/nano technology application. Proc. SPIE 8763, 2013, 87632A1-87632A7.
[13] Fiala P., Drexler P., Nespor D.: Principal tests and verification of a resonance-based solar harvester utilizing micro/nano technology. Microsystem Technologies 20(4-5), 2014, 845–860.
[14] Fiala P., Drexler P.: Power supply sources based on resonant energy harvesting. Microsystem Technologies-Micro-And Nanosystems-Information Storage and Processing Systems 18(7-8), 2012, 1181–1192.
[15] Fiala P., Friedl M.: Application of an electromagnetic numerical model in accurate measurement of high velocities. Informatyka, Automatyka, Pomiary w Gospodarce i Ochronie Środowiska 5(3), 2015, 3–10.
[16] Fiala P., Gescheidtova E., Jirku T.: Tuned Structures for Special THz Applications. Progress in Electromagnetics Research Symposium (PIERS 2009) 2009, 151–155.
[17] Fiala P., Kadlec R., Drexler P.: Modeling multilayered samples of inorganic and organic speckle structures. Progress in Electromagnetics Research Symposium, 2019, 2646–2651 [https://doi.org/10.1109/PIERS-Spring46901.2019.9017266].
[18] Fiala P., Machac J., Polivka J.: Microwave noise field behaves like white light. Progress In Electromagnetics Research 111(1), 2011, 311–330.
[19] Fiala P., Maxa J.: Numerical Models of a Multilayered Graphene Structure, Progress in Electromagnetics Research Symposium (PIERS-Toyama) 2018, 527–532 [https://doi.org/10.23919/PIERS.2018.8598000].
[20] Fiala P., Nespor D., Drexler P., Steinbauer M.: Numerical Model of a Nanoelectric Line from a Graphene Component. Microsystem Technologies 1, 2016, 1–18.
[21] Fiala P., Szabó Z., Friedl M.: EMHD models respecting relativistic processes of trivial geometries. Progress in Electromagnetics Research Symposium, 2011, 95–98.
[22] Fiala P., Werner P., Osmera P., Dohnal P.: Using a multiscale toroidal element to model a hydrogen atom. Progress in Electromagnetics Research Symposium - Fall (PIERS - FALL), 2017, 956–960.
[23] Fiala P., Werner P., Osmera P., Gescheidtova E., Drexler P., Kriz T.: Periodical structures and multiscale modelling. Progress in Electromagnetics Research Symposium, 2017, 1698–1703.
[24] Geim A.K., Novoselov K.S.: The rise of graphene. Nature Materials 6(3), 2009, 183-91.
[25] Haňka L.: Teorie elektromagnetického pole, paperback SNTL. Praha 1971.
[26] Heyrovska R., Narayan S.: Structures of Molecules at the Atomic Level: Caffeine and Related Compounds. Philippine Journal of Science 140(2), 2008, 119–124.
[27] Heyrovska R.: Atomic Structures of Graphene, Benzene and Methane with Bond Lengths as Sums of the Single, Double and Resonance Bond Radii of Carbon. General Physics, 2008, arXiv:0804.4086
[28] Heyrovska R.: Methane, benzene and graphene, internal research report. 2008 http://arxiv.org/ftp/arxiv/papers/0804/0804.4086.pdf .
[29] Holmes J., Ishimaru A.: Relativistic communications effects associated with moving space antennas. IEEE Transactions on Antennas and Propagation 17(4), 1969, 484–488.
[30] Hui F., Pan Ch., Shi Y., Ji Y., Grustan-Gutierrez E., Lanza M.: On the use of two dimensional hexagonal boron nitride as dielectric. Microelectronic Engineering 163, 2016, 119–133.
[31] Jović D., Jaćević V., Kuča K., Boríšev I., Mrdjanovic J., Petrovic D., Djordjevic A.: The puzzling potential of carbon nanomaterials: General properties, application, and toxicity. Nanomaterials 10(8), 2020, 1–30 [https://doi.org/10.3390/nano10081508].
[32] Kadlec R., Drexler P.: Analysing the Responses of Layered Materials with Varied Parameters. Progress in Electromagnetics Research Symposium, 2017, 988–992.
[33] Kadlec R., Fiala P.: The Response of Layered Materials to EMG Waves from a Pulse Source. Progress In Electromagnetics Research M 42(1), 2015, 179–187.
[34] Kikuchi H.: Electrohydrodynamics in dusty and dirty plasmas, gravito-electrodynamics and EHD. Kluwer, Boston 2001.
[35] Kim H.-J., Kang G.-H., Kim S.-H., Park S.: Enhancement of Electromagnetic Wave Shielding Effectiveness of Carbon Fibers via Chemical Composition Transformation Using H_2 Plasma Treatment. Nanomaterials 10, 2020, 1611.
[36] Kragh H.: Niels Bohr and the Quantum Atom: The Bohr Model of Atomic Structure 1913–1925. Oxford Scholarship online, 2012 [https://doi.org/10.1093/acprof:oso/9780199654987.001.0001].
[37] Madrova T.: Supravodivost ve čtvrtém skupenství (Superconductivity in the fourth state) – diploma thesis. Brno University of Technology. Brno 2020.
[38] Marinho B., Ghislandi M., Tkalya E., et al.: Electrical conductivity of compacts of graphene, multi-wall carbon nanotubes, carbon black, and graphite powder. Powder Technology 221, 2012, 351–358.
[39] Maxwell J. C.: A treatise on electricity and magnetism. London Macmillan and co., Publishers to the University of Oxford, Oxford 1873.
[40] Ozmaian M., Fathizadeh A., Jalalvand M. et al.: Diffusion and self-assembly of C60 molecules on monolayer graphyne sheets. Sci Rep 6, 2016, 21910, [https://doi.org/10.1038/srep21910].

[41] Shin E., Lee B., Jo S., Jeong G.: Investigation of early stage of carbon nanotube growth on plasma-pretreated inconel plates and comparison with other superalloys as substrates. Nanomaterials 10(8), 2020, 1–11 [https://doi.org/10.3390/nano10081595].

[42] Steinbauer M., Fiala P., Szabo Z., Bartusek K.: Experiments with accuracy of the air ion field measurement. Advances in Electrical and Electronic Engineering 8(7), 2008, 276–279.

[43] Stratton J. A.: Electromagnetic Theory. Wiley, New York 1941.

[44] Sun Y., Luo S., Sun H. et. al.: Engineering closed-cell structure in lightweight and flexible carbon foam composite for high-efficient electromagnetic interference shielding. Carbon 136, 2018, 299–308.

[45] Szalay S., Barcza G., Szilvási T., et al.: The correlation theory of the chemical bond. Nature-Scientific Reports 7, 2017, 2237 [https://doi.org/10.1038/s41598-017-02447-z].

[46] Urban R., Drexler P., Fiala P., Nespor D.: Numerical Model of a Large Periodic Structure. Proc. PIERS, 2014, 2350–2354.

[47] Van Bladel J.: Motion of a conducting loop in a magnetic field. IEE Proceedings 13.5, Pt. A, no. 4, 1988, 217–222.

[48] Weisstein E. W.: Galerkin Method. MathWorld, 2015, http://mathworld.wolfram.com/GalerkinMethod.html.

[49] Werner P.: Modeling the basic ring structures in elementary particles of matter. DTEEE FEEC BUT, Brno 2018.

[50] Yang S. L., Sobota J. A., Howard C. A., Pickard C. J., Hashimoto M., Lu D. H., Mo S. K., Kirchmann P. S., Shen, Z. X.: Superconducting graphene sheets in CaC_6 enabled by phonon-mediated interband interactions. Nature Comunnications 5(1), 2014, 3493.

[51] Yarim C., Daybelge U., Sofyali A.: Search for the general relativistic effects on the motion of a spacecraft. 4th International Conference Recent Advances in Space Technologies RAST'09, 2009, 553–556.

[52] Zhang D., Ranjan B., Tanaka T., Sugioka K.: Multiscale hierarchical micro/nanostructures created by femtosecond laser ablation in liquids for polarization-dependent broadband antireflection. Nanomaterials 10(8), 2020, 1–15 [https://doi.org/10.3390/nano10081573].

Assoc. Prof. Miloslav Steinbauer
e-mail: steinbau@feec.vutbr.cz

Miloslav Steinbauer has been an associate professor in electrical engineering at Brno University of Technology since 2010. Between 1995 and 2000, he pursued basic research in the simulation of reflections, crosstalk, and distortion on multi-wire lines. Since 2003, he has investigated applications of nuclear magnetic resonance, participated in experiments involving electrical impedance tomography, measured extremely small and extremely fast signals, and designed sensors and methodology to measure parameters of ultrashort electromagnetic pulses with the power of 100 MW and to monitor fast unrepeatable voltage and current waveforms (up to 10 kA, 100 kV). Since 2015, he has also focused on NQR spectroscopy. Miloslav Steinbauer is a regular reviewer of IEEE and PIER & JEMWA journals.

https://orcid.org/0000-0002-1358-6974

M.Sc. Roman Pernica
e-mail: xperni05@stud.feec.vutbr.cz

Roman Pernica received an M.Sc. in electrical engineering from Brno University of Technology (BUT) in 2001. Since then he has been active in HV device design, delivering models and ensuring their implementation. He is currently working towards a Ph.D. at BUT, investigating the influence of nanosurfaces on the electrical strength and HV properties of material interfaces.

https://orcid.org/0000-0002-6672-0137

M.Sc. Jiri Zukal
e-mail: xzukal03@stud.feec.vutbr.cz

Jiří Zukal was born in Brno, the Czech Republic, in 1969. He received an M.Sc. in electrical engineering and computer science from Brno University of Technology (BUT) in 1995. He has worked as a sales technician in his field of expertise; his interests are within electrical applications in the automotive industry. Jiří Zukal is a member of the Innovation Scout, Automotive OEM Professionals, and UMI groups and communities. As an IEEE.technical support aide for the EEU region, he focuses on electrical mobility projects. He is currently pursuing Ph.D. studies in robust harvesting at BUT.

https://orcid.org/0000-0002-5550-587X

Ph.D. Radim Kadlec
e-mail: kadlec@feec.vutbr.cz

Radim Kadlec received a Ph.D. degree in electrical engineering from Brno University of Technology (BUT), Brno, the Czech Republic, in 2014. Since 2008, he has been with the Department of Theoretical and Experimental Electrical Engineering, BUT. His research interests are directed towards the analysis and numerical modeling of light conditions at the interface of mediums and also include the modeling of electromagnetic waves. Further, Radim Kadlec focuses on electrical installations, smart homes, and safety in electrical engineering. Since 2015, he has been a member of the research team within the INWITE project, which comprises the research into innovative concepts of wireless communication systems to provide high reliability, speed, and capacity, jointly ensuring widely applicable digital security.

https://orcid.org/0000-0002-3252-4859

Ph.D. Tibor Bachorec
e-mail: bachorec@feec.vutbr.cz

Tibor Bachorec received an M.Sc. (1992) in microelectronics from Brno University of Technology (BUT). From 1989 to 1990, he had studiednumerical methods for physical computations, together with electron and ion optics. In 2006, he obtained a Ph.D. in theoretical electrical engineering. He has engaged in collaborations with industry to execute projects centered on applied numerical modeling, such as the following ones: 2008–2011: Meyer Werft - Jos. L. Meyer GmbH, Papenburg, Germany: Optimization calculations of vessel parts; 2006 CAD-FEM GmbH, Aadorf, Switzerland: Numerical modeling for nuclear power; 2005 CAD-FEM GmbH, Chemnitz, Germany: Numerical modeling of trainsets; 2004 Rücker GmbH, Hamburg, Germany: Numerical modeling for the aerospace industry; 2003 CAD-FEM GmbH, Burgdorf, Germany: Numerical modeling of aircraft elements; 2003 CAD-FEM GmbH, Stuttgart, Germany: Numerical simulations of flow in hydraulic systems; 2001–2002 Meyer Werft-Jos. L. Meyer GmbH, Papenburg, Germany: Optimization calculations of vessel parts.

https://orcid.org/0000-0002-6249-1509

Prof. Pavel Fiala
e-mail: fialap@feec.vutbr.cz

Pavel Fiala received a Ph.D. in electrical engineering from Brno University of Technology (BUT) in 1998. Since 2014,03, he has been a full professor in theoretical electrical engineering. His professional interests are within modeling and analyzing coupled field problems via numerical methods formulated with partial differential equations by using the finite element, boundary element, and finite difference methods.. Pavel Fiala is a member of the SPIE, APS, OSA, Electromagnetic Academy, Cambridge, USA (since 2007), and a reviewer of the Elsevier, IEEE, and Springer journals.

https://orcid.org/0000-0002-7203-9903

otrzymano/received: 4.11.2020 *przyjęto do druku/accepted: 10.12.2020*

http://doi.org/10.35784/iapgos.2346

X-RAY DIFFRACTION AND MÖSSBAUER SPECTROSCOPY INVESTIGATIONS OF THE (Al, Ni, Co)-DOPED $AgFeO_2$ SYNTHESIZED BY HYDROTHERMAL METHOD

Karolina Siedliska
Lublin University of Technology, Department of Electronics and Information Technologies, Lublin, Poland

Abstract. *Delafossite $AgFeO_2$, $AgFe_{0.9}Al_{0.1}O_2$, $AgFe_{0.9}Ni_{0.1}O_2$, and $AgFe_{0.9}Co_{0.1}O_2$ powders were synthesized by hydrothermal method. The structural analysis and hyperfine interactions investigations were performed by X-ray diffraction and the Mössbauer spectroscopy. It was found that the (Al, Ni, Co)-doped delafossite phases with traces of metallic silver can be obtained during hydrothermal synthesis. Investigations revealed that the type of the incorporated element has an impact on the structural properties of the obtained delafossites. However, doping of cobalt, nickel, and alumina ions to the $AgFeO_2$ delafossite structure does not cause significant changes in the values of the hyperfine interactions parameters. The of the Mössbauer spectra confirm the paramagnetic character of the obtained compounds at room temperature.*

Keywords: delafossites, hydrothermal synthesis, X-ray diffraction, Mössbauer spectroscopy

BADANIA METODĄ DYFRAKCJI PROMIENIOWANIA X ORAZ SPEKTROSKOPII EFEKTU MÖSSBAUERA $AgFeO_2$ DOMIESZKOWANEGO JONAMI Co, Ni i Al WYTWARZANEGO METODĄ HYDROTERMALNĄ

Streszczenie. *Proszkowe próbki delafosytów $AgFeO_2$, $AgFe_{0.9}Al_{0.1}O_2$, $AgFe_{0.9}Ni_{0.1}O_2$, and $AgFe_{0.9}Co_{0.1}O_2$ zostały wytworzone metodą hydrotermalną. Badania pozwalające na analizę strukturalną oraz oszacowanie parametrów oddziaływań nadsubtelnych przeprowadzono z wykorzystaniem dyfrakcji rentgenowskiej oraz spektroskopii efektu Mössbauera. Udowodniono, że za pomocą metody hydrotermalnej istnieje możliwość wytworzenia delafosytu $AgFeO_2$ domieszkowanego jonami glinu, niklu i kobaltu z niewielką ilością zanieczyszczeń metalicznym srebrem. Badania wykazały, że rodzaj domieszki ma wpływ na właściwości strukturalne otrzymanych materiałów. Domieszkowanie jednak nie wpłynęło znacząco na zmiany wartości parametrów oddziaływań nadsubtelnych. Kształt zarejestrowanych widm mössbauerowskich potwierdza paramagnetyzm otrzymanych materiałów w temperaturze pokojowej.*

Słowa kluczowe: delafosyty, synteza hydrotermalna, dyfrakcja rentgenowska, spektroskopia mössabuerowska

Introduction

Delafossites are an interesting class of materials with a wide range of physical properties due to a variety of chemical compositions. They are described by the general formula of ABO_2, where A denotes monovalent cation of the *semi*-noble or the noble metal, i.e., Ag, Cu, Pd, or Pt. Site B may be occupied by trivalent cation of a. transition metal element (e.g., Cr, Fe, Mn, Ni, Co) or b. *p*-block element (e.g., Al, Ga, In, Tl) or c. rare earth element (e.g., Sc, La, Nd, Eu) [11]. Delafossite structure is depicted as stacking of two alternated layers. The first one consists of slightly distorted edge-shared $B^{III}O_6$ octahedra, the latter one is a monovalent layer of the closed-packed A^I ions. Linear coordination of A^I by two oxygen atoms along the *c*-axis leads to interlinkage of the adjacent BO_2 layers, where each oxygen is coordinated by four cations (one in the A-position and three in the B-site). Considering the stacking pattern of the alternated layers, the delafossite structure can form two polytypes, i.e., rhombohedral 3R type (space group R-3m) and hexagonal 2H polytype (space group I6_3/*mmc*) [15]. To date, numerous ABO_2 compounds have been reported with high *p*-type conductivity (10^{-2}–10^2 $S \cdot cm^{-1}$) and high optical transparency (50%–85%), dependent on their chemical compositions and film depositions method [16]. These delafossite oxides could play important role in diverse photoelectronic and photoelectrochemical applications, such as field electron emitters, light-emitting diodes, solar cells, photocatalysts, functional windows, etc. [1].

Recently, much attention has been paid to developing new magnetic materials, e.g., multiferroics, diluted magnetic semiconductors, or magneto-optic materials [8, 13]. Delafossites also seem to be promising candidates for these purposes. Iron-based compounds, with the general formula $AFeO_2$ (where A denotes Ag or Cu elements), exhibit quite exotic magnetic properties. Below the Néel temperature, they have a complicated magnetic structure caused by frustrated exchange interactions induced by the triangular lattice system of Fe ions. This type of spins arrangement is responsible for inducing ferroelectric polarization, which can be described by the inverse Dzyaloshinskii-Moriya effect [9]. It is the reason, that both iron-based compounds, $AgFeO_2$, and $CuFeO_2$ are identified as multiferroics in the low temperature regime. Nevertheless, due to difficulties with the preparation of high-quality samples, the explaining of the iron-based delafossites properties is still the open question.

Modification of the delafossite properties can be realized by the ion substitution of trivalent B^{3+} cation [12, 19]. Recently, it was reported that the nickel doping of silver ferrite enhances significantly the $AgFeO_2$ catalytic activity [21]. Likewise, the cobalt doping in copper delafossites induces interesting phenomena. Dong et. al synthesized thin films of cobalt doped transparent $CuAlO_2$ semiconductors which exhibited weak ferromagnetism at room temperature [3]. Elkhouni et al. presented several papers devoted to the cobalt substitution of the $CuCrO_2$ and proved that the incorporation of the magnetic ions can induce new spin ordering and enhance magnetization [5, 6]. Wheatley et al. showed that the addition of the diluted amounts of Al to the $CuFeO_2$ host greatly improves samples conductivity [20].

To our knowledge, studies of $AgFeO_2$ delafossite doped with different ions at Fe position have been carried out only by several researchers (e.g., doping Cr to $AgFeO_2$ reported in [4]). Therefore, the lack of experimental data motivates further studies on the incorporation of the Al, Ni, and Co ions into the delafossite structure. Recognizing the structural properties of the doped $AgFeO_2$ will enrich knowledge about new delafossite family members and give information over possibilities of modifications of their physical properties in purpose to obtain advanced materials.

In this work, we synthesized $AgFeO_2$, $AgFe_{0.9}Al_{0.1}O_2$, $AgFe_{0.9}Ni_{0.1}O_2$, and $AgFe_{0.9}Co_{0.1}O_2$ samples by the hydrothermal method. The main goal of this study was to determine the impact of doping on the structural properties and hyperfine interactions parameters. The materials were characterized by X-ray diffraction and Mössbauer spectroscopy.

1. Experimental methods

The samples of $AgFeO_2$, $AgFe_{0.9}Al_{0.1}O_2$, $AgFe_{0.9}Ni_{0.1}O_2$, and $AgFe_{0.9}Co_{0.1}O_2$ were synthesized by the hydrothermal method. All of the chemicals were purchased with analytical grade and used without further purification. As started reagents nitrates $Ag(NO_3)$, $Fe(NO_3)_3 \cdot 9H_2O$, $Al(NO_3)_3 \cdot 9H_2O$, $Ni(NO_3)_2 \cdot 6H_2O$, $Co(NO_3)_2 \cdot 6H_2O$, and NaOH were utilized. Firstly, the pure silver ferrite was synthesized. The iron and silver nitrates were dissolved in distilled water in the molar ratio of 1:1. Then, the NaOH solution was added slowly until the pH~12 was reached. Afterward, the obtained solution was stirred for 15 minutes to obtain a homologous precursor. Then the prepared precursor was transferred into a 100-mL Teflon-lined stainless-steel autoclave and placed into an oven at 180°C for 24 h. After cooling to room temperature, the brownish precipitate was collected and washed with deionized water and absolute ethanol several times. Finally, the product was dried in an oven at 180°C overnight to achieve $AgFeO_2$ powder. For the purpose to obtain $AgFe_{0.9}Al_{0.1}O_2$, $AgFe_{0.9}Ni_{0.1}O_2$, and $AgFe_{0.9}Co_{0.1}O_2$ similar procedure was employed. The only difference was in the molar ratios of the starting reagents, which followed the formulas of the compounds listed above.

X-ray diffraction (XRD) studies were performed using a PanAlitical X'Pert Pro diffractometer working with a Cu lamp. For the phase and structural analysis, the X'Pert HighScore Plus software equipped with the ICDD PDF2 database was used. ^{57}Mössbauer spectra (MS) were registered at room temperature using a Polon spectrometer working in a transmission geometry and at constant acceleration mode. As a source of 14.4 keV gamma radiation of the ^{57}Co in a rhodium matrix was used. All values of the isomer shift within this paper are related to the α-Fe standard.

2. Results and discussion

Figure 1 shows the XRD patterns of $AgFeO_2$, $AgFe_{0.9}Al_{0.1}O_2$, $AgFe_{0.9}Ni_{0.1}O_2$, and $AgFe_{0.9}Co_{0.1}O_2$ powders registered at room temperature. In the case of an un-doped sample of $AgFeO_2$, in the pattern only peaks characteristic for the silver ferrite phase are visible. It confirmed the purity of the delafossite phase. Comparison of the results with database standards corresponding to the hexagonal polytype 2*H*-$AgFeO_2$ (PDF2 Card No. 01-075-2147) and rhombohedral 3*R*-$AgFeO_2$ (PDF2 Card No. 00-029-1141) proved that the mixture of both phases was obtained. The lattice parameters for the un-doped sample were determined from the diffractograms, and they were as follows: a = 3.039(1) Å and c = 12.390(1) Å for 2*H* polytype, and a = 3.039(1) Å and c = 18.588(5) Å for 3*R* polytype. Parameters are comparable for all studied Al, Ni, and Co-doped silver ferrites. Their values are slightly higher in comparison to the results obtained in our work for $AgFeO_2$ synthesized by the co-precipitation method [17]. Moreover, the significant anisotropic broadening of diffraction lines observed in the case of co-precipitated materials is not seen now in XRD patterns registered for $AgFe_{0.9}Al_{0.1}O_2$ and $AgFe_{0.9}Co_{0.1}O_2$ (Fig. 1). It can mean a better level of crystallinity of the hydrothermally synthesized materials and a lower amount of defects in the crystalline structure in comparison to co-precipitated powder samples of $AgFeO_2$.

In the case of $AgFe_{0.9}Al_{0.1}O_2$, $AgFe_{0.9}Ni_{0.1}O_2$, and $AgFe_{0.9}Co_{0.1}O_2$ samples additional peaks, marked as metallic silver, are visible in the diffractograms (Fig.1). Similarly, as it was reported in [17] for the $AgFe_{1-x}Co_xO_2$ (x = 0–0.2) series of samples synthesized by the co-precipitation method there were no peaks indicated another impurity phase. The absence of the CoO, NiO, and Al_2O_3 oxides can prove that our attempt the replacing the Fe ions with Al, Ni, and Co ions in the delafossite structure was realized successfully.

Bringing the assumption that B^{3+} should replace Fe^{3+} ions during substitution, the appearance of metallic silver is quite unexpected. Nevertheless, because cobalt(II) nitrate and nickel(II) nitrate were used as starting chemicals during synthesis, we postulate that in our case trivalent iron ions were substituted by divalent cobalt and nickel ions. This assumption may explain the appearance of metallic silver as a secondary phase in the case of the $AgFe_{0.9}Ni_{0.1}O_2$ and $AgFe_{0.9}Co_{0.1}O_2$ samples. The lower valence of cobalt and nickel ions than Fe^{3+} may be the reason for the emergence of oxygen vacancies in the octahedral layer, which at the same time causes the lack of oxygen in some linear bonds O-Ag-O. Similar interpretations were reported in [2, 7] where the substitutions of B-site trivalent ions in $CuBO_2$ delafossites by cations like Co^{2+}, Sn^{4+} induced the appearance of the secondary phases like CuO oxide during the synthesis process. Thus, obtained results suggest that the substituting ions were rather Co^{2+} and Ni^{2+} than trivalent ions and obtained powders are non-stoichiometric compounds with oxygen deficiency described by formulas $AgFe_{0.9}Ni_{0.1}O_{2-\delta}$ and $AgFe_{0.9}Co_{0.1}O_{2-\delta}$.

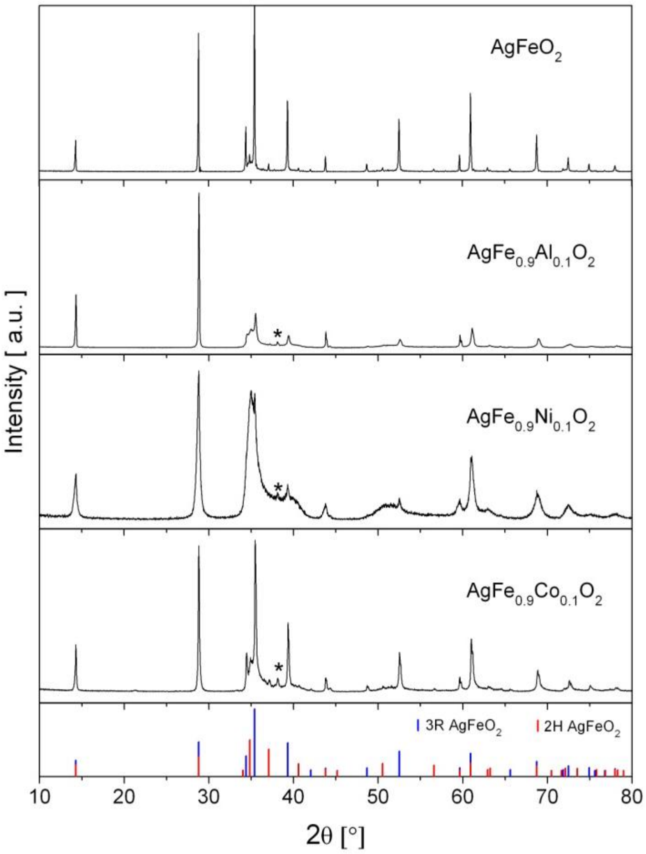

Fig. 1. XRD patterns registered for $AgFeO_2$, $AgFe_{0.9}Al_{0.1}O_2$, $AgFe_{0.9}Ni_{0.1}O_2$, and $AgFe_{0.9}Co_{0.1}O_2$ samples; asterisks indicate metallic silver peak

Nevertheless, the above assumptions can not explain the appearance of the silver impurities in the case of $AgFe_{0.9}Al_{0.1}O_2$. The valence of both B-site ions is +3, so we can not assume the oxygen deficiencies. A possible explanation can be taken from Zwiener et. al [22]. They conducted comprehensive studies on the synthesis of $AgAlO_2$ under hydrothermal conditions and found that only optimized reaction conditions allow obtaining pure phase $AgAlO_2$ (temperature 210°C, reaction time 30 h). According to this work, the presence of the Ag by-product might be connected with the limited stability of the delafossite phase under the hydrothermal reaction conditions. Because of the lack of literature data confirmed these findings, we conclude that the appearance of the small amount of metallic silver in the $AgFe_{0.9}Al_{0.1}O_2$ sample might be connected with the complexity of the hydrothermal reaction in general and this problem needs further studies.

Moreover, the shapes of the diffractograms for particular samples are quite different. For $AgFeO_2$, diffraction lines are sharp and well separated. The original shape is more or less maintained for samples doped with nickel and cobalt ions, but the intensities of particular peaks are quite different. It may be connected with the appearance of some strains of the crystalline structure induced by the introduction to the structure ions with different values of radii at B position (Fe^{3+} – 0.645Å, Ni^{2+} – 0.69Å, Co^{2+} – 0.745Å, Al – 0.535Å) [14].

For the sample $AgFe_{0.9}Ni_{0.1}O_2$, significant anisotropic broadening of diffraction lines is observed. It may be seen that only peaks belonging to the (00*l*) family are sharp and well separated, but the peaks connected with the (10*l*) are much more broadened. It suggests that crystallite sizes ranged from a few to several dozen nm. Similar results were observed for co-precipitated $AgFeO_2$ in [18], where the shape of the spectra suggested that the powder particles have an elongated shape in the one crystallographic direction.

It is also worth mentioning that all the samples are a mixture of two polytypes, 2*H* and 3*R*. In the case of the un-doped sample, the polytype content was estimated to be as follows: 2*H* – 5%, and for 3*R* – 95%. Likewise, for the $AgFe_{0.9}Al_{0.1}O_2$ and $AgFe_{0.9}Co_{0.1}O_2$, the rhombohedral polytype is the dominating phase. However, for $AgFe_{0.9}Ni_{0.1}O_2$ it has been estimated that the ratio of the two polytypes is approximately 1:1. Hence, one can conclude, that the type of doped ions also has an impact on the phase composition of the obtained sample.

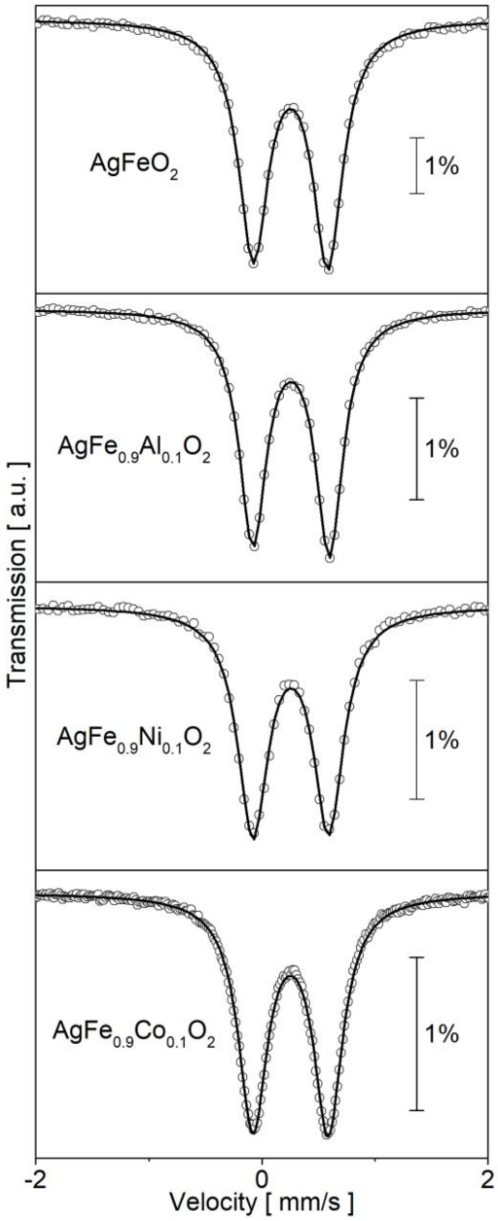

Fig. 2. Room-temperature Mössbauer spectra of the $AgFeO_2$, $AgFe_{0.9}Al_{0.1}O_2$, $AgFe_{0.9}Ni_{0.1}O_2$, and $AgFe_{0.9}Co_{0.1}O_2$ samples

Results of the Mössbauer spectroscopy studies are presented in Fig. 2 and Table I. All the Mössbauer spectra registered at room temperature for the investigated samples consist of one quadrupole doublet corresponding to the delafossite phase. It confirms their paramagnetic character. The obtained hyperfine interactions parameters are summarized in Table 1. Values of isomer shifts (δ) and quadrupole splitting (Δ) are similar for all investigated samples and are in good agreement with literature data reported for the $AgFeO_2$ compound [10]. It is worth to mention that the numerical fitting of Mössbauer spectra was made by one component despite 3*R* and 2*H* polytypes coexisting in the material. This is because ^{57}Fe ions have the same nearest neighborhood in both structures, namely iron ions have 6 oxygen ions in the first, 6 iron ions in the second, and 6 silver ions in the third coordination sphere. Moreover, the interatomic distances between iron and the nearest neighbors are practically the same for both polytypes [18]. Thus, the well-resolved doublet with the value of the isomer shift 0.362(1) mm/s seen in MS spectra registered for un-doped sample confirms the existence of high-spin Fe^{3+} ions in an octahedral oxygen environment. The values of isomer shift determined for the $AgFe_{0.9}Al_{0.1}O_2$, $AgFe_{0.9}Ni_{0.1}O_2$, and $AgFe_{0.9}Co_{0.1}O_2$ samples confirm that only high-spin Fe^{3+} ions in the octahedral coordination are present in the studied materials. Rather high values of the quadrupole splitting mean that a strong electric field gradient (EFG) occurs in the Fe^{3+} position in the crystalline lattice.

The width of the spectral lines Γ (half-width at half maximum) for the un-doped sample and doped samples are slightly higher from the natural width (Γ = 0.12 mm/s according to the certificate of the Mössbauer source manufactured by RITVERC GmbH). No distinct differences in the width lines values are seen. Hence, it may be surmised that the incorporation of the Al, Ni, and Co ions in the delafossite structure has random distribution.

Table 1. The results from the fitting of the Mössbauer spectra registered at room temperature: δ – isomer shift, Δ – quadrupole splitting, Γ – the width of spectral lines. The uncertainty of all values is 0.001 mm/s

Sample	δ [mm/s]	Δ [mm/s]	Γ [mm/s]	χ
$AgFeO_2$	0.362	0.658	0.159	0.89
$AgFe_{0.9}Al_{0.1}O_2$	0.366	0.676	0.145	0.95
$AgFe_{0.9}Ni_{0.1}O_2$	0.360	0.666	0.156	1.26
$AgFe_{0.9}Co_{0.1}O_2$	0.363	0.668	0.160	1.12

3. Conclusions

Delafossite $AgFeO_2$, $AgFe_{0.9}Al_{0.1}O_2$, $AgFe_{0.9}Ni_{0.1}O_2$, and $AgFe_{0.9}Co_{0.1}O_2$ fine powders were successfully synthesized by hydrothermal method. The XRD study proved the obtaining of (Al, Ni, Co)-doped delafossite phases with traces of metallic silver as the secondary phase. In the case of $AgFe_{0.9}Ni_{0.1}O_2$, and $AgFe_{0.9}Co_{0.1}O_2$, the lack of cobalt and nickel-containing secondary products suggests that Co^{2+} and Ni^{2+} substitute Fe^{3+} ions in delafossite lattice. The presence of metallic silver in the $AgFe_{0.9}Al_{0.1}O_2$ sample can be explained under the assumption of the complexity of the hydrothermal process. Moreover, some changes in the $AgFeO_2$ structure depending on the type of the incorporated ion were seen.

The Mössbauer spectroscopy studies revealed no distinct changes in the values of hyperfine interactions parameters. They confirm the paramagnetic character of the obtained samples at room temperature. Obtained results suggest that the hydrothermal synthesis causes the random distribution of the incorporated ions in the silver ferrite structure.

Acknowledgments

The author wants to thank prof. Elżbieta Jartych for Her support and fruitful discussions, dr Rafał Panek for carrying out the X-ray diffraction measurements, and dr Tomasz Pikula for helping in the interpretation of the XRD results.

References

[1] Abdelhamid H. N.: Delafossite Nanoparticle as New Functional Materials: Advances in Energy, Nanomedicine and Environmental Applications. Materials Science Forum 832, 2015, 28–53.

[2] Daniel U., Dabici A., Iuliana S., Miclau M.: Photovoltaic Performance of Co-Doped $CuCrO_2$ for p-Type Dye-Sensitized Solar Cells Application. Energy Procedia 112, 2017 497–503.

[3] Dong C. J., Yu W. X., Xu M., Cao J. J., Zhang Y., Chuai Y. H., Wang Y. D.: Evidence of Room Temperature Ferromagnetism in Co-Doped Transparent $CuAlO_2$ Semiconductor. Journal of Alloys and Compounds 512, 2012 195–98.

[4] El-Bassuony A. A. H., Abdelsalam H. K.: Attractive Improvement in Structural, Magnetic, Optical, and Antimicrobial Activity of Silver Delafossite by Fe/Cr Doping. Journal of Superconductivity and Novel Magnetism 31, 2018, 3691–3703.

[5] Elkhouni T., Amami M., Colin C. V., Strobel P., Salah A. B: Synthesis, Structural and Magnetic Studies of the $CuCr_{1-x}Co_xO_2$ Delafossite Oxide. Journal of Magnetism and Magnetic Materials 330, 2013, 101–105.

[6] Elkhouni T., Amami M., Colin C. V., Salah A. B: Structural and Magnetoelectric Interactions of (Ca, Mg)-Doped Polycrystalline Multiferroic $CuFeO_2$. Materials Research Bulletin 53, 2014, 151–57.

[7] Gall R. B., Ashmore N., Marquardt M. A., Tan X., Cann D. P.: Synthesis, Microstructure, and Electrical Properties of the Delafossite Compound $CuGaO_2$. Journal of Alloys and Compounds 391, 2005, 262–66.

[8] Khomskii D. I.: Classifying Multiferroics: Mechanisms and Effects. Physics 2, 2009, 1–7.

[9] Khomskii D. I.: Ferroelectrics, Magnetoelectrics, and Multiferroics. In Transition Metal Compounds. Cambridge University Press, Cambridge 2014, 269–309.

[10] Presniakov I., Rusakov V., Sobolev A., Gapchka A., Matsnev M., Belik A. A.: ^{57}Fe Mössbauer Study of New Multiferroic $AgFeO_2$. Hyperfine Interactions 226, 2014, 41–50.

[11] Prewitt C. T., Robert D. S., Rogers D. B.: Chemistry of Noble Metal Oxides. II. Crystal Structures of Platinum Cobalt Dioxide, Palladium Cobalt Dioxide, Copper Iron Dioxide, and Silver Iron Dioxide. Inorganic Chemistry 10, 1971, 719–723.

[12] Ray N., Gupta V., Sarma L., Kush P., Nag J., Sapra S.: Tuning the Electronic and Magnetic Properties of $CuAlO_2$ Nanocrystals Using Magnetic Dopants. ACS Omega 3, 2018, 509–513.

[13] Sato K., Katayama-Yoshida H.: First Principles Materials Design for Semiconductor Spintronics. Semiconductor Science and Technology 17, 2002, 367–76.

[14] Shannon R. D.: Revised Effective Ionic Radii and Systematic Studies of Interatomic Distances in Halides and Chalcogenides. Acta Crystallographica: Section A 32, 1976 751–767.

[15] Shannon R. D., Rogers D. B., Prewitt C. T.: Chemistry of Noble Metal Oxides. I. Syntheses and Properties of ABO_2 Delafossite Compounds. Inorganic Chemistry 10, 1971, 713–718.

[16] Sheets W. C., Stampler E. S., Bertoni M. I., Sasaki M., Marks T. J., Mason T. O., Poepplemeier K. R.: Silver Delafossite Oxides. Inorganic Chemistry 47, 2008, 2696–2705.

[17] Siedliska K., Pikula T., Franus W., Jartych E.: X-Ray Diffraction and ^{57}Fe Mössbauer Spectroscopy Studies of Co-Doped $AgFeO_2$. Acta Physica Polonica A 134, 2018, 1040–1043.

[18] Siedliska K., Pikula T., Surowiec Z., Chocyk D., Jartych E.: X-ray Diffraction and ^{57}Fe Mössbauer Spectroscopy Studies of Delafossite $AgFeO_2$ Prepared by Co-Precipitation Method. Journal of Alloys and Compounds 690, 2017, 182–188.

[19] Taddee C., Kamwanna T., Amornkitbamrung V.: Characterization of Transparent Superconductivity Fe-doped $CuCrO_2$ Delafossite Oxide. Applied Surface Science 380, 2016, 237–242.

[20] Wheatley R. A., Roble M., Gence L., Acuna C., Rojas-Aedo R., Hidalgo-Rojas D., Guzmann-De La Creda D. E., Vojkovic S., Seifert B., Volkmann U. G., Diaz-Droguett D. E.: Structural, Optoelectronic and Photo-Thermoelectric Properties of Crystalline Alloy $CuAl_xFe_{1-X}O_2$ Delafossite Oxide Materials. Journal of Alloys and Compounds, 2020, in press.

[21] Zhao Y., An H., Dong G., Feng J., Wei T., Ren Y., Ma J.: Oxygen Vacancies Induced Heterogeneous Catalysis of Peroxymonosulfate by Ni-Doped $AgFeO_2$ Materials: Evolution of Reactive Oxygen Species and Mechanism. Chemical Engineering Journal 388, 2020, 124371.

[22] Zwiener L., Jones T., Wolf E. H., Girgdies F., Plodinec M., Klyushin A. Y., Willinger E., Rosowski F., Schogl R., Frei E.: Synthesis and Characterization of Ag-Delafossites $AgBO_2$ (B : Al, Ga, In) from a Rapid Hydrothermal Process. European Journal of Inorganic Chemistry 18, 2019, 2333–2345.

M.Sc. Karolina Siedliska
e-mail: k.siedliska@pollub.pl

Karolina Siedliska is a graduate of the Lublin University of Technology. Currently works in the Department of Electronics and Information Technologies. She is also a Ph.D. candidate at the Electronic Engineering and Computer Sciences Faculty. Her scientific activities include the synthesis of magnetic materials and their characterizations.

https://orcid.org/0000-0002-2740-8132

otrzymano/received: 1.10.2020 *przyjęto do druku/accepted: 10.12.2020*

http://doi.org/10.35784/iapgos.2107

COMPUTER PREDICTION OF TECHNOLOGICAL REGIMES OF RAPID CONE-SHAPED ADSORPTION FILTERS WITH CHEMICAL REGENERATION OF HOMOGENEOUS POROUS LOADS

Andrii Bomba[1], Yurii Klymyuk[1], Ihor Prysiazhniuk[2]
[1]National University of Water and Environmental Engineering, Department of Applied Mathematics, Rivne, Ukraine
[2]Rivne State University of Humanities, Department of Hanging Mathematics, Rivne, Ukraine

Abstract. *Mathematical models for predicting technological regimes of filtration (water purification from the present impurities), backwashing, chemical regeneration and direct washing of rapid cone-shaped adsorption filters, taking into account the influence of temperature effects on the internal mass transfer kinetics at constant rates of the appropriate regimes, are formulated. Algorithms for numerical-asymptotic approximations of solutions of the corresponding nonlinear singularly perturbed boundary value problems for a model cone-shaped domain bounded by two equipotential surfaces and a flow surface are obtained. The proposed models in the complex allow computer experiments to be conducted to investigate the change of impurity concentrations in the filtration flow and on the surface of the load adsorbent, temperature of the filtration flow, filtration coefficient and active porosity along the filter height due to adsorption and desorption processes, and on their basis, to predict a good use of adsorbents and increase the protective time of rapid cone-shaped adsorption filters with chemical regeneration of homogeneous porous loads.*

Keywords: mathematical model, process of water purification, adsorption, rapid cone-shaped filter, chemical regeneration, homogeneous porous load

KOMPUTEROWE PROGNOZOWANIE TRYBÓW TECHNOLOGICZNYCH SZYBKICH STOŻKOWYCH FILTRÓW ADSORPCYJNYCH Z CHEMICZNĄ REGENERACJĄ JEDNORODNYCH POROWATYCH OBCIĄŻEŃ

Streszczenie. *Sformułowano matematyczne modele do prognozowania trybów technologicznych filtracji (oczyszczanie wody z obecnych zanieczyszczeń), płukania wstecznego, regeneracji chemicznej i bezpośredniego przemywania szybkich stożkowych adsorpcyjnych filtrów z uwzględnieniem wpływu temperatury na kinetykę wewnętrznego przenoszenia masy przy zachowaniu stałych prędkości odpowiednich trybów. Opracowano się algorytmy numerycznie asymptotycznych aproksymacji rozwiązań odpowiadających problemów nieliniowych pojedynczo zaburzonych brzegowych dla domeny modelu o kształcie stożka, ograniczonej dwiema powierzchniami ekwipotencjalnymi i powierzchnią przepływu. Proponowane modele w kompleksie pozwalają na prowadzenie eksperymentów komputerowych w celu zbadania zmiany stężeń zanieczyszczeń w strumieniu filtracyjnym i na powierzchni adsorbentu obciążającego, temperatury przepływu filtracji, współczynnika filtracji oraz porowatości czynnej wzdłuż wysokości filtra ze względu na procesy adsorpcji i desorpcji, na ich podstawie przewidzieć bardziej optymalne zastosowania adsorbentów i wydłużenia czasu ochronnego szybkich stożkowych filtrów adsorpcyjnych z chemiczną regeneracją jednorodnych porowatych obciążen.*

Slowa kluczowe: model matematyczny, proces oczyszczania wody, adsorpcja, szybki stożkowy filtr, regeneracja chemiczna, jednorodne porowate obciążenie

Introduction

Any water needs to be purified before it can be used for domestic and drinking water supply. The main methods of water purification are clarification, decolorization and disinfection. The final stage is its purification from various impurities, in particular, calcium and magnesium salts, the total content of which determines the hardness of the water, as well as iron removal, in rapid adsorption filters with chemical regeneration of porous loads [4, 6]. They use natural (bentonite, montmorillonite, peat), artificial (activated carbon, artificial zeolites, polysorbs) and synthetic (nanostructured carbon sorbents) materials as adsorbents [17]. The rate of the adsorption process depends on the concentration, nature and structure of the impurities, filtration rate and temperature seepage, and type and properties of the adsorbent [5]. Maintaining a constant set filtration rate is achieved by automatically adjusting the increase in the opening of the valve on the filtrate pipeline as the resistance of the filter load increases due to the accumulation of impurity particles in it. The impulse to increase the opening of the valve on the filtrate pipeline is a change in the water level on the filter (controlled by a float device) or water flow in the filtrate pipeline (controlled by a throttle device and a differential pressure gauge) [11]. When the latch is fully open, the filter is switched off to regenerate the porous load. First, the backwash regime with a high water supply rate (2–3 times higher than the filtration rate), which lasts for 5–20 minutes and allows the filter material of the porous load to loosen and large particles of impurities to be removed. Next, a regime of chemical regeneration is carried out with a high feed rate of a solution of a certain reagent (potassium permanganate $KMnO_4$ is usually used), which starts the process of chemical restoration of the adsorption capacity of the porous load, and lasts for 10–30 minutes. Impurity particles from the filter material pass into the reagent solution. Finally, a regime of direct rinsing at a high water supply rate, lasting up to 10 minutes, seals the filter material of the porous load and removes residues of impurities and the chemical solution of the reagent.

The increasing needs for purified water in industrial enterprises and the growing cost of filter materials require research, on the one hand, into more optimal use of adsorbents and increasing the duration of filters by choosing their shape, in particular, taking into account the influence of changes in the temperature of the filtration flow along the filter height on the process of adsorption water purification, and on the other hand, into restoration of the filtration properties of porous loads by chemical regeneration for their reuse [4, 6].

1. Literature review

As an analysis of the literature sources shows, in particular [2, 3, 5, 7, 8, 12, 13, 15, 16, 18, 19], a significant contribution to the development of the theoretical foundations of filtering liquids through porous loads has been made by many scientists, both domestic and foreign. Note that mathematical models for predicting the technological processes of filtration and regeneration of porous loads by domestic researchers often use the model of D. M. Mintz [15] with constant rates of the respective processes and temperature, or some modification (improved model). In [10], its spatial generalization is proposed to predict the process of water purification from impurities in rapid cone-shaped filters while maintaining a constant filtration rate. The model proposed in this work is more efficient for theoretical studies aimed at optimizing the filtering process parameters (duration, shape, filter size, layer height, etc.) by introducing additional equations to determine the change in active porosity and filtration coefficient of filter load along its height, taking into account diffusion in the filtration flow and on the surface of the load grains. An urgent task is to generalize the appropriate model for computer prediction of technological regimes of filtration, backwashing, chemical regeneration and direct washing of rapid cone-shaped adsorption filters, taking into account the influence of temperature effects on the internal mass transfer kinetics at constant rates of the appropriate regimes.

These models in the complex will allow providing computer experiments to predict a better use of adsorbents and increasing the protective time of rapid cone-shaped adsorption filters with chemical regeneration of homogeneous porous loads by taking into account not only the change in the filtration flow rate along the filter height, but also the effect of temperature on the coefficients that characterize the rates of mass transfer during adsorption and desorption, as well as on filtration coefficient.

2. Formulation of the problem

Let's develop a model of technological regimes of filtration, backwash, chemical regeneration and direct washing of rapid cone-shaped adsorption filters with chemical regeneration of a homogeneous porous load. We assume that in the filtration regime, the convective components of mass transfer and adsorption outweigh the contribution of diffusion and desorption, and in the backwash, chemical regeneration and direct washing regimes, the convective components of mass transfer and desorption outweigh the contribution of diffusion and adsorption. In addition, due to changes in the temperature of the filtration flow due to adsorption and desorption processes, the influence of temperature effects on the internal kinetics of mass transfer is taken into account. We assume that the convective components of mass transfer and adsorption outweigh the contribution of diffusion and desorption. In addition, the impact of temperature effects on the internal kinetics of mass transfer is taken into account due to changes in the temperature of the filtration flow due to adsorption and desorption processes. So, for the domain $G = G_z \times (0, \infty)$, where G_z is a spatial one-connected domain ($z = (x, y, z)$) bounded by smooth, orthogonal interconnecting lines, by two equipotential surfaces S_*, S^* and by the flow surface S^{**} (Fig. 1), the corresponding spatial model problems for predicting technological regimes of rapid cone-shaped adsorption filters, taking into account the reverse influence of process characteristics (impurity concentration, respectively, in the filtration flow and on the surface of the adsorbent) on the load characteristics (filtration coefficients, porosity, adsorption, desorption) will consist of equations describing the motion of the filtration flow and the equation of continuity:

$$\left\{ \vec{v} = \kappa_*^* \cdot grad\ \varphi,\ div\ \vec{v} = 0, \right. \tag{1}$$

Next are equations for determining the change in impurity concentrations in the filtration flow and on the surface of the load adsorbent, temperature of the filtration flow, filtration coefficient and active porosity along the filter height, respectively, for the filtration regime:

$$\begin{cases} (\sigma \cdot C)'_t = div\,(D \cdot grad\ C) - \vec{v} \cdot grad\ C - \\ -\alpha \cdot C + \beta \cdot U, \\ (\sigma \cdot U)'_t = div\,(D^* \cdot grad\ U) + \alpha \cdot C - \beta \cdot U, \\ (\sigma \cdot T)'_t = div\,(D^{**} \cdot grad\ T) - \vec{v} \cdot grad\ T + \\ +\gamma \cdot (\alpha \cdot C - \beta \cdot U), \\ \kappa'_t = -\mu \cdot U,\ \sigma'_t = -\lambda \cdot U, \end{cases} \tag{2}$$

backwashing, chemical regeneration and direct washing regimes:

$$\begin{cases} (\sigma \cdot C)'_t = div\,(D \cdot grad\ C) - \vec{v} \cdot grad\ C + \\ +\beta \cdot U - \alpha \cdot C, \\ (\sigma \cdot U)'_t = div\,(D^* \cdot grad\ U) - \beta \cdot U + \alpha \cdot C, \\ (\sigma \cdot T)'_t = div\,(D^{**} \cdot grad\ T) - \vec{v} \cdot grad\ T + \\ +\gamma \cdot (\beta \cdot U - \alpha \cdot C), \\ \kappa'_t = \mu \cdot U,\ \sigma'_t = \lambda \cdot U, \end{cases} \tag{3}$$

which are supplemented by the following boundary conditions, respectively, for filtration and direct washing regimes:

$$\left\{ \varphi\big|_{S_*} = \varphi_*,\ \varphi\big|_{S^*} = \varphi^*,\ \varphi'_{\vec{n}}\big|_{S^{**}} = 0, \right. \tag{4}$$

$$\begin{cases} C\big|_{S_*} = c_*^*,\ C'_{\vec{n}}\big|_{S^*} = 0,\ C'_{\vec{n}}\big|_{S^{**}} = 0, \\ U\big|_{S_*} = u_*^*,\ U'_{\vec{n}}\big|_{S^*} = 0,\ U'_{\vec{n}}\big|_{S^{**}} = 0, \\ T\big|_{S_*} = T_*^*,\ T'_{\vec{n}}\big|_{S^*} = 0,\ T'_{\vec{n}}\big|_{S^{**}} = 0, \end{cases} \tag{5}$$

backwash and chemical regeneration regimes:

$$\left\{ \varphi\big|_{S^*} = \varphi_*,\ \varphi\big|_{S_*} = \varphi^*,\ \varphi'_{\vec{n}}\big|_{S^{**}} = 0, \right. \tag{6}$$

$$\begin{cases} C\big|_{S^*} = c_*^*,\ C'_{\vec{n}}\big|_{S_*} = 0,\ C'_{\vec{n}}\big|_{S^{**}} = 0, \\ U\big|_{S^*} = u_*^*,\ U'_{\vec{n}}\big|_{S_*} = 0,\ U'_{\vec{n}}\big|_{S^{**}} = 0, \\ T\big|_{S^*} = T_*^*,\ T'_{\vec{n}}\big|_{S_*} = 0,\ T'_{\vec{n}}\big|_{S^{**}} = 0, \end{cases} \tag{7}$$

and initial conditions:

$$\begin{cases} C\big|_{t=0} = c_0^0,\ U\big|_{t=0} = u_0^0,\ T\big|_{t=0} = T_0^0, \\ \kappa\big|_{t=0} = \kappa_0^0,\ \sigma\big|_{t=0} = \sigma_0^0, \end{cases} \tag{8}$$

where $\varphi = \varphi(x, y, z)$, and $\vec{v} = \vec{v}(v_x, v_y, v_z)$ is respectively the potential and the velocity vector of the filtration, $0 \le \varphi_* < \varphi < \varphi^* < \infty$, $v = |\vec{v}| = \sqrt{v_x^2(x,y,z) + v_y^2(x,y,z) + v_z^2(x,y,z)} >> 0$, κ_*^* is the initial filtration coefficient, $\kappa_*^* > 0$, $\vec{n}$ is outer normal to the corresponding surface, $C = C(x, y, z, t)$ and $U = U(x, y, z, t)$ are the concentrations of impurities, respectively, in the filtration flow and on the surface of the adsorbent load, $T = T(x, y, z, t)$ is the temperature of the filtration flow at point (x, y, z) at time t, $\kappa = \kappa(x, y, z, t)$ is the filtration coefficient, $\sigma = \sigma(x, y, z, t)$ is the active porosity, D and D^* are the impurity diffusion coefficients, respectively, in the filtration flow and on the surface of the adsorbent, $D = \varepsilon \cdot d_0$, $d_0 > 0$, $D^* = \varepsilon \cdot d_0^*$, $d_0^* > 0$, D^{**} is the coefficient of thermal conductivity of the filtration flow, $D^{**} = \varepsilon \cdot d_0^{**}$, $d_0^{**} > 0$, α and β are coefficients that characterize the rate of mass transfer, respectively, in the adsorption of impurities from the filtration flow on the surface of the load adsorbent and the desorption of impurities from the surface of the load adsorbent into the filtration flow, for the model problem of predicting the filtration regimes $\alpha = \sum_{s_1=0}^{2} \sum_{s_2=0}^{2-s_1} \varepsilon^{s_1+s_2} \cdot \alpha_{s_1,s_2} \cdot v^{s_1} \cdot T^{s_2}$, $\alpha_{s_1,s_2} \in \mathrm{R}$ ($s_1 = \overline{(0,2)}$, $s_2 = \overline{(0, 2-s_1)}$), $\beta = \varepsilon \cdot \sum_{s_1=0}^{2} \sum_{s_2=0}^{2-s_1} \varepsilon^{s_1+s_2} \cdot \beta_{s_1,s_2} \cdot v^{s_1} \cdot T^{s_2}$, $\beta_{s_1,s_2} \in \mathrm{R}$ ($s_1 = \overline{(0,2)}$, $s_2 = \overline{(0, 2-s_1)}$) and for the model problems of predicting the backwashing, chemical regeneration and direct washing regimes $\alpha = \varepsilon \cdot \sum_{s_1=0}^{2} \sum_{s_2=0}^{2-s_1} \varepsilon^{s_1+s_2} \cdot \alpha_{s_1,s_2} \cdot v^{s_1} \cdot T^{s_2}$, $\alpha_{s_1,s_2} \in \mathrm{R}$ ($s_1 = \overline{(0,2)}$, $s_2 = \overline{(0, 2-s_1)}$), $\beta = \sum_{s_1=0}^{2} \sum_{s_2=0}^{2-s_1} \varepsilon^{s_1+s_2} \cdot \beta_{s_1,s_2} \cdot v^{s_1} \cdot T^{s_2}$, $\beta_{s_1,s_2} \in \mathrm{R}$ ($s_1 = \overline{(0,2)}$, $s_2 = \overline{(0, 2-s_1)}$), γ, μ and λ are coefficients characterizing the rate of change, respectively, of the filtration flow temperature, filtration coefficient and active porosity due to adsorption and desorption processes, $\mu = \varepsilon \cdot \sum_{s=0}^{2} \varepsilon^s \cdot \mu_s \cdot T^s$, $\mu_{r,s} \in \mathrm{R}$ ($s = \overline{(0,2)}$), $\lambda = \varepsilon \cdot \lambda_0$, $\lambda_0 > 0$, $\alpha = \alpha(x, y, z, t)$, $\beta = \beta(x, y, z, t)$, $\gamma = \gamma(x, y, z, t)$, $\mu = \mu(x, y, z, t)$ are continuous limited functions, ε is a small parameter ($\varepsilon > 0$) which characterizes the predominance of certain components of the process, $c_*^* = c_*^*(x, y, z, t)$, $c_0^0 = c_0^0(x, y, z)$, $u_*^* = u_*^*(x, y, z, t)$, $u_0^0 = u_0^0(x, y, z)$, $T_*^* = T_*^*(x, y, z, t)$, $T_0^0 = T_0^0(x, y, z)$, $\kappa_0^0 = \kappa_0^0(x, y, z)$,

$\sigma_0^0 = \sigma_0^0(x,y,z)$ are quite smooth functions, consistent with each other on the lines of intersection of surfaces S_*, S^* and S^{**} of domain G [1].

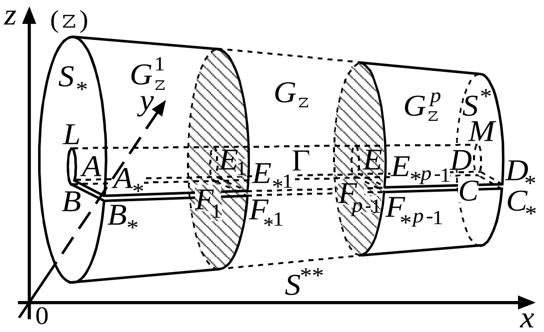

Fig. 1. Spatial filtering domain G_z with conditional section Γ (cone-shaped filter)

3. Materials and methods

The problem is solved in the same way as in [10] by fixing on the surface S_* some point A ($A = B$) and sequential execution of conditional sections $\Gamma_1 = ALMDBLMC$ and $\Gamma_2 = ADD_*A_*BCC_*B_*$ along the corresponding surfaces of the flow (we denote for convenience $\Gamma = \Gamma_1 \cup \Gamma_2$). The model problems of forecasting of technological regimes of filtration (1), (2), (4), (5), (8), backwash (1), (3), (6)–(8), chemical regeneration (1), (3), (6)–(8) and direct wash (1), (3), (4), (5), (8) in rapid cone-shaped filter with chemical regeneration of porous load reduced to the solving of the problems in the received one-connected domain $G_z \setminus \Gamma$ that is a curvilinear parallelepiped $ABCDA_*B_*C_*D_*$, bounded by two equipotential surfaces ABB_*A_*, CDD_*C_* and four flow surfaces $ABCD = ALMD \cup BLMC$, $A_*B_*C_*D_*$, $ADD_*A_* = BCC_*B_*$ (Fig. 1), The surfaces are smooth and orthogonal to each other at angular points and along the edges, with the addition of the impermeability condition $\varphi'_n\big|_\Gamma = 0$ along section Γ:

$$\begin{cases} \varphi\big|_{ABB_*A_*} = \varphi_*,\ \varphi\big|_{CDD_*C_*} = \varphi^*, \\ \varphi'_n\big|_{ABCD \cup A_*B_*C_*D_* \cup ADD_*A_* \cup BCC_*B_*} = 0, \end{cases} \tag{9}$$

$$\begin{cases} C\big|_{ABB_*A_*} = c_*^*,\ C'_n\big|_{CDD_*C_*} = 0, \\ C'_n\big|_{ADD_*A_* \cup BCC_*B_* \cup ABCD \cup A_*B_*C_*D_*} = 0, \\ U\big|_{ABB_*A_*} = u_*^*,\ U'_n\big|_{CDD_*C_*} = 0, \\ U'_n\big|_{ADD_*A_* \cup BCC_*B_* \cup ABCD \cup A_*B_*C_*D_*} = 0, \\ T\big|_{ABB_*A_*} = T_*^*,\ T'_n\big|_{CDD_*C_*} = 0, \\ T'_n\big|_{ADD_*A_* \cup BCC_*B_* \cup ABCD \cup A_*B_*C_*D_*} = 0, \end{cases} \tag{10}$$

backwash, chemical regeneration and direct wash regimes:

$$\begin{cases} \varphi\big|_{CDD_*C_*} = \varphi_*,\ \varphi\big|_{ABB_*A_*} = \varphi^*, \\ \varphi'_n\big|_{ABCD \cup A_*B_*C_*D_* \cup ADD_*A_* \cup BCC_*B_*} = 0, \end{cases} \tag{11}$$

$$\begin{cases} C\big|_{CDD_*C_*} = c_*^*,\ C'_n\big|_{ABB_*A_*} = 0, \\ C'_n\big|_{ADD_*A_* \cup BCC_*B_* \cup ABCD \cup A_*B_*C_*D_*} = 0, \\ U\big|_{CDD_*C_*} = u_*^*,\ U'_n\big|_{ABB_*A_{**}} = 0, \\ U'_n\big|_{ADD_*A_* \cup BCC_*B_* \cup ABCD \cup A_*B_*C_*D_*} = 0, \\ T\big|_{CDD_*C_*} = T_*^*,\ T'_n\big|_{ABB_*A_*} = 0, \\ T'_n\big|_{ADD_*A_* \cup BCC_*B_* \cup ABCD \cup A_*B_*C_*D_*} = 0, \end{cases} \tag{12}$$

the initial conditions (8) and the conditions of further "gluing" of the banks of conditional section Γ:

$$\begin{cases} \varphi\big|_{ALMD} = \varphi\big|_{BLMC},\ \varphi'_n\big|_{ALMD} = \varphi'_n\big|_{BLMC}, \\ \varphi\big|_{ADD_*A_*} = \varphi\big|_{BCC_*B_*},\ \varphi'_n\big|_{ADD_*A_*} = \varphi'_n\big|_{BCC_*B_*} \end{cases} \tag{13}$$

and conditions of agreement of values of impurity concentrations in the filtration flow and on the surface of the load adsorbent and values of the filtration flow temperature on the conditional sections of section Γ:

$$\begin{cases} C\big|_{ALMD} = C\big|_{BLMC},\ C'_n\big|_{ALMD} = C'_n\big|_{BLMC}, \\ C\big|_{ADD_*A_*} = C\big|_{BCC_*B_*},\ C'_n\big|_{ADD_*A_*} = C'_n\big|_{BCC_*B_*}, \\ U\big|_{ALMD} = U\big|_{BLMC},\ U'_n\big|_{ALMD} = U'_n\big|_{BLMC}, \\ U\big|_{ADD_*A_*} = U\big|_{BCC_*B_*},\ U'_n\big|_{ADD_*A_*} = U'_n\big|_{BCC_*B_*}, \\ T\big|_{ALMD} = T\big|_{BLMC},\ T'_n\big|_{ALMD} = T'_n\big|_{BLMC}, \\ T\big|_{ADD_*A_*} = T\big|_{BCC_*B_*},\ T'_n\big|_{ADD_*A_*} = T'_n\big|_{BCC_*B_*}. \end{cases} \tag{14}$$

Similar to [9], problems (1), (9), (13) and (1), (11), (13) are replaced by the more general direct problem of finding a spatial analogue of the conformal mapping of the one-connected domain $G_z \setminus \Gamma$ to the corresponding domain of complex potential which is rectangular parallelepiped $G_w = A'B'C'D'A'_*B'_*C'_*D'_*$ (Fig. 2), where $G_w = \{w = (\varphi,\psi,\eta):\ \varphi_* < \varphi < \varphi^*,\ 0 < \psi < Q_*,\ 0 < \eta < Q^*\}$, Q_*, Q^* are unknown parameters, $Q = Q_* \cdot Q^*$ is the full filtration flow, with subsequent finding of conditions of "gluing" on the banks of conditional section Γ. The algorithm for solving these problems is obtained in [9], in particular, the velocity field $\vec{v}$, parameters Q_*, Q^*, Q and a number of other variables are found. By replacing variables $x = x(\varphi,\psi,\eta)$, $y = y(\varphi,\psi,\eta)$, $z = z(\varphi,\psi,\eta)$ in equations (2), (3) and conditions (10), (12), (8), (14), we obtain model problems for predicting the technological regimes of a rapid cone-shaped adsorption filter with chemical regeneration of porous load for the domain $G_w \times (0,\infty)$, described by the systems of equations, respectively, for the filtration regime:

$$\begin{cases} (\tilde{\sigma}\cdot c)'_t = D\cdot(b_1\cdot c''_{\varphi\varphi} + b_2\cdot c''_{\psi\psi} + b_3\cdot c''_{\eta\eta} + \\ +b_4\cdot c'_\psi + b_5\cdot c'_\eta) - \tilde{v}^2/\kappa_*^*\cdot c'_\varphi - \tilde{\alpha}\cdot c + \tilde{\beta}\cdot u, \\ (\tilde{\sigma}\cdot u)'_t = D^*\cdot(b_1\cdot u''_{\varphi\varphi} + b_2\cdot u''_{\psi\psi} + b_3\cdot u''_{\eta\eta} + \\ +b_4\cdot u'_\psi + b_5\cdot u'_\eta) + \tilde{\alpha}\cdot c - \tilde{\beta}\cdot u, \\ (\tilde{\sigma}\cdot \tilde{T})'_t = D^{**}\cdot(b_1\cdot \tilde{T}''_{\varphi\varphi} + b_2\cdot \tilde{T}''_{\psi\psi} + b_3\cdot \tilde{T}''_{\eta\eta} + \\ +b_4\cdot \tilde{T}'_\psi + b_5\cdot \tilde{T}'_\eta) - \tilde{v}^2/\kappa_*^*\cdot \tilde{T}'_\varphi + \tilde{\gamma}\cdot(\tilde{\alpha}\cdot c - \tilde{\beta}\cdot u), \\ \tilde{\kappa}'_t = -\tilde{\mu}\cdot u,\ \tilde{\sigma}'_t = -\lambda\cdot u, \end{cases} \tag{15}$$

backwash, chemical regeneration and direct wash regimes:

$$\begin{cases} (\tilde{\sigma}\cdot c)'_t = D\cdot(b_1\cdot c''_{\varphi\varphi} + b_2\cdot c''_{\psi\psi} + b_3\cdot c''_{\eta\eta} + \\ +b_4\cdot c'_\psi + b_5\cdot c'_\eta) - \tilde{v}^2/\kappa_*^*\cdot c'_\varphi + \tilde{\beta}\cdot u - \tilde{\alpha}\cdot c, \\ (\tilde{\sigma}\cdot u)'_t = D^*\cdot(b_1\cdot u''_{\varphi\varphi} + b_2\cdot u''_{\psi\psi} + b_3\cdot u''_{\eta\eta} + \\ +b_4\cdot u'_\psi + b_5\cdot u'_\eta) - \tilde{\beta}\cdot u + \tilde{\alpha}\cdot c, \\ (\tilde{\sigma}\cdot \tilde{T})'_t = D^{**}\cdot(b_1\cdot \tilde{T}''_{\varphi\varphi} + b_2\cdot \tilde{T}''_{\psi\psi} + b_3\cdot \tilde{T}''_{\eta\eta} + \\ +b_4\cdot \tilde{T}'_\psi + b_5\cdot \tilde{T}'_\eta) - \tilde{v}^2/\kappa_*^*\cdot \tilde{T}'_\varphi + \tilde{\gamma}\cdot(\tilde{\beta}\cdot u - \tilde{\alpha}\cdot c), \\ \tilde{\kappa}'_t = \tilde{\mu}\cdot u,\ \tilde{\sigma}'_t = \lambda\cdot u, \end{cases} \tag{16}$$

which are supplemented by the following boundary conditions:

$$\begin{cases} c\big|_{\varphi=\varphi_*}=\tilde{c}_*^*,\ c'_\varphi\big|_{\varphi=\varphi^*}=0, \\ c_\psi\big|_{\psi=0}=c'_\psi\big|_{\psi=Q_*}=c'_\eta\big|_{\eta=0}=c'_\eta\big|_{\eta=Q^*}=0, \\ u\big|_{\varphi=\varphi_*}=\tilde{u}_*^*,\ u'_\varphi\big|_{\varphi=\varphi^*}=0, \\ u'_\psi\big|_{\psi=0}=u'_\psi\big|_{\psi=Q_*}=u'_\eta\big|_{\eta=0}=u'_\eta\big|_{\eta=Q^*}=0, \\ \tilde{T}\big|_{\varphi=\varphi_*}=\tilde{T}_*^*,\ \tilde{T}'_\varphi\big|_{\varphi=\varphi^*}=0, \\ \tilde{T}'_\psi\big|_{\psi=0}=\tilde{T}'_\psi\big|_{\psi=Q_*}=\tilde{T}'_\eta\big|_{\eta=0}=\tilde{T}'_\eta\big|_{\eta=Q^*}=0, \end{cases} \tag{17}$$

initial conditions:

$$\begin{cases} c\big|_{t=0}=\tilde{c}_0^0,\ u\big|_{t=0}=\tilde{u}_0^0,\ \tilde{T}\big|_{t=0}=\tilde{T}_0^0, \\ \tilde{\kappa}\big|_{t=0}=\tilde{\kappa}_0^0,\ \tilde{\sigma}\big|_{t=0}=\tilde{\sigma}_0^0 \end{cases} \tag{18}$$

and conditions of consistency of the values of impurity concentrations in the filtration flow and on the surface of the load adsorbent and the values of the filtration flow temperature on the conditional surfaces of section Γ:

$$\begin{cases} c\big|_{\eta=0,\psi=\bar{\psi}}=c\big|_{\eta=0,\psi=Q_*-\bar{\psi}},\ c'_{\bar{n}}\big|_{\eta=0,\psi=\bar{\psi}}=c'_{\bar{n}}\big|_{\eta=0,\psi=Q_*-\bar{\psi}}, \\ c\big|_{\psi=0}=c\big|_{\psi=Q_*},\ c'_{\bar{n}}\big|_{\psi=0}=c'_{\bar{n}}\big|_{\psi=Q_*}, \\ u\big|_{\eta=0,\psi=\bar{\psi}}=u\big|_{\eta=0,\psi=Q_*-\bar{\psi}},\ u'_{\bar{n}}\big|_{\eta=0,\psi=\bar{\psi}}=u'_{\bar{n}}\big|_{\eta=0,\psi=Q_*-\bar{\psi}}, \\ u\big|_{\psi=0}=u\big|_{\psi=Q_*},\ u'_{\bar{n}}\big|_{\psi=0}=u'_{\bar{n}}\big|_{\psi=Q_*}, \\ \tilde{T}\big|_{\eta=0,\psi=\bar{\psi}}=\tilde{T}\big|_{\eta=0,\psi=Q_*-\bar{\psi}},\ \tilde{T}'_{\bar{n}}\big|_{\eta=0,\psi=\bar{\psi}}=\tilde{T}'_{\bar{n}}\big|_{\eta=0,\psi=Q_*-\bar{\psi}}, \\ \tilde{T}\big|_{\psi=0}=\tilde{T}\big|_{\psi=Q_*},\ \tilde{T}'_{\bar{n}}\big|_{\psi=0}=\tilde{T}'_{\bar{n}}\big|_{\psi=Q_*}, \end{cases} \tag{19}$$

where $c=c(\varphi,\psi,\eta,t)=C(x(\varphi,\psi,\eta),\ y(\varphi,\psi,\eta),\ z(\varphi,\psi,\eta),t)$, …, for the model problem of predicting the filtration regimes: $\tilde{\alpha}=\sum_{s_1=0}^{2}\sum_{s_2=0}^{2-s_1}\varepsilon^{s_1+s_2}\cdot\tilde{\alpha}_{s_1,s_2}\cdot\tilde{v}^{s_1}\cdot\tilde{T}^{s_2}$, $\tilde{\alpha}_{s_1,s_2}\in \mathrm{R}$ ($s_1=(0,2)$, $s_2=(0,2-s_1)$), $\tilde{\beta}=\varepsilon\cdot\sum_{s_1=0}^{2}\sum_{s_2=0}^{2-s_1}\varepsilon^{s_1+s_2}\cdot\tilde{\beta}_{s_1,s_2}\cdot\tilde{v}^{s_1}\cdot\tilde{T}^{s_2}$, $\tilde{\beta}_{s_1,s_2}\in \mathrm{R}$ ($s_1=(0,2)$, $s_2=(0,2-s_1)$) and for model problems of predicting of backwash, chemical regeneration and direct washing regimes: $\tilde{\alpha}=\varepsilon\cdot\sum_{s_1=0}^{2}\sum_{s_2=0}^{2-s_1}\varepsilon^{s_1+s_2}\cdot\tilde{\alpha}_{s_1,s_2}\cdot\tilde{v}^{s_1}\cdot\tilde{T}^{s_2}$, $\tilde{\alpha}_{s_1,s_2}\in \mathrm{R}$ ($s_1=(0,2)$, $s_2=(0,2-s_1)$), $\tilde{\beta}=\sum_{s_1=0}^{2}\sum_{s_2=0}^{2-s_1}\varepsilon^{s_1+s_2}\cdot\tilde{\beta}_{s_1,s_2}\cdot\tilde{v}^{s_1}\cdot\tilde{T}^{s_2}$, $\tilde{\beta}_{s_1,s_2}\in \mathrm{R}$ ($s_1=(0,2)$, $s_2=(0,2-s_1)$), $\tilde{\mu}=\varepsilon\cdot\sum_{s=0}^{2}\varepsilon^{s}\cdot\tilde{\mu}_s\cdot\tilde{T}^{s}$, $\tilde{\mu}_{r,s}\in \mathrm{R}$ ($s=(0,2)$), $b_1=\varphi_x'^2+\varphi_y'^2+\varphi_z'^2=\tilde{v}^2/\kappa_*^{*2}$, $b_2=\psi_x'^2+\psi_y'^2+\psi_z'^2$, $b_3=\eta_x'^2+\eta_y'^2+\eta_z'^2$, $b_4=\psi''_{xx}+\psi''_{yy}+\psi''_{zz}$, $b_5=\eta''_{xx}+\eta''_{yy}+\eta''_{zz}$, $b_s=b_s(\varphi,\psi,\eta)$ ($s=(1,5)$), $\tilde{v}=\tilde{v}(\varphi,\psi,\eta)$, $\bar{\psi}\in[0,Q_*/2]$.

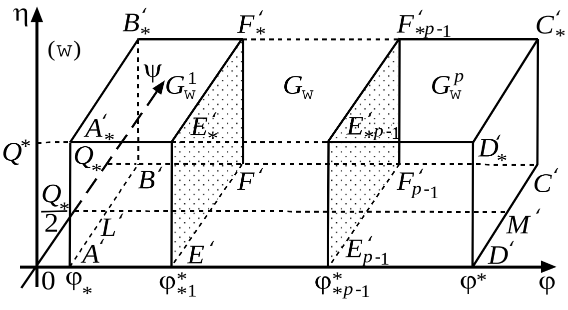

Fig. 2. Spatial domain of complex potential G_w

Similar to [10], a numerically asymptotic approximation of the solution (c, u, $\tilde{T}$, $\tilde{\kappa}$, $\tilde{\sigma}$) of problems (15), (17)–(19) and (16)–(19) with accuracy $O(\varepsilon^{n+1})$ was found in the form of the following series:

$$c=\sum_{i=0}^{n}\varepsilon^i\cdot c_i+\sum_{i=0}^{n+1}\varepsilon^i\cdot\sum_{j=1}^{2}P_{1,j,i}+\sum_{i=0}^{n+1}\varepsilon^i\cdot\sum_{j=3}^{6}P_{1,j,i}+R_{1,n+1},$$

$$u=\sum_{i=0}^{n}\varepsilon^i\cdot u_i+\sum_{i=0}^{n+1}\varepsilon^i\cdot\sum_{j=1}^{2}P_{2,j,i}+\sum_{i=0}^{n+1}\varepsilon^i\cdot\sum_{j=3}^{6}P_{2,j,i}+R_{2,n+1},$$

$$\tilde{T}=\sum_{i=0}^{n}\varepsilon^i\cdot \tilde{T}_i+\sum_{i=0}^{n+1}\varepsilon^i\cdot\sum_{j=1}^{2}P_{3,j,i}+\sum_{i=0}^{n+1}\varepsilon^i\cdot\sum_{j=3}^{6}P_{3,j,i}+R_{3,n+1},$$

$$\tilde{\kappa}=\sum_{i=0}^{n}\varepsilon^i\cdot \tilde{\kappa}_i+\sum_{i=0}^{n+1}\varepsilon^i\cdot\sum_{j=1}^{2}P_{4,j,i}+\sum_{i=0}^{n+1}\varepsilon^i\cdot\sum_{j=3}^{6}P_{4,j,i}+R_{4,n+1},$$

$$\tilde{\sigma}=\sum_{i=0}^{n}\varepsilon^i\cdot \tilde{\sigma}_i+\sum_{i=0}^{n+1}\varepsilon^i\cdot\sum_{j=1}^{2}P_{5,j,i}+\sum_{i=0}^{n+1}\varepsilon^i\cdot\sum_{j=3}^{6}P_{5,j,i}+R_{5,n+1},$$

where $c_i=c_i(\varphi,\psi,\eta,t)$, $u_i=u_i(\varphi,\psi,\eta,t)$, $\tilde{T}_i=\tilde{T}_i(\varphi,\psi,\eta,t)$, $\tilde{\kappa}_i=\tilde{\kappa}_i(\varphi,\psi,\eta,t)$, $\tilde{\sigma}_i=\tilde{\sigma}_i(\varphi,\psi,\eta,t)$ ($i=(0,n)$) are members of regular parts of asymptotic, $P_{s,j,i}=P_{s,j,i}(\phi_j,\psi,\eta,t)$ ($s=(0,5)$, $j=(1,2)$, $i=(0,n+1)$) are the boundary layer type functions around $\varphi=\varphi_*$ and $\varphi=\varphi^*$ (corrections at the entrance to the filter), $P_{s,j,i}=P_{s,j,i}(\varphi,\psi_{j-2},\eta,t)$ ($s=(0,5)$, $j=(3,4)$, $i=(0,n+1)$), $P_{s,j,i}=P_{s,j,i}(\varphi,\psi,\eta_{j-4},t)$ ($s=(0,5)$, $j=(5,6)$, $i=(0,n+1)$) are boundary layer type functions, respectively, around $\psi=0$, $\psi=Q_*$, $\eta=0$ and $\eta=Q^*$ (corrections on the side wall of the filter and the shores of conditional section Γ), $\varphi_1=(\varphi-\varphi_*)/\varepsilon$, $\varphi_2=(\varphi^*-\varphi)/\varepsilon$, $\psi_1=\psi/\sqrt{\varepsilon}$, $\psi_2=(Q_*-\psi)/\sqrt{\varepsilon}$, $\eta_1=\eta/\sqrt{\varepsilon}$, $\eta_2=(Q^*-\eta)/\sqrt{\varepsilon}$ are the corresponding regulatory transformations (stretches), $R_{s,n+1}(\varphi,\psi,\eta,t,\varepsilon)$ ($s=(0,5)$) are the remaining members. In particular, for c_i, u_i, $\tilde{T}_i$, $\tilde{\kappa}_i$, $\tilde{\sigma}_i$ ($i=0,n$) of problems (15), (17)–(19), we obtained the formulas:

$$c_0=\begin{cases} e^{-\tilde{q}_1}\cdot(\hat{g}_0+\tilde{c}_*^*(\psi,\eta,t-\tilde{f}(\varphi,\psi,\eta)), & t\ge\tilde{f}, \\ e^{-\tilde{q}_2}\cdot(\hat{\hat{g}}_0+\tilde{c}_0^0(\tilde{f}^{-1}(\tilde{f}(\varphi,\psi,\eta)-t,\psi,\eta),\psi,\eta)), & t<\tilde{f}, \end{cases}$$

$$u_0=\frac{1}{\tilde{\sigma}_0^0}\cdot\int_0^t\tilde{g}_i(\varphi,\psi,\eta,\hat{t})d\hat{t}+\tilde{u}_0^0,$$

$$\tilde{T}_0=\begin{cases} \hat{\tilde{g}}_0+\tilde{T}_*^*(\psi,\eta,t-\tilde{f}(\varphi,\psi,\eta)), & t\ge\tilde{f}, \\ \hat{\hat{\tilde{g}}}_0+\tilde{T}_0^0(\tilde{f}^{-1}(\tilde{f}(\varphi,\psi,\eta)-t,\psi,\eta),\psi,\eta), & t<\tilde{f}, \end{cases}$$

$$\tilde{\kappa}_0=\tilde{\kappa}_0^0,\ \tilde{\sigma}_0=\tilde{\sigma}_0^0,$$

$$c_i=\begin{cases} e^{-\tilde{q}_1(\varphi,\psi,\eta,t)}\cdot\hat{g}_i(\varphi,\psi,\eta,t), & t\ge\tilde{f}, \\ e^{-\tilde{q}_2(\varphi,\psi,\eta,t)}\cdot\hat{\hat{g}}_i(\varphi,\psi,\eta,t), & t<\tilde{f}, \end{cases}$$

$$u_i=\frac{1}{\tilde{\sigma}_0^0}\cdot\int_0^t\tilde{g}_i(\varphi,\psi,\eta,\hat{t})d\hat{t},$$

$$\tilde{T}_i=\begin{cases} \hat{\tilde{g}}_i(\varphi,\psi,\eta,t), & t\ge\tilde{f}, \\ \hat{\hat{\tilde{g}}}_i(\varphi,\psi,\eta,t), & t<\tilde{f}, \end{cases}$$

$$\tilde{\kappa}_i=\int_0^t\breve{g}_i(\varphi,\psi,\eta,\hat{t})d\hat{t},$$

$$\tilde{\sigma}_i=\int_0^t\breve{\breve{g}}_i(\varphi,\psi,\eta,\hat{t})d\hat{t}\quad (i=\overline{1,n}),$$

where:

$$\tilde{q}_1(\varphi,\psi,\eta,t)=\kappa_*^*\cdot\tilde{\alpha}_{0,0}\cdot\int_{\varphi_*}^{\varphi}\frac{d\hat{\varphi}}{\tilde{v}^2(\hat{\varphi},\psi,\eta)},$$

$$\tilde{q}_2(\varphi,\psi,\eta,t)=\tilde{\alpha}_{0,0}\cdot\int_0^t\frac{d\hat{t}}{\tilde{\sigma}_0^0(\tilde{f}^{-1}(\hat{t}+\tilde{f}(\varphi,\psi,\eta)-t,\psi,\eta),\psi,\eta)},$$

$$\widehat{g}_i(\varphi,\psi,\eta,t)=\int\limits_{\varphi_*}^{\varphi}\frac{g_i(\widehat{\varphi},\psi,\eta,\tilde{f}(\widehat{\varphi},\psi,\eta)-\tilde{f}(\varphi,\psi,\eta)+t)}{\tilde{v}^2(\widehat{\varphi},\psi,\eta)}\cdot e^{\tilde{q}_1(\widehat{\varphi},\psi,\eta,t)}d\widehat{\varphi},$$

$$\hat{\hat{g}}_i(\varphi,\psi,\eta,t)=\int\limits_0^t\frac{g_i(\tilde{f}^{-1}(\widehat{t}+\tilde{f}(\varphi,\psi,\eta)-t,\psi,\eta),\psi,\eta,\widehat{t})}{\tilde{\sigma}_0^0(\tilde{f}^{-1}(\widehat{t}+\tilde{f}(\varphi,\psi,\eta)-t,\psi,\eta),\psi,\eta)}\cdot e^{\tilde{q}_2(\varphi,\psi,\eta,\widehat{t})}d\widehat{t},$$

$$\bar{\hat{g}}_i(\varphi,\psi,\eta,t)=\kappa_*^*\cdot\int\limits_{\varphi_*}^{\varphi}\frac{\bar{\tilde{g}}_i(\widehat{\varphi},\psi,\eta,\tilde{f}(\widehat{\varphi},\psi,\eta)-\tilde{f}(\varphi,\psi,\eta)+t)}{\tilde{v}^2(\widehat{\varphi},\psi,\eta)}d\widehat{\varphi},$$

$$\bar{\hat{\hat{g}}}_i(\varphi,\psi,\eta,t)=\int\limits_0^t\frac{\bar{\tilde{g}}_i(\tilde{f}^{-1}(\widehat{t}+\tilde{f}(\varphi,\psi,\eta)-t,\psi,\eta),\psi,\eta,\widehat{t})}{\tilde{\sigma}_0^0(\tilde{f}^{-1}(\widehat{t}+\tilde{f}(\varphi,\psi,\eta)-t,\psi,\eta),\psi,\eta)}d\widehat{t},$$

$$g_i(\varphi,\psi,\eta,t)=I(i,1)\cdot(d_0\cdot(b_1\cdot c''_{(i-1)\varphi\varphi}+b_2\cdot c''_{(i-1)\psi\psi}+$$
$$+b_3\cdot c''_{(i-1)\eta\eta}+b_4\cdot c'_{(i-1)\psi}+b_5\cdot c'_{(i-1)\eta})-\sum_{l=1}^{i}(\tilde{\sigma}_l\cdot c'_{(i-l)t}+\tilde{\sigma}'_{l\,t}\cdot c_{i-l}))-$$
$$-(I(i,1)\cdot(\sum_{l=1}^{i}\tilde{\alpha}_{l,0}\cdot\tilde{v}^l\cdot c_{i-l}+\sum_{l=0}^{i-1}\tilde{\alpha}_{0,1}\cdot\tilde{T}_l\cdot c_{i-1-l}-$$
$$-\sum_{l=0}^{i-1}\tilde{\beta}_{l,0}\cdot\tilde{v}^l\cdot u_{i-1-l})+I(i,2)\cdot(\sum_{l=0}^{i-2}\sum_{k=0}^{l}\tilde{\alpha}_{0,2}\cdot\tilde{T}_k\cdot\tilde{T}_{l-k}\cdot c_{i-2-l}+$$
$$+\sum_{l=0}^{i-2}\tilde{\alpha}_{2,2}\cdot\tilde{v}\cdot\tilde{T}_l\cdot c_{i-2-l}-\sum_{l=0}^{i-2}\tilde{\beta}_{0,1}\cdot\tilde{T}_l\cdot u_{i-2-l})+I(i,3)\times$$
$$\times(\sum_{l=0}^{i-3}\sum_{k=0}^{l}\tilde{\beta}_{0,2}\cdot\tilde{T}_k\cdot\tilde{T}_{l-k}\cdot u_{i-3-l}+\sum_{l=0}^{i-3}\tilde{\beta}_{2,2}\cdot\tilde{v}\cdot\tilde{T}_l\cdot u_{i-3-l})),$$

$$\tilde{g}_i(\varphi,\psi,\eta,t)=\sum_{l=0}^{i}\tilde{\alpha}_{l,0}\cdot\tilde{v}^l\cdot c_{i-l}+I(i,1)\cdot(d_0^*\cdot(b_1\cdot u''_{(i-1)\varphi\varphi}+$$
$$+b_2\cdot u''_{(i-1)\psi\psi}+b_3\cdot u''_{(i-1)\eta\eta}+b_4\cdot u'_{(i-1)\psi}+b_5\cdot u'_{(i-1)\eta})-$$
$$-\sum_{l=1}^{i}(\tilde{\sigma}_l\cdot u'_{(i-l)t}+\tilde{\sigma}'_{l\,t}\cdot u_{i-l}))+(I(i,1)\cdot(\sum_{l=0}^{i-1}\tilde{\alpha}_{0,1}\cdot\tilde{T}_l\cdot c_{i-1-l}-$$
$$-\sum_{l=0}^{i-1}\tilde{\beta}_{l,0}\cdot\tilde{v}^l\cdot u_{i-1-l})+I(i,2)\cdot(\sum_{l=0}^{i-2}\sum_{k=0}^{l}\tilde{\alpha}_{0,2}\cdot\tilde{T}_k\cdot\tilde{T}_{l-k}\cdot c_{i-2-l}\times$$
$$+\sum_{l=0}^{i-2}\tilde{\alpha}_{2,2}\cdot\tilde{v}\cdot\tilde{T}_l\cdot c_{i-2-l}-\sum_{l=0}^{i-2}\tilde{\beta}_{0,1}\cdot\tilde{T}_l\cdot u_{i-2-l})-I(i,3)\times$$
$$\times(\sum_{l=0}^{i-3}\sum_{k=0}^{l}\tilde{\beta}_{0,2}\cdot\tilde{T}_k\cdot\tilde{T}_{l-k}\cdot u_{i-3-l}+\sum_{l=0}^{i-3}\tilde{\beta}_{2,2}\cdot\tilde{v}\cdot\tilde{T}_l\cdot u_{i-3-l}),$$

$$\bar{\tilde{g}}_i(\varphi,\psi,\eta,t)=\gamma\cdot\sum_{l=0}^{i}\tilde{\alpha}_{l,0}\cdot\tilde{v}^l\cdot c_{i-l}+I(i,1)\cdot(d_0^{**}\cdot(b_1\cdot\tilde{T}''_{(i-1)\varphi\varphi}+$$
$$+b_2\cdot\tilde{T}''_{(i-1)\psi\psi}+b_3\cdot\tilde{T}''_{(i-1)\eta\eta}+b_4\cdot\tilde{T}'_{(i-1)\psi}+b_5\cdot\tilde{T}'_{(i-1)\eta})-$$
$$-\sum_{l=1}^{i}(\tilde{\sigma}_l\cdot\tilde{T}'_{(i-l)t}+\tilde{\sigma}'_{l\,t}\cdot\tilde{T}'_{i-l}))+\gamma\cdot(I(i,1)\cdot(\sum_{l=0}^{i-1}\tilde{\alpha}_{0,1}\cdot\tilde{T}_l\cdot c_{i-1-l}-$$
$$-\sum_{l=0}^{i-1}\tilde{\beta}_{l,0}\cdot\tilde{v}^l\cdot u_{i-1-l})+I(i,2)\cdot(\sum_{l=0}^{i-2}\sum_{k=0}^{l}\tilde{\alpha}_{0,2}\cdot\tilde{T}_k\cdot\tilde{T}_{l-k}\cdot c_{i-2-l}+$$
$$+\sum_{l=0}^{i-2}\tilde{\alpha}_{2,2}\cdot\tilde{v}\cdot\tilde{T}_l\cdot c_{i-2-l}-\sum_{l=0}^{i-2}\tilde{\beta}_{0,1}\cdot\tilde{T}_l\cdot u_{i-2-l})-I(i,3)\times$$
$$\times(\sum_{l=0}^{i-3}\sum_{k=0}^{l}\tilde{\beta}_{0,2}\cdot\tilde{T}_k\cdot\tilde{T}_{l-k}\cdot u_{i-3-l}+\sum_{l=0}^{i-3}\tilde{\beta}_{2,2}\cdot\tilde{v}\cdot\tilde{T}_l\cdot u_{i-3-l})),$$

$$\breve{g}_i(\varphi,\psi,\eta,t)=-(I(i,1)\cdot\tilde{\mu}_0\cdot u_{i-1}+I(i,2)\cdot\sum_{l=0}^{i-2}\tilde{\mu}_1\cdot\tilde{T}_l\cdot u_{i-2-l}+$$
$$+I(i,3)\cdot\sum_{l=0}^{i-3}\sum_{k=0}^{l}\tilde{\mu}_2\cdot\tilde{T}_k\cdot\tilde{T}_{l-k}\cdot u_{i-3-l}),\ \breve{\breve{g}}_i(\varphi,\psi,\eta,t)=-\lambda_0\cdot u_{i-1}$$

and to find c_i, u_i, $\tilde{T}_i$, $\tilde{\kappa}_i$, $\tilde{\sigma}_i$ ($i=\overline{0,n}$) in problems (16)–(19), the following formulas are obtained:

$$c_0=\begin{cases}\widehat{g}_0(\varphi,\psi,\eta,t)+\tilde{c}_*^*(\psi,\eta,t-\tilde{f}(\varphi,\psi,\eta)), & t\geq\tilde{f},\\ \hat{\hat{g}}_0(\varphi,\psi,\eta,t)+\tilde{c}_0^0(\tilde{f}^{-1}(\tilde{f}(\varphi,\psi,\eta)-t,\psi,\eta),\psi,\eta), & t<\tilde{f},\end{cases}$$

$$u_0=\tilde{u}_0^0\cdot e^{-\frac{\tilde{\beta}_{0,0}}{\tilde{\sigma}_0^0}\cdot t},$$

$$\tilde{T}_0=\begin{cases}\bar{\hat{g}}_0(\varphi,\psi,\eta,t)+\tilde{T}_*^*(\psi,\eta,t-\tilde{f}(\varphi,\psi,\eta)), & t\geq\tilde{f},\\ \bar{\hat{\hat{g}}}_0(\varphi,\psi,\eta,t)+\tilde{T}_0^0(\tilde{f}^{-1}(\tilde{f}(\varphi,\psi,\eta)-t,\psi,\eta),\psi,\eta), & t<\tilde{f},\end{cases}$$

$$\tilde{\kappa}_0=\tilde{\kappa}_0^0,\ \tilde{\sigma}_0=\tilde{\sigma}_0^0,$$

$$c_i=\begin{cases}\widehat{g}_i(\varphi,\psi,\eta,t), t\geq\tilde{f},\\ \hat{\hat{g}}_i(\varphi,\psi,\eta,t), t<\tilde{f},\end{cases}$$

$$u_i=\frac{\tilde{g}_i(\varphi,\psi,\eta,t)}{\tilde{\beta}_{0,0}}\cdot(1-\cdot e^{-\frac{\tilde{\beta}_{0,0}}{\tilde{\sigma}_0^0}\cdot t}),$$

$$\tilde{T}_i=\begin{cases}\bar{\hat{g}}_i(\varphi,\psi,\eta,t), t\geq\tilde{f},\\ \bar{\hat{\hat{g}}}_i(\varphi,\psi,\eta,t), t<\tilde{f},\end{cases}$$

$$\tilde{\kappa}_i=\int\limits_0^t\breve{g}_i(\varphi,\psi,\eta,\widehat{t})d\widehat{t},$$

$$\tilde{\sigma}_i=\int\limits_0^t\breve{\breve{g}}_i(\varphi,\psi,\eta,\widehat{t})d\widehat{t}\ \ (i=\overline{1,n}),$$

where:

$$\widehat{g}_i(\varphi,\psi,\eta,t)=\kappa_*^*\cdot\int\limits_{\varphi_*}^{\varphi}\frac{g_i(\widehat{\varphi},\psi,\eta,\tilde{f}(\widehat{\varphi},\psi,\eta)-\tilde{f}(\varphi,\psi,\eta)+t)}{\tilde{v}^2(\widehat{\varphi},\psi,\eta)}d\widehat{\varphi},$$

$$\hat{\hat{g}}_i(\varphi,\psi,\eta,t)=\int\limits_0^t\frac{g_i(\tilde{f}^{-1}(\widehat{t}+\tilde{f}(\varphi,\psi,\eta)-t,\psi,\eta),\psi,\eta,\widehat{t})}{\tilde{\sigma}_0^0(\tilde{f}^{-1}(\widehat{t}+\tilde{f}(\varphi,\psi,\eta)-t,\psi,\eta),\psi,\eta)}d\widehat{t},$$

$$\bar{\hat{g}}_i(\varphi,\psi,\eta,t)=\kappa_*^*\cdot\int\limits_{\varphi_*}^{\varphi}\frac{\bar{\tilde{g}}_i(\widehat{\varphi},\psi,\eta,\tilde{f}(\widehat{\varphi},\psi,\eta)-\tilde{f}(\varphi,\psi,\eta)+t)}{\tilde{v}^2(\widehat{\varphi},\psi,\eta)}d\widehat{\varphi},$$

$$\bar{\hat{\hat{g}}}_i(\varphi,\psi,\eta,t)=\int\limits_0^t\frac{\bar{\tilde{g}}_i(\tilde{f}^{-1}(\widehat{t}+\tilde{f}(\varphi,\psi,\eta)-t,\psi,\eta),\psi,\eta,\widehat{t})}{\tilde{\sigma}_0^0(\tilde{f}^{-1}(\widehat{t}+\tilde{f}(\varphi,\psi,\eta)-t,\psi,\eta),\psi,\eta)}d\widehat{t},$$

$$g_i(\varphi,\psi,\eta,t)=\sum_{l=0}^{i}\tilde{\beta}_{l,0}\cdot\tilde{v}^l\cdot u_{i-l}+I(i,1)\cdot(d_0\cdot(b_1\cdot c''_{(i-1)\varphi\varphi}+$$
$$+b_2\cdot c''_{(i-1)\psi\psi}+b_3\cdot c''_{(i-1)\eta\eta}+b_4\cdot c'_{(i-1)\psi}+b_5\cdot c'_{(i-1)\eta})-$$
$$-\sum_{l=1}^{i}(\tilde{\sigma}_l\cdot c'_{(i-l)t}+\tilde{\sigma}'_{l\,t}\cdot c_{i-l}))+(I(i,1)\cdot(\sum_{l=0}^{i-1}\tilde{\beta}_{0,1}\cdot\tilde{T}_l\cdot u_{i-1-l}-$$
$$-\sum_{l=0}^{i-1}\tilde{\alpha}_{l,0}\cdot\tilde{v}^l\cdot c_{i-1-l})+I(i,2)\cdot(\sum_{l=0}^{i-2}\sum_{k=0}^{l}\tilde{\beta}_{0,2}\cdot\tilde{T}_k\cdot\tilde{T}_{l-k}\cdot u_{i-2-l}+$$
$$+\sum_{l=0}^{i-2}\tilde{\beta}_{2,2}\cdot\tilde{v}\cdot\tilde{T}_l\cdot u_{i-2-l}-\sum_{l=0}^{i-2}\tilde{\alpha}_{0,1}\cdot\tilde{T}_l\cdot c_{i-2-l})-I(i,3)\times$$
$$\times(\sum_{l=0}^{i-3}\sum_{k=0}^{l}\tilde{\alpha}_{0,2}\cdot\tilde{T}_k\cdot\tilde{T}_{l-k}\cdot c_{i-3-l}+\sum_{l=0}^{i-3}\tilde{\alpha}_{2,2}\cdot\tilde{v}\cdot\tilde{T}_l\cdot c_{i-3-l}),$$

$$\tilde{g}_i(\varphi,\psi,\eta,t)=I(i,1)\cdot(d_0^*\cdot(b_1\cdot u''_{(i-1)\varphi\varphi}+b_2\cdot u''_{(i-1)\psi\psi}+$$
$$+b_3\cdot u''_{(i-1)\eta\eta}+b_4\cdot u'_{(i-1)\psi}+b_5\cdot u'_{(i-1)\eta})-\sum_{l=1}^{i}(\tilde{\sigma}_l\cdot u'_{(i-l)t}+\tilde{\sigma}'_{l\,t}\cdot u_{i-l}))-$$
$$-(I(i,1)\cdot(\sum_{l=1}^{i}\tilde{\beta}_{l,0}\cdot\tilde{v}^l\cdot u_{i-l}+\sum_{l=0}^{i-1}\tilde{\beta}_{0,1}\cdot\tilde{T}_l\cdot u_{i-1-l}-$$
$$-\sum_{l=0}^{i-1}\tilde{\alpha}_{l,0}\cdot\tilde{v}^l\cdot c_{i-1-l})+I(i,2)\cdot(\sum_{l=0}^{i-2}\sum_{k=0}^{l}\tilde{\beta}_{0,2}\cdot\tilde{T}_k\cdot\tilde{T}_{l-k}\cdot u_{i-2-l}+$$
$$+\sum_{l=0}^{i-2}\tilde{\beta}_{2,2}\cdot\tilde{v}\cdot\tilde{T}_l\cdot u_{i-2-l}-\sum_{l=0}^{i-2}\tilde{\alpha}_{0,1}\cdot\tilde{T}_l\cdot c_{i-2-l})+I(i,3)\times$$
$$\times(\sum_{l=0}^{i-3}\sum_{k=0}^{l}\tilde{\alpha}_{0,2}\cdot\tilde{T}_k\cdot\tilde{T}_{l-k}\cdot c_{i-3-l}+\sum_{l=0}^{i-3}\tilde{\alpha}_{2,2}\cdot\tilde{v}\cdot\tilde{T}_l\cdot c_{i-3-l})),$$

$$\bar{\tilde{g}}_i(\varphi,\psi,\eta,t)=\tilde{\gamma}\cdot\sum_{l=0}^{i}\tilde{\beta}_{l,0}\cdot\tilde{v}^l\cdot u_{i-l}+I(i,1)\cdot(d_0^{**}\cdot(b_1\cdot\tilde{T}''_{(i-1)\varphi\varphi}+$$
$$+b_2\cdot\tilde{T}''_{(i-1)\psi\psi}+b_3\cdot\tilde{T}''_{(i-1)\eta\eta}+b_4\cdot\tilde{T}'_{(i-1)\psi}+b_5\cdot\tilde{T}'_{(i-1)\eta})-$$
$$-\sum_{l=1}^{i}(\tilde{\sigma}_l\cdot\tilde{T}'_{(i-l)t}+\tilde{\sigma}'_{l\,t}\cdot\tilde{T}'_{i-l}))+\gamma\cdot(I(i,1)\cdot(\sum_{l=0}^{i-1}\tilde{\beta}_{0,1}\cdot\tilde{T}_l\cdot u_{i-1-l}-$$
$$-\sum_{l=0}^{i-1}\tilde{\alpha}_{l,0}\cdot\tilde{v}^l\cdot c_{i-1-l})+I(i,2)\cdot(\sum_{l=0}^{i-2}\sum_{k=0}^{l}\tilde{\beta}_{0,2}\cdot\tilde{T}_k\cdot\tilde{T}_{l-k}\cdot u_{i-2-l}+$$
$$+\sum_{l=0}^{i-2}\tilde{\beta}_{2,2}\cdot\tilde{v}\cdot\tilde{T}_l\cdot u_{i-2-l}-\sum_{l=0}^{i-2}\tilde{\alpha}_{0,1}\cdot\tilde{T}_l\cdot c_{i-2-l})-I(i,3)\times$$

$$\times\left(\sum_{l=0}^{i-3}\sum_{k=0}^{l}\tilde{\alpha}_{0,2}\cdot\tilde{T}_k\cdot\tilde{T}_{l-k}\cdot c_{i-3-l}+\sum_{l=0}^{i-3}\tilde{\alpha}_{2,2}\cdot\tilde{v}\cdot\tilde{T}_l\cdot c_{i-3-l}\right)),$$

$$\breve{g}_i(\varphi,\psi,\eta,t)=I(i,1)\cdot\tilde{\mu}_0\cdot u_{i-1}+I(i,2)\cdot\sum_{l=0}^{i-2}\tilde{\mu}_1\cdot\tilde{T}_l\cdot u_{i-2-l}+$$

$$+I(i,3)\cdot\sum_{l=0}^{i-3}\sum_{k=0}^{l}\tilde{\mu}_2\cdot\tilde{T}_k\cdot\tilde{T}_{l-k}\cdot u_{i-3-l}\ ,\ \breve{\breve{g}}_i(\varphi,\psi,\eta,t)=\lambda_0\cdot u_{i-1},$$

$\tilde{f}=\tilde{f}(\varphi,\psi,\eta)=\kappa_*^*\cdot\int_{\varphi_*}^{\varphi}\frac{\tilde{\sigma}_0^0(\hat{\varphi},\psi,\eta)}{\tilde{v}^2(\hat{\varphi},\psi,\eta)}d\hat{\varphi}$ is the time of passing of the respective particles of the impurity from point $(x(\varphi_*,\psi,\eta),y(\varphi_*,\psi,\eta),z(\varphi_*,\psi,\eta))\in G_z$ to point $(x(\varphi,\psi,\eta),y(\varphi,\psi,\eta),z(\varphi,\psi,\eta))\in G_z$, $\tilde{f}^{-1}$ is function inverted according to $\tilde{f}$ with respect to variable φ, $I(a,b)=\begin{cases}1, & a\ge b,\\ 0, & a<b.\end{cases}$

4. Conclusions

The mathematical models for predicting the technological regimes of filtration (water purification from the present impurities), backwashing, chemical regeneration and direct washing of rapid cone-shaped adsorption filters, taking into account the influence of temperature effects on the internal mass transfer kinetics at a constant rate of the appropriate regimes, have been formed. Algorithms for numerical-asymptotic approximations of solutions of the corresponding nonlinear singularly perturbed boundary value problems for a model cone-shaped domain bounded by two equipotential surfaces and a flow surface have been obtained under the condition that in the filtration regime, the convective components of mass transfer and adsorption outweigh the contribution of diffusion and desorption, and in the backwashing of chemical regeneration and direct washing regimes, the convective components of mass transfer and desorption outweigh the contribution of diffusion and adsorption. The proposed models in the complex allow computer experiments to be conducted to investigate the change of impurity concentrations in the filtration flow and on the surface of the load adsorbent, the temperature of the filtration flow, the filtration coefficient, and the active porosity along the filter height due to adsorption and desorption processes, and on their basis good use of adsorbents to be predicted, and the protective time of rapid cone-shaped adsorption filters with chemical regeneration of homogeneous porous loads be increased.

References

[1] Bomba A. Ya., Klymiuk Yu. Ye.: Mathematical modeling of spatial singular-perturbed filtration-convection-diffusion processes. TzOV firma "Assol", Rivne 2014.
[2] Bomba A. Ya., Prysiazhniuk I. M., Prysiazhniuk O. V.: Methods of perturbation theory for predicting heat transfer processes in porous and microporous media. O. Zen, Rivne 2017.
[3] Bomba A. Ya., Safonyk A. P.: Modeling of nonlinearly perturbed processes of purification of liquids from multicomponent contaminants. NUVHP, Rivne 2017.
[4] Edzwald J.: Water Quality & Treatment. A Handbook on Drinking Water, McGraw-Hill Professional, 2010.
[5] Heikkinen M., Poutiainen H., Liukkonen M., Heikkinen T., Hiltunen Y.: Self-organizing maps in the analysis of an industrial wastewater treatment process. Mathematics and Computers in Simulation 82(3), 2011, 450–459.
[6] Hendricks D. W.: Fundamentals of water treatment unit processes: physical, chemical, and biological. CRC Press, Boca Raton 2011.
[7] Ives K. J.: Deep-bed water filters. New developments. Filtr. and Separ. 6(1), 1969, 42–48.
[8] Kalteh A. M., Hjorth P., Berndtsson R.: Review of the self-organizing map (SOM) approach in water resources: analysis, modelling and application. Environmental Modelling and Software 23(7), 2008, 835–845.
[9] Klimjuk Ju. Je.: Construction of filtration fields for rapid filters conical shape with homogeneous porous loads. Proceedings of II International scientific conference “World Science in 2016: Results”. Lulu Press, Morrisville 2017, 95–99.
[10] Klimjuk Ju. Je.: Prediction of changes in the characteristics of filter materials in rapid cone-shaped waterpurifying filters. Innovative solutions in modern science 8(27), 2018, 72–84.
[11] Nevzorova A.B.: Fundamentals of automation of water supply and sanitation. UO BelGUT, Gomel 2005.
[12] Maleki A., Pajootan E., Hayati B.: Ethyl acrylate grafted chitosan for heavy metal removal from wastewater: Equilibrium, kinetic and thermodynamic studies. Journal of the Taiwan Institute of Chemical Engineers 51(0), 2015, 127–134.
[13] Maier H. R., Dandy G. C.: Neural networks for the prediction and forecasting of water resources variables: a review of modelling issues and applications. Environmental Modelling and Software 15(1), 2000, 101–124.
[14] Makarevich N. A., Bogdanovich N. I.: The theoretical basis of adsorption. SAFU, Arkhangelsk 2015.
[15] Mincz D. M.: Theoretical foundations of water purification technology. Strojizdat, Moscow 1964.
[16] Safonyk A. P.: Modelling the filtration processes of liquids from multicomponent contamination in the conditions of authentication of mass transfer coefficient. International Journal of Mathematical Models and Methods in Applied Sciences 9, 2015, 189–192.
[17] Sakalova H. V., Vasylinych T. M.: Investigation of the efficiency of purification of heavy metal ions from wastewater using natural adsorbents. TOV Tvory, Vinnytsia 2019.
[18] Vries D., Bertelkamp C., Schoonenberg Kegel F., Hofs B., Dusseldorp J., Bruins J. H., de Vet W., van den Akker B.: Iron and manganese removal: Recent advances in modelling treatment efficiency by rapid sand filtration. Water Research 109, 2017, 35–45.
[19] Zevi Y., Dewita S., Aghasa A., Dwinandha D.: Removal of Iron and Manganese from Natural Groundwater by Continuous Reactor Using Activated and Natural Mordenite Mineral Adsorption. International IOP Conf. Ser., Earth Environ. Sci, 111, 2018, 012016, 1–7.

Prof. Andrii Ya. Bomba
e-mail: abomba@ukr.net

Professor of the Department Computer Science and Applied Mathematics of the National University of Water and Environmental Engineering, Rivne, Ukraine.
He is the author of over 450 scientific works, including 9 monographs. A well-known specialist in mathematical modeling and computational methods. Academician of the UNGA. Member of four editions of collections of scientific works and two Specialized Scientific Councils for the defense of theses.

http://orcid.org/0000-0001-5528-4192

Ph.D. Yurii Ye. Klymyuk
e-mail: klimyuk@ukr.net

Associate professor of the Department Computer Science and Applied Mathematics of the National University of Water and Environmental Engineering, Rivne, Ukraine.
Engaged in scientific mathematical modeling of natural and technological processes, computer simulation of technological processes, computer techniques and computer technologies, programming.

http://orcid.org/0000-0003-3672-8469

Ph.D. Ihor M. Prysiazhniuk
e-mail: igorpri79@gmail.com

Associate professor of the Department of Mathematics of Rivne State University of Humanities, Rivne, Ukraine.
Engaged in applied and computational mathematics, mathematical modeling of technological processes, numerical modeling and analysis, differential equations in applied mathematics, physics and engineering, computer simulation.

http://orcid.org/0000-0003-4531-1788

otrzymano/received: 3.08.2020 *przyjęto do druku/accepted: 10.12.2020*

http://doi.org/10.35784/iapgos.2101

FREQUENCY RESPONSE OF NORRIS GAP DERIVATIVES AND ITS PROSPERITIES FOR GAS SPECTRA ANALYSIS

Sławomir Cięszczyk
Lublin University of Technology, Department of Electronics and Information Technology, Lublin, Poland

Abstract. *The article deals with an analysis of the properties of Norris gap derivatives. It discusses issues related to determining information from optical spectra measured with spectrometers. Impulse responses of differentiating filters were introduced using both Norris and Savitzky-Golay methods. The amplitude-frequency responses of the first and second order Norris differentiating filters were compared. The length impact of both segment and gaps on the frequency characteristics of filters was compared. The processing of exemplary gas spectra using the discussed technique was subsequently presented. The effect of first and second order derivatives on the spectra of carbon monoxide rotational lines for low resolution measurements is investigated. The Norris method of derivatives are very simple to implement and the calculation of their parameters does not require the use of advanced numerical methods.*

Keywords: Norris method, optical spectra derivative, spectroscopy, signal processing

WŁAŚCIWOŚCI CZĘSTOTLIWOŚCIOWE POCHODNYCH TYPU NORRIS GAP I ICH ZASTOSOWANIE DO ANALIZY WIDM GAZÓW

Streszczenie. *Artykuł przedstawia analizę właściwości pochodnych według metody Norrisa. Omówiono w nim zagadnienia związane z wyznaczaniem informacji z widm optycznych mierzonych spektrometrami. Przedstawiono odpowiedzi impulsowe filtrów różniczkujących zarówno metodą Norrisa jak też Savitzky-Golay. Porównano odpowiedzi amplitudowo-częstotliwościowe filtrów różniczkujących Norrisa pierwszego i drugiego rzędu. Porównano wpływ zarówno długości segmentów jak i rozstępu (luk) na charakterystyki częstotliwościowe filtrów. Kolejno zaprezentowano przetwarzanie przykładowych widm gazu z wykorzystaniem omawianej techniki. Przedstawiono także wpływ pochodnych pierwszego i drugiego rzędu na widma linii rotacyjnych tlenku węgla dla pomiarów o małej rozdzielczości. Metoda pochodnych według Norrisa jest bardzo prosta w implementacji a obliczanie jej parametrów nie wymaga stosowania zaawanasowanych metod numerycznych.*

Słowa kluczowe: metoda Norrisa, pochodne widm optycznych, spektroskopia, przetwarzanie sygnałów

Introduction

Spectroscopy is an analytical method finding increasing use in various fields, as it provides a quick and cheap alternative to many other types of techniques. Information are obtained as a result of the analysis of radiation, which interacts with the tested sample mainly by transmittance, reflectance or radiation emitted by the sample [16]. In the field of spectroscopy, in addition to the continuous development of measuring equipment, new methods of data analysis are essential. Data processing algorithms should be adapted to the type of analyzed signals and information to be obtained. New produced devices have better resolution which allows additional information to be obtained. Unfortunately, increasing the dimensions of the data sometimes makes it difficult to interpret. The type of processed data (qualitative or quantitative) also changes the approach to the algorithms used. The first step in determining information is data acquisition. After that, there is the data processing pipeline where very different computational methods may be utilised. Before starting to develop an algorithm for the analysis of specific spectra, the type of data and their complexity should be defined. Including what features can be determined and what distortions the signal contains.

The measured spectrum contains from several hundred to several thousand variables. In addition to substantial information, the spectra also contain other types of artifacts. The measured spectrum always contains an unwanted distorted background continuum signal, interference and noise. We understand interferences to be components having a shape with a specific structure. Background usually has a shape slowly varying with the wavelength. The typical shape of a baseline is [13]: offset, slope and curvature. There are many preprocessing methods to improve the spectral signal, extract some features and reduce the non-informative components. In the case of background correction for a single spectral line, the simplest method is three-point correction which assumes a parabolic type distortion [18]. More advanced methods use a specific spectral window. Heuristic methods are also often used, the result of which depends most on the experience of the experimenter. For some types of spectra, the best properties are obtained by means of derivatives. The first derivative causes elimination of a background constant value and the second derivative suppresses a linear varying background. So derivatives are able to significantly reduce continuous background. Additionally, derivatives increase the spectral resolution and improve the selectivity of the analysis. The second derivative of the typical spectral lines (Gauss or Lorentz) has a narrower shape than the original lines. Derivative filters belong to feature extraction algorithms, which consist in determining new signal features. Unfortunately, the differentiation operation reduces the signal-to-noise ratio and is therefore often related to smoothing of data, wherein, the smoothing is performed before or simultaneously with the derivative. The effect of achieving a well-smoothed derivative requires designing a low-pass filter with a low cut-off frequency [7].

In spectroscopy, derivatives are performed mainly by two methods: by a simple point difference and by the Savitzky-Golay method. Savitzky-Golay (SG) filters have been proposed for the analysis of chemical data [17]. Many modifications of the original SG method were made, and new versions of filters with various properties are proposed even recently [2, 3, 11]. It should be noted that the SG filters are not optimal and their frequency response is not ideal. SG filters are characterized by low computational complexity when used. However, determining their coefficients requires the use of tables or appropriate computer programs. This article will introduce the properties of the little-known Norris gap derivative method [15]. The analysis will be carried out from the signal processing and spectroscopic data analysis perspective. The considered method has proven positive properties as a preprocessing method for PLS model calibration [20]. The gap derivatives are shortly determined as an approximation of an analytical derivative by simple finite difference [5]. The frequency response of Norris derivative filters with smoothing will be derived in the next paragraphs. The effect of the parameters on the shape of the main-lobe and side-lobe will be determined. An exemplary optical spectrum containing rotational lines of gases will also be analyzed.

1. Savitzky-Golay and Norris derivative

The first derivative represents the rate of change of function. Similarly, the second derivative measures the value of change of the first derivative. In the digital world, "derivative" means calculating the differences between some wavelength. The simples' difference of adjacent wavenumbers is very sensitive (amplifies) to high frequency noise, less more mid-frequency and produces high attenuation of low-frequency noise. In the simplest version, the difference is calculated between adjacent points on the spectrum. Simple forward difference:

$$f_d(x) = \left(f(x+h) - f(x)\right)/h \qquad (1)$$

But the difference may by calculated between two spectrum points which are separated by two or more points. The separation width is called a gap [4]. Increasing the gap can severely change the derivative shape and in practice can be applied only in very slowly changing spectra. A first-order gap derivative is given be following equation [5]:

$$f'(x) = \frac{f(x+g/2) - f(x-g/2)}{g} \qquad (2)$$

A second order gap derivative is:

$$f''(x) = \frac{f(x+g) - 2f(x) + f(x-g)}{g^2} \qquad (3)$$

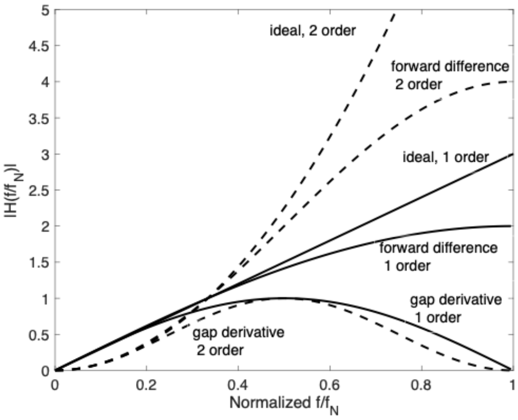

Fig. 1. Frequency response of first and second order derivative: ideal, simple forward difference, gap derivative

The frequency responses in Figure 1 have been scaled so that their shapes can be compared. Unscaled characteristics are those for the simple forward difference. The frequency has been normalized to the Nyquist frequency which is half of the sampling frequency.

The Norris derivative consists of calculation of the difference between two values which are averages of two adjacent points [9]. Further, the number of averages points, called segments, can be increased. At the same time, the gap between particular segments can be changed [10]. The bigger the gap, the broader the shape of the results with additional stronger noise suppression.

Example impulse response of Norris first derivative filters [9]:

Segment=1, gap=1, h[n]=[-1,0,1]
Segment=1, gap=3, h[n]=[-1,0,0,0,1]
Segment=3, gap=1, h[n]=[-1,-1,-1,0,1,1,1]/3
Segment=3, gap=3, h[n]=[-1,-1,-1,0,0,0,1,1,1]/3

Example impulse response of Norris second derivative filters [9]:

Segment=1, gap=1, h[n]=[1,0,-2,0,1]
Segment=1, gap=3, h[n]=[1,0,0,0,-2,0,0,0,1]
Segment=3, gap=1, h[n]=[1,1,1,0,-2,-2,-2,0,1,1,1]/3
Segment=3, gap=3, h[n]=[1,1,1,0,0,0,-2,-2,-2,0,0,0,1,1,1]/3

The theoretical basis of the Savitzky-Golay method, including derivative filters, consist of a least-square polynomial approximation of a curve between a section of data. The derivative is a slope of the curve in the central point of the data window. The SG differentiation filter is a finite impulse filter described by two parameters: the order of the polynomial of approximation, and the size of the data window. The filter coefficients are integers with an appropriate scaling factor [14].

Example impulse response of Savitzky-Golay first derivative filters [6, 8]:
Window=3, polynomial degree=2, h[n]=[-1,0,1]/2
Window=5, polynomial degree=2, h[n]=[-2,-1,0,1,2]/10
Window=7, polynomial degree=2, h[n]=[-3,-2,-1,0,1,2,3]/28
Window=5, polynomial degree=3, h[n]=[1,-8,0,8,-1]/12

Example impulse response of Savitzky-Golay second derivative filters [6, 8]:
Window=5, polynomial degree=2(3), h[n]=[2,-1,-2,-1,2]/7
Window=7, polynomial degree=2(3), h[n]=[5,0,-3,-4,-3,0,5]/42
Window=9, polynomial degree=2(3), h[n]=[28,7,-8,-17,-20,-17,-8,7,28]/462
Window=5, polynomial degree=4(5), h[n]=[-1,16,-30,16,-1]/12

2. Frequency response of Norris derivative filters

Spectrometers tends to produce drift related to instrumental and environmental factors which are fluctuations of the radiation source, detector sensitivity, temperature and sample changes. Unfortunately, drift is not independent in nature and cannot be eliminated even by multivariate calibration models [1]. Derivative methods can be used for this purpose. At the same time, the noise that appears at higher frequencies should also be taken into account. To analyze such problems in signal processing, frequency response characteristics are used. The shape of the main-lobe and the level of the side-lobes indicate the properties of a particular filter. However, they are very rarely analyzed in the processing of spectroscopic data. The most frequently analyzed are the shapes of specific spectra that have been processed using a given filter.

The frequency response of an ideal first order differentiator is a line with some slope what gives some kind of high-pass filter $H(e^{j\omega}) = j\omega$. To attenuate the high frequency, additional low-pass filtering is applied. As a result, we get a low-pass differential filter [19]. The ideal frequency limited differentiator has a frequency response that equals zero for a high frequency. As can be seen in Figure 2, this property in Norris filters can be observed by using a gap (central difference operator). But only the use of segments 3 and 5 effectively eliminates the higher frequencies (Fig. 3, 5). For efficient filtering of high frequencies, a long filter response is required, e.g. 5 segments and 5 gaps.

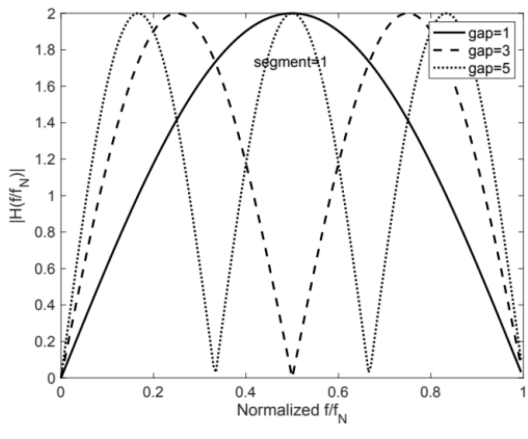

Fig. 2. Frequency response of first derivative of Norris filter for segment = 1 and for different gaps

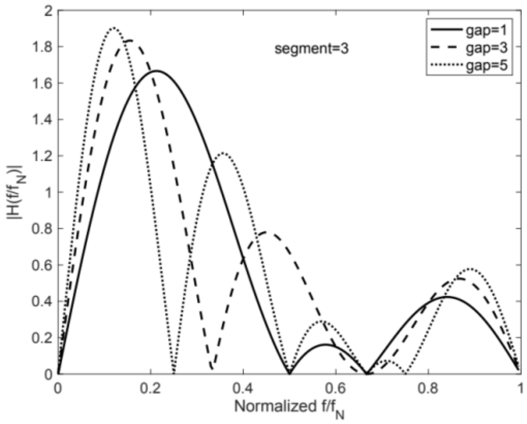

Fig. 3. Frequency response of first derivative of Norris filter for segment = 1 and for different gaps

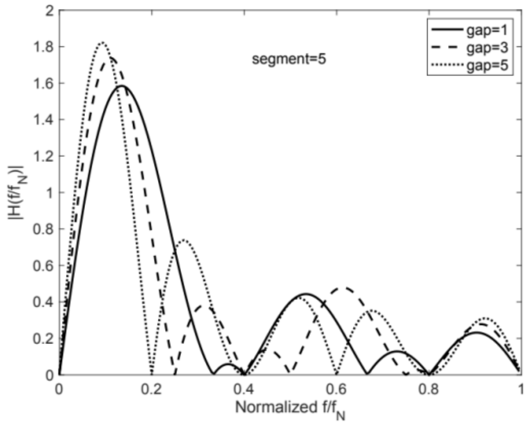

Fig. 4. Frequency response of first derivative of Norris filter for segment = 1 and for different gaps

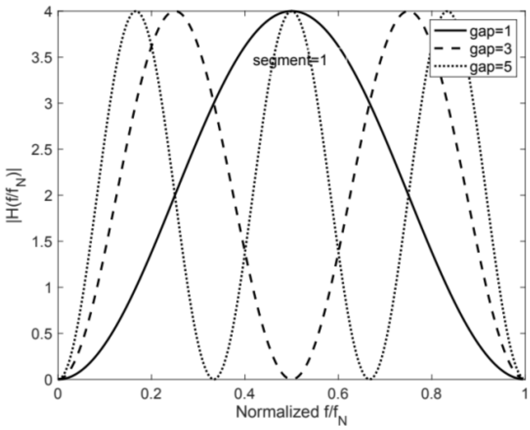

Fig. 5. Frequency response of second order Norris derivative filters for different segments and gaps

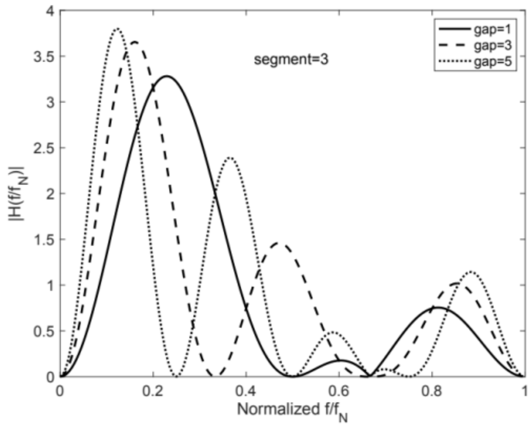

Fig. 6. Frequency response of second order Norris derivative filters for different segments and gaps

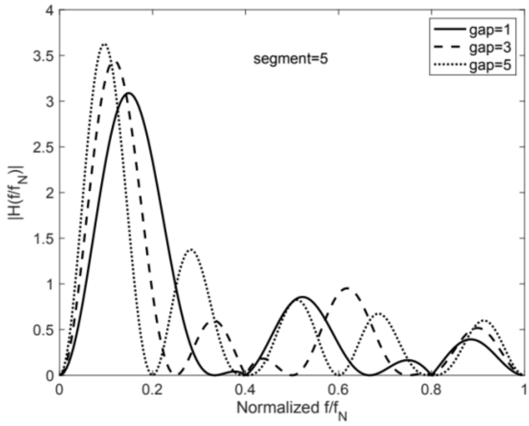

Fig. 7. Frequency response of second order Norris derivative filters for different segments and gaps

Similar to first order analysis can be performed for second order derivative. The ideal frequency response of the filters is increased square as a function of frequency ω^2 with a constant π phase. Figure 4 presents the frequency response for segment = 1 and with three value of gap. Figures 5 and 6 reflect the impact of increasing the segment length as a responsible of low-pass filtering effect.

It is very important to mention that normalization for a Norris derivative is performed only for segments and not for the convolution interval length [9].Therefore, the ratio of the side lobe to the main lobe, and not its actual value, should be compared.

3. Gas spectra processing by Norris derivative

The derivative eliminates constant baseline (offset) variation, and the second derivative eliminates the baseline linear trend. Additionally, the derivative enhances weaker absorption lines and is able to resolve closely spaced bands. The second derivative of a symmetric band also gives symmetric and negative shapes. But for asymmetric bands, the second derivative peaks are shifted. In practice, before calculating derivative spectra proper selection of algorithm parameters is required. The basic information here can be the shape of the original measured spectrum [12].

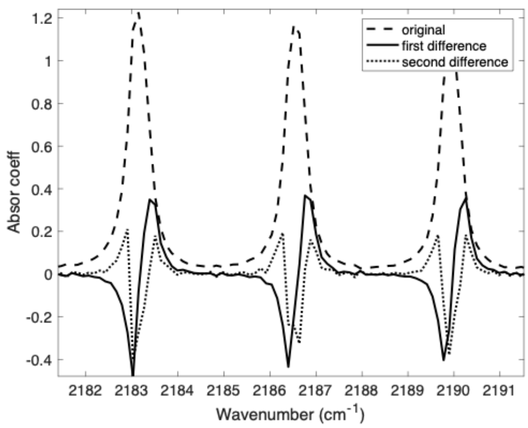

Fig. 8. Carbon monoxide spectrum with first and second difference

Figure 8 presents part of the carbon monoxide spectrum in the mid-infrared, which consists of three example rotational lines. Additionally, the first and second difference of the spectrum is presented. Because of the relatively low resolution, the spectrum consists of only a few points representing each spectral line shape, so the derivatives are nonregular with visible noise visible in the second difference. The derivatives presented in Figures 8 and 9 are normalized and shifted in amplitude for clear comparison. The increased gap caused the shape to be wider and softly smoothed.

By application of a segment length of 3 or 5 (Figure 8 and 9), the processed spectral lines are very smooth and rounded. Applying wider segments leads to visible noise elimination and stronger regularity of the obtained shapes. Obtaining optimal parameters of differentiation requires analysis of its effect on zero order spectra.

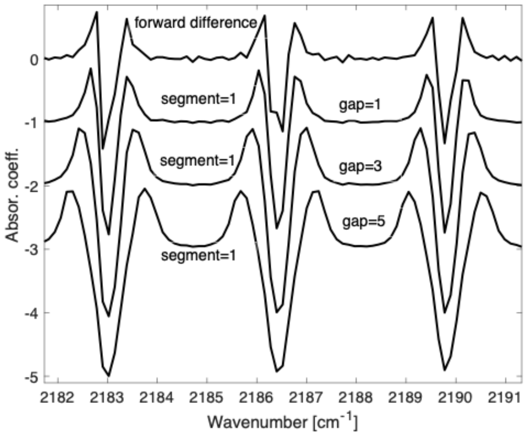

Fig. 9. Influence of gap of second derivative on infrared spectra of carbon monoxide

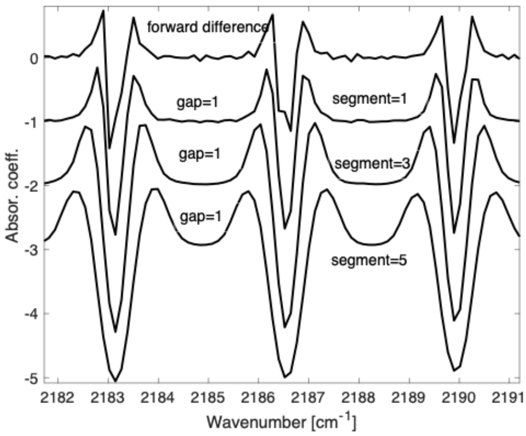

Fig. 10. Influence of segments of second derivative on infrared spectra of carbon monoxide

It should also be noted that in the spectra of the second derivative, a high side lobe levels appears, which can interfere with other closely spaced neighbored rotational lines.

4. Summary

The article presents the issue of the pre-processing of spectrometric data in order to eliminate undesired artifacts. One of the most frequently used methods for this purpose is the use of derivatives. In practice, most frequently, first and second order derivatives are used. They can be calculated with simple differences and with more sophisticated methods such as Savitzky-Golay. The Norris method is simpler than the Savitzky-Golay algorithm and uses two parameters: gap and segment. Gap increases the length of the window on which the derivative is executed and is responsible for the differentiation properties. The segment is the length of the signal fragment that is averaged and is therefore responsible for the low-pass properties of the filter. The length of the filter impulse response depends on the gap and segment.

The article presents the frequency response characteristics of Norris filters for the combination of gap values equaling 1, 3 and 5; and segments equaling 1, 3 and 5. Their frequency responses are not perfect, but with such a relatively short impulse response length, they can be considered to be correct. It can be observed that by increasing both the gap and segment size, a better signal-to-noise ratio is achieved.

It should be noted that, in practice, the selection of the derivative method is performed experimentally for each type of data by performing calculations for several filter parameters. By performing calculations for several values of gap and segments, their optimal Norris derivative can be quickly selected.

References

[1] Brown C. D., Vega-Montoto L., Wentzell P. D.: Derivative preprocessing and optimal corrections for baseline drift in multivariate calibration. Applied Spectroscopy 54(7), 2000, 1055–1068.
[2] Candan Ç., Inan H.: A unified framework for derivation and implementation of Savitzky–Golay filters. Signal Processing 104, 2014, 203–211.
[3] Dai W., Selesnick I., Rizzo J. R., Rucker J., Hudson T.: A nonlinear generalization of the Savitzky-Golay filter and the quantitative analysis of saccades. Journal of vision 17(9), 2017, 10–19.
[4] Davies A. M. C.: Derivative? What Do You Mean "Derivative"? NIR news 4(4), 1993, 10–11.
[5] De Jong S. A., O'Brien W. L., Lu Z., Cassidy B. M., Morgan S. L., Myrick M. L.: Optimization of gap derivatives for measuring blood concentration of fabric using vibrational spectroscopy. Applied Spectroscopy 69(6), 2015, 733–748.
[6] Figueiredo N. S., Ferreira L. H., Dutra O. O.: An Approach to Savitzky-Golay Differentiators. Circuits, Systems, and Signal Processing 38(9), 2019, 4369–4379.
[7] Giakas G., Baltzopoulos V.: Optimal digital filtering requires a different cut-off frequency strategy for the determination of the higher derivatives. Journal of biomechanics 30(8), 1997, 851–855.
[8] Gorry P. A.: General least-squares smoothing and differentiation by the convolution (Savitzky-Golay) method. Analytical Chemistry 62(6), 1990, 570–573.
[9] Hopkins D. W.: What is a Norris derivative?. NIR news 12(3), 2001, 3–5.
[10] Hopkins D.W.: Revisiting the Norris derivative quotient math in regression. NIR news 27(7), 2016, 23–28.
[11] Kennedy H. L.: Improving the frequency response of Savitzky-Golay filters via colored-noise models. Digital Signal Processing 102, 2020, 102743.
[12] Kus S., Marczenko Z., Obarski N.: Derivative UV-VIS spectrophotometry in analytical chemistry. Chem. Anal 41(6), 1996, 889–927
[13] Lee L. C., Liong C. Y., Jemain A. A.: A contemporary review on Data Preprocessing (DP) practice strategy in ATR-FTIR spectrum. Chemometrics and Intelligent Laboratory Systems 163, 2017, 64–75.
[14] Luo J., Ying K., He P., Bai J.: Properties of Savitzky-Golay digital differentiators. Digital Signal Processing 15(2), 2005, 122–136.
[15] Pan T., Zhang J., Shi X.: Flexible vitality of near-infrared spectroscopy – Talking about Norris derivative filter. NIR news 31(1-2), 2020, 24–27.
[16] Pasquini C.: Near infrared spectroscopy: A mature analytical technique with new perspectives – A review. Analytica Chimica Acta 1026, 2018, 8–36.
[17] Savitzky A., Golay M. J.: Smoothing and differentiation of data by simplified least squares procedures. Analytical chemistry 36(8), 1964, 1627–1639.
[18] Van Veen E. H., de Loos-Vollebregt M. T. C.: Application of mathematical procedures to background correction and multivariate analysis in inductively coupled plasma-optical emission spectrometry. Spectrochimica Acta Part B: Atomic Spectroscopy 53(5), 1998, 639–669.
[19] Wulf M., Staude G., Knopp A., Felderhoff T.: Efficient design of FIR filter based low-pass differentiators for biomedical signal processing. Current Directions in Biomedical Engineering 2(1), 2016, 215–219.
[20] Yang Y., Pan T., Zhang J.: Global optimization of Norris derivative filtering with application for near-infrared analysis of serum urea nitrogen. American Journal of Analytical Chemistry 10(5), 2019, 143–152.

D.Sc. Eng. Sławomir Cięszczyk
e-mail: s.cieszczyk@pollub.pl

Sławomir Cięszczyk is an associate professor at the Department of Electronics and Information Technology at the Lublin University of Technology. He received the Ph.D. degree in 2008 and the D.Sc. Degree in habilitation in 2018. His research interests include optical sensors, open-path spectroscopy, signal processing, data analysis, numerical methods, simulation and modeling.

https://orcid.org/0000-0002-3986-2690

otrzymano/received: 29.07.2020 *przyjęto do druku/accepted: 10.12.2020*

http://doi.org/10.35784/iapgos.2225

BIT ERROR NOTIFICATION AND ESTIMATION IN REDUNDANT SUCCESSIVE-APPROXIMATION ADC

Serhii Zakharchenko, Roman Humeniuk
Vinnytsia National Technical University, Department of Computer Facilities, Vinnytsia, Ukraine

Abstract. *The article is devoted to research on the possibilities to use redundant number systems for bit error notification in a successive-approximation ADC during the main conversion mode. The transfer function of a successive-approximation ADC with a non-binary radix is analyzed. If the radix is less than 2, not all possible code combinations appear on the converter output. The process of formation of unused combinations is investigated. The relationship between the bit's deviations and the list of unused combinations is established. The possibilities of estimating the bit error value without interrupting the process of analog-to-digital conversion is considered.*

Keywords: successive-approximation ADC, redundant number systems, ADC transfer function

POWIADOMIENIE O BŁĘDZIE BITOWYM I OCENA W STOPNIOWEJ REDUNDANTNEJ APROKSYMACJI ACP

Streszczenie. *Artykuł jest poświęcony badaniu możliwości wykorzystania redundantnych systemów liczbowych do powiadamiania o błędach bitowych w stopniowej aproksymacji ACP podczas konwersji głównej. Analizowana jest funkcja transferu stopniowej aproksymacji ACP z niebinarną podstawą. Jeśli podstawa jest mniejsza niż 2, nie wszystkie możliwe kombinacje kodów pojawią się na wyjściu konwertera. Badany jest proces tworzenia nieużywanych kombinacji, i ustalane są relacje między odchyleniami bitu a listą nieużywanych kombinacji. Autorzy również przeanalizowali możliwości oceny wartości błędu bitowego bez przerywania procesu konwersji analogowo-cyfrowej.*

Słowa kluczowe: stopniowa aproksymacja ACP, redundantne systemy liczbowe, funkcja transferu ACP

Introduction

Successive-approximation ADCs are very popular now due to their high resolution at the level of 14–18 binary digits, and relatively high sampling rate in the range from 50 kHz to 50 MHz. However, if the number of bits exceeds 12–14, we have the influence of external factors, such as temperature change, which leads to bit errors. The maximum absolute errors will be in the most significant bits (MSB) [1]. The result of this is the increasing of differential and integral nonlinearities. There are two main ways to resolve this problem: technological and algorithmic. The technological methods are time- and cost-consuming, and provide the ability to improve the linearity by several bits. The universal method to overcome this problem is to use a calibration procedure for the MSBs [2, 3, 6]. The traditional calibration procedure is performed after the device is turned on and is periodically repeated during operation. The ADC can operate in either the main conversion mode or calibration. New calibration technologies allow the general and calibration modes to be combined [4, 5]. Using a non-binary radix provides the opportunity for notification of MSB deviations [7].

1. Transfer function analysis for successive-approximation ADC with non-binary radix

The ADC transfer function (TF) determines the relationship between the input analog signals with the output code combination. When we are using a binary numeral system, each value of the input analog signal corresponds to one relevant code combination. At the same time, when using a redundant positional numeral system (radix less than 2), there are zones of TF, where one value of the input signal corresponds to several output code combinations, as shown in Fig. 1a. However due to the successive-approximation algorithm in the output code, we will have only one of the possible output combinations (Fig. 1b), which we will call "used" (UC). Accordingly, those combinations that do not occur in the output code will be called "unused" (UnC). For example, in Fig. 1, the TF for radix 1.618 does not include combinations 0011, 0110, 0111 and 1011. These combinations will be UnC. The quantity and location of the UnC are determined by the radix, ADC resolution and bit errors.

The combination location on the TF is defined by the equation:

$$A(K^s) = \sum_{i=0}^{n-1} a_i \cdot Q_i , \tag{1}$$

where K – code combination, s – number of code combinations (decimal notation of binary combinations), n – ADC resolution, $Q_i = \alpha^i (1+\delta_i)$ – bit value with number i, where α – radix, δ_i – i-bit deviation. $a_i \in \{0,1\}$ – bit values of K.

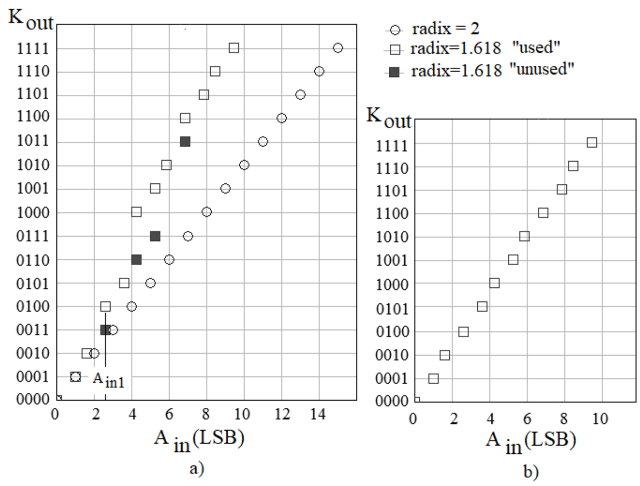

Fig. 1. ADC transfer function 4-bit ADC: a) for radix 2 and 1.618, b) for radix 1.618 without UnC

The combination will be "unused" if there is a "used" combination of output code with a larger code combination number, s, and a smaller value of the input analog signal:

$$A(K_{UC}^{s1}) \le A(K_{UnC}^{s2}), \tag{2}$$

where the value of the input analog signal corresponding to the UnC with the number s2 and the UC with the number s1, respectively, and s1 > s2. For example, UnC number 6 (0110) and UC number 8 (1000) in Fig. 1 form a pair of code combinations for which condition (2) is satisfied. Similar pairs form combinations with numbers 3 (0011) and 4 (0100), 7 (0111) and 8 (1000), 11 (1011) and 12 (1100).

UnCs form the groups with one and more successive code combinations. For example, for the TF on Fig. 1, there are three zones of unused combinations. The central zone, which we will call the (n-1)-level zone, has two successive combinations: 0110 and 0111. The (n-2)-level zone has two subzones, which contain the 0011 and 1011 combinations. The difference between combinations is in the first, most significant bit (MSB). This bit identifies the subzone number: 0 – for 0011 and 1 – for 1011.

The value of K_{UC}^{s1} for any zone or subzone is explicitly defined, it follows the largest UnC and we will call it the border following combination (BFC). It is very important that the values of BFC do not depend on the radix, no ADC resolution and they can be defined by the next rule:

- for the (n-1)-level zone, $BFC_{n-1}^{0} = 100...$ – the MSB = 1, then all following "0"s;
- for the (n-2)-level zone, $BFC_{n-2}^{0} = 0100...$, $BFC_{n-2}^{1} = 1100...$ – the first MSB indicates the number of the subzone, the next bit "1", then all following "0"s;
- For the (n-k)-level zone – k-1, the first MSB indicates the number of the subzone, the next bit "1", then all following "0"s.

From equation (2) follows the condition for the existence of zone unused combinations:

$$A(K_{UC}^{s1}) \le A(K_{UnC}^{s1-1}), \tag{3}$$

In other words, the value of the input analog signal, which converts into the BFC, must be less than or equal to the input analog signal, which converts into the code combination that immediately precedes the BFC. From (3), we derive the existence of the the inequality for zone (n-k)-level:

$$Q_{n-k} \le \sum_{i=0}^{n-k-1} Q_i. \tag{4}$$

Because the smallest level zone has only one UnC and the other zones have more than one, it is reasonable to find only the smallest level zone. For example, we have an ideal n-bit (without bit errors) redundant ADC with a radix of 1.7, then in equation (4) will become true beginning from (n-k) = 3. In fact, the number of the smallest level zone of the ideal redundant ADC is defined only by the radix. The relationship between the smallest level zone number (SLZN) and the radix is shown in Table 1.

Table 1. Radix and smallest level zone number relations

The radix	1.618	1.84	1.93	1.96
Smallest level zone number	2	3	4	5

Therefore, the quantity of zones of unused combinations may be calculated as n – SLZN.

Because the radix and ADC resolution are constant, transition from unused combination to used ones and vice-versa is forced only by a change in δ_i .

2. Influence of single bit deviation on the transition of UC to UnC and vice-versa

The deviation of the MSB value is not equal to zero, while the other bits are ideal. From equation (1), we derive:

$$A(K^s) = a_{n-1} \cdot \alpha^{n-1} \cdot (1 + \delta_{n-1}) + \sum_{i=0}^{n-2} a_i \cdot \alpha^i. \tag{5}$$

As a result, the first part of the TF will not change because $a_{n-1} = 0$, while the second part of the TF will be shifted left if $\delta_i < 0$, or right if $\delta_i > 0$. Fig. 2 shows the reaction of the TF of the successive-approximation ADC with a radix of 1.8 on the deviation of the MSB value: in Fig. 2a, the value of the deviation of the MSB is equal to zero, in Fig. 2b, it is equal to +5%, and in Fig. 2c, it is equal -5%.

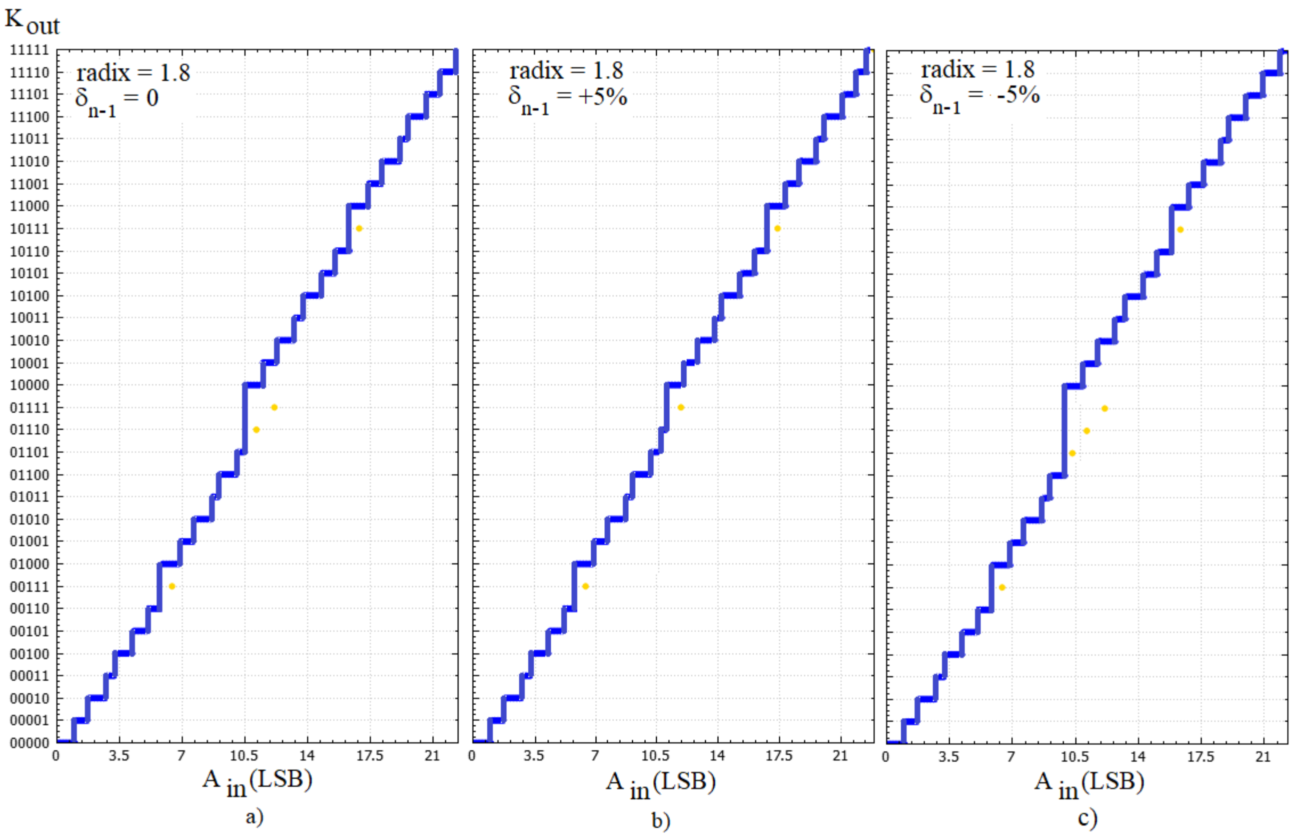

Fig. 2. ADC transfer function 5-bit ADC for radix 1.8: a) without MSB value deviation, b) with positive MSB value deviation, c) with negative MSB value deviation

Hence, the consequence of positive MSB values shifting is the 01110-combination transition from "unused" to "used". On the other hand, the consequence of negative MSB values shifting is the 01101-combination transition from "used" to "unused". The border MSB deviation value for the 01110-combination transition may be calculated from:

$$\alpha^{n-1} \cdot (1+\delta_{n-1}) = \alpha^{n-2} + \alpha^{n-3} + \alpha^{n-4}, \tag{6}$$

and after transformation:

$$\delta_{n-1} = \frac{\alpha^{n-2} + \alpha^{n-3} + \alpha^{n-4} - \alpha^{n-1}}{\alpha^{n-1}}. \tag{7}$$

For a radix of 1.8 and n = 5, the border MSB shifting value according to (7) will be 0.036, or 3.6%. In the same way, the border MSB deviation value for the 01101-combination will be:

$$\delta_{n-1} = \frac{\alpha^{n-2} + \alpha^{n-3} + \alpha^{n-5} - \alpha^{n-1}}{\alpha^{n-1}}. \tag{8}$$

For a radix of 1.8 and n = 5, the border MSB shifting value will be calculated according to (8), it will be -0.04, or -4%. In other words, for a 5-bit successive-approximation ADC with a radix of 1.8, the presence of 2 "unused" combinations in the central (n-1)-level zone (Fig. 2a) guarantees that the MSB value shifting borders are from -4% to 3.6%. It is important that the MSB value shifting does not influence the other zones of "unused" combinations, for example the (n-2)-level zone in Fig. 2.

The value deviation is not equal to zero for the (n-2) bit, but all other bits including the MSB are ideal. From equation (1), we derive:

$$A(K^s) = a_{n-1} \cdot \alpha^{n-1} + a_{n-1} \cdot \alpha^{n-2}(1+\delta_{n-2}) + \sum_{i=0}^{n-3} a_i \cdot \alpha^i. \tag{9}$$

The border (n-2) deviation value for the 01110-combination transition may be calculated from:

$$\alpha^{n-1} = \alpha^{n-2}(1+\delta_{n-2}) + \alpha^{n-3} + \alpha^{n-4}. \tag{10}$$

and after transformation:

$$\delta_{n-2} = \frac{\alpha^{n-1} - \alpha^{n-2} - \alpha^{n-3} - \alpha^{n-4}}{\alpha^{n-2}}. \tag{11}$$

For a radix of 1.8 and n=5 (n-2)-bit let us shift values accordingly (11), they will be -0.06, or -6%. In a similar way, the border (n-2)-bit deviation value for the 01101-combination will be:

$$\delta_{n-2} = \frac{\alpha^{n-1} - \alpha^{n-2} - \alpha^{n-3} - \alpha^{n-5}}{\alpha^{n-2}}. \tag{12}$$

For a radix of 1.8 and n = 5, the border (n-2)-bit shifting value, calculated according to (12), will be 0.07, or 7%.

The (n-2)-bit deviation will influence not only the (n-1)-level zone, but also the (n-2)-level zone. For ideal bit values, it is only one "unused" combination in every subzone of the (n-2)-level zone (Fig. 2): X0111, where X equals 0 for the first subzone and 1 for the second. The result of the (n-2)-bit deviation will be the transmission X0111 combination to the "used" category or the transmission X0110 combination to UnC. To calculate the condition for the first transmission, we will use the next equation:

$$\alpha^{n-2}(1+\delta_{n-2}) = \alpha^{n-3} + \alpha^{n-4} + \alpha^{n-5}. \tag{13}$$

Or after transformation:

$$\delta_{n-2} = \frac{\alpha^{n-3} + \alpha^{n-4} + \alpha^{n-5} - \alpha^{n-2}}{\alpha^{n-2}}. \tag{14}$$

In fact, equation (14) is the same as (7), which means that the (n-2) bit shifting value for a radix of 1.8 and n = 5 will be 0.036, or 3.6%. In a similar way, the border (n-2)-bit deviation value for the X0110-combination will be:

$$\delta_{n-2} = \frac{\alpha^{n-3} + \alpha^{n-4} - \alpha^{n-2}}{\alpha^{n-2}}. \tag{15}$$

For a radix of 1.8 and n=5, the border (n-2)-bit shifting value according to (15) will be -0.14, or -14%.

The (n-i)-bit value shifting will influence the UnC quantity in the (n-i)-level zone and other zones with numbers less than (n-i).

3. Influence of multiple-bit deviation on the transition of UC to UnC and vice-versa

Let the MSB and (n-2) bit values deviations be not equal to zero, while the other bits are ideal. From equation (1), we derive:

$$A(K^s) = a_{n-1} \cdot \alpha^{n-1} \cdot (1+\delta_{n-1}) + \\ + a_{n-2} \cdot \alpha^{n-2} \cdot (1+\delta_{n-2}) + \sum_{i=0}^{n-3} a_i \cdot \alpha^i. \tag{16}$$

The border MSB and (n-2) bit deviation values for the 01110 and 01101 combinations can be calculated from (17) and (18) accordingly:

$$\alpha^{n-1} \cdot (1+\delta_{n-1}) = \alpha^{n-2} \cdot (1+\delta_{n-2}) + \alpha^{n-3} + \alpha^{n-4}. \tag{17}$$

$$\alpha^{n-1} \cdot (1+\delta_{n-1}) = \alpha^{n-2} \cdot (1+\delta_{n-2}) + \alpha^{n-3} + \alpha^{n-5}. \tag{18}$$

The graphical interpretation of equations (14), (15), (17) and (18) for a radix of 1.8 and n=5 are shown in Fig. 3.

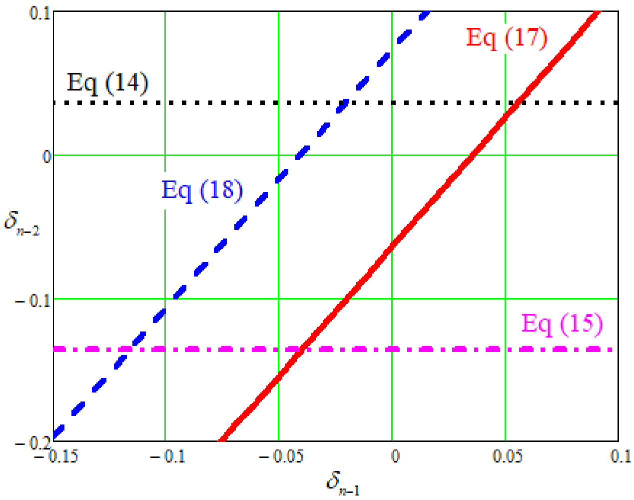

Fig. 3. Graphical interpretation of equations (14), (15), (17) and (18)

Fig. 3 demonstrates the opportunities to control two MSB deviations. If the bit value deviations δ_{n-1} and δ_{n-2} are inside the parallelogram created by equations (14), (15), (17) and (18), the quantity of "unused" combinations in the (n-1) and (n-2)-level zones will not change, and vice-versa – if the quantity of "unused" combinations has changed, it means that the bit value deviations exceeded certain thresholds. To control the "unused" combinations, it is not necessary to interrupt the main conversion if the input analog signal captures the main zones of "unused" combinations.

4. Bit deviation estimation based on UnC analysis

Control of the quantity of "Unused" combinations not only identifies the fact of bit deviation, but estimates this deviation. The relationship between the quantity of UnCs in a certain zone of "unused" combinations and bit deviations is shown above. The reverse task is to estimate the bit deviation if the quantity of UnCs in a certain zone is known. For a start description of the simplest situation, when only one bit has deviated and its number is known.

For example, the ADC transfer function looks like Fig. 2c. It is known that the bit deviation is only the MSB and the quantity of UnCs is equal to three (Fig. 2c).

To calculate the upper bound of the MSB deviation, it is necessary to equate the analog signal for combination 10000 (BFC for (n-1)-level zone of UnCs) with the analog signal for the 01101 combination – the smallest UnC:

$$\alpha^{n-1}\cdot(1+\delta_{n-1}^{\max 3})=\alpha^{n-2}+\alpha^{n-3}+\alpha^{n-5}. \qquad (19)$$

The lower bound of δ_{n-1} can be calculated from:

$$\alpha^{n-1}\cdot(1+\delta_{n-1}^{\min 3})=\alpha^{n-2}+\alpha^{n-3}, \qquad (20)$$

which corresponds to the 01100 combination – the last UC between the series UnC. The average value of δ_{n-1} can be calculated as:

$$\delta_{n-1}^{avr3}=\frac{\delta_{n-1}^{\max 3}+\delta_{n-1}^{\min 3}}{2}. \qquad (21)$$

For the sample in Fig. 2c, the values of $\delta_{n-1}^{\max 3}$, $\delta_{n-1}^{\min 3}$ and δ_{n-1}^{avr3} will be: -0.04, -0.14, and -0.09.

It is obvious that $\delta_{n-1}^{\max 3}=\delta_{n-1}^{\min 2}$, and $\delta_{n-1}^{\min 3}=\delta_{n-1}^{\max 4}$.

The second situation is where only two bits have deviations and their numbers are known. Fig. 4 shows the graphical diagram that can be used to estimate the deviations of two MSBs for a 5-bit ADC with a radix of 1.8.

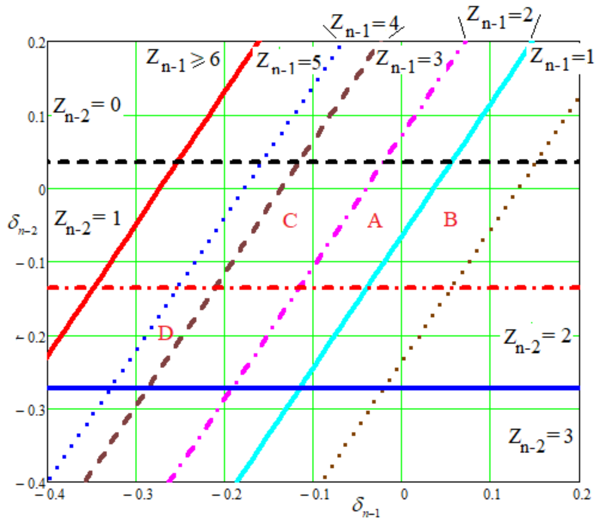

Fig. 4. Graphical diagram for estimation of two-MSB deviations

Z_{n-1} and Z_{n-2} are the quantities of "unused" combinations in the (n-1) and (n-2)-level zones, respectively. For example, parallelogram A corresponds to two UnCs in the (n-1)-level zones and one UnC in the (n-2)-level zone as in Fig. 2a. The point is that δ_{n-1} =0, δ_{n-2} =0 is inside parallelogram A. Parallelogram B corresponds to one UnC in the (n-1)-level zone and one UnC in the (n-2)-level zone as in Fig. 2b. Parallelogram C corresponds to three UnCs in the (n-1)-level zone and one UnC in the (n-2)-level zone as in Fig. 2c. Parallelogram D corresponds to four UnCs in the (n-1)-level zone and two UnCs in the (n-2)-level zone.

It is important that, to estimate the deviations of two bits, it is necessary to have the information about the "unused" combinations in two correspondent UnC zones.

To calculate the deviation values, it is necessary to define the parallelogram center in coordinates δ_{n-1}, and δ_{n-2}. For example, in Fig. 3, the first step is to calculate δ_{n-2}^{avr} by means of averaging δ_{n-2}, received from (14) and (15):

$$\delta_{n-2}^{avr}=\frac{\delta_{n-2}^{\max}+\delta_{n-2}^{\min}}{2}. \qquad (22)$$

The next step is to substitute δ_{n-2}^{avr} into (17) and (18), and calculate $\delta_{n-1}^{\max}(\delta_{n-2}^{avr})$ and $\delta_{n-1}^{\min}(\delta_{n-2}^{avr})$. The last step is to average the received values:

$$\delta_{n-1}^{avr}=\frac{\delta_{n-1}^{\max}(\delta_{n-2}^{avr})+\delta_{n-1}^{\min}(\delta_{n-2}^{avr})}{2} \qquad (23)$$

Based on (22–23), the values of δ_{n-2}^{avr} and δ_{n-1}^{avr} for regions A, B, C and D in Fig. 4 shown in Table 2.

Table 2. Estimated values of deviations of two MSB for for radix 1.8 and n = 5

Region	A	B	C	D
δ_{n-2}^{avr}	-0.05	-0.05	-0.05	-0.20
δ_{n-1}^{avr}	-0.03	0.05	-0.12	-0.27

5. Conclusion

The article shows the opportunity to analytically identifiy the "unused" combinations in the transfer function of a redundant ADC. The simple way to calculate the list of "unused combinations" allows the bit error notification and bit deviation to be estimated for successive-approximation ADCs during the main conversion without using external units and procedures. The relationships between the different zones of "unused" combinations allow the time and computing resources to implement this method to be significantly reduced.

References

[1] Chakradhar A., Rajesh Kumar Srivastava, Sreenivasa Rao Ijjada: Calibration Techniques of Analog to Digital Converters (ADCs). International Journal of Innovative Technology and Exploring Engineering 8, 2019, 415–419.

[2] Hae-Seung Lee.: A Self-calibrating 15-bit CMOS A/D Converter. IEEE J. Solid-State Circuits 19(6), 1984, 813–817.

[3] Hae-Seung Lee, Hodges D. A.: Self-calibration technique for A/D converters. IEEE Transactions on circuits and systems 30(3), 1983, 188–190.

[4] Khen-Sang Tan, Kiriaki S., de Wit M.: Error correction techniques for high-performance differential A/D Converters. IEEE J. Solid-State Circuits 25(6), 1990, 1318–1327.

[5] McCreary J. L.: Matching properties, and voltage and temperature dependence of MOS capacitors. IEEE J. Solid-State Circuits 16, 1981, 608–616.

[6] McNeill J., Coln M. C. W., Larivee B. J.: "Split ADC" Architecture for Deterministic Digital Background Calibration of a 16-bit 1-MS/s ADC. IEEE J. Solid-State Circuits 40(12), 2005, 2437–2445.

[7] Zakharchenko S., Zakharchenko M., Humeniuk R.: Method of determining the unused combinations in the ADC of successive approximation with weight redundancy. International Conference Methods and Means of Encoding, Protection and Compression of Information (MMEPCI 2017), 114–117.

Ph.D. Serhii Zakharchenko
e-mail: zahar@vntu.net

Serhii Zakharchenko is Associate Professor of the Department of Computer Engineering at the Vinnytsia National Technical University. His main scientific interests include analog-to-digital conversion and redundant number systems.

http://orcid.org/0000-0003-3977-2908

M.Sc. Roman Humeniuk
e-mail: romchik003@gmail.com

Roman Humeniuk is a Ph.D. Student in the Department of Computer Engineering at the Vinnytsia National Technical University. His main scientific interests include programming, and the software testing process.

http://orcid.org/0000-0001-9986-8894

otrzymano/received: 4.09.2020 *przyjęto do druku/accepted: 10.12.2020*

http://doi.org/10.35784/iapgos.2066

DEVELOPMENT OF A MODULAR LIGHT-WEIGHT MANIPULATOR FOR HUMAN-ROBOT INTERACTION IN MEDICAL APPLICATIONS

Adam Kurnicki[1], Bartłomiej Stańczyk[2]
[1]Lublin University of Technology, Automation and Metrology Department, Lublin, Poland, [2]Accrea Engineering, Lublin, Poland

Abstract. *The article focuses on the design and implementation of mechanics, electronics and control system for a light-weight, modular, robotic manipulator for performing activities that require robot-human interaction in selected medicine-related applications. At the beginning, the functional requirements and physical architecture of such manipulator are discussed. The structure and control systems of the essential manipulator components/joint modules are presented in detail. Next, we introduce the software architecture of the master controller. Finally, examples of the current implementations of the modular manipulator are given.*

Keywords: modular manipulator, physical architecture, control architecture

OPRACOWANIE MODUŁOWEGO LEKKIEGO MANIPULATORA DO INTERAKCJI CZŁOWIEK-MASZYNA W ZASTOSOWANIACH MEDYCZNYCH

Streszczenie. *Artykuł prezentuje zagadnienia związane z projektowaniem mechaniki, elektroniki i układów sterowania dla lekkiego, modułowego manipulatora robotycznego dedykowanego do wykonywania czynności wymagających interakcji człowiek-robot w wybranych aplikacjach medycznych. W pierwszej części artykułu omówiono wymagania funkcjonalne i architekturę fizyczną manipulatora. Następnie przedstawiono strukturę i układy sterowania podstawowych elementów manipulatora – modułów napędowych przegubów. Zaprezentowano architekturę oprogramowania sterowania implementowaną w sterowniku nadrzędnym. Na koniec podano przykłady zrealizowanych implementacji opracowanego manipulatora modułowego.*

Słowa kluczowe: manipulator modułowy, architektura fizyczna, architektura oprogramowania

Introduction

The rise and popularization of robot technology has already led to significant transformation in many fields of science and technology. In the 21st century, robots have not just played a significant role in industrial fields; their applications have also expanded to non-industrial fields. Various service and entertainment robots have entered family homes. Some are developed for medical or medicine-related applications in: surgery, rehabilitation, telediagnostics and to support mobility-impaired persons. They gradually become an important part of peoples' daily lives.

Most of the medical or medicine-related robotic systems utilize a wide variety of manipulators designed for physical human-robot interactions (PHRI). A general diagram of a PHRI system is presented in Fig. 1. An example of such a system is a teleoperation system where during telesurgery [5] or a remote medical examination [7], the user (doctor) generates commands for the manipulator via an input device (usually a haptic interface). Additionally, the doctor can feel the contact forces during the interaction with the environment, since the forces sensed at the manipulator end-effector are conveyed to his hand via a haptic interface. A display allows the user to observe the manipulation environment and to check the robot's operational status/mode. All measurement, control and vision signals are transmitted, usually over a long distance, via the Internet.

Another typical case of a PHRI system is an application in which the manipulator is used by persons with severe physical disabilities. This solution is dedicated especially for people who have no upper-limb or its usage is strongly limited. The manipulator is usually integrated with a powered wheelchair [1, 8] and helps them in performing activities of daily living such as picking up and moving objects, eating and drinking, opening doors and switching lights and their TV on/off. In such a case, the user generates tasks for the manipulator with the use of a wheelchair joystick system, sometimes supported by additional specialized interfaces (e.g. sip-and-puff, body-machine interface [6]). Since the manipulator is placed close to the user, he/she can observe the arm movement directly and there is no need to transmit vision and control signals via the Internet. The user display, which is connected directly (by cable or Wi-Fi) to the manipulator controller, shows the actual arm state/mode. For users who are functionally locked-in due to any of a variety of neurological or physical conditions, instead of a classical input device, a brain computer interface [10] can be used.

From a design point of view, in order to be more commercially successful, the weight of the manipulator must be reduced while supporting a similar or increased payload, and the price should be decreased in comparison to available solutions. Reducing the weight of the manipulator will reduce the power consumption (e.g. allowing longer usage of the wheelchair batteries) and will increase the user safety. A lighter arm will also be less restrictive on the allowable user weight as specified by the wheelchair manufacturer. In order to achieve this, lightweight robots are normally designed using two approaches [3]. One approach is to design cable-driven robots by the allocation of motors in the base and transmission of their motions to the joints by tendon-like mechanisms, e.g. the design of the Barrett WAM arm or the Igus arm presented in [10]. This type of design leads to highly dexterous, naturally backdrivable and compliant actuations.

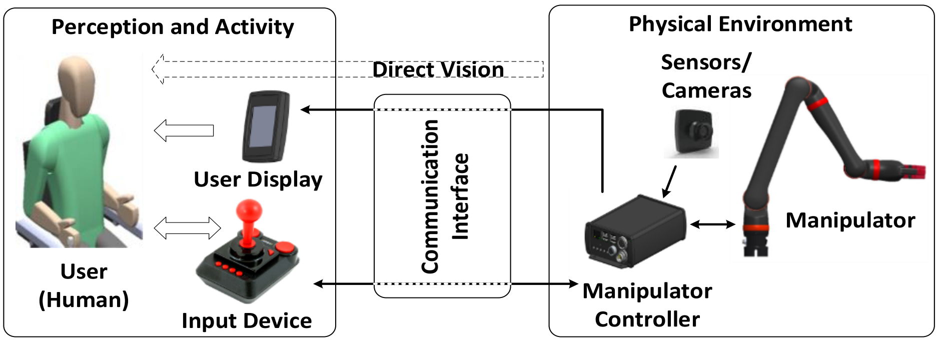

Fig. 1. General diagram of systems for physical human-robot interaction

The disadvantage of such solution is their large footprint with lower interchangeability. The other approach is to design with highly integrated components and to make the major structural components out of more technologically advanced materials such as composite materials [1, 8, 11]. The disadvantage of this solution is the higher cost of these materials. An advantage is the possibility to build modular (with better interchangeability), highly reliable and much more compact manipulators.

The goal of this project was to design a reliable, safe modular manipulator which is more cost-effective and compact, and has a greater or equal payload-to-weight ratio than the manipulators available on the market. The benefits of modularization [4], such as:

- versatility – using a few identical or different modules, various robots with different functionalities can be built quickly,
- reconfigurability – the kinematic structure of a robot may be modified by changing the mechanical configuration of the modules in the arm,
- scalability – the number of degrees of freedom of the robot can be changed by adding or removing the joint modules to the system,

allow a quasi-universal system to be developed, which can be used not only for one specific application, but can be easily adapted (configured) to different medicine-related applications.

The designed modular system is quite complex and hence required a solid development methodology. In this project, the methodology used was a result of merging the user-centred design approach (ISO-13407) and the "Design methodology of mechatronic systems" (VDI 2206). As a consequence, at the initial stage of the project development, the physical architecture of the manipulator was designed. This architecture, together with the chosen system requirements, is presented in section 1.

1. Functional requirements and physical architecture

According to the aforementioned system development methodology, the first step, which precedes the design process, is specification of the functional requirements. The most important requirements are the following:

- The structure of the manipulator shall be modular and configurable with the use of a maximum of 7 rotational joints and a maximum of 3 types of drive modules,
- The arm shall be capable of lifting a minimum of a 1 kg payload with an approx. 1 m reach,
- The maximum weight of the arm shall not exceed 5 kg,
- The width of the joint/link (length and diameter of the module) shall not exceed 9 cm – compactness – important especially for a wheelchair arm,
- The drive modules shall be multiturn, independent and complete mechatronic systems with switchable control modes (e.g. position/velocity/torque) and configurable parameters (e.g. motion limits, sensors calibration coefficients, etc.) by a higher level controller,
- It shall be possible to integrate the arm with a power wheelchair: mechanics, controller (via an IOM module) and 24 VDC battery power supply,
- The arm shall allow for eating and drinking from a bottle or cup, opening and closing doors and cupboards, switching on/off standard household equipment,
- The behavior (movement) of the arm shall be commanded by: a simple on/off joystick interface (implementation of standard control modes which allows: plane and up/down movement to be performed or to open/close and change the orientation of the gripper), 6DoF joystick (e.g. SpaceMouse) and external PC-based controller equipped with ROS (Robot Operating System) [13],
- The arm should operate only outside of a configurable *No Go Zone* and with limited speed in its definable vicinity (*Safety Zone* with configurable width),
- Additional safety features [2] shall be implemented to prevent non-controlled motion of the arm (e.g. self-check, failure detection and handling).

Based on the requirements analysis, the physical architecture presented in Fig 2 was designed. It has the form of a high-level diagram, where the whole system is split into two main physical components: *Arm* (manipulator) and *Master Controller* with their input/output interfaces. Both components can be supplied with voltage between 19 and 30 VDC, which is fully compatible with wheelchair batteries.

The *Arm* consists of: an aluminum base (with power and Ethernet sockets), up to seven joint modules connected by carbon fiber links (with power and Ethernet cables inside) and an end-effector (e.g. gripper). They are controlled by slave controllers run at a frequency of 1 kHz. The structure of the joint modules is described in section 2.

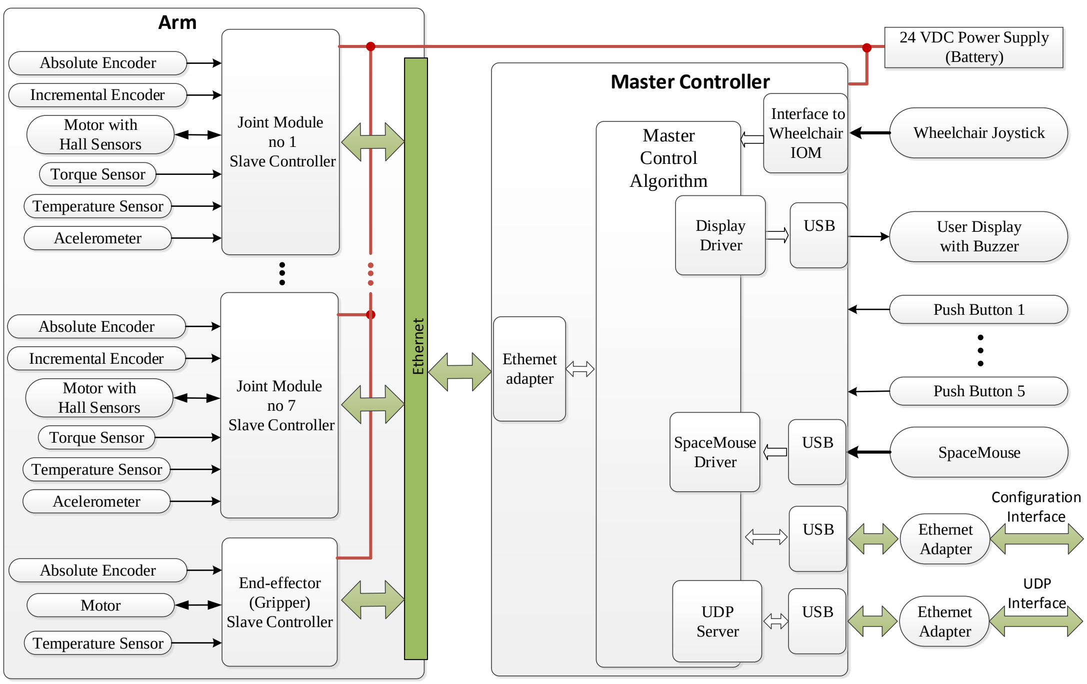

Fig. 2. Manipulator physical architecture

The *Master Controller* is based on a small, single-board Raspberry Pi 3 computer running real-time Linux. The real-time system allows for the execution of the master control algorithm at a frequency of 1 kHz. The software architecture of this algorithm is presented in section 3. The master control algorithm is supported by software drivers for the USB-connected external devices (user display, SpaceMouse) and by a UDP server which allows control-measurement data to be exchanged with an optional, higher-level control system based on a PC with a UDP client and, e.g., ROS. Push buttons and wheelchair controller signals are connected through a simple electronic logical interface to GPIOs on the Raspberry Pi.

Such an architecture and all of the above functional requirements imposed the implementation of a hierarchical two-level control system with a *Master Controller* at the higher-level and distributed slave controllers at the lower-level. The communication between the lower- and higher-level elements is performed at a frequency of 1 kHz via a real-time, Ethernet-based network.

A custom-designed PC application directly configures (through an Ethernet adapter connected to a USB port) the *Master Controller* and particular slave controllers.

2. Joint modules

Based on the manipulator requirements and the architecture presented in section 1, joint drive modules with two sizes and a three fingered gripper were designed. Each of them has integrated mechanics, electronics and control circuitry in one independent mechatronic system. A schematic diagram of a joint drive module is shown in Fig. 3.

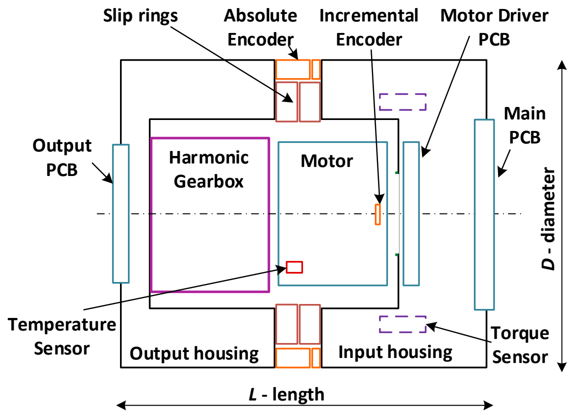

Fig. 3. Schematic diagram of the joint drive module

The structure of the drive module is based on two cylindrical load-bearing housings made of aluminum. They are mechanically connected to the drive system which consists of a brushless DC motor and a harmonic gearbox. Since the arm must be capable of lifting a 1 kg weight, two module sizes L – large and S – small (see Fig. 4) have been designed. They differ in the nominal output torque and the type of the components used. Their main parameters are collected in Table 1. The L-sized modules are normally mounted at the beginning of a serial manipulator kinematic chain and the S-sized at the end.

Table 1. Main parameters of joint modules

Module size	*D* [mm]	*L* [mm]	Nominal output torque [Nm]
L	75	71	12
S	62	55	5

Each module also contains: an incremental encoder mounted between the rotor and the stator of the motor, an absolute encoder mounted between the input and the output housing, a temperature sensor fixed at the stator windings and a strain gauge-based torque sensor glued onto the housing. In order to fulfill the multiturn requirement, custom-designed slip rings are used. They transmit the power and Ethernet signals between the input and output sides of the module.

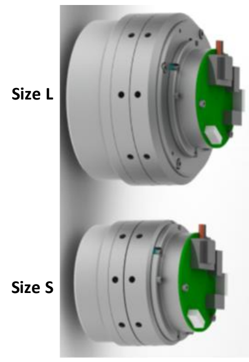

Fig. 4. Overview of L and S sizes of joint drive modules

The module electronics, shown in the block diagram in Fig. 5, was split across three PCBs. The first one, connected directly to the motor stator, is called the Motor Driver PCB and contains the hall sensors and the motor power stage with a driver. The second one, fixed at the left side of the output housing, is called the Output PCB and contains the power and Ethernet sockets. The last one, called the Main PCB, is mounted at right side of the input housing and supports the slave control algorithm implemented in a microcontroller.

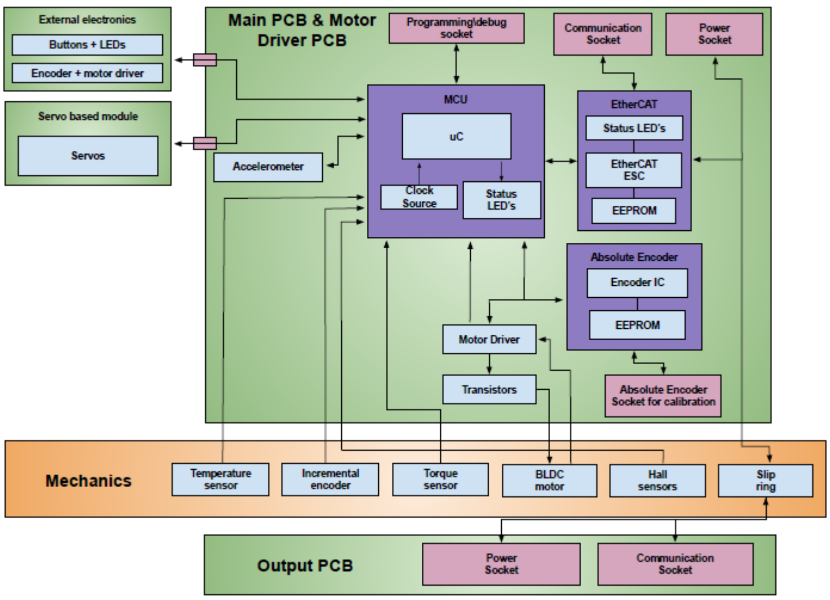

Fig. 5. Electronics block diagram of the joint module

The microcontroller peripherals are used to acquire the measurement data from the sensors (i.e. the accelerometer, the temperature sensor, the absolute and incremental encoders, the hall sensors and the torque sensor) and to generate commands and PWM signals for the motor power stage driver. They also communicate with the slave controller by handling the physical layer of the communication (i.e. processing of the frames exchanged with the manipulator master controller).

In the software layer, the communication is handled by the *Slave Ethernet Stack*. Through it, commands (demands) and configuration parameters are received and actual slave controller statuses are sent from/to the master controller. The *Slave Ethernet Stack* is part of the slave control algorithm, the architecture of which is presented in Fig. 6.

All input signals acquired from the sensors (hardware inputs) as well as demands from the master controller are validated and/or filtered and scaled in the *Data Acquisition & Signal Conditioning* block. For safety reasons (module self-check) these signals are analyzed and compared with thresholds, with each other or with modelled signals in the *Module Monitoring* block. If an anomaly is detected or if a fault is reported by the hardware, the block generates information about the critical or non-critical module failure, or only a warning. Based on the self-check result (monitoring status) and control commands received from the master controller, the *Decision Maker* manages the slave controller activities. The *Decision Maker*, which was designed in the form of a multilayered state machine [7], generates information about its current state (i.e. controller status), manages the *Cascade Controller* (enables/disables, switches working modes, etc.), switches the *Control Modes* of the slave controller (e.g. between: position, velocity, torque and failure handling control modes) and selects a proper filter structure for the demanded joint position signal.

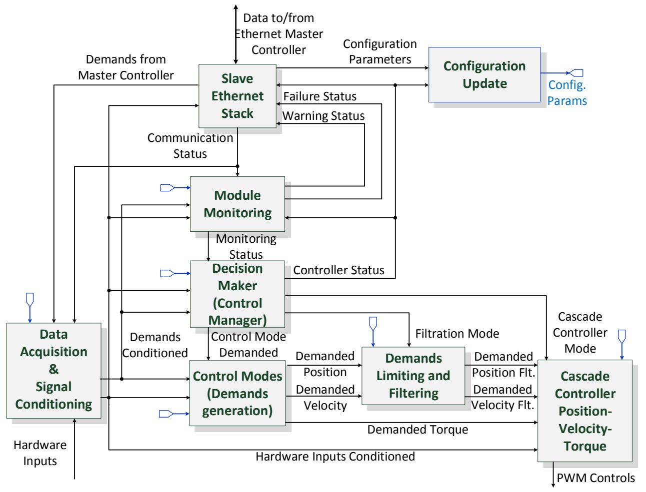

Fig. 6. The software architecture of the joint slave controller

The *Cascade Controller* has a standard position-velocity-torque cascade control structure presented with details in [7].

The *Demands Limiting and Filtering* block consists of: a filter (used to smooth the demanded joint position) and a speed limiter which limits the demanded joint velocity to a maximum permitted velocity when the joint is away from its physical limit and to a small value (zero) when close to it.

3. Master controller software architecture

A simplified software architecture of the master controller is presented in Fig. 7. It is an evolution of our previous work [7].

In general, it is used to generate the position $\boldsymbol{q}_{sd}$, velocity $\dot{q}_{sd}$ and torque $\boldsymbol{\tau}_{sd}$ demanded values for the slave controllers. These demanded values can be generated (by switchable applications of the *Joint Space Control Modes* block) and conditioned (by the *Joint Demands Filter with Speed Limiter, Integrator and Collision Handling* block) directly in joint space, based on the position $\boldsymbol{q}_{UDPd}$, velocity $\dot{q}_{UDPd}$ or torque $\boldsymbol{\tau}_{UDPd}$ demanded values received from the external interface. However in most cases, generation of $\boldsymbol{q}_{sd}$ or $\dot{q}_{sd}$ signals for slave controllers is more complex. First, the demanded task space velocity vector $\dot{\boldsymbol{X}}_d = [\dot{\boldsymbol{x}}_d, \dot{\boldsymbol{\omega}}_d]$ or demanded pose ξ_d is genarated (by switchable applications of the *Task Space Control Modes* block) in task space, based on: wheelchair joystick signals $\boldsymbol{W}_{jd}$ or SpaceMouse joystick signals $\boldsymbol{S}_{jd}$ or a demanded pose ξ_{UDPd} received from the external interface. These demanded signals are partially conditioned (by the *Task Space Demands Filter and Admittance Control* block). Next, values of demanded joints velocities $\dot{q}_{sd}$ are calculated by the *IK* (*Inverse* Kinematics) algorithm from demanded task velocity vector $\dot{\boldsymbol{X}}_{sd}$. Finally, demanded joints velocities are limited and integrated (by *Speed Limiter and Integrator*) to obtain values of $\boldsymbol{q}_{sd}$ signals.The *IK* algorithm utilizes the velocity-based inverse kinematics algorithm [7]:

$$\dot{\boldsymbol{q}}_{sd} = \boldsymbol{J}_s^{\#} \cdot \dot{\boldsymbol{X}}_{sd}, \tag{1}$$

where: $\boldsymbol{J}_s^{\#}$ is a Moore–Penrose pseudoinverse of the arm's Jacobian $\boldsymbol{J}_s$. It is a solution designed to minimize the quadratic cost function of the joint velocities (according to the least square method [9]). In order to avoid the least square inverse method's problems with singularities, the weighted dumped least square (WDLS) method was introduced for the manipulator IK algorithm as a modification of the DLS method [9]. Then minimizing the cost function:

$$g(\dot{\boldsymbol{q}}_{sd}, \dot{\boldsymbol{X}}_{sd}) = \frac{1}{2}(\dot{\boldsymbol{X}}_{sd} - \boldsymbol{J}_s\dot{\boldsymbol{q}}_{sd})^T \boldsymbol{W}_x (\dot{\boldsymbol{X}}_{sd} - \boldsymbol{J}_s\dot{\boldsymbol{q}}_{sd})^T + \frac{1}{2}\dot{\boldsymbol{q}}_{sd}^T \boldsymbol{W}_q \dot{\boldsymbol{q}}_{sd}, \tag{2}$$

where: $\boldsymbol{W}_x$ and $\boldsymbol{W}_q$ are symmetric positive-definite weighting matrices associated with the errors in the task space and joint space, respectively, giving the following solution:

$$\dot{\boldsymbol{q}}_{sd} = (\boldsymbol{J}_s^T \boldsymbol{W}_x \boldsymbol{J}_s + \boldsymbol{W}_q)^{\#} \boldsymbol{J}_s^T \boldsymbol{W}_x \dot{\boldsymbol{X}}_{sd}. \tag{3}$$

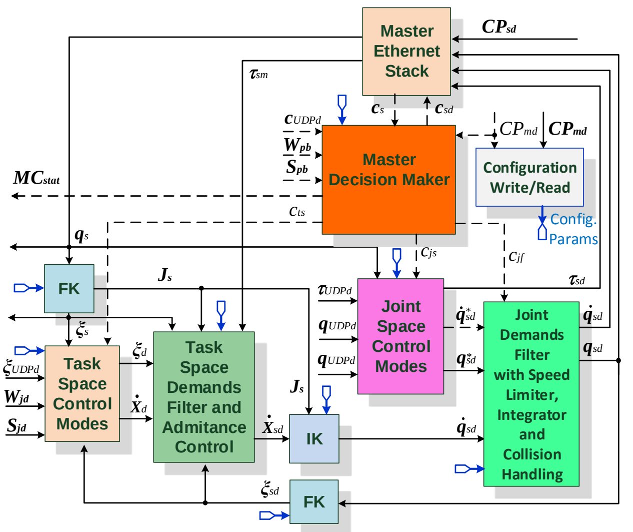

Fig. 7. Master controller software architecture

There is one additional, very important block, which was designed in the form of a finite state machine and manages the whole system – the *Master Decision Maker* (*MDM*). The *MDM*, based on slave controller statuses $\boldsymbol{c}_s$ and control commands received from the external devices (i.e. from: external interface – $\boldsymbol{c}_{UPDd}$, wheelchair buttons – $\boldsymbol{W}_{pb}$ and SpaceMouse buttons – $\boldsymbol{S}_{pb}$), generates the demanded control modes for the slave controllers $\boldsymbol{c}_{sd}$ and commands: $\boldsymbol{c}_{ts}$ and $\boldsymbol{c}_{js}$ which switch the task space, and joint space control modes of the master controller. The *MDM* reports its current state by signal $\boldsymbol{MC}_{stat}$.

The configuration parameters of particular master controller's blocks can be updated on demand (triggered by the high state of the CP_{md} signal), with values coded in the $\boldsymbol{CP}_{md}$ signal. Both signals used in the configuration process are received from externally connected (through Ethernet) PC application. A $\boldsymbol{CP}_{sd}$ signal, received from the same source, is used for the configuration of the slave controllers.

4. Conclusion

The joint modules and the master controller presented in this article have already been implemented in two real medicine-related applications. The first solution is a modular, easy-to-reconfigure, light-weight manipulator mounted on wheelchair. This manipulator, shown in Fig. 8, helps to cope with physical disability in everyday life.

Fig.8. Modular manipulator on a wheelchair

The second type of the manipulator was developed in order to replace a very heavy and user-unfriendly arm of the RAMCIP (Robotic Assistant for MCI Patients at home) robot [12]. The RAMCIP robot with our manipulator is shown in Fig. 9.

In both cases, custom-designed grippers were used, with electronics and control systems similar to the one dedicated to the joint modules presented in section 2. Preliminary evaluation results with real users have confirmed the operational correctness of both the manipulators and their control systems. Our future development related to the modular manipulator will concentrate on its implementation as an arm for remote ultrasound examination.

Fig. 9. Modular manipulator on a RAMCIP robot

Acknowledgements

The work presented in this paper was supported in part by the Lublin Enterprise Support Agency as part of the "Research and innovation" project, activity 1.2, RPO WL 2014-2020.

References

[1] Campeau-Lecours A., et al.: Kinova Modular Robot Arms for Service Robotics Applications. International Journal of Robotics Applications and Technologies 5(2), 2017, 49–71 [http://doi.org/10.4018/IJRAT.2017070104].
[2] Dibekci A., Bebek O.: Improving the Safety of Medical Robotic Systems. 7th IEEE International Conference on Biomedical Robotics and Biomechatronics, 2018, 73–78, [http://doi.org/10.1109/BIOROB.2018.8487914].
[3] Fang H., Guo L., Bai S.: A Light Weight Arm Designed with Modular Joints. Bai S., Ceccarelli M. (eds): Recent Advances in Mechanism Design for Robotics. Mechanisms and Machine Science 33, 2015, 47–54 [http://doi.org/10.1007/978-3-319-18126-4_5].
[4] Guan Y., Jiang L., Zhangy X., Zhang H., Zhou X.: Development of novel robots with modular methodology. IEEE/RSJ International Conference on Intelligent Robots and Systems 2009, 2385–2390, [http://doi.org/10.1109/IROS.2009.5354051].
[5] Hassan T., Hameed A., Nisar S., Kamal N., Hasan O., Al-Zahrawi: A Telesurgical Robotic System for Minimal Invasive Surgery. IEEE Systems Journal 10(3), 2016, 1035–1045 [http://doi.org/10.1109/JSYST.2014.2331146].
[6] Jain S., Farshchiansadegh A., Broad A., Abdollahi F., Mussa-Ivaldi F., Argall B.: Assistive robotic manipulation through shared autonomy and a Body-Machine Interface. IEEE International Conference on Rehabilitation Robotics, 2015, 526–531, [http://doi.org/10.1109/ICORR.2015.7281253].
[7] Kurnicki A., Stańczyk B.: Manipulator Control System for Remote USG Examination. Journal of Automation, Mobile Robotics and Intelligent Systems 13(2), 2019, 48–59 [http://doi.org/10.5604/20830157.1121333].
[8] Schrock P., Farelo F., Alqasemi R., Dubey R.: Design, simulation and testing of a new modular wheelchair mounted robotic arm to perform activities of daily living. IEEE International Conference on Rehabilitation Robotics, 2009, 518–523, [http://doi.org/10.1109/ICORR.2009.5209469].
[9] Siciliano B., Sciavicco L., Villani L., Oriolo G.: Robotics. Modelling, Planning and Control. Advanced Textbooks in Control and Signal Processing, Springer-Verlag, London 2009 [http://doi.org/10.1007/978-1-84628-642-1].
[10] Tremblay T., Padir T.: Modular Robot Arm Design for Physical Human-Robot Interaction. IEEE International Conference on Systems, Man, and Cybernetics, 2013, 4482–4487, [http://doi.org/10.1109/SMC.2013.762].
[11] Vogel J., Haddadin S., Simeral J. D., Stavisky S.D., Bacher D., Hochberg L. R., Donoghue J. P.: Continuous Control of the DLR Light-Weight Robot III by a Human with Tetraplegia Using the BrainGate2 Neural Interface System. Khatib O., Kumar V., Sukhatme G. (eds): Experimental Robotics. Springer Tracts in Advanced Robotics 79. Springer, Berlin, Heidelberg 2014 [http://doi.org/10.1007/978-3-642-28572-1_9].
[12] Ramcip project homepage, https://ramcip-project.eu/ (accessed: 27.06.2020).
[13] ROS Homepage, https://www.ros.org/ (accessed: 27.06.2020).

Ph.D. Eng. Adam Kurnicki
e-mail: a.kurnicki@pollub.pl

Received his Ph.D. (2004) in technical science and his M.Sc. (1999) from the Faculty of Electrical Engineering and Computer Science, TU Lublin, Poland. He is a lecturer in the Automation and Metrology Department, TU Lublin, where he is involved in research on control systems dedicated mainly for robotic systems used in medical related applications.

https://orcid.org/0000-0002-4988-7322

Ph.D. Eng. Bartłomiej Stańczyk
e-mail: b.stanczyk@accrea.com

Received his Ph.D. (2006) in technical science from TU Muenchen, Germany and his M.Sc. in electrical and control engineering (1998) from TU Lublin, Poland. Between 1998 and 2006, worked as a research assistant at TU Lublin (Poland), Berlin and Munich (Germany), involved in various research projects on robust and digital control. During his Ph.D. period, he focused on teleoperation, redundant kinematics and impedance control of robotic manipulators. Since 2014, he is full time technical director of ACCREA.

https://orcid.org/0000-0002-2319-7358

otrzymano/received: 3.07.2020 *przyjęto do druku/accepted: 10.12.2020*

http://doi.org/10.35784/iapgos.2308

TAKING INTO ACCOUNT THE PHASE INSTABILITY OF GENERATORS CAUSED BY THE INFLUENCE OF IONIZING RADIATION OF SPACE ON THE PARAMETERS OF CARRIER FREQUENCY SYNCHRONIZATION SYSTEMS

Oleksandr Turovsky[1], Sergei Panadiy[2]
[1]State University of Telecommunications, Department of Mobile and Video Information Technologies, Kyiv, Ukraine, [2]State University of Telecommunications, Educational and Scientific Center, Kyiv, Ukraine

Abstract. *The article investigates the possibilities of closed and combined synchronization systems for operation in the conditions of phase instability of generators caused by the influence of ionizing radiation of outer space. The inconsistency of the closed-type synchronization system with respect to minimizing the variance of phase errors and increasing the dynamics during carrier frequency tracking is shown. For the combined synchronization system, the article clarifies the process of open communication synthesis and proposes analytical dependences that allow the technique of open communication synthesis to be specified taking into account the phase instability of generators caused by the ionizing radiation of space.*

Keywords: adjustable phase instability of the generator, ionizing radiation

ROZLICZANIE FAZY NIESTABILNOŚCI GENERATORÓW SPOWODOWANE WPŁYWEM KOSMICZNEGO PROMIENIOWANIA JONIZUJĄCEGO NA PARAMETRY SYSTEMÓW SYNCHRONIZACJI CZĘSTOTLIWOŚCI NOŚNYCH

Streszczenie. *W artykule zbadano możliwości pracy zamkniętych i kombinowanych układów synchronizacji w warunkach niestabilności fazowej generatorów spowodowanej wpływem promieniowania jonizującego przestrzeni kosmicznej. Pokazana jest niespójność systemu synchronizacji typu zamkniętego w odniesieniu do minimalizacji wariancji błędów fazowych i zwiększania dynamiki podczas śledzenia częstotliwości nośnej. Dla połączonego systemu synchronizacji w artykule wyjaśniono proces syntezy otwartej komunikacji i zaproponowano analityczne zależności pozwalające określić technikę syntezy otwartej komunikacji z uwzględnieniem niestabilności fazowej generatorów wywołanej promieniowaniem jonizującym przestrzeni.*

Słowa kluczowe: regulowana niestabilność faz generatora, promieniowanie jonizujące przestrzeni

Introduction

Phase synchronization systems are widely implemented in various radio engineering devices of communication, radar and control technology, as well as in devices of precise magnetic recording. In particular, in phase-coherent telecommunications and control systems, they are used to restore carrier and clock frequencies and for coherent demodulation of analog and digital signals with angular modulation [17].

The operation of synchronization systems is characterized by the influence of a number of disturbances and noise on their operation. Namely, additive fluctuation noise, perturbation of useful angular modulation (in the case of carrier frequency filtering), phase and frequency jumps and others. In space communication lines, for example, the main external perturbations are additive Gaussian noise and Doppler frequency shifts.

1. Formulation of the problem

Along with the external influence on the quality of the phase synchronization, the system can have internal disturbances, the main of which in phase-coherent systems are the instability of the adjustable generator [6].

In turn, one of the types of generator noise can be noise caused by the influence of one of the types of external noise, namely noise caused by the influence of ionizing space radiation (ISR) on the element base of the devices and components of communication systems [12].

The main factors of outer space that have a radiative effect on the materials and electronic equipment of space communications are [3]:

- fluxes of electrons and protons of the radiation belts of the Earth;
- streams of protons, solar cosmic rays and galactic heavy charged particles.

The effects of radiation exposure are:

- accumulation of ionization effects and structural damage in materials;
- general failures and failures of elementary electronic devices when exposed to protons and other ionizing particles of cosmic radiation.

The requirements for general stability, strength and stability of the equipment of space communication systems are determined by the integral effects in the materials of the elements under the influence of the ISR.

Short-term failures and reversible failures can be observed in the equipment due to the manifestation of ionization effects in semiconductor devices under the influence of ionizing radiation in outer space. In this case, the differential characteristics of the radiation, and the energy release density in sensitive volumes of semiconductors, are decisive.

In general, the effect of ISR on the generators of the synchronization system is manifested in the form of changes both in the conditions of the course of internal processes on which the principle of operation of these devices is based, and changes in the internal structure of the material from which they are made, which also affects the course of internal processes in them. Thus, under the influence of ionizing radiation in the generators, there is a phenomenon called the radiation effect – a change in technical characteristics under the influence of radioactive radiation.

Radiation effects lead to reversible (stationary) and irreversible (quasistable) changes in the technical characteristics of devices [5, 12].

One of the external manifestations of radiation effects in the semiconductor element base of the generator with the composition of the synchronization system is an increase in its internal noise [5].

Spacecraft synchronization systems operating under the influence of ionizing radiation of outer space must be characterized by low phase error dispersion and high speed. It is obvious that for efficient operation of the radio device as a whole, it is necessary to directly ensure high accuracy of the phase synchronization system in steady and transient modes under the influence of both external and internal perturbations [17].

The issue of determining the directions of development, analysis and improvement of known closed-type synchronization systems (CTSS) and the synthesis of new combined synchronization schemes (CSS), characterized by high noise immunity, accuracy and speed when working under the influence of both external and internal disturbances is an urgent and timely scientific task.

2. Analysis of recent research and publications

The issues of analysis of the known and the development of new schemes of phase synchronization systems, taking into account different sources of perturbations, were considered in a number of scientific works.

In [1], an algorithm for estimating phase noise based on the application of calculated coefficients of discrete discrete-cosine transformation is presented and a number of implementations of the proposed algorithm are proposed. The algorithm takes into account both the displacement of the carrier particle and phase noise, but the proposed algorithm does not take into account the assessment of the influence of internal factors, namely the instability of the generator under the influence of ISR, which adjusts to the efficiency of the synchronization system.

In [7], the results of a study of CSS with open communication under the influence of external perturbations are presented. It is noted that in contrast to simple CSS, a promising combined automatic control system in which the synthesis of open communication is offered under the condition of increasing the order of astatism has its own features due to specific input nodes of closed and open control channels. In this paper, there is no assessment of the capabilities of such a CSS to improve efficiency, taking into account the instability of the generators in the communication channel.

In [3, 10, 16], the optimization of the parameters of the filter and the system as a whole for the class of CSS is investigated. The obtained results showed that the CSS, due to their inherent contradictions, do not allow in some cases to ensure the required quality of work. This is especially noticeable when you want to improve the quality of the system on two or more conflicting indicators. The influence of generator instability under the influence of ISR in these works was not evaluated.

Great opportunities for improving the quality of synchronization systems exist in the class of CSS, which can combine the principles of regulation of deviation and perturbation, which were defined as promising areas for improving synchronization systems in [15, 17]. In [10], the importance of assessing the impact of generator instability was determined, but in it and in [1], there is no assessment of the impact of generator instability.

In such works on CSS as [4, 9], there are analyses of CSS dynamics in simple open communication consisting of the frequency discriminator (FD) and various filters (or without them), without consideration of noise both from external and from internal sources.

In [14], it was noted that the effect of generator instability can be significant. Taking it into account and minimizing it can be one of the ways to increase the efficiency of the phase synchronization system. The assessment of the impact of this instability is not described in this paper.

3. Purpose and objectives of this study

The problem of taking into account the impact of instability of generators in the communication channel caused by ISR on the efficiency of the CTSS and CSS has not been solved at present and is an urgent scientific problem, the solution of which is devoted to this article.

In the general case, the phase modulation of the signal contains four components [18]:

$$\phi_{vh}(t) = d(t) + M(t) + \Delta\psi(t) + N(t) \qquad (1)$$

where: $d(t)$ – Doppler shift at the input; $M(t)$ – useful angular modulation; $\Delta\psi(t)$ – generator instability.

As noted earlier, the increase in the internal noise of the generator of the synchronization system under the influence of ISR causes a change in its operation in the direction of increasing the instability of the work [12].

Coherent reception requires accurate knowledge of the current phase of the carrier oscillation. When using the synchronization system as a phase filter, the input signal is, in accordance with expression (1) the sum $d(t)+\Delta\psi(t)$, where $\Delta\psi(t)=\psi_1(t)-\psi_2(t)$, $\psi_2(t)$ – instability of the substratum generator. Processes $M(t)$ and $N(t)$ represent a hindrance.

The variance of the phase error is caused by the instability of its operation under the influence of ISR, which consists of four components [2]:

$$\sigma_\phi^2 = \sigma_d^2 + \sigma_{\Delta\phi}^2 + \sigma_M^2 + \sigma_N^2 \qquad (2)$$

The transfer function $W_3(S)$ will be:

$$\sigma_1^2 = \sigma_d^2 + \sigma_{\Delta\phi}^2 = \frac{1}{2\pi}\int_{-\infty}^{\infty} \left|W_\phi(j\omega)\right|^2 G_S(\omega)\,d\omega\,, \qquad (3)$$

$$\sigma_2^2 = \sigma_M^2 + \sigma_N^2 = \frac{1}{2\pi}\int_{-\infty}^{\infty} \left|W_\phi(j\omega)\right|^2 G_n(\omega)\,d\omega\,, \qquad (4)$$

where: $W(S)=1-W_\phi(S)$.

For this case, $G_S(\omega)=G_d(\omega)+G_{\Delta k}(\omega)$, and $G_n(\omega)=G_M(\omega)+G_N(\omega)$.

The transfer function for the error of the CTSS is defined by expression (5) [3, 10]:

$$W(S) = \frac{1}{1+W_1(S)W_2(S)W_3(S)} = \frac{T_2(S+1)S}{a_0S^2+a_1S+a_2} = \frac{D_{\phi з0}(S)S^{\nu_з}}{F_з(S)} \qquad (5)$$

hence, the transfer function $W_3(S)$ will be:

$$W_3(S) = [W_1(S)W_2(S)W_3(S)]/[1+W_1(S)W_2(S)W_3(S)] \qquad (6)$$

From expressions (5) and (6), it is seen that the value can be minimized only by appropriate selection of the parameters of the links $W_1(S)-W_3(S)$.

Since these parameters are included in the characteristic CTSS equation: $F_3(S)$ = 0, changing them in order to reduce the variance of the phase error will worsen the quality of the transient process in the CTSS system [1].

Let us determine the possibilities of minimizing the variance of the phase error in CSS and the method of synthesis of open communication from the condition min σ_ϕ^2.

The block diagram of the linear model of KSS with an additional link, accepted for research, is shown in Fig. 1.

According to the transfer function for error CSS from expression (5), we find [7, 8]:

$$W_K(S) = \frac{\left[D_1(S)D_2(S)F_4(S)+F_1(S)F_2(S)D_4(S)\right]D_3(S)}{\left[F_1(S)F_2(S)F_3(S)+D_1(S)D_2(S)D_3(S)\right]F_4(S)} = \frac{D_K(S)}{F_K(S)} \qquad (7)$$

where: $F_K(S)=F_3(S)\times F_4(S)$.

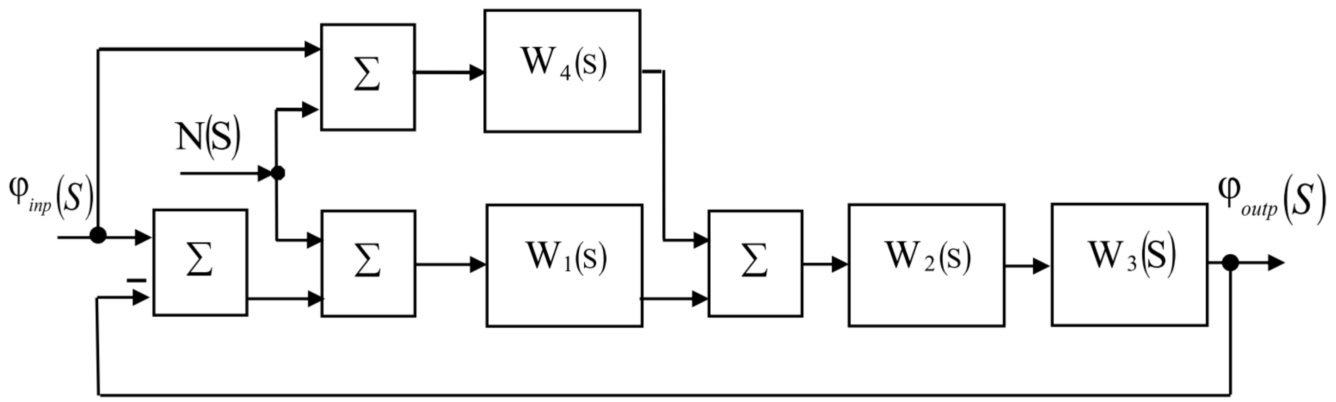

Fig. 1. Block diagram of a linear model of a combined synchronization system with an additional link

Since the numerators of the transfer functions of the KSS given by expressions (5), (7) include polynomials $F_4(S)$, and $D_4(S)$, by appropriate selection of their parameters, you can further minimize the variance of the phase error.

Taking into account that the polynomial $F_4(S)$ is included in the characteristic equation of CSS in the form of a factor, so the roots introduced by it can be chosen so that they do not affect the transient process of the initial system.

If you want the condition to be met:

$$F_4(S) = F_1(S)F_2(S), \tag{8}$$

then the transfer functions of the CSS by error and the output signal, respectively, will be:

$$W_{\phi K}(S) = \frac{F_1(S)F_4(S) + D_3(S)D_4(S)}{F_1(S)F_2(S)F_3(S) + D_1(S)D_2(S)D_3(S)} = \frac{D_{\phi K}(S)}{F_3(S)} \tag{9}$$

$$W_K(S) = \frac{\left[D_1(S)D_2(S) + D_4(S)\right]D_3(S)}{F_1(S)F_2(S)F_3(S) + D_1(S)D_2(S)D_3(S)} = \frac{D_K(S)}{F_3(S)} \tag{10}$$

In this case, the characteristic equations of the CTSS and CSS are the same, that is, $F_K(S) = F_3(S)$, the open bond can be synthesized only from the condition min σ_ϕ^2.

Consider the case of monitoring the carrier frequency against the background of noise at $d(t) = M(t) = 0$ and compare the possibilities of minimizing the variance of the phase error in the CTSS and CSS.

If you want to consider component $d(t)$, you need to consider the spectra:

$$G_S(\omega) = G_d(\omega) + G_{\Delta\varphi}(\omega),\ G_n(\omega) = G_M(\omega) + G_N(\omega) \tag{11}$$

As is known [6, 13], the energy spectrum of instabilities of generators can be represented as:

$$G_{\Delta\phi}(\omega) = N_T + \left(2\pi N_f\right)/\left|j\omega\right|, \tag{12}$$

where N_T and N_f constants characterize the thermal noise and type noise $1/f$, respectively.

In this case, the expression for the variance of the phase error in the CTSS will be [14]:

$$\sigma_{\phi 3}^2 = \sigma_{\Delta\psi}^2 + \sigma_N^2 = \frac{r+1}{4r}\frac{N_T}{W_{L3}} + G(r)\frac{N_f}{W_{L3}^2} + \frac{N_0 W_{L3}}{2A_0^2} \tag{13}$$

where $r = \frac{A_0 K T_1^2}{T_2}$, and $W_{L3PIF} = \frac{r+1}{2T_1\left(1 + T_1/rT_2\right)}$ two-way noise band of the proportional-integrating filter (PIF) $G(r) \approx 1.5$.

From this expression, it is seen that the change of the noise band in different ways affects the value of the variance of the phase error, which is caused by the instability of the generators and additive noise.

If we take the derivative by W_{L3} and equate it to zero, we find W_{L3OPT}, the analysis of which shows that the minimum phase error dispersion is obtained by including an ideal filter (IF) in a closed loop instead of a proportional-integrating filter (PIF), which as was shown in [1], degrades the dynamics of the CTSS.

At $P_c/P = 6\cdot 10^4$, $N_T = 0$, $N_f = 0.08$ the following values will be optimal in terms of $\min \sigma_\varphi^2$: r = 7; W_{L3} = 26 Hz. Thus, we receive $G(r) = 1.6$, $\sigma_\phi = \sqrt{\sigma_\phi^2} = 1.93^\circ$.

The inclusion of an IF in the CTSS instead of a UIF slightly expands the noise band of the system [5].

$$W_{L3IF} \approx (r+1)/(2T_1)$$

and

$$W_{L3IF}/W_{L3PIF} = 1 + T_1/(rT_2) \geq 1.$$

The same increase in noise band can be obtained with a closed-loop PIF by appropriate selection of the parameters of the open channel.

Define the type and parameters of the open link, which obtains a CSS with the same band as a CTSS with an IF, but with a closed-loop PIF, the parameters of which can be selected from the condition of ensuring the required quality of system dynamics.

In other words, we will synthesize an open connection from the condition:

$$W_{LK} = W_{L3IF}, \tag{14}$$

which will optimize the system to a minimum dispersion of the phase error without deterioration of the dynamics.

In Fig. 1 $W_1(S)$ – transfer function of the phase discriminator (PD), $W_2(S)$ – filter, $W_3(S)$ – adjustable generator (AG), which have the following form [7]:

$$W_1(S)=K_1+\left(\frac{W_1(S)}{F_1(S)}\right),\ W_3(S)=\left(\frac{K_3}{S}\right)=\frac{D_3(S)}{F_3(S)} \quad (15)$$

where $K_1 = A_1 K_{FD}$; K_1 – gain PD; S – Laplace operator.

In the following, we will consider the systems of synchronization with the PIF in a closed loop with a transfer function of the form [8, 13]:

$$W_2(S)=\frac{(T_1S+1)}{(T_2S+1)} \quad (16)$$

The general form of the transfer function $W_4(S)$ of open communication, which satisfies the condition v_k = l is determined by the expression [7, 8]:

$$W_4(S)=\frac{\left(\sum_{i=v_3}^{n}K_{4i}S^i\right)}{\left(\sum_{j=0}^{m}K_{4j}S^j\right)}=\frac{D_4(S)}{F_4(S)} \quad (17)$$

where v_3 the order of astatism of the original system without communication.

If, in formulas (9), (10), to substitute expressions for transfer functions of links of the system of Fig. 1 of (15), (16) and (17), for n = 1, we obtain:

$$W_{\varphi K}(S)=\left(b_0S^2+b_1S\right)/\left(a_0S^2+a_1S+a_2\right)=D_{\varphi K}(S)/F_3(S) \quad (18)$$

$$W_K(S)=\left(C_0S+C_1\right)/\left(a_0S+a_1S+a_2\right)=DK(S)/F_3(S) \quad (19)$$

where $b_0=T_2$, $b_1=1-K_3K_4$, $G_1=A_0K_1K_3$, $G_0=A_0K_1T_1+K_3K_4$.

The bilateral noise band of a CSS with PIF in a closed loop will be [11, 20].

$$W_{LK}=\frac{1}{2\pi}\int_{-\infty}^{\infty}\left|W_K(j\omega)\right|^2 d\omega=W_{L3\Pi I\Phi}+\Delta W_L \quad (20)$$

$$W_L=\frac{\beta^2r(K_3K_4)^2+2\beta r(K_3K_4)}{2T_1(1+\beta)} \quad (21)$$

where $\beta=T_1/(rT_2)$.

From condition (14), we find the required value of ΔW_L. Taking into account the expressions ΔW_L IF and ΔW_{L3} PIF, we have:

$$\Delta W_L=W_{L3I\Phi}-W_{L3\Pi I\Phi}=\beta(r+1)/\left[2T_1(1+\beta)\right] \quad (22)$$

Comparing expressions (21) and (22), we obtain the following equation:

$$\alpha_0(K_3K_4)^2+\alpha_1(K_3K_4)^2+\alpha_2=0, \quad (23)$$

where: $\alpha_0=\beta^2r$; $\alpha_1=2\beta r$; $\alpha_{21}=-\beta(r+1)$.

If we solve equation (23), we find the value of parameter K_4 at which the optimal transfer function CSS from the condition min σ_ϕ^2 is provided at the required quality of the system dynamics.

For the above numerical values, we have $K_4=57/K_3$.

You can increase the absolute values of the roots of the characteristic equation, for example, by increasing the value of filter parameter T_2. The noise band of the system, equal to:

$$W_{L3PIF}=\frac{r+1}{2T_1\left[1+T_1/(rT_2)\right]}=\frac{A_0K(A_0K+1)}{2\left[A_0K+1/T_2\right]}$$

will decrease, deviating from the optimal value. Therefore, the open connection must be chosen to compensate for this deviation.

Explaining expression (21), we obtain the expression for increment ΔW_L, as follows:

$$\Delta W_L=\frac{1}{2(mA_0KT_2+1)}(K_3K_4)^2+\frac{A_0K}{(mA_0K+1/T_2)}(K_3K_4) \quad (24)$$

From this expression, it is seen that at any arbitrarily small value of parameter T_2, with increasing the parameter K_4 of open communication, you can get any necessary increase in the noise band [15].

Therefore, the increase in the absolute value of the roots of the characteristic equation while maintaining the optimal value of the variance of the phase error is limited only by the physically achievable value of filter parameter T_2.

If it is also necessary to take into account the Doppler effect $(d(t)\neq 0)$, then the method of calculation of open communication remains unchanged, only in formula (3), at $G_S(\omega)$ it is necessary to substitute the sum $G_S(\omega)=G_{\Delta\phi}+G_d(\omega)$.

The Doppler shift at the input of the system is determined by a function of polynomial type [18]:

$$d(t)=\phi_0+\sum_{r=0}^{N-1}\left(\Omega_r t^{r+1}\right)\left|(r+1)\right| \quad (25)$$

If we take, for example, in the calculation of the Doppler shift (25) r =0, we will receive $G_d(\omega)=\varphi_0^2/\omega^2+\Omega_0^2/\omega^4$. Thus, taking into account the component $G_d(\omega)$ changes only the optimal value of the noise band of the CSS.

It should be noted that further promising research in the direction of solving the problem posed in this article is the solution of the problem of assessing the carrier frequency of the synchronization scheme considered in the work under conditions of exposure to ionizing radiation. In turn, the solution of scientific problems on the estimation of the carrier frequency of useful signals involves the choice of the estimation parameter and the method of their determination. As such a method of operation for signals that are transmitted in burst mode, it is proposed to use the maximum likelihood rule using a sliding fast Fourier [20]. In this case, the reference signal synchronization system itself can be improved by the open-loop synthesis method, which is described in sufficient detail in [20].

3. Conclusions

1. The paper considers the influence of the phase instability of synchronization system generators caused by the influence of ionizing radiation of outer space on minimizing the phase error dispersion in CTSS and CSS.
2. It is shown that for CTCC, minimization of the phase error variance by reducing the parameters of the transfer functions of the components of the system in the case of phase instability of the generators will worsen the quality of the transient process.
3. Increasing the noise bandwidth of the proportional-integrating filter of the input signal CTSS to the parameters of the ideal filter degrades the dynamics of this system.
4. For CSS in the conditions of phase instability of generators caused by influence of ISR, an increase in the noise bandwidth of an input signal can be achieved by applying in the closed circuit of UIF and implementation of the corresponding selection of parameters of transfer function of a link of the open channel.
5. In the conditions of phase instability of KSS generators by selection of parameters of PIF, it is possible to provide the necessary dynamics of the system and to achieve preservation of the optimum value of a variance of a phase error in it.
6. Taking into account Doppler noise in the conditions of phase instability of generators for CTSS and CSS requires a reduction of the optimal value of the noise bandwidth.
7. The analytical dependences proposed in the work allow us to specify the method of synthesis of open communication for CSS taking into account the phase instability of the generators caused by the influence of ISR against the background of the Doppler frequency shift.

References

[1] Bhatti J., Noels N., Moeneclaey M.: Low–complexity frequency offset and phase noise estimation for burst–mode digital transmission. Proc. IEEE PIMRC 2011, 1662–1669.

[2] Bondarenko V. N.: Noise immunity of receiving spectrally effective noise-like signals. Siberian Federal University, Krasnoyarsk 2015.

[3] Boyko Y. M.: Otsinuvannya of specific indicators in the attachment of synchronization of signals to telecommunications. Bulletin of the Khmelnytskyi National University 1, 2015, 204–213.

[4] Boyko Y. M., Yriomenko O. I.: Analysis of models of synchronization systems in digital receivers. Materials of the XIV International Scientific and Practical Conference. Odessa National Communications Academy im. Popova, Odessa 2015, 192–194.

[5] Davydov L. N., Zakharchenko A. A., Kutniy D. V., Kutniy V. E., Neklyudov I. M., Rybka A. V., Shlyakhov I. N.: Radiation resistance of semiconductor detectors of corpuscular and gamma radiation. VISNIK Kharkiv National University 657 1(26), 2005, 3–22.

[6] Gabrielian D. D., Yengibaryan I. A., Safaryan O. A.: New method of generator frequency stabilization. REDS: Telecommunication Devices and Systems 4(1), 2014, 30–34.

[7] Grosu F., Bîrzu A., Lazar A., Grosu I.: Coupling Systems for a New Type of Phase Synchronization. Mathematical Problems in Engineering 2016, 3574029, [http://doi.org/10.1155/2016/3574029].

[8] Horowitz P., Hill W.: The Art of Electronics. Cambridge University Press, Cambridge 2015.

[9] Kucher D. B., Makogon V. P.: Renewal of nonsense in coherent demodulation to a signal with an uninterrupted phase by means of a link. Science and Technology of the Powers of the Defense Forces of Ukraine 2(11), 2013, 148–149.

[10] Lyons R. G.: Understanding Digital Signal Processing. Prentice Hall, Boston 2010.

[11] Nasir A., Durrani S., Kennedy R.: Particle filters for joint timing and carrier estimation: Improved resampling guidelines and weighted bayesian cramer–rao bounds. IEEE Trans. Commun. 60(5), 2012, 1407–1419.

[12] Ohshima T., Onodaa S.: Radiation Resistance of Semiconductors. Radiation Applications. An Advanced Course in Nuclear Engineering 07. Springer, Singapore 2018.

[13] Polikarovskikh A. I.: Modern reference generators for systems of synthesis of frequencies and signals. Bulletin of the Voronezh State Technical University 10(4), 2014, 100–108.

[14] Safaryan O. A.: Method for estimating the frequency of generators in the conditions of unpredictable changes in the duration of the measurement interval. Bulletin of DSTU 14(4)(79), 2014, 142–149.

[15] Salim O., Nasir A., Mehrpouyan H., Xiang W., Durrani S., Kennedy R. Channel, phase noise, and frequency offset in OFDM systems: Joint estimation, data detection, and hybrid cramer-rao lower bound. IEEE Trans. Commun. 62(9), 2014, 3311–3325.

[16] Scheers B., Nir V.: A Modified Direct-Sequence Spread Spectrum Modulation Scheme for Burst Transmissions. Military Communications and Information Systems Conference MCC'2010, 366–3673.

[17] Shakhtarin B. I.: Analysis of synchronization systems in the presence of interference. Hot line – Telecom, Moscow 2016.

[18] Sklyar B.: Digital communication. Theoretical foundations and practical application. Publishing house "Williams", Moscow 2003.

[19] Turovsky O., Drobyk O., Makarenko A., Khakhlyuk O.: Estimates of the carrier frequency of the signal received by the satellite communication system in package mode. International Journal of Advanced Trends in Computer Science and Engineering 9, 2020, 3223–3228, [https://doi.org/10.30534/ijatcse/2020/115932020].

[20] Turovsky O., Khlaponin Y., Muhi-Aldin H. M. et al.: Combined system of phase synchronization with increased order of astatism in frequency monitoring mode. CEUR Workshop Proceedings 2616, 2020, 53–62.

Ph.D. Oleksandr Turovsky
e-mail: s19641011@ukr.net

Oleksandr Turovsky is a Ph.D. in Technology (Candidate of Sciences in Technology), Associate Professor, Professor of the Department of Mobile and video information technologies, State University of Telecommunications, Kyiv. Research interests – systems of satellite telecommunications, assessment of the carrier frequency of the incoming signal of receiving devices of communication and data transmission systems, systems for synchronizing the carrier frequency of radio engineering devices, assessing the influence of various factors and external conditions on the operation of systems and devices of radio engineering devices.

https://orcid.org/0000-0002-4961-0876

M.Sc. Sergei Panadiy
e-mail: s.panad64571@gmail.com

Sergei Panadiy is a candidate of sciences degree seeking applicant, State University of Telecommunications, Kyiv. Research interests – systems of satellite telecommunications, assessing the influence of various factors and external conditions on the operation of systems and devices of radio engineering devices.

https://orcid.org/0000-0002-0573-8915

otrzymano/received: 26.09.2020 *przyjęto do druku/accepted: 10.12.2020*

http://doi.org/10.35784/iapgos.2082

MULTI-CHANNEL DIGITAL-ANALOG SYSTEM BASED ON CURRENT-CURRENT CONVERTERS

Olexiy Azarov, Yevhenii Heneralnytskyi, Nataliia Rybko
Vinnitsa National Technical University, Vinnitsa, Ukraine

Abstract. *An approach to building a multi-channel digital-analog system is proposed, in which, unlike the known ones, a code-current converter, a controlled current generator, and also a current communication block are used. For a given accuracy, this saves on the analog system equipment. It has been shown that the proposed principle of building a controlled current source in the form of a highly linear push-pull amplifier – current scalar on bipolar transistors with a grounded load – has a high output resistance and wide bandwidth, which allows the use of current switching to implement the multi-channel system mode.*

Keywords: DAC, frequency response, phase response, linearity error of the transfer characteristic

WIELOKANAŁOWY SYSTEM CYFROWO-ANALOGOWY OPARTY NA PRZETWORNIKACH PRĄD-PRĄD

Streszczenie. *Proponowane jest podejście do budowy wielokanałowego systemu cyfrowo - analogowego, w którym w odróżnieniu od znanego jednego przetwornika oferowany jest kod - prąd, generator prądu sterowanego, a także blok komunikacji prądów. Pozwala to zaoszczędzić na danej dokładności na sprzęcie analogowym systemu. Wykazano, że proponowana zasada budowy sterowanego generatora prądu w postaci wysoce liniowego wzmacniacza dwutaktowego – skaler prądu na tranzystorach bipolarnych z uziemionym obciążeniem ma wysoką rezystancję wyjściową i szerokie pasmo, co pozwala na zastosowanie przełączania prądu do realizacji trybu systemu wielokanałowego.*

Słowa kluczowe: DAC, pasmo przenoszenia, przejście fazowe, błąd liniowości charakterystyki przenoszenia

Introduction

Many electronic systems [2, 6, 7, 11], such as programmable power supplies, signal distribution systems with a DAC in each information channel, multi-channel information transmission systems with sampling and storage devices with an analog multiplexer, use groups of digital-to-analog converters. At the same time, in some cases, it is advisable to use one DAC with multiplexer and output devices to capture or buffer the output signal. First of all, this refers to time distribution systems based on a single DAC with multiplexer and output devices for capturing or buffering the output signal.

It should be noted that in the case of using multiple DACs in the above systems, a number of important features need to be taken into account. First, each DAC has its own individual static errors and, if it is necessary to calibrate them, the system that implements this is complicated. Second, despite the ability to provide the required performance by the group DAC, it increases the power consumption and requires additional digital equipment.

On the other hand, the use of a single DAC requires an increase in its speed compared to the speed of any of the DACs in a group, as well as a high speed multi-channel output signal switch. A promising way to meet these requirements is the current principle in making these devices. Thus, the DAC must be made in the form of a code-current converter (CCC), the output buffer of the CCC is based on a controlled current generator (CCG), and a multi-channel analog switch is based on high-speed diode switches.

However, this approach is somewhat new, especially in the construction of CCGs, and it has not been sufficiently considered in the scientific and technical literature, so the topic of the article on the construction of a multi-channel digital-analog system on a single code-converter and controlled generator is urgent.

Research methods – providing increased speed of high-line multichannel code-analog conversion based on the current principle, in particular, using a controlled current generator.

1. Research objectives

The authors performed an assessment of the characteristics of various types of the equipment, in particular, their technical data, characteristic features, advantages and disadvantages:

1. to offer a generalized block diagram of a multichannel digital-analog system based on a single code-current converter and a controlled current generator;
2. to offer and analyze the principle of construction of a controlled current generator in the form of a highly linear push-pull amplifier – current scalar (PPACS) on bipolar transistors with a grounded load;
3. to estimate the static errors (zero offset and linearity) of the PPACS, as well as its speed, in particular the amplitude-frequency characteristic by computer simulation;
4. to consider the possibility of calibrating the error of the zero offset current ($I_{ZO.0}$) of the proposed multi-channel digital-analog system, by introducing corrections presented in digital form;
5. to provide practical recommendations for the practical implementation and application of the proposed multi-channel digital-analog system.

2. Solving research problems

Analyzing the purpose of the research, as well as the set of functions to be implemented, it is possible to heuristically synthesize the system as the block circuit shown in Figure 1. This circuit contains a code-current converter (CCC), controlled current generator (CCG), current switch unit (CSU), digital code adder (DCA), table of zero offset channel error correction codes, address bus (AB) of channel selection, set of output devices (SOD) to which currents I_1, I_2, ..., I_k are supplied, and control block (CB), which ensures the functioning of the digital-analog system.

The system works in two modes. In the first mode, the zero offset errors of the source devices are determined. To do this, the DCA input receives zero codes ΔC_{in} and zero offset errors ΔC_0 .

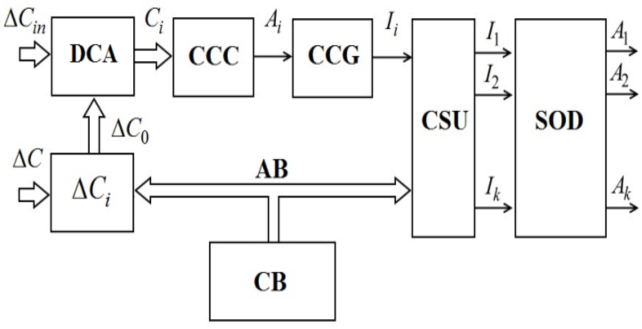

Fig. 1. Block circuit of a multi-channel digital-analog system with calibration $I_{ZO.0}$

Next the values of the zero offset errors $\Delta A_0, \Delta A_1 .... \Delta A_i$ are measured, the codes of which are sequentially entered in the table of corrections ΔC_i. The first mode is then completed and the system is ready to perform the main function. In the second mode, which is the main one, the work is done as follows. The ***i***-th number of the required channel is selected by the CB command, and the converted code ΔC_{in} and the correction code ΔC_i are sent to the adder inputs. From the DCA output, the total code $C_i = C_{in} + \Delta C_i$ is sent to the CCC input and converted into a corresponding analog value A_i (current), the value of which is equal to:

$$I_i = \sum_0^{n-1} \cdot\ \alpha_i \cdot I_j,$$

where: $\alpha_i\ \in \{0;1\}$ is the binary bit coefficient C_i; I_j is the value of the current of the j-th digit of the CCC, and n is the number of digits of the CCC.

The generated I_i is sent to the controlled current generator. It has the following requirements: high output resistance, as well as a wide bandwidth [9]. This is due to the specifics of the key current elements. Figure 2 shows a block circuit of the CCG and the current switch unit. Moreover, the first should be implemented in the form of a high-line push-pull DC amplifier (PPDCA), the schematic of which is considered in [1].

To ensure high output resistance R_{out} in the PPDCA, we have used negative feedback with the current removal method. During operation, the input current I_{in} is sent to the input push-pull cascade (InPPC) at the outputs of which we have branched components I' and I'', which in turn are sent to the block of current gain and balancing (BCGB), where they are amplified and further branched into paraphase components I'_{out}, I''_{out}, $\bar{I}'_{out}$ and $\bar{I}''_{out}$.

These components are sent to the direct and inverse inputs of the current reflectors CM1 and CM2. And the first outputs CM1 and CM2 combine to form the output bus (Out) of the circuit. At the same time, the second outputs CM1 and CM2 are connected to the inputs of the reflectors CM3 and CM4, the outputs of which are also integrated into the feedback bus (33).

Modes of cascades on a direct current (operating points) are set by generators of working currents I_p and mI_p.

Let us determine the low-signal current gain coefficient C_i when breaking the loop FB in the form:

$$C_i = \frac{I_{out}}{I_{in}}.$$

Let us assume that the PPDCA is built according to the scheme shown in Figure 2 [1]. Then it is easy to show that:

$$|I'| \approx |I''| = \frac{\beta_n \cdot \beta_p}{\beta_n + \beta_p} \quad ,$$

where: β_n and β_p are low-signal current gain coefficient n-p-n and p-n-p of transistors, respectively.

Similarly, we have:

$$|I'_{out}| \approx |I''_{out}| \approx |\bar{I}'_{out}| \approx |\bar{I}''_{out}| = \frac{\beta_n \cdot \beta_p}{\beta_n + \beta_p} \quad .$$

Taking into account the above, we finally get:

$$C_i = 2 \cdot \frac{\beta^2{}_n \cdot \beta^2{}_p}{(\beta_n + \beta_p)^2} \quad . \tag{1}$$

Substituting the values β_n and β_p in (1) for integrated transistors npn – NUHFARRY, pnp – PUHFARRY, we find the value C_i.

The feedback current I_{FB} is formed at the second output of the circuit. It is easy to show that when the loop FB breaks, the current transfer coefficient is $C_{i\ FB} \approx 2 \cdot C_i$.

Closing the circuit FB with resistors R_m (scale) and $R_\perp$, we obtain a controlled current generator, the transfer coefficient of which is equal to:

$$C_{ti} = \frac{C_{i\ fb}}{1 + æC_{i\ fb}},$$

where: $æ = \frac{R_\perp}{R_m + R_\perp}$ is the transfer coefficient I_{FB} at the input of the circuit. Thus, taking into account that $æC_{i\ fb} \gg 1$, we finally get:

$$C_{ti} = \frac{R_m + R_\perp}{R_\perp}. \tag{2}$$

It should be noted that expression (2) will be valid provided that $R_m \geq R_{in}$, where R_{in} is the input low signal resistance InPPC when the FB loop is broken. The low-signal value of this resistance is equal to the parallel connection of the input resistors InPPC from the elements T1 and T2 [1]. If $I_p = 1$ mA, then $R_{in} = 5$ kΩ.

Thus, it is desirable that the condition $R_m \geq 5$ kΩ is met. The output low-signal resistance R_{out} of the CCG depends on both the output resistances R_{out1} and R_{out2}, and reflectors CM1 and CM2, respectively, and the depth FB, in particular, on the value of C_{ti} and C_i.

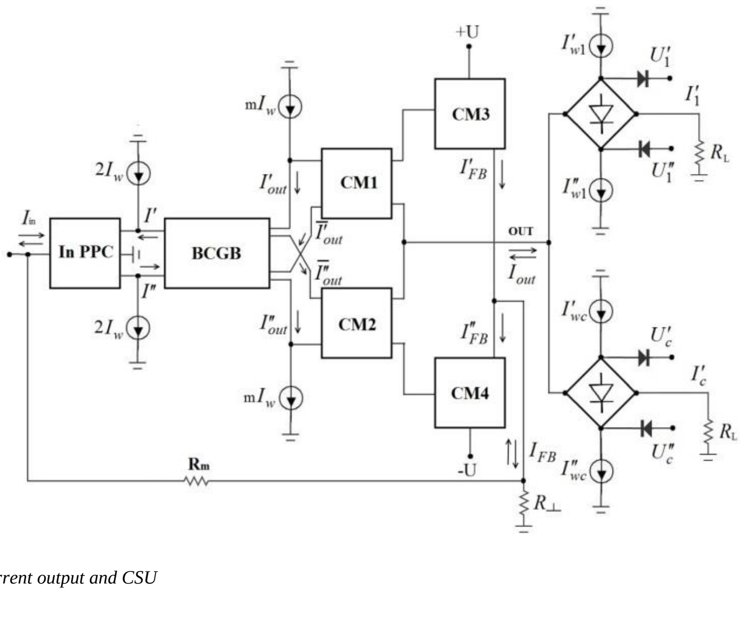

Fig. 2. Block circuit of PPDCA with current output and CSU

It is known from the theory of transistor amplifier circuits in the case of using a negative connection with current removal [10] that this leads to an increase in the output resistance. In our case, we have:

$$R_{out} = (R_{out1} \| R_{out2}) \cdot (1 + æK_{i33}),$$

where: $R_{out1} \approx \frac{1}{2} \cdot R_{c\ n-p-n}$, $R_{out2} \approx \frac{1}{2} \cdot R_{c\ p-n-p}$ are the low-signal resistances of the collector junctions of the p-n-p and n-p-n transistors.

Taking into account that:

$$R_{out1} \| R_{out2} = \frac{1}{2} \cdot \frac{R_{c\ n-p-n} \cdot R_{c\ p-n-p}}{R_{c\ n-p-n} + R_{c\ p-n-p}},$$

We have:

$$R_{out} = \frac{1}{2} \cdot \frac{R_{c\ n-p-n} \cdot R_{c\ p-n-p}}{R_{c\ n-p-n} + R_{c\ p-n-p}} \cdot (1 + \frac{1}{C_{ti\ fb}} \cdot C_i), \tag{3}$$

Formula (3) is valid if the condition $R_m \gg R_{in}$ is met. If $*R_m$ is not high enough, then in (3), you need to substitute the coefficient:

$$\gamma_{FB} = \frac{R_m + R_\perp}{R_{in} + R_m + R_\perp},$$

It takes into account the loss of current transfer from the FB circuit to the PPDCA input. In the case of building a CCG on the above transistors and $I_p = 1\,\text{mA}$, in mode $R_{in} = 0$, we have 1.4 GΩ.

If R_{in} changes in a certain range, then R_{out} changes due to the dependence of R_c on the current collector.

Computer simulation of the dependence $R_{out} = f(I_{out})$ allowed us to obtain a set of initial characteristics in the range $I_{in} = -100\ \mu\text{A} \div 100\ \mu\text{A}$, in particular for $C_{ti} = 10$, (R_m = 2.0 kΩ, $R_\perp$ = 225 Ω) as shown in Figure 3.

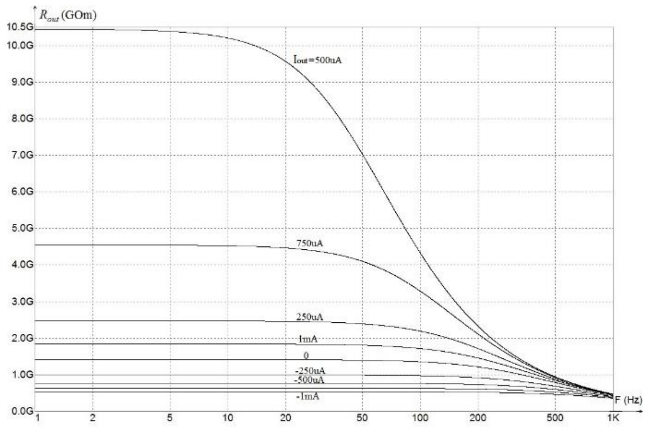

Fig. 3. Graphs of dependence $R_{out} = f(I_{out})$ in the frequency band at $C_{ti} = 10$

The graphs show that the output resistance decreases slightly when the direction I_{out} changes from direct to inverse.

The dependence R_{out} as well as the linearity errors on C_{ti} are given in the following table.

Table 1. Linearity errors and output resistance PPDCA

C_{ti}	2	5	10	20	100
R_{out}[MΩ]	406	688	1200	401	40
ΔI_{LIN}[nA]	0.98	1.4	2.1	42	2100
δI_{LIN} [%]	$0.98 \cdot 10^{-4}$	$1.4 \cdot 10^{-4}$	$2.1 \cdot 10^{-4}$	$42 \cdot 10^{-4}$	$21 \cdot 10^{-3}$

The change R_{out} is explained by the fact that in the range $I_{out} = -1\,\text{mA} \div 1\,\text{mA}$ at the outputs CM1 and CM2, the balance mode changes, during which there is a redistribution of collector currents between the p-n-p and n-p-n transistors, which have a significant difference between current gain β_n and β_p, and also different collector resistances.

The CCG output is connected to the bridge diode keys (BDK) of the current switch unit. The BDK operating points are set by operating current generators I'_{w1}, I''_{w1}, I'_{w2}, I''_{w2},…, I'_{wc}, I''_{wc}, and control is carried out by digital signals (voltages) U'_1, U''_1, U'_2, U''_2,…, U'_c, U''_c, respectively. It should be noted that to ensure the functioning of the BDK, it is necessary that the values of operating currents I'_{wi} and I''_{wi} are slightly greater than I_{out}. If the levels I'_{wi} and I''_{wi} are at the level of milliamperes, then the BDK supports correspond to tens of ohms.

Under these conditions, the relative methodological error of the switching currents is equal to:

$$\delta I_{cm} = \frac{R_{BDK}}{R_{BDK} + R_{out}},$$

where: R_{out} is the output resistance of the CCG. If R_{out} has the meaning of hundreds of units of MΩ, then δI_m has is of the order $\sim 10^{-5} \div 10^{-4}\%$.

Of course, using the proposed principle of switching currents, this error can be ignored in most cases.

At the same time, due to the presence of the instrumental component of switching errors:

$$\delta I_{BDK} = \frac{|I'_{wi}| - |I''_{wi}|}{I_w},$$

As a result of the fundamental limitations on the exact fit of the levels I'_{wi} and I''_{wi}, this component must be taken into account in the form of corrections made in the form of codes ΔK in the table of corrections to the multi-channel code-analog system. For convenience of zero offset error $I_{ZO.0}$, the CCG and BDK should be summed and generated in the form of correction codes for the corresponding channel.

It should also be noted that the application of the principle of current amplification allows us to achieve the maximum speed of the CCG, which is determined by the cutoff frequencies of bipolar transistors. So the bandwidth of a single gain PPDCA when $R_L = 100\,\Omega$ reaches $\sim 1.6\,\text{GHz}$. This can be seen from the amplitude-frequency characteristic of the device, the graph of which is shown in Figure 4.

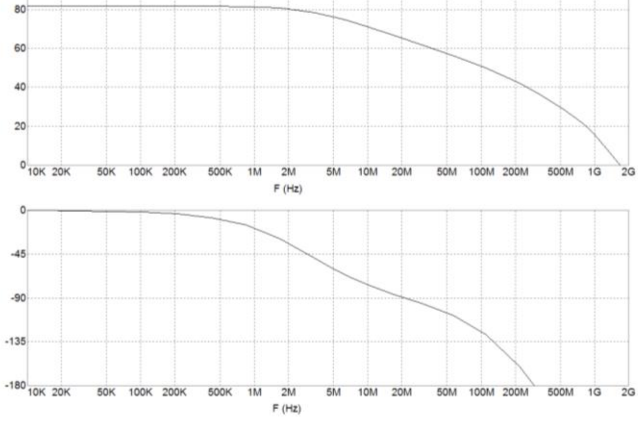

Fig. 4. Amplitude-frequency characteristic of PPDCA with a load of 100 Ω

It is necessary to look at the recommendations for the use of types of output devices that are loads for the CCG and CSU, as well as this DA system. To maintain high speed and minimal linearity errors, it is desirable that the input supports R_{out} of the output devices are low; not more than hundreds of ohms. This is easy to achieve in current-voltage converters built on operational amplifiers, as well as sampling devices – storage of integrated type [3, 4, 5]. In some cases, the load can be the control winding of the stepper motor in the tracking code – the angle of rotation of the shaft [8].

3. Conclusions

1) An approach to building a multi-channel digital-analog system is proposed, in which, unlike the known ones, there is a code-current converter, a controlled current generator, and a current communication block. For a given accuracy, this saves on the analog system equipment.
2) The proposed principle of construction of a controlled current generator in the form of a highly linear push-pull amplifier – current scalar based on bipolar transistors with a grounded load has been analyzed. It has been shown that this device has a high output resistance and a wide bandwidth, which allows current switching to be used to implement a multi-channel system mode.
3) By computer simulation, the errors of zero offset $I_{\text{ZO.0}}$ and linearity have been analyzed and it has been proved that $I_{\text{ZO.0}}$ can be reduced by calibration by introducing corrections presented in digital form.
4) Practical recommendations and conditions of practical application of the considered multichannel DA system have been given for different types of output devices performing the role of a load.

References

[1] Azarov O., Generalnytsky E.: High-line push-pull amplifier-current scaler on bipolar transistors with grounded load. Visnyk of Vinnytsia Polytechnic Institute 5, 2019, 55–61.
[2] Azarov O. D., Bogomolov S. V.: Fundamentals of the theory of high-line analog devices based on push-pull amplifier circuits. Universum, Vinnytsia 2013.
[3] Azarov O. D., Garnaga V. A.: Push-pull DC amplifiers for multi-bit converters of self-calibrating information. Universum, Vinnytsia 2011.
[4] Azarov O. D., Krupelnytsky L. V.: Analog-digital devices of self-correcting systems for measurement and processing of low-frequency signals. Universum, Vinnytsia 2005.
[5] Azarov O. D., Teplitsky M. Y., Bilichenko N. O.: High-speed push-pull DC amplifiers with balanced feedback. VNTU, Vinnytsia 2016.
[6] Azarov O. D., Teplitsky M. Y., Garnaga V. A.: Push-pull DC amplifiers based on bidirectional current reflectors. Problems of informatization and control 2(34), 2011, 15–22.
[7] Connelly J.: Analog Integrated Circuits. Mir Publishing House, Moscow 1977, 107–112.
[8] Karandakov G. V., Kryvenko V. I.: Electrical engineering, electronics and microprocessor technology. NTU, Kyiv 2008.
[9] McCarth M., Collins A.: Switches and Multiplexers. Analog Dialogue 31, 1997, 20–22.
[10] Stepanenko I. P.: Fundamentals of the theory of transistors and transistor circuits. Energy, Moscow 1977.
[11] Zeveke G. V., Ionkin P. A., Netushil A. V., Strakhov S. V.: Fundamentals of circuit theory. Energy, Moscow 1975.

D.Sc. Olexiy Azarov
e-mail: azarov2@vntu.edu.ua

Ukrainian scientist, Doctor of Technical Sciences, Professor, Dean of the Faculty of Information Technology and Computer Engineering of Vinnytsia National Technical University, Honored Worker of Education of Ukraine, Honored Worker of Education of Ukraine, Academician of the International Personnel Academy.

https://orcid.org/0000-0002-8501-1379

M.Sc. Yevhenii Heneralnytskyi
e-mail: gesvntu@gmail.com

Postgraduate student of Vinnytsia National Technical University, Faculty of Information Technology and Computer Engineering, majoring in computer engineering. Ph.D. student of VNTU.

https://orcid.org/0000-0003-0205-382X

M.Sc. Nataliia Viktorivna Rybko
e-mail: rybkonatvik@gmail.com

Lecturer at the Department of Foreign Languages and the Center for Technical Translation. She teaches English and German, theory and practice of translation, terminology, business English. Works as a Deputy Dean for Educational Work at the Faculty of Management and Information Security. Research interests: features of translation of economic literature from English into Ukrainian.

https://orcid.org/0000-0002-6968-3044

otrzymano/received: 12.07.2020 *przyjęto do druku/accepted: 10.12.2020*

http://doi.org/10.35784/iapgos.2396

A COMPUTER SYSTEM FOR ACQUISITION AND ANALYSIS OF MEASUREMENT DATA FOR A SKEW ROLLING MILL IN MANUFACTURING STEEL BALLS

Marcin Buczaj[1], Andrzej Sumorek[2]

[1]Lublin University of Technology, Department of Electrical Engineering and Electrotechnologies, Lublin, Poland, [2]Lublin University of Technology, Department of Structural Mechanics, Lublin, Poland

Abstract. *The article presents the concept and capabilities of a computer system for analysing measurement data for a skew rolling mill used to produce steel balls. The computer system for data acquisition and analysis consists of cooperating systems designed to perform control and measurement tasks during the operation of a skew rolling mill. Their main task is to collect and record data related to the measured physical parameters of the batch rolling process. This system registers the current and analyses the radial forces and torque acting on the rolled element by the rolling tool. The process of data acquisition, analysis and archiving is carried out by means of an NI USB 6009 measuring card together with the attached systems of transducers and force and torque sensors and a computer with an installed application. The measurement application was developed in the LabVIEW environment. The application algorithm is based on the state machine architecture and enables the configuration of measurement elements and technical parameters, checking the functioning of the control and measurement system and the acquisition and archiving of measurement data.*

Keywords: data acquisition, measurement techniques, force and torque measurement, programming environments

KOMPUTEROWY SYSTEM DO AKWIZYCJI I PRZETWARZANIA DANYCH POMIAROWYCH DLA WALCARKI SKOŚNEJ PRZY WYTWARZANIU KUL STALOWYCH

Streszczenie. *W artykule została przedstawiona koncepcja oraz zaprezentowane możliwości komputerowego systemu do analizy danych pomiarowych dla walcarki skośnej wykorzystanej do wytworzenia kul stalowych. Komputerowy system akwizycji i analizy danych to współpracujące ze sobą układy przeznaczone do realizacji zadań kontrolno-pomiarowych podczas pracy walcarki skośnej. Ich głównym zadaniem jest zbieranie i rejestracja danych związanych z mierzonymi parametrami fizycznymi procesu walcowania skośnego wsadu. Układ ten umożliwia bieżącą rejestrację i analizę sił promieniowych i momentu obrotowego działającego na walcowany element przez narzędzie walcujące. Realizacja procesu akwizycji, analizy i archiwizacji danych odbywa się za pomocą karty pomiarowej NI USB 6009 wraz dołączonymi do niej układami przetworników i czujników siły i momentu obrotowego oraz komputera z zainstalowaną aplikacją. Aplikacja pomiarowa została opracowania w środowisku LabVIEW. Algorytm aplikacji został oparty o architekturę maszyny stanu i umożliwia konfigurację elementów pomiarowych i parametrów technicznych, sprawdzenie funkcjonowania układu kontrolno-pomiarowego oraz akwizycję i archiwizację danych pomiarowych.*

Słowa kluczowe: akwizycja danych, techniki pomiarowe, pomiar siły i momentu obrotowego, środowiska programistyczne

Introduction

Metal forming processes, including rolling, are widely used in the engineering industry and are particularly important in the metallurgical industry. Rolling processes are used to produce balls, rings, pipes, as well as more complex shapes such as drills bits. This is due to the numerous advantages of this method of processing and forming metal products [3]. The main advantages of this process are:

- high efficiency,
- material saving,
- small amount of production waste,
- high precision of formed elements,
- low production costs and limited energy consumption of the process.

One of the basic products obtained in the rolling process is balls. Balls, especially steel ones, are used for the production of rolling bearings, as well as other machine and equipment components. Balls can also be used as tools to process other materials. They are often used as grinders in ball mills and are used for grinding: metal ores, coal, cement, sand and other materials [2, 7].

Generally, the processes of plastic forming are quite well known. However, there is a constant need to develop new processing techniques. Knowing the technical and physical parameters of production processes is particularly important for the teams of constructors and inventors, where checking one's own ideas and comparing research results with computer calculations and simulations allows to specify the machining process, to determine the most favourable technical parameters and to determine and become acquainted with the parameters of the equipment [1, 4–6, 8].

Verification of theoretical assumptions concerning the processes of shaping the product is performed by means of specially dimensioned machines equipped with appropriate sensors. The measurement systems used allow the control and monitoring of the current operating parameters of the device and the evaluation of the forming processes. The system for managing, supervising and collecting measurement data should be distinguished by its flexibility and compatibility with other systems enabling data processing. The article presents a computer system for monitoring and archiving measurement data from force and torque sensors developed in the LabVIEW programming environment by National Instruments, cooperating with an NI-USB-6009 measurement card.

1. Ball rolling process and the structure of a skew rolling mill

Ball screw rolling in a skew rolling mill consists in forming forgings of balls from a solid bar between two oblique rollers (equipped with screw blanks), with separation of the finished product. Only one ball is formed with each rotation of the rolls [2, 3]. The process of making balls in a skew rolling machine is shown in Fig. 1.

Screw rolling of forgings in skew rolling mills is one of the most efficient methods of producing this type of semi-finished products. It is characterised by many advantages, which include, among others, small material losses, greater accuracy in relation to forged or cast semi-finished products, easy automation and a favourable structure layout, which improves the strength properties and increases the durability of such shaped products.

The inclined rolling mill used in the research has a segmental structure and consists of a load-bearing frame, drive system, rolling cage and drive transmission system (Fig. 2). Its basic technical parameters are as follows:

- horizontal position of the rollers in the work cage;
- nominal diameter of the rolls: 320 mm;
- working length of the roll barrel: 400 mm;
- min/max distance of the rollers' axes: 300÷350 mm;
- two rotational speeds of the rolls: 15 rpm and 30 rpm;
- nominal torque on one cylinder (at 15 rpm): 20 kN·m;

- rated torque on one cylinder (at 30 rpm): 10 kN·m;
- machine total weight: 17,500 kg;
- rated power of two-speed drive motor: 60÷80 kW.

Fig. 3 shows the tools that plasticise the material subjected to the rolling process. In Fig. 4, the output of the process of producing balls in a skew rolling mill is presented.

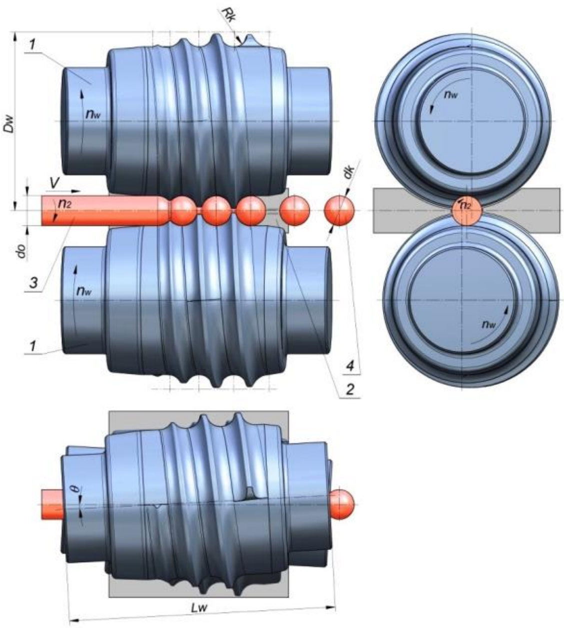

Fig. 1. Diagram of the ball rolling process in a skew rolling mill:1– rollers with screw blanks, 2 – guides, 3 – batch, 4 – shaped ball [2, 3]

Fig. 2. Skew rolling machine

Fig. 3. Tool for producing balls in the process of rolling in a skew rolling machine

Fig. 4 Balls obtained by processing a metal bar in a skew rolling machine

2. Characteristics of the measuring system

The data acquisition system ensures the registration of two or three (depending on the chosen measurement option) technical parameters of the skew rolling process. The choice of the option depends on the type and shape of the processed material. The figures are:

- shaft torque – BCM model 1816 torque sensor;
- radial force on the first working roller – CL-16 strain gauge force sensor with a CL-72U-3U transducer from ZEPWN;
- radial force on the second working roller – CL-16 strain gauge force sensor with a CL-72U-3U transducer from ZEPWN.

The 1816 series sensor (Fig. 5), manufactured by BCM, is a non-contact rotary torque transducer with an air bearing among the rotor and stator via to allow the product to function under the immense rotating speed of 6000 rpm. It has a 1.5 mm air gap on the rotor and the stator. Its non-contact feature lowers the maintenance requirements and makes it durable enough for extended utilisation. In addition, it has a 5–2000 Nm torque capacity transducer, with a 0.5 % fs precision and an output signal of 10±5 kHz [9].

Fig. 5. Model 1816 BCM rotary torque sensor installed on the shaft of a skew rolling machine

The CL16 strain gauge force sensor (Fig. 6) together with the CL 72-3U amplifier from ZEPWN is a sensor designed for measuring static tensile and compressive forces. The sensor-amplifier system is characterised by high accuracy in class 0.5 and 1 in a wide range of measurements (from 10% to 100% of the measuring range). The system generates a signal in the measuring track in the range from 0 V to 10 V DC [11, 12].

Fig. 6. One of the two tensometric force sensor by ZEPWN mounted on a skew rolling machine

Data recording concerns the recording of 2 physical parameters (torque and radial force) at 3 measurement points. Additionally, the data acquisition system has two reserve channels for connecting additional sensors (e.g. shift sensor). The mutual configuration of the control system elements and data acquisition is presented in Fig. 7.

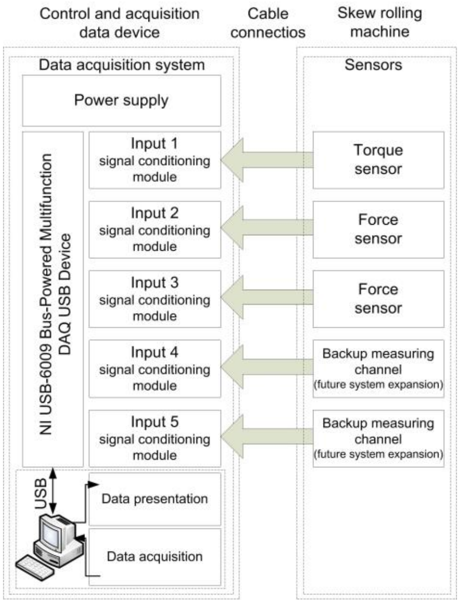

Fig. 7. Schematic diagram of the control and data acquisition system connected to a skew rolling machine

Data from the measurement sensors are collected by a USB-6009 measurement card from National Instruments (Fig. 8). The measurement card allows measurement and generation of both analogue and digital signals. The card is equipped with 8 analogue inputs with a resolution of 13 bits, allowing measurement of voltages from –10 V to 10 V in relation to the ground terminal. There is a possibility of program switching of the voltage measurement method and connecting the inputs in pairs to 14-bit inputs. The card has two independent voltage outputs with a resolution of 12 bits, generating variable voltage values of any shape within the range from 0 V to 5 V. They are protected against overload by an internal 50 Ω resistor switched on in a series. The maximum sampling frequency of the analogue signals is 48 kS/s. The digital part of the card contains 12 digital connectors in two ports working both as inputs and outputs, and two DC voltage sources of +2.5 V and 5 V and a ground output. The card is also equipped with a counter with a 12-bit resolution [10].

In the measuring system, the signals from the measuring sensors are connected to single-ended voltage inputs on the NI-USB 6009 measuring card working in the range of ±10 V.

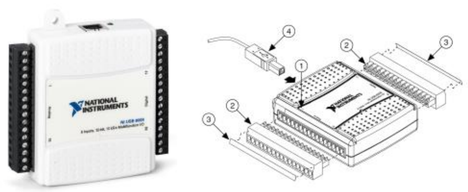

Fig. 8. National Instruments USB-6009 Data Acquisition Card (1 – overlay label with pin orientation guides, 2 – screw terminal connector plug, 3 – signal label, 4 – USB cable)

3. Application for acquisition and presentation of measurement data

The data acquisition software was implemented in the LabVIEW Professional Development System graphical programming environment (2017, version 17.0f2, 64 bit, National Instruments). The LabVIEW programming environment and the USB-6009 measurement card come from the same manufacturer.

The developed data acquisition system performs the following functions related to the management and monitoring of physical parameters of the diagonal rolling process: configuration and testing of control and measurement system elements, data acquisition during the measurement process, recording and presentation of measurement data and preliminary processing of file data.

The state machine architecture was used to create an algorithm for program operation. This allows, from the user's point of view, to go straight to the selected range of actions. The only exception to this rule is an obligatory declaration of the disk directory in which the hardware settings and measurement results will be stored. Without this initial action, it is not possible to call up other procedures. It is possible to return to these settings and modify them at any time when using the program.

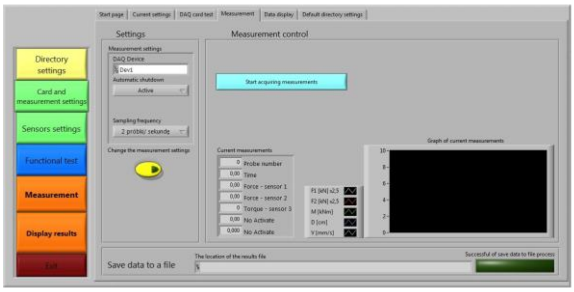

Fig. 9. Measurement process window of the application

Figures 9 and 10 show two front windows of the application panel, in which it is possible to carry out the measurement process and to present current sensor readings and to display previously archived measurement data (Fig. 10).

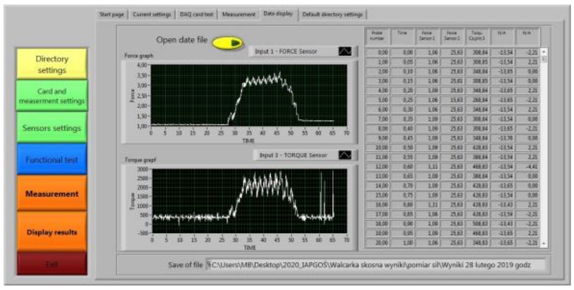

Fig. 10. Data presentation window of the application

The complete measurement procedure with data recording results in storing the measurement data collected from the detection devices in the folder indicated by the user. The values obtained in the current measurement process are available for viewing in graphical and text form in the main program window after selecting the "Displaying results" tab.

Due to the large variety of registered values, the range of measurement values and the amount of data, it is more convenient to view the results in software dedicated to data processing and analysis. The described data acquisition system automatically saves data in files in the *.tsv format (tab separated value), which is transparent and supported by practically every data processing environment. This solution enables system users to further process measurement data in other application programs. It also allows the use of additional mathematical and computational formulas, and thus the comparison of the results obtained with other measurement data or those obtained from modelling and computer simulation processes.

4. Presentation of measurement data and test results

A computer system for the acquisition and processing of measurement data for a skew rolling machine is used during the process of manufacturing steel balls in laboratory (testing) conditions using real materials. The practical research included the measurement of two or three signals related to the process of forming and manufacturing steel balls. The number of signals used was related, among others, to the form of the semi-finished products.

An example set of measurement data obtained from the data acquisition system is shown in Fig. 11 (the value of radial force was determined on the basis of data from the ZEPWN company's force sensor, and the value of torque on the basis of the BCM company's torque sensor).

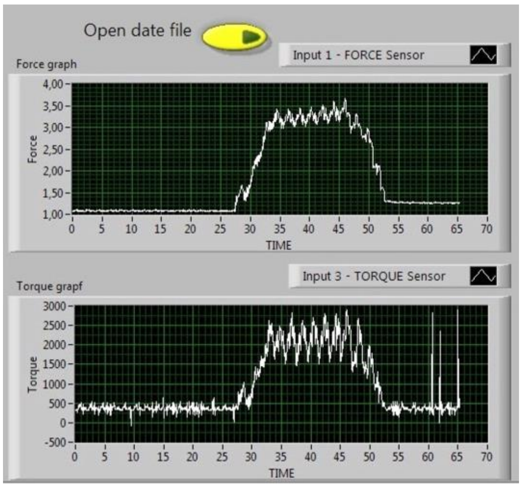

Fig. 11. Measurement data presentation in the application

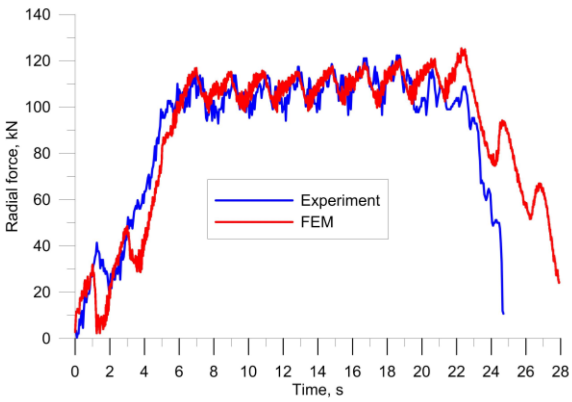

Fig. 12. Comparison of measurement data with FEM simulation (force measurement)

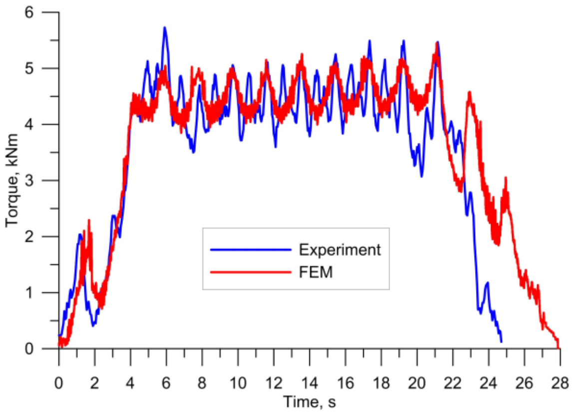

Fig. 13. Comparison of measurement data with FEM simulation (torque measurement)

Measurement data can be edited in popular software (e.g. Microsoft Excel). Thanks to this functionality of the measurement data acquisition system, it is possible to process the measurement data and present them in a program convenient for the user.

One of the research elements aimed at checking the regularity and correctness of the data obtained by means of the measurement system discussed was to check the measurement data received with the calculation data obtained on the basis of FEM simulations (Finite Element Method). The simulations were carried out with the use of the specialized Simufact Forming software (ver. 15). The simulation parameters reflected the real process parameters, that is: tool rotation speed – 30 rpm, diameter of the formed ball – 40 mm, batch material – steel bar of type C67, and initial batch temperature – 1000°C. The described model of object was divided into 35,000 elements. The initial size of the element was 1 mm. The eight nodal elements of first-order were used.

The radial force and torque time courses for the sample measurement data and the data obtained from the FEM simulations are shown in Fig. 12 and Fig. 13. Both diagrams show slight mutual deviations and differences between the courses.

5. Conclusions

On the basis of a series of tests and measurements related to the process of manufacturing steel balls in a skew rolling mill using a computer system for the acquisition and processing of measurement data, it was found that the system discussed is very useful in practical applications.

The system allows for effective acquisition of measurement data crucial in the determination of significant technical parameters of the forming process during the production of metal balls in a skew rolling mill.

The data obtained by means of the measuring system are consistent and comparable with the calculation data obtained from FEM simulations. A comparative analysis of the material obtained from experimental testing and simulation calculations shows minor differences. These may result from certain general criteria and coefficients adopted in the modelling process.

The measurement system shown allows the measurement data to be archived in such a way that they can be further processed by other external programs. This provides the possibility to increase the analytical capabilities of the measurement data and use them in programs dedicated to the processing of such data.

References

[1] Filippova M. V., Temlyantsev M. V., Peretyatko V. N., Prudkii E. E.: Rolling of metal balls. Steel in Translation 47, 2014, 435–439 [https://doi.org/10.3103/S0967091217070038].
[2] Gontarz A., Tomczak J., Pater Z., Bulzak T.: Effect of the Forming Zone Length on Helical Rolling Processes for Manufacturing Steel Balls. Materials 18, 2019, 1–13 [https://doi.org/10.3390/ma12182917].
[3] Pater Z., Tomczak J.: Walcowanie śrubowe kul do młynów kulowych. Politechnika Lubelska. Lublin 2012.
[4] Pater Z., Tomczak J., Bartnicki J., Lovell M. R., Menezes P. L.: Experimental and numerical analysis of helical-wedge rolling process for producing steel balls. International Journal of Machine Tools & Manufacture 67, 2013, 1–7 [https://doi.org/10.1016/j.ijmachtools.2012.12.006].
[5] Pater Z., Tomczak J., Bulzak T., Martyniuk S.: A helical wedge rolling process for producing a ball pin. Archives of Civil and Mechanical Engineering 4, 2019, 1316–1326 [https://doi.org/10.1016/j.promfg.2018.12.039].
[6] Pater Z., Tomczak J.: FEM Modelling of a helical wedge rolling process for axisymmetric parts. Advances in Science and Technology Research Journal 1, 2018, 115–126 [https://doi.org/10.12913/22998624/81767].
[7] Tomczak J., Pater Z., Kazanecki J., Bartnicki J., Chyła P.: Badania procesu kształtowania kul w walcach śrubowych. Mechanik 11, 2012, 927–931.
[8] Yang H., Zhang L., Hu Z.: The analysis of the stress and strain in skew rolling. Advanced Materials Research 538-541, 2012, 1650–1653 [https://doi.org/10.4028/www.scientific.net/AMR.538-541.1650].
[9] https://www.directindustry.com/prod/bcm-sensor-technologies-bvba/product-56103-659831.html (accessed: 12.11.2020).
[10] National Instruments, USB-6009 Multifunction I/O Device, https://www.ni.com/pl-pl/support/model.usb-6009.html (accessed: 12.11.2020).
[11] Tensometryczny czujnik siły typu CL14U. Karta produktu. ZEPWN Zakład Elektroniki Pomiarowej Wielkości Nieelektrycznych, Marki.
[12] Wzmacniacz CL 72-3U w obudowie. Karta produktu. ZEPWN Zakład Elektroniki Pomiarowej Wielkości Nieelektrycznych, Marki.

Ph.D. Eng. Marcin Buczaj
e-mail: m.buczaj@pollub.pl

Marcin Buczaj is an academic teacher in the Department of Electrical Engineering and Electrotechnologies of the Faculty of Electrical Engineering and Computer Science of the Lublin University of Technology. Research interests are surveillance systems, security systems, electrical installations, measurement systems and graphical interfaces for measurement systems.

https://orcid.org/0000-0002-7624-1674

Ph.D. Eng. Andrzej Sumorek
e-mail: a.sumorek@pollub.pl

Andrzej Sumorek is an academic teacher in the Department of Structural Mechanics of the Faculty of Building and Architecture of the Lublin University of Technology.
Research interests are data acquisition, graphical interfaces for measurement systems, energy saving electrotechnologies, electrostatic filters for dust removal.

https://orcid.org/0000-0002-7521-6709

otrzymano/received: 17.11.2020 *przyjęto do druku/accepted: 10.12.2020*

http://doi.org/10.35784/iapgos.2357

RESEARCH ON A MAGNETIC FIELD SENSOR WITH A FREQUENCY OUTPUT SIGNAL BASED ON A TUNNEL-RESONANCE DIODE

Alexander V. Osadchuk, Vladimir S. Osadchuk, Iaroslav A. Osadchuk
Vinnytsia National Technical University, Faculty of Information Communication, Radio Electronics and Nanosystems.

Abstract. *Based on the consideration of physical processes in a tunnel-resonant diode under the action of a magnetic field, the construction of an autogenerating magnetic field sensor with a frequency output signal is proposed. The use of devices with negative differential resistance makes it possible to significantly simplify the design of magnetic field sensors in the entire RF frequency range. Depending on the operating modes of the sensor, an output signal can be obtained in the form of harmonic oscillations, as well as in the form of pulse oscillations of a special form.*

The study of the characteristics of the magnetic field sensor is based on the complete equivalent circuit of the tunnel-resonant diode. The equivalent circuit takes into account both the capacitive and inductive properties of the tunneling resonant diode. The inductive component exists under any operating conditions, as a result of the fact that the current flowing through the device is always lagging behind the voltage that caused it, which corresponds to the inductive response of a tunnel-resonant diode.

Keywords: self-oscillator, tunneling resonant diode, negative differential resistance, frequency, quantum heterostructure

BADANIA MAGNETYCZNEGO CZUJNIKA POLA Z SYGNAŁEM WYJŚCIOWYM CZĘSTOTLIWOŚCIOWYM W OPARCIU O DIODĘ TUNELOWO-REZONANSOWĄ

Streszczenie. *Na podstawie uwzględnienia procesów fizycznych zachodzących w diodzie tunelowo-rezonansowej pod działaniem pola magnetycznego proponuje się skonstruowanie autogeneracyjnego czujnika pola magnetycznego o częstotliwościowym sygnale wyjściowym. Zastosowanie urządzeń o ujemnej rezystancji różnicowej pozwala znacznie uprościć konstrukcję czujników pola magnetycznego w całym zakresie częstotliwości RF. W zależności od trybu pracy czujnika sygnał wyjściowy można uzyskać w postaci oscylacji harmonicznych, a także w postaci oscylacji impulsów o specjalnej postaci.*

Badanie charakterystyk czujnika pola magnetycznego opiera się na pełnym obwodzie zastępczym tunelowej diody rezonansowej. Obwód zastępczy uwzględnia zarówno właściwości pojemnościowe, jak i indukcyjne tunelowej diody rezonansowej. Składowa indukcyjna istnieje w każdych warunkach pracy, na skutek tego, że prąd przepływający przez urządzenie jest zawsze opóźniony w stosunku do napięcia, które go spowodowało, co odpowiada odpowiedzi indukcyjnej diody tunelowo-rezonansowej.

Słowa kluczowe: samoscylator, tunelowa dioda rezonansowa, ujemna rezystancja różnicowa, częstotliwość, heterostruktura kwantowa

Introduction

The characteristics of sensors determine the accuracy and reliability of control systems and regulation of devices for monitoring technological processes, environmental characteristics, the safety of industrial installations, and so on. Therefore, strict requirements are imposed on magnetic field sensors. They should be economical, ensure high measurement accuracy, have minimal dimensions, weight and power consumption, be compatible with modern computers and be able to be manufactured using standard integral technology [8, 14, 19].

At present, the existing semiconductor magnetic field sensors do not satisfy the above requirements. They have a low output signal, low accuracy and sensitivity, and require analog-to-digital converters and amplifying devices for further signal processing. A promising scientific direction, eliminating the shortcomings of existing analog magnetic field sensors, is the creation of sensors that implement the principle of transformation "magnetic field induction - frequency" based on self-generated nanoelectronic structures with negative differential resistance. Tunneling resonance diodes belong to such nanoelectronic structures. The operation of these devices is based on the effect of electron tunneling through quantum heterostructures as they move perpendicularly to the plane of potential barriers separating quantum heterostructures.

1. Formulation of the problem

The theoretical foundations of the operation of tunnel resonance diodes were laid by L. Esaki and R. Tzu [6, 7, 23]. Indeed, in these works, they were the first to investigate the negative differential resistance in AlGaAs/GaAs nanostructures as a result of resonant electron tunneling through potential barriers. The unique properties of tunnel-resonant diodes are their microwave properties together with negative differential resistance, which made it possible to build logic devices, memory devices, switches, resonant amplifiers, generators, sensors and many other devices on their basis [15–18].

The influence of the magnetic field on the characteristics of tunneling-resonant diodes was investigated in a number of works [1, 9, 10], while the diodes acted as analog magnetic field sensors, however, the development and creation of magnetic field sensors with a frequency output signal has hardly been studied. Therefore, this work is devoted to the development of a mathematical model of a magnetic field sensor with a frequency output signal based on a tunnel resonance diode, which made it possible to obtain the main characteristics of the sensor.

2. Theoretical research

Before proceeding to the consideration of the mathematical model of the magnetic field sensor based on a tunnel-resonant diode, we need to briefly consider its structure, energy diagram, the density of electronic states and its dependence on the electron energy, current-voltage characteristic, the transparency coefficient of potential barriers on the energy of electrons tunneling through these barriers. This knowledge is necessary for the development of a mathematical model and the possibility of using it as a magnetic field sensor with a frequency output.

The classical structure of a tunnel-resonant diode, which is a two-dimensional semiconductor quantum heterostructure, consists of a nanometer-length GaAs gallium arsenide film, on which a nanometer-sized layer of gallium arsenide aluminate AlGaAs with a wider band gap is deposited on both sides. When $x = 0.3$, the band gap of $Al_xGa_{1-x}As$ is approximately 2 eV, while for GaAs, it is 1.4 eV. This leads to the fact that a potential barrier with an almost rectangular shape and a height of 0.4 eV for electrons and 0.2 eV for holes arises as a result of the rupture of the bottom of the conduction band and the top of the valence band. On one side and the other, gallium arsenide aluminate is sprayed with n+ -GaAs serving as an emitter and a collector; and all film layers are located on a GaAs substrate [22]. From an energy point of view, the conduction band of a tunneling-resonant diode has two potential barriers, between which a quantum well is located (Fig. 1a) [5]. This structure of the diode is called a two-barrier heterojunction nanostructure. As a result, electrons from the emitter region need to tunnel through barriers and a quantum well to get into the reservoir area when they move perpendicular to the walls of the barrier. The motion of electrons in the quantum well is limited by the direction of the z coordinate, while in the plane (x, y) they are free and their behavior is the same as in three-dimensional semiconductor bodies (Fig. 1b) [5].

In this case, the wave function of an electron can be represented as a product of wave functions in coordinates x, y, z [3, 12].

$$\psi = \psi_x \psi_y \psi_z \tag{1}$$

where $\psi(x)$ and $\psi(y)$ are solutions to the Schrödinger equation for a free electron, that is, they describe a traveling wave. At the same time, the wave function $\psi(z)$ is a solution of the same Schrödinger equation only for an electron in a rectangular potential well $U(z)$ [12].

$$\psi(z) = \left(\frac{2}{a}\right)^2 \sin\left(\frac{\pi n z}{a}\right), \quad n = (1, 2, ...) \tag{2}$$

where a is the width of the potential well.

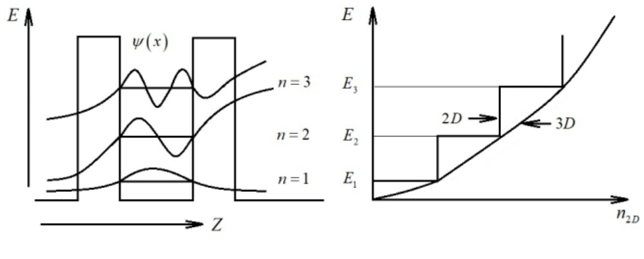

a) b)

Fig. 1. Schematic representation of the energy diagram of the conduction band of a tunnel-resonant diode with three energy levels and a change in the wave function with different electron energies (a); dependence of the density of quantum states on the electron energy for quantum two-dimensional and classical three-dimensional structures (b) [5]

The total energy of an electron in a potential well is described by the expression [12]:

$$\begin{aligned} E(K_x, K_y, n) &= \frac{\hbar^2}{2m^*}\left(K_x^2 + K_y^2\right) + E_n = \\ &= \frac{\hbar^2}{2m^*}\left(K_x^2 + K_y^2\right) + \frac{\pi^2\hbar^2}{2m^* a^2} n^2, \quad n = (1, 2...) \end{aligned} \tag{3}$$

where $\hbar = h/2\pi$ is Planck's constant; m^* is the effective mass of an electron; K_x, K_y are projections of the wave vector of electrons on the x and y axes; E_n is the energy levels in a quantum well; and n is the number of energy levels in the quantum well.

In Fig. 1b, a graph of the function of the density of states versus the change in the energy of electrons is shown, from which it can be seen that the function has a stepwise character, with all of the steps having the same width, but located at discrete values of energy E_n. Based on Fig. 1b, we can say that energy values between 0 and E_1 are prohibited. In the energy range $E_1 < E < E_2$, electrons can be located in the subband, which corresponds to $n = 1$. Two subzones can be located simultaneously in the energy range between E_1 and E_2, according to $n = 1$ and $n = 2$.

This leads to the fact that the density of the states function doubles in value. In general, it is described by the formula [5]:

$$n_{2D}(E) = \frac{m^*}{\pi\hbar^2 a}\sum_n \theta(E - E_n), \quad n = (1, 2, ...) \tag{4}$$

where $\theta(E - E_n)$ is a step function; $\hbar = (h/2\pi)$. The solid line in Fig. 1b is a parabolic curve for the three-dimensional case, which shows the difference between two-dimensional and three-dimensional systems. This difference is more pronounced at small values of the quantity n.

To obtain the current-voltage characteristics of the tunnel-resonant diode, the Schrödinger equation is used in the general form [21]:

$$-\frac{\hbar^2}{2m^*}\frac{\partial^2 \psi_n}{\partial \vec{r}^2} + U(\vec{r})\psi_n(\vec{r}) = E(\vec{K})\psi_n(\vec{r}) - E_n(0)\psi_n(\vec{r}) \tag{5}$$

where $\psi_n(\vec{r})$ is the wave function of an electron, which depends on the radius vector $\vec{r}$, which corresponds to an electron with energy level n; $U(\vec{r})$ – potential energy of barriers; $\vec{K}$ – wave vector of the electron; $E(\vec{K})$ – electron energy; $E_n(0)$ – energy of an electron in a quantum well at $K = 0$ when the energy of the resonance level E_0 is equal to the bottom of the conduction band E_c. Based on equation (5), a function of the current density of the applied voltage is obtained, which is called the Tsu-Esaki function [2, 4, 23]

$$J = \frac{qm^* kT}{2\pi^2\hbar^3}\int_{E_C}^{\infty} T(E_Z)\log\left[\frac{1+\exp\left(\frac{E_F - E_Z}{kT}\right)}{1+\exp\left(\frac{E_F - E_Z - qU}{kT}\right)}\right]dE_Z \tag{6}$$

where k is Boltzmann constant; T – absolute temperature; E_F – Fermi level in the conduction band of the emitter; U – applied voltage; $T(E_Z)$ – transparency coefficient of electrons passing through potential barriers and a quantum well.

For a more accurate description of the current-voltage characteristic, it is necessary to take into account the phonon scattering of electrons, scattering by impurities, scattering at layer boundaries, and scattering of electrons by alloys. A numerical kinetic model based on Green's functions [21] most accurately describes the current-voltage characteristic of tunneling-resonant diodes. One of the problems in calculating the current-voltage characteristic is the determination of the transparency coefficient $T(E_Z)$ two-barrier quantum heterostructure.

The transparency coefficient of a potential barrier is understood as the ratio of the flux density of electrons passing through the barrier to the electron flux density of the incident wave. The coefficient of reflection of electrons from the barrier is determined by the ratio of the flux density of reflected electrons from the barrier to the flux density of electrons incident on the barrier. Let us consider the case when electrons interact with a rectangular potential barrier of width a whose height $U(z)$ is more energy E electrons $(U(z) > E)$. In this case, the transparency coefficient $T(E)$ is described by the expression [5, 11]:

$$T(E) \cong e^{-\frac{2}{\hbar}\int_{z_1}^{z_2}\sqrt{2m^*(U(z)-E)}dz} \tag{7}$$

where z_1 and z_2 are turning points in the condition $E = U(z_1) = U(z_2)$. Reflection coefficient $R(E)$ in this case is determined based on the relation $R(E) = 1 - T(E)$.

The situation changes significantly in the process of tunneling electrons through the double barrier when the function $T(E)$ takes on a more complex form and is a product of two quantities: T_E for the first barrier or emitter, and T_K for a second barrier or collector:

$$T(E) = T_E \cdot T_K \tag{8}$$

The problem is solved most easily when the barriers are identical. The coefficient of such a two-barrier structure is described by the equation [12]:

$$T(E) = \frac{T_0^2}{T_0^2 + 4R_0 \cos^2(\xi a - Q)} \tag{9}$$

where the values T_0 and R_0 – transparency and reflection coefficients for a single barrier; $\xi = 1/\hbar\sqrt{2m^*(U_0 - E)}$; and Q – a phase angle.

Let us proceed to consider the influence of the magnetic field on the parameters of the tunnel-resonant diode. In bulk 3D crystals under the influence of magnetic field B, the electron energy quantum is only in the plane perpendicular to B, however, in two-dimensional electronic systems, the energy spectrum can be quantized completely. This idea is based on the solution of the Schrödinger equation for electrons in such a system when a magnetic field is applied to it, which is directed along the z axis perpendicular to the plane of the system. The Schrödinger equation for the wave function $\psi(r) = \psi(x, y)$ two-dimensional system takes the form [12]:

$$\left[-\frac{\hbar^2}{2m^*}\frac{\partial^2}{\partial x^2} + \frac{1}{2m^*}\left(i\hbar\frac{\partial}{\partial y} + qBx \right)^2 \right]\psi(x, y) = E\psi(x, y) \tag{10}$$

where q – electron charge; B – magnetic induction; and E – the energy of electrons. After transformations in square brackets, the equation takes the form:

$$\left[-\frac{\hbar^2}{2m^*}\left(\frac{\partial^2}{\partial x^2} + \frac{\partial^2}{\partial y^2} \right) - \frac{i\hbar qBx}{m^*} - \frac{(qBx)^2}{2m^*} \right]\psi(x, y) = E\psi(x, y) \tag{11}$$

The solution to equation (11) is presented in the form [12]:

$$\psi(x, y) = \varphi(x)e^{iKy} \tag{12}$$

where the plane wave corresponds to the coordinate y. Substituting expression (12) into equation (11), we obtain an equation for the functional dependence on coordinate x in the form [12]:

$$\left[-\frac{\hbar^2}{2m^*}\frac{d^2}{dx^2} + \frac{1}{2}m^*\omega_c^2\left(x - x_0^2 \right) \right]\psi(x) = E\psi(x) \tag{13}$$

where the value ω_c equals:

$$\omega_c = \frac{qB}{m^*} \tag{14}$$

and x_0 has the form [12]:

$$x_0 = \frac{hK}{qB} \tag{15}$$

Expression (13) is the Schrödinger equation for a one-dimensional harmonic oscillator, since the application of x_0 to x means the shift of the center of the parabolic potential by the amount x_0, so the parameter x_0 called the center of coordinates.

Thus, the solution of equation (13) provides an important result, which shows that the eigenstates of a two-dimensional system in a magnetic field are determined by the expression [12]:

$$E_n = \left(N + \frac{1}{2} \right)\hbar\omega_C, \quad N = 0,1,2... \tag{16}$$

where N is the Landau levels.

The obtained energy values depend on quantum number N and the magnitude of magnetic field B through cyclotron frequency ω_c.

Thus, we can conclude that in strong magnetic fields, which are directed perpendicular to the plane of a two-dimensional quantum heterostructure, electrons move along cyclotron orbitals with frequency ω_c, which is determined by equation (14). Moreover, their energy is quantized according to the rules of a harmonious quantum oscillator. It follows from the above that the function of the density of states of a two-dimensional electron gas after the application of magnetic field B for each of the Landau levels turns into an δ-function. Fig. 2 shows that the lowest of the Landau levels corresponds to the energy $h\omega_c/2$, and it lies above the bottom of the parabolic zone. Due to the scattering of electrons by impurities, the lines broaden, blurring δ - functions, as shown in Fig. 2 [12].

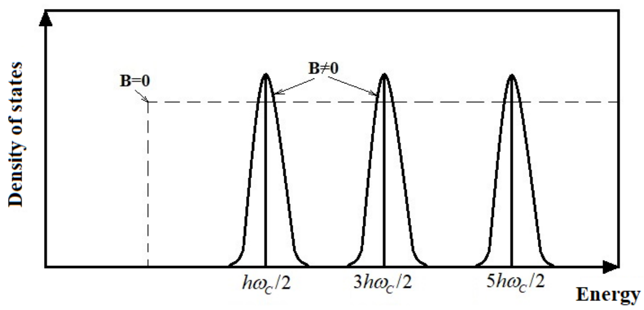

Fig. 2. Dependence of the function of the density of states of a two-dimensional electron gas on the energy in a magnetic field; for comparison, similar dependences are presented for a two-dimensional system at $B = 0$ [12]

After the application of magnetic field B, all Landau levels in energy range $h\omega_c$ turn into one common Landau level. In this case, degeneracy coefficient D of the Landau levels is described by the expression [12]:

$$D = \frac{qB}{2\pi h} \tag{17}$$

As can be seen from formula (17), the degeneracy of the Landau levels increases linearly with the applied magnetic field. The allowed energy levels, when the magnetic field is perpendicular to the two-dimensional system, lie on concentric circles with a constant radius $K^2 = K_x^2 + K_y^2 = (2qB/\hbar)(N + 1/2)$.

Thus, the kinetic energy of an electron in a quantum well is [21]:

$$E_{R,n} = E_R(U) + \left(N + \frac{1}{2}\right)\hbar\omega_c \pm g^{*}\mu B \tag{18}$$

where $E_R(U)$ – energy of electrons, which depends on the applied voltage U; $g^{*}\mu B$ – magnetic energy of the electron spin; μ – electron mobility; B – magnetic induction; and g^{*} – Lande coefficient [13, 21, 24].

Let us move on to considering the mathematical model of a magnetic field sensor with a frequency output based on a tunnel-resonant diode. The main characteristic of such a device is the dependence of the resonant frequency of a generator built on a diode, from the measured value, in our case, the magnetic induction. This dependence can be determined based on the electrical circuit of the sensor, which is shown in Fig. 3.

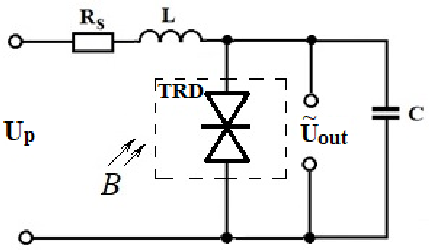

Fig. 3. Electrical diagram of a magnetic field sensor

In the tunnel-resonant diode, the current-voltage characteristic has a falling section corresponding to the existence of a differential negative resistance in this section. The descending section arises due to a decrease in the current that passes through the double-barrier quantum heterostructure due to a decrease in the transparency coefficient of potential barriers due to an increase in the energy of tunneling electrons with increasing voltage and the action of a magnetic field in comparison with the energy resonance level. The negative differential resistance converts the DC electric field energy of the tunnel-resonant diode power supply into AC electric field energy. The electrical circuit of the sensor (Fig. 3) is powered from constant voltage source U_P. Loss resistance R_S, which includes all of the ohmic resistances of the circuit, external inductance L, which is connected in series to the internal inductance of the diode, and also contains the inductance of the circuit terminals, external capacitance C, which is connected in parallel to the internal capacitance of the diode, as well as the tunnel-resonant diode itself, on which the magnetic field acts.

An equivalent sensor circuit for calculating its characteristics is presented in Fig. 4.

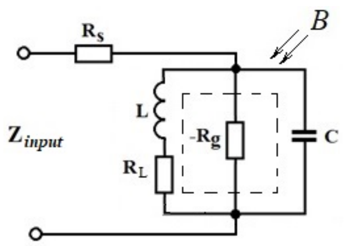

Fig. 4. Equivalent circuit of a magnetic field sensor

Power source $I(U)$ at the operating point on the descending section of the current-voltage characteristic determined the ratio $U/I(U)$, which corresponds to negative differential resistance R_g (Fig. 4).

Based on the equivalent circuit (Fig. 4), we calculate input impedance Z_{input}, on the basis of which we determine the resonant frequency. The impedance is expressed as:

$$\begin{aligned}
Z_{input} = R_s &+ \frac{\left[\frac{R_g}{1+(\omega C R_g)^2}\right]^2 R_L + \left[\frac{R_g}{1+(\omega C R_g)^2}\right](\omega L)^2}{\left[\frac{R_g}{1+(\omega C R_g)^2}+R_L\right]^2 + \left[\omega L - \frac{\omega C R_g^2}{1+(\omega C R_g)^2}\right]^2} + \\
&+ \frac{\left[\frac{\omega C R_g^2}{1+(\omega C R_g)^2}\right]^2 R_L + \left[\frac{R_g}{1+(\omega C R_g)^2}\right] R_L^2}{\left[\frac{R_g}{1+(\omega C R_g)^2}+R_L\right]^2 + \left[\omega L - \frac{\omega C R_g^2}{1+(\omega C R_g)^2}\right]^2} + \\
&+ j\frac{\left[\frac{R_g}{1+(\omega C R_g)^2}\right]^2 (\omega L) - \left[\frac{\omega C R_g^2}{1+(\omega C R_g)^2}\right] R_L^2}{\left[\frac{R_g}{1+(\omega C R_g)^2}+R_L\right]^2 + \left[\omega L - \frac{\omega C R_g^2}{1+(\omega C R_g)^2}\right]^2} + \\
&+ j\frac{-\left[\frac{\omega C R_g^2}{1+(\omega C R_g)^2}\right](\omega L)^2 + \left[\frac{\omega C R_g^2}{1+(\omega C R_g)^2}\right]^2 (\omega L)}{\left[\frac{R_g}{1+(\omega C R_g)^2}+R_L\right]^2 + \left[\omega L - \frac{\omega C R_g^2}{1+(\omega C R_g)^2}\right]^2}.
\end{aligned} \tag{19}$$

Let us equate to zero the imaginary component of Eq. (19) and determine resonant frequency f_{res}, which is described by the formula:

$$\begin{aligned}
&\omega^4\left[R_g^4(B)C^3L^2\right] + \\
&+\omega^2\left[C^3R_g^4(B)R_L^2 + CR_g^2(B)L^2 - R_g^4(B)C^2L\right] + \\
&+\left[CR_g^2(B)R_L^2 - R_g^2(B)L\right] = 0
\end{aligned} \tag{20}$$

The solution to equation (20) is the expression:

$$f_{res} = \frac{1}{2\pi}\sqrt{\frac{C^3R_g^4(B){R_L}^2 + CR_g^2(B)L^2 - R_g^4(B)C^2L + A}{2C^3R_g^4(B)L^2}} \tag{21}$$

where:

$$\begin{aligned}
A = sqrt&\Big[\left(C^3R_g^4(B){R_L}^2 + CR_g^2(B)L^2 - R_g^4(B)C^2L\right)^2 - \\
&-4C^3R_g^4(B)L^2\left(CR_g^2(B){R_L}^2 - R_g^2(B)L\right)\Big]
\end{aligned}$$

3. Experimental research

When a magnetic field is applied to a tunnel-resonant diode, in the direction parallel to the current, a change in the energy of the electrons tunneling through potential barriers occurs, leading to a change in the current through the device. The change in current causes a change in the negative differential resistance, which in turn uniquely changes the resonant frequency. The change in the intrinsic capacitance and inductance of the diode is four orders of magnitude less in relation to the values of the external capacitance and inductance, therefore, their effect on the resonant frequency can be ignored [20, 25].

Fig. 5 shows the theoretical and experimental dependences of the resonant frequency, that is, the sensor conversion function on the action of the magnetic field. As can be seen from Fig. 5, the conversion function increases with an increase in the magnetic field induction while maintaining a constant sensor supply voltage. This is due to the fact that the main contribution to the frequency change is made by the component of the change in the electron energy according to the law $\left(N+\frac{1}{2}\right)h\omega_c$, that is, the energies of the cyclotron orbitals of electron motion.

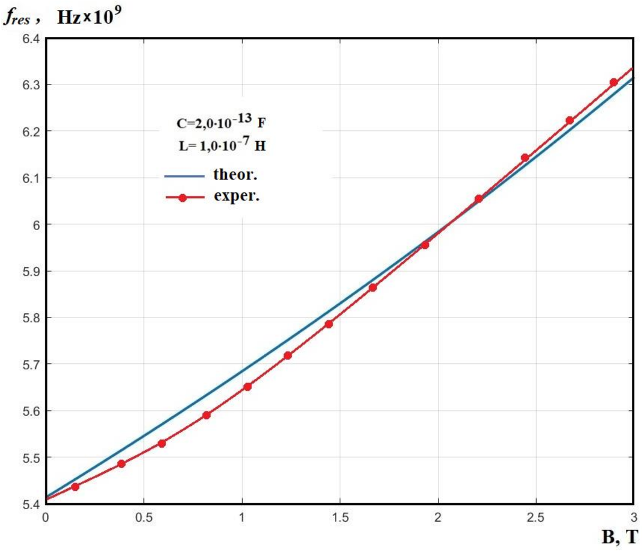

Fig. 5. Theoretical and experimental dependence of the sensor conversion function on the action of the magnetic field

The sensitivity of the magnetic field sensor is determined by the first derivative of the conversion function with respect to magnetic induction, that is, equal to the ratio kHz/mT. Fig. 6 shows the theoretical dependence of the sensor sensitivity function on the action of the magnetic field, its analytical expression is a complex expression and is described by the equation:

$$
\begin{aligned}
S_B = 0.0562687 \cdot \Bigg(& \frac{1}{C^3 R_g^3(B) R_L{}^2} \Bigg(4C^3 R_g^3(B) R_L{}^2 \left(\frac{\partial R_g(B)}{\partial B} \right) + \\
& + 2C R_g(B) L^2 \left(\frac{\partial R_g(B)}{\partial B} \right) - 4 R_g^3(B) C^2 L \left(\frac{\partial R_g(B)}{\partial B} \right) + \\
& + \frac{1}{2} \Big(2 \left(C^3 R_g^4(B) R_L{}^2 + C R_g^2(B) L^2 - R_g^4(B) C^2 L \right) \times \\
& \times \Bigg(4C^3 R_g^3(B) R_L{}^2 \left(\frac{\partial R_g(B)}{\partial B} \right) + 2C R_g(B) L^2 \left(\frac{\partial R_g(B)}{\partial B} \right) - \\
& - 4 R_g^3(B) C^2 L \left(\frac{\partial R_g(B)}{\partial B} \right) \Bigg) - 16 C^3 R_g^3(B) L^2 \times \\
& \times \left(C R_g^2(B) R_L^2 - R_g^2(B) L \right) \left(\frac{\partial R_g(B)}{\partial B} \right) - 4C^3 R_g^4(B) L^2 \times \\
& \times \Bigg(2C R_g(B) R_L{}^2 \left(\frac{\partial R_g(B)}{\partial B} \right) - 2 R_g(B) L \left(\frac{\partial R_g(B)}{\partial B} \right) \Bigg) \Big) \Bigg) \Bigg/ A \Bigg) - \\
& - \frac{1}{C^3 R_g^5(B) L^2} \Big(4 \Big(C^3 R_g^4(B) R_L{}^2 + C R_g^2(B) L^2 - R_g^4(B) C^2 L \times A \times \\
& \times \left(\frac{\partial R_g(B)}{\partial B} \right) \Big) \Big) \Bigg) \Bigg/ \sqrt{\frac{C^3 R_g^4(B) R_L{}^2 + C R_g^2(B) L^2 - R_g^4(B) C^2 L + A}{C^3 R_g^4(B) L^2}}
\end{aligned}
\tag{22}
$$

As can be seen from the graph (Fig. 6), the sensitivity value varies from 250 kHz/mT to 300 kHz/mT, the optimal area, when the change in the sensitivity function is only 10 kHz/mT, is the range of magnetic field induction change from 1 T to 3 T. The complex nature of the behavior of the sensitivity function on the magnetic field is explained by the complex dependence of the sensor conversion function on the change in negative differential resistance when a magnetic field is applied.

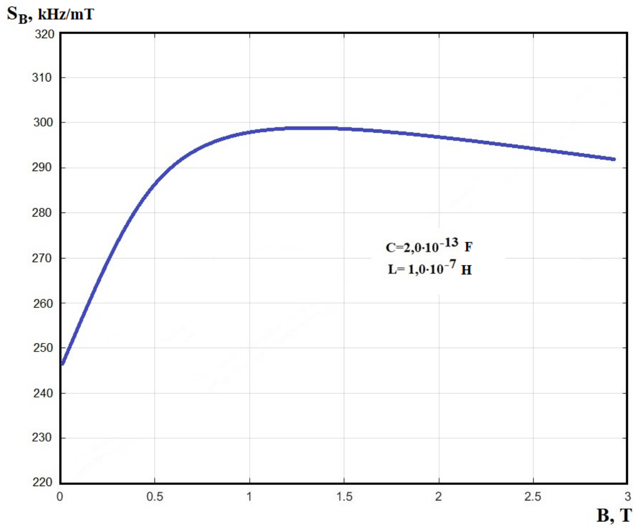

Fig. 6. Dependence of the sensitivity of the sensor on the action of the magnetic field

4. Conclusions

1) A mathematical model of a magnetic field sensor has been developed, with which the analytical dependences of the conversion and sensitivity functions are determined. It is shown that the main contribution to the conversion function is made by the change in the energy of electrons during their motion in cyclotron orbitals under the influence of a magnetic field. It changes the negative differential resistance, which in turn changes the output frequency of the magnetic sensor. The sensitivity of the magnetic field sensor varies from 250 kHz/mT to 300 kHz/mT in the range of magnetic field induction from zero to 3 Tesla. In this case, the output frequency varied from $5.4 \cdot 10^9$ Hz to $6.3 \cdot 10^9$ Hz.
2) Based on the consideration of physical processes in a tunnel-resonant diode under the influence of a magnetic field, it is proposed to design magnetic field sensors with a frequency output signal. These sensors have significant advantages over analog magnetic field sensors. Their advantages are the ability to operate in the microwave range, increasing the microminiaturization of the sensor down to the nanoscale, the ability to measure magnetic induction from tens of millitesla to tens of tesla with wireless transmission of the measured information over a distance.

References

[1] Awan J. T.: Optical and Transport of pin GaAs-AlAs resonant tunneling diode. UFS Car 2014.
[2] Azarov O. D., Garnaga V. A.: Push-pull DC amplifiers for multi-bit converters of self-calibrating information. Universum, Vinnytsia 2011
[3] Azarov O. D., Krupelnytsky L. V.: Analog-digital devices of self-correcting systems for measurement and processing of low-frequency signals. Universum, Vinnytsia 2005.
[4] Azarov O. D., Teplitsky M. Yu., Bilichenko N. O.: High-speed push-pull DC amplifiers with balanced feedback. VNTU, Vinnytsia 2016.
[5] Borisenko V. E. et al.: Nanoelectronics: theory and practice textbook. Binom. Knowledge Laboratory, Moscow 2013.
[6] Chand L. L., Esaki L., Tsu R.: Resonant tunneling in semiconductor double barriers. Appl. Phys. Lett. 24, 1974, 593–595.
[7] Esaki L., Tsu R.: Superlattics and negative differential conductivity in semiconductors. IBM J. Res. Develop. 14/1970, 61–65.
[8] Gotra S.Yu.: Microelectronic sensors of physical quantities. League – press, Lviv 2020.

[9] Halimatus S., Warsuzarina M., Nabihah A., Jabbar M.: Resonant Tunneling Diode Design for Oscillator Circuit. International Postgraduate Conference – Physics, 2017, 1–8.
[10] Huber J. L.: Physics of Novel InAs / AlSb / GaSb Resonant Interband Tunneling Structures. A Dissertation in Candidacy for the Degree of Doctor of Philosophy. Yale University, USA 1997.
[11] Karandakov G. V., Kryvenko V. I.: Electrical engineering, electronics and microprocessor technology. NTU, Kyiv 2008.
[12] Martinez-Duart J. M. et al.: Nanotechnology for micro- and optoelectronics. Technosphere, Moscow 2009.
[13] McCarthy M., Collins A.: Switches and Multiplexers. Analog Dialogue 31(3), 1997, 20–22.
[14] Meizda F.: Electronic measuring instruments and measurement methods. Mir, Moscow 1990.
[15] Osadchuk I. A., Osadchuk A. V., Osadchuk V. S., Semenov A. O.: Nanoelectronic Pressure Transducer with a Frequency Output Based on a Resonance Tunnel Diode. 2020 IEEE 15th International Conference on Advanced Trends in Radioelectronics, Telecommunications and Computer Engineering (TCSET), Lviv-Slavske, Ukraine 2020, 452–457, [http://doi.org/10.1109/TCSET49122.2020.235474].
[16] Osadchuk V. S., Osadchuk A. V.: Radiomeasuring Microelectronic Transducers of Physical Quantities. Proceedings of the 2015 International Siberian Conference on Control and Communications (SIBCON), Omsk 2015 [http://doi.org/10.1109/SIBCON.2015.7147167].
[17] Osadchuk V. S., Osadchuk A. V., Osadchuk I. A.: Microelectronic pressure transducer with frequency output based on tunnel resonance diode. Bulletin of Khmelnytsky National University – Technical science 1, 2015, 97–101.
[18] Osadchuk V. S., Osadchuk A. V.: The Microelectronic Radiomeasuring Transducers of Magnetic Field with a Frequency Output. Elektronika ir Elektrotechnika 4, 2011, 67–70 [http://doi.org/10.5755/j01.eee.110.4.289].
[19] Osadchuk V.S., Osadchuk A.V.: Microelectronic sensors of magnetic field with frequency output. Universum, Vinnitsa 2013.
[20] Romanyuk N. et al.: Microfacet distribution function for physically based bidirectional reflectance distribution functions. Proc. SPIE 8698, 86980L [http://doi.org/10.1117/12.2019338].
[21] Sun J. P., Haddad G. J. et al.: Resonant Tunneling Diodes: Models and Properties. Proceedings of The IEEE 86(4), 1998, 641–661.
[22] Sze S. M., Kwok K. Ng.: Physics of Semiconductor Devices. Wiley-Interscience 2007.
[23] Tsu R., Esaki L.: Tunneling in a finite superlattice. Appl. Phys. Lett. 22, 1973, 562–564.
[24] Vasilevskyi O. M., Yakovlev M. Y., Kulakov P. I.: Spectral method to evaluate the uncertainty of dynamic measurements. Technical Electrodynamics 4, 2017, 72–78.
[25] Vasilevskyi O. M.: Methods of determining the recalibration interval measurement tools based on the concept of uncertainty. Technical Electrodynamics 6, 2014, 81–88.

Prof. Alexander Osadchuk
e-mail: osadchuk.av69@gmail.com

Doctor of Technical Sciences, Professor, Head of the Department Radio Engineering of Vinnitsa National Technical University, Academician of the Academy Metrology Ukraine. Author of over 850 publications, including 30 monographs, 15 textbooks, 280 patents for inventions in Ukraine and the Russian Federation, more than 500 scientific articles in professional journals, of which 56 are in the scientometric databases Scopus and Web of Science.

https://orcid.org/0000-0001-6662-9141

Prof. Vladimir Osadchuk
e-mail: osadchuk.vs38@gmail.com

Doctor of Technical Sciences, Professor, Professor of the Department Radio Engineering of Vinnitsa National Technical University, Honored Worker of Science and Technology of Ukraine, Academician of the Academy of Engineering Sciences of Ukraine. Author of more than 900 publications, including 22 monographs, 14 textbooks, more than 350 copyright certificates and patents for inventions and more than 550 scientific articles in professional journals, of which 35 are in scientometric databases Scopus and Web of Science.

https://orcid.org/0000-0002-3142-3642

Associate Professor Iaroslav Osadchuk
e-mail: osadchuk.j93l@gmail.com

Candidate of Technical Sciences, Associate Professor of the Department Radio Engineering, Vinnytsia National Technical University. Author of more than 150 publications, including 4 monographs, 50 patents for inventions and more than 100 scientific articles in professional journals, of which 19 are in scientometric databases Scopus and Web of Science.

https://orcid.org/0000-0002-5472-0797

otrzymano/received: 08.10.2020 *przyjęto do druku/accepted: 10.12.2020*

http://doi.org/10.35784/iapgos.2374

DIGITAL CONTACT POTENTIAL PROBE IN STUDYING THE DEFORMATION OF DIELECTRIC MATERIALS

Kanstantsin Pantsialeyeu, Anatoly Zharin, Oleg Gusev, Roman Vorobey, Andrey Tyavlovsky, Konstantin Tyavlovsky, Aliaksandr Svistun
Belarusian National Technical University, Instrumentation Engineering Faculty, Minsk, Belarus

Abstract. *The paper reviews the results of a study on the surface electrostatic charges of dielectrics obtained using the contact potential difference (CPD) technique. Initially, the CPD technique was only applied to the study of metal and semiconductor surfaces. The conventional CPD measurement technique requires full compensation of the measured potential that, in the case of dielectrics, could reach very high values. Such high potentials are hard to compensate. Therefore, the conventional CPD method is rarely applied in the study of dielectric materials. Some important improvements recently made to the CPD measurement technique removed the need for compensation. The new method, which does not require compensation, has been implemented in the form of a digital Kelvin probe. The paper describes the principles of the non-compensation CPD measurement technique which was developed for mapping the electrostatic surface charge space distribution across a wide range of potential values. The study was performed on polymers such as low-density polyethylene (LDPE) and polytetrafluoroethylene (PTFE).*

Keywords: surface charge distribution, contact potential difference, Scanning Kelvin Probe, dielectrics materials

MIERNIK CYFROWY DO POMIARÓW KONTAKTOWEJ RÓŻNICY POTENCJAŁÓW PRZEZNACZONY DO KONTROLI DEFORMACJI MATERIAŁÓW DIELEKTRYCZNYCH

Streszczenie. *W artykule przedstawiono wyniki badań rozkładu wymuszonych ładunków na powierzchni dielektryków metodą kontaktowej różnicy potencjałów (angl. CPD). Wcześniej metoda CPD była stosowana jedynie do badań powierzchni metali lub półprzewodników. Trudności stosowania metody CPD w stosunku do dielektryków wynikają z konieczności całkowitej kompensacji potencjału powierzchniowego, wartość którego może być wysoka. W praktyce taka kompensacja może być utrudniona. W związku z tym metoda CPD nie jest stosowana do badań dielektryków. Ostatnio do techniki pomiarów metodą CPD wprowadzono szereg udoskonaleń, które wyeliminowały konieczność całkowitej kompensacji mierzonych wartości. Nowa metoda, która nie wymaga kompensacji, została zrealizowana w postaci cyfrowej sondy Kelvina. W artykule przeanalizowano zasady działania sondy nie wymagającej kompensacji oraz jej zastosowanie do określenia rozkładu ładunku na powierzchni dielektryków w szerokim zakresie wartości potencjału. Badania przeprowadzono na materiałach polimerowych, takich jak polietylen o małej gęstości (LDPE) i politetrafluoroetylen (PTFE).*

Słowa kluczowe: rozkład ładunku powierzchniowego, kontaktowa różnica potencjałów, skanująca sonda Kelvina, materiały dielektryczne

Introduction

The generation of static charges in polymer materials under deformation is usually referred to in textbooks as the electroelastic effect [4]. Francis Aston showed interest to this effect in 1901. He used a capacitor made of two brass plates between which rubber was placed. Aston observed a sharp deviation of the quadrant electrometer mirror when the capacitor was loaded. Aston suggested that the resulting charge is associated with the polarization of the dielectric under deformation. Later, Brain, in 1923, explained this effect by piezoelectricity [2].

Significant theoretical interest in the electroelastic effect re-emerged in 1960. The authors of [5] suggested three mechanisms of dielectric (in particular, rubber) charging during the deformation: 1) the appearance of charges of one sign on the specimens; 2) the appearance of charges of different signs on opposite sides; and 3) redistribution of surface charges without the formation of new ones. Subsequent experiments have shown that potentials on the electrometer arise only due to redistribution of charges. Similar experiments on polymers were carried out in 1972 [3], which showed effects similar to piezo effects.

Such studies have not lost their relevance at the present time. First, understanding of polymer charge mechanisms is of significant practical interest, for example, in manufacturing antistatic and insulating materials, fiber production, polymer recycling, etc. [7] Second, there is now a large arsenal of methods for the study of surface electrostatic potentials, and new methods are constantly being developed that can clarify the existing theoretical positions [7, 8, 14].

Currently, transmission electron microscopy (TEM), an atomic force microscope operating in Kelvin probe mode (KPFM), and electrostatic force microscopy (EFM) as well as a number of electrostatic capacitance probes are used to study the surface charge distribution on dielectrics. A special feature of these methods is the ability to measure only within a small local area of the surface. Surface examination of the specimens as a whole is not provided. The most promising method for non-contact and non-destructive measurement of surface electrostatic potential at micro- and macroscopic scales is the Scanning Kelvin Probe (SKP). Traditionally, this method is used to investigate the surface of metals and semiconductors [11–13, 15]. It determines the work function of the investigated metal surface by measuring the contact potential difference (CPD) between the sample's surface and the reference electrode. One should consider that the conventional CPD probe implements the neutral-zero method of measurements, i.e. it requires full compensation of the measured potential. In the case of dielectrics, this potential could reach very high values. Therefore, the Scanning Kelvin Probe (with micro and macro range resolution) is almost never used for the study of dielectrics materials, however some important improvements were made recently to the CPD measurement technique which eliminated the need for compensation. This technique is implemented in a Digital CPD Probe.

The research work presented in this paper was devoted to experimental studies of the spatial distribution of the surface electrostatic potential on polymers under mechanical stress conditions using the newly developed Digital Kelvin probe.

1. Measurement technique and research device

The Kelvin probe technique takes its name from William Thomson (Lord Kelvin), who first introduced it in 1898 [6]. Kelvin used a parallel capacitor of Zinc and Copper plates to explain the Alessandro Volta experiments and to study the charge transfer upon electrical contact. His study implemented a zero CPD measurement method.

In 1932, William Zisman introduced a new method to measure the CPD. He mounted a vibrating reference electrode above a surface of a sample under study [21]. The output voltage varied periodically as the reference electrode vibrated, and the peak-to-peak voltage depended on the difference between the CPD and the external bias voltage. Hence the vibrating capacitor that serves as the basis for the conventional CPD probe. This method is completely non-contact and non-destructive for samples [17–20]. In modern measuring systems, the bias voltage is generated automatically by means of special tracking systems [1]. Such tracking systems include phase- or amplitude-sensitive detectors (Lock-in) and integrators. The operating principle of the conventional CPD probe is explained in the Fig. 1 [9].

The conventional CPD measurement technique requires full compensation of the measured potential which, in the case of dielectrics, could reach very high values. Therefore, the conventional CPD technique is almost never used for the study of dielectrics materials. Recent improvements to the CPD measurement technique made by the authors eliminate the need for compensation. The non-compensation (or indirect) measurement technique is implemented in the Digital CPD Probe. Fig. 2 shows the structural scheme of the Digital CPD Probe [10].

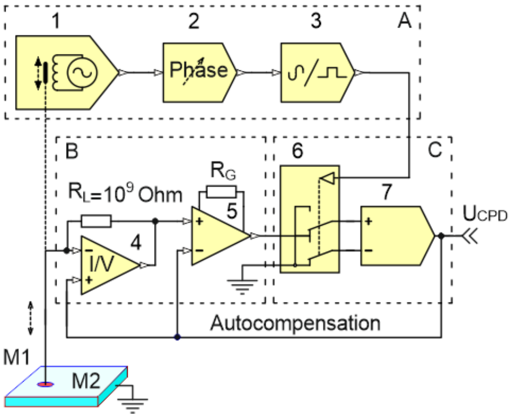

Fig. 1. Basic structure of the conventional CPD Probe: M1, M2 – surfaces of the vibrating reference electrode and sample, respectively; A – modulator (1 – vibrator, 2 – phase shifter, 3 –converter); B – preamplifier (4 – current-to-voltage converter; 5 – instrumentation amplifier); C – phase detector-integrator (Lock-In, 6 – switch, 7 – integrator); U_{CPD} – contact potential difference signal [9]

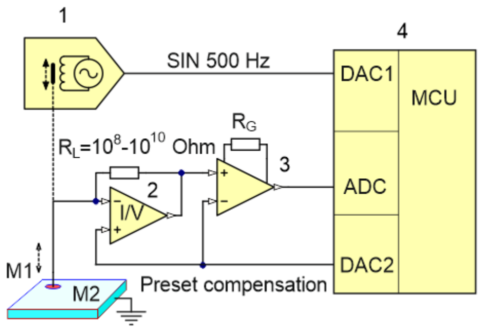

Fig. 2. Basic structure of the Digital CPD Probe: M1 and M2 – surfaces of the vibrating reference electrode and sample, respectively; 1 – modulator consisting of a piezoelectric plate and driver; 2 – current-to-voltage converter; 3 – instrumentation amplifier; 4 – ARM Cortex-M4 microcontroller (MCU) [10]

The Digital CPD Probe is based on an ARM Cortex-M4 microcontroller (MCU). The measuring cycle consists of at least two successive determinations of the output signal amplitude at established values of compensation voltage. The CPD value is determined by interpolating a linear relationship obtained from at least two points (Fig. 3). This approach provides for operation of the Digital CPD Probe in high signal mode with a high signal-to-noise ratio.

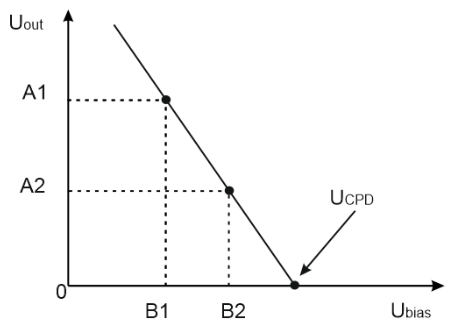

Fig. 3. Principle of Digital CPD Probe basic measuring mode

The MCU generates the compensation voltage and harmonic signal for the probe oscillations via special drivers. This solution synchronizes the oscillations and the readings of the measuring signals at appropriate compensation voltages. the measurement data array is processed using the digital signal processing (DSP) algorithms of the MCU in real-time. The DSP algorithms are mostly used to determine the amplitude of the signal, which in turn is used to calculate the CPD. The additional goal of the DSP is to improve the signal quality (using filters, spectral line detection or fast Fourier transform). In the digital CPD probe, phase detection and integration of the output signal for automatic compensation of the measured value is not necessary. This significantly reduces the measurement time and errors of feedback loop and digital-to-analog conversion [16].

Fig. 4 shows the operating mode of the Digital CPD Probe for electrostatic potential measurement. The fixed compensation voltages (B1 and B2) are selected from outside the range of possible CPD values. This allows for CPD measurements over a wide range, up to hundreds of volts. In this case, the CPU generates compensation potentials which do not exceed ±10 Volts. The CPD value (U_{CPD}) is determined by formula (1):

$$U_{CPD} = -\frac{B_1 \cdot A_2 + B_2 \cdot A_1}{A_1 - A_2} \qquad (1)$$

where A_1 and A_2 – amplitude of the alternating signal at the corresponding preset compensation potentials B_1 and B_2.

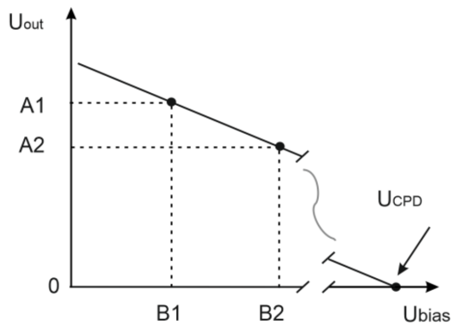

Fig. 4. Measuring operation mode of the Digital CPD Probe for high electrostatic potentials (up to several hundred volts)

The study of the spatial distribution of the surface electrostatic potential was carried out with a developed measuring system that implements a Scanning Kelvin Probe. The main technical characteristics of the developed Scanning system are given in Table 1.

Table 1. Main technical characteristics of the Scanning system

Parameters	Characteristics
Main controlled parameter	Electrostatic potential
Electrostatic potential probe	Digital Kelvin–Zisman contact potential difference probe
Diameter of the electrostatic potential probe, mm	1
Error of surface potential measurement, mV	±2
Positioning system	3 axis
Positioning accuracy, µm	±5
Spatial resolution, µm	10
Scanning area, mm	200 × 200
Mapping points	100 to 100,000

2. Results and discussion

The response of the surface electrostatic potential of polymer materials to external mechanical action was found earlier in [8]. This study used matrix high-pressure polyethylene (LDPE) 12203-250 grade as samples. The registered deviations of the surface electrostatic potential (similar to Fig. 5b) were caused by the action of a vacuum clamp that was used to fix the specimens on the object table of the scanning system. We could not estimate the pressure with which the vacuum clamp acts on the specimens. This pressure was not quantitatively estimated as it was not significant from the point of view of any mechanical properties of the material, but it turned to be significant for its charge distribution. To assess this, additional measurements were taken.

From Fig. 5, one can see that the electrostatic potential is distributed relatively uniformly over the surface when the vacuum clamp is turned off. After turning on the clamp, we observe a redistribution of the surface electrostatic potential in the clamping area. Further, we see the process of relaxation and a decrease in residual stresses (the clamp off). The homogeneity of the electrostatic potential distribution was completely restored after 14 hours.

Measurements performed on the composite polymers (LDPE +6% carbon nanomaterial and LDPE +3% nano-sized silica) showed similar results. But it was not possible to register any changes in the distribution of the surface electrostatic potential on samples with a combined filler (LDPE + carbon nanotubes + carbon nanomaterial + nano-sized silica with different mass ratios). The obtained results allow for some conclusions concerning the effect of the combined filler on the mechanical properties of the material. This effect correlates well with a known statement that carbon-filled composite materials or materials with carbon nanotubes have a high resistance to static or cyclic mechanical stress.

To evaluate the capabilities of the Digital CPD probe in studying the stress-strain state of dielectric materials, a system for mechanical stretching of specimens was built. The system was integrated with a scanning system for electrostatic potentials. This made it possible to obtain the distribution of the electrostatic potential maps in the course of loading.

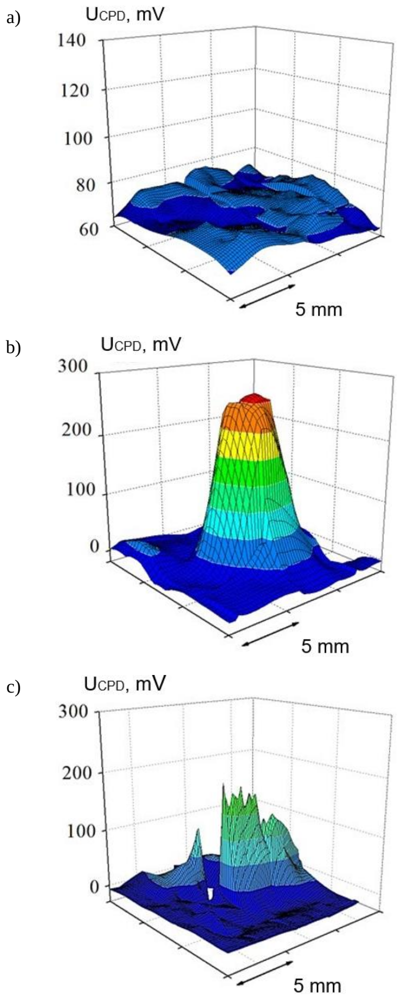

Fig. 5. Electrostatic potential distribution maps of low-density polyethylene (LDPE) with a short-term application of mechanical load: a) before loading; b) after loading; c) in the course of relaxation (up to 4 hours after loading

Fig. 6 shows the surface electrostatic potential distribution maps of samples after the mechanical tensile load. The samples under study were made of Polytetrafluoroethylene (PTFE) F4. These samples were loaded with a 1 kgf step and scanned for the surface electrostatic potential. The loading led to electrostatic potential heterogeneity with sharp extremes propagating from the center of the deformed area of the material outwards. This area and the surface relative potential increase with increasing load. Under further loading, the potential reaches saturation.

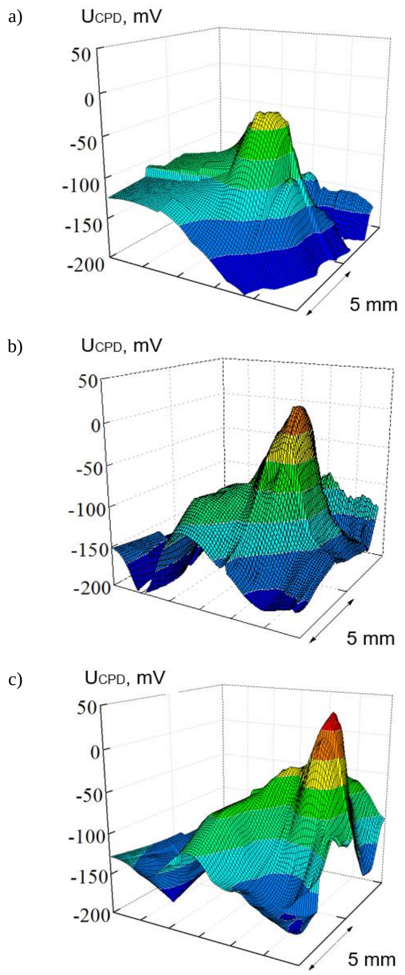

Fig. 6. Electrostatic potential distribution maps of low-density polyethylene (LDPE) with a short-term application of mechanical load: a) before loading; b) after loading; c) in the course of relaxation (up to 4 hours after loading)

3. Conclusion

The paper describes the principle of the Non-compensation (or indirect) CPD measurement technique, which was developed for mapping the spatial distribution of electrostatic surface charge in a wide range of permissible values. The indirect measurement technique is implemented in the Digital CPD Probe. The obtained results include the identification of promising opportunities for the CPD technique, and in particular, application of the Digital CPD Probe for studying charged dielectrics. In scanning mode, this technique can be applied both to study the surface electrostatic potential (charge) distribution and to study its redistribution from the load, including in vitro study. The research shows that the surface electrostatic potential for some dielectric materials and polymer composites is a highly sensitive parameter to changes in the stress-strain state. Therefore, the considered measuring technique can be applied to the non-contact and non-destructive detection of deformation dispositions, control of residual stresses, relaxation and other parameters of the dielectric materials in the stress-strain state, and also to the study of their mechanisms.

References

[1] Baumgartner H.: New method for the distance control of a scanning Kelvin microscope. Measurement science & technology 2(3), 1992, 237–238.
[2] Brain K. R.: Investigations of piezo-electric effects with dielectrics. Proceedings of the Physical Society of London 36(1), 1923.
[3] Broadhurst M. G., Malmberg C. G., Mopsik F. I., Harris W. P.: Piezo- and pyro-electricity in polymer electrets. Conference on Electrical Insulation & Dielectric Phenomena. Annual Report, 1972 [http://doi.org/10.1109/ceidp.1972.7734193].
[4] Davies D. K.: Charge generation on dielectric surfaces. Journal of Physics D: Applied Physics 2(11), 1969, 1533–1537 [http://doi.org/10.1088/0022-3727/2/11/307].
[5] Dogadkin B. A., Gul V. E., Morozova N. A.: The Effect of Electric Charges Formed during Repeated Deformations on the Fatigue Resistance of Vulcanizates. Rubber Chemistry and Technology 33(4), 1960 [http://doi.org/10.5254/1.3542237].
[6] Kelvin L.: Contact electricity of metals. Philosophical Magazine (series 5) 46(278), 1898, 82–120 [http://doi.org/10.1080/14786449808621172].
[7] Lei Zhang, Zhiwei Chen, Jiale Mao, Shuang Wang, Yiting Zheng: Quantitative evaluation of inclusion homogeneity in composites and the applications (Review Article). Journal of Materials Research and Technology 9(3), 2020 [http://doi.org/10.1016/j.jmrt.2020.01.067].
[8] Pantsialeyeu K. U., Krautsevich A. U., Rovba I. A., Lysenko V. I., Vorobey R. I., Gusev O. K., Zharin A. L.: Analysis of the electrophysical and photoelectric properties of nanocomposite polymers by the modified Kelvin probe. Devices and Methods of Measurements 8(4), 2017, 386–397 (in russian) [http://doi.org/10.21122/2220-9506-2017-8-4-55-62].
[9] Pantsialeyeu K., Mikitsevich U., Zharin A.: Design of the contact potentials difference probes. Devices and Methods of Measurements 7(1), 2016, 7–15 (in russian) [http://doi.org/10.21122/2220-9506-2016-7-1-7-15].
[10] Pantsialeyeu K., Svistun A., Tyavlovsky A., Zharin A.: Digital contact potential difference probe. Devices and Methods of Measurements 7(2), 2016, 136–144 (in russian) [http://doi.org/10.21122/2220-9506-2016-7-2-136-144].
[11] Pantsialeyeu K., Svistun A., Zharin A.: Methods for local changes in the plastic deformation diagnostics on the work function. Devices and Methods of Measurements 10(1), 2015, 56–63.
[12] Pilipenko V., Solodukha V., Zharin A., Gusev O., Vorobey R., Pantsialeyeu K., Tyavlovsky A., Tyavlovsky K., Bondariev V.: Influence of rapid thermal treatment of initial silicon wafers on the electrophysical properties of silicon dioxide obtained by pyrogenous oxidation. High Temperature Material Processes: An International Quarterly of High-Technology Plasma Processes 23(3), 2019, 283–290 [http://doi.org/10.1615/HighTempMatProc.2019031122].
[13] Qin W. G., Shaw D. A.: Theoretical model on surface electronic behaviour: strain effect. Phys. B: Condensed Matter 6(16), 2009, 2247–2250.
[14] Sviridenok A., Zharin A., Krautsevich A., Tyavlovsky A.: The effect of high-dispersion fillers on adhesive and frictional properties of ethylene-vinyl acetate copolymer. Journal of Friction and Wear 35, 2014, 255–262.
[15] Sykes J. M., Doherty M.: Interpretation of Scanning Kelvin Probe potential maps for coated steel using semi-quantitative current density maps. Corrosion Science 50, 2008, 2773–2778 [http://doi.org/10.1016/j.corsci.2008.07.023].
[16] Tyavlovsky A. K., Zharin A. L., Gusev O. K., Kierczynski K.: Kelvin Probe error compensation based on harmonic analysis of measurement signal. Przeglad Elektrotechniczny 90, 2014, 251–254.
[17] Vorobey R. I. Gusev O. K. Tyavlovsky A. K., Svistun A. I., Shadurskaja L., Yarzhembiyskaja N., Kerczynski K.: Controlling the characteristics of photovoltaic cell based on their own semiconductors. Przeglad Elektrotechniczny 91(8), 2015, 81–85 [http://doi.org/10.15199/48.2015.08.21].
[18] Wicinski M., Burgstaller W., Hassel A. W.: Lateral resolution in scanning Kelvin probe microscopy. Corrosion Science 104, 2016, 1–8 [http://doi.org/10.1016/j.corsci.2015.09.008].
[19] Zharin A., Pantsialeyeu K., Kierczyński K.: Charge sensitive techniques in control of the homogeneity of optical metallic surfaces. Przegląd Elektrotechniczny 92(8), 2016, 190–193 [http://doi.org/10.15199/48.2016.08.52].
[20] Zharin A., Pantsialeyeu K., Opielak M., Rogalski P.: Charge sensitive techniques in tribology studies. Przegląd Elektrotechniczny 92(11), 2016, 239–243 [http://doi.org/10.15199 / 48.2016.11.58].
[21] Zisman W.: A new method of measuring contact potential differences in metals. Review of Scientific Instruments 3(7), 1932, 367–370 [http://doi.org/10.1063/1.1748947].

Ph.D. Kanstantsin Pantsialeyeu
e-mail: k.pantsialeyeu@bntu.by

Ph.D., Associate Professor of the Department of Information Measuring Devices and Technologies of Belarusian National Technical University. Fields of research: Charge sensitive methods for detecting mechanical effects on the surface of friction materials.

http://orcid.org/0000-0001-7113-1815

Prof. Anatoly Zharin
e-mail: zharin@bntu.by

Doctor of technical sciences, professor of the Department of Information Measuring Devices and Technologies of Belarusian National Technical University. Fields of research: modern electronics and computer technology; experimental physics; solid state physics; tribology; composite materials.

http://orcid.org/0000-0001-7213-4532

Prof. Oleg Gusev
e-mail: gusev@bntu.by

Doctor of technical sciences, Vice-Rector for Academic Activity of Belarusian National Technical University, professor of the Department of Information Measuring Devices and Technologies of Belarusian National Technical University. Fields of research: modern electronics and computer technology; experimental physics; solid state physics; semiconductor materials; optoelectronics.

http://orcid.org/0000-0001-5180-1121

Ph.D. Roman Vorobey
e-mail: vorobey@bntu.by

Ph.D., Associate Professor, Head of the Department of Information Measuring Devices and Technologies of Belarusian National Technical University. Fields of research: instrumentation engineering; metrology and information measuring devices and systems; semiconductor materials; optoelectronics.

http://orcid.org/0000-0003-2851-6108

Ph.D. Andrey Tyavlovsky
e-mail: tyavlovsky@bntu.by

Ph.D., Associate Professor of the Department of Information Measuring Devices and Technologies of Belarusian National Technical University. Fields of research: Probe electrometry and research parameters of precision surfaces based on the Kelvin-Zisman method.

http://orcid.org/0000-0003-2579-1016

Ph.D. Konstantin Tyavlovsky
e-mail: ktyavlovsky@bntu.by

Ph.D., Associate Professor of the Department of Information Measuring Devices and Technologies of Belarusian National Technical University. Fields of research: Probe electrometry and research parameters of precision surfaces based on the Kelvin-Zisman method; semiconductor materials; optoelectronics.

http://orcid.org/0000-0001-8020-0165

Ph.D. Aliaksandr Svistun
e-mail: aisvistun@bntu.by

Ph.D., Associate Professor, Head of the Instrumentation Engineering faculty of Belarusian National Technical University. Fields of research: Probe electrometry; metrological provision of multiparameter measurement of optical radiation.

http://orcid.org/0000-0002-9593-8880

otrzymano/received: 27.10.2020 *przyjęto do druku/accepted: 10.12.2020*

http://doi.org/10.35784/iapgos.2379

OVERVIEW OF AOI USE IN SURFACE-MOUNT TECHNOLOGY CONTROL

Magdalena Michalska
Lublin University of Technology, Department of Electronics and Information Technology, Lublin, Poland

Abstract. *Surface-mount technology is now widely used in the production of printed circuit boards in the electronics industry and has gained many supporters. The miniaturization of electronic components has forced the introduction of machines for visual inspection of assembly correctness, which is more accurate and faster than the human eye, magnifier or microscope. Automatic Optical Inspection (AOI) is a control process that detects defects and errors in the initial PCB manufacturing process. It has become an indispensable element of contract assembly, increasing the quality of services offered and production efficiency. It uses new designs of measuring heads, miniaturization of equipment, software processing the obtained images of boards, and complicated image transformation algorithms.*

Keywords: Automatic Optical Inspection, defect inspection, solder joints, surface-mount technology

PRZEGLĄD WYKORZYSTANIA AOI W PROCESIE KONTROLI MONTAŻU POWIERZCHNIOWEGO

Streszczenie. *Technologia montażu powierzchniowego jest obecnie szeroko stosowana w produkcji zespołów obwodów drukowanych w przemyśle elektronicznym. Zyskała ona bardzo wielu zwolenników. Miniaturyzacja komponentów elektronicznych wymusiła wprowadzenie maszyn wizualnej kontroli poprawności montażu, bardziej dokładnych i szybszych niż ludzkie oko, lupa czy mikroskop. Automatyczna Inspekcja Optyczna (AOI) to proces kontroli wykrywania wad i błędów w początkowym procesie produkcji obwodów drukowanych. Staje się nieodzownym elementem montażu kontraktowego, wpływając na zwiększenie jakości oferowanych usług i efektywności produkcji. Wykorzystywane są w niej nowe konstrukcje głowic pomiarowych, miniaturyzacja sprzętu, oprogramowanie przetwarzące otrzymane obrazy płytek, skomplikowane algorytmy przekształcania obrazu.*

Słowa kluczowe: Automatyczna kontrola optyczna, kontrola defektów, połączenia lutowane, technologia montażu powierzchniowego

Introduction

In many respects, surface mounting technology is assessed as better than through-hole mounting. The occurrence of defective products when using this technology is mainly due to technological problems, but sometimes it is also caused by management problems or human error [23]. Automatic Optical Inspection is used to control SMT [20]. It is here that any assembly errors are easily detected. The AOI device scans the printed circuits in terms of features characteristic of PCB surfaces [28].

1. Basics of AOI

Components used for surface-mount technology are characterized by small dimensions. They have flat housings and "flange" solder tips that engage the end of the housing. On the other hand, the soldering tips are of larger sizes [10]. Figure 1 shows some of the electronic components used in the production of PCBs. The components attach directly to the boards. When more elements are required on a smaller surface, the plate is printed on both sides. Connecting the leads takes place in a specially designed furnace.

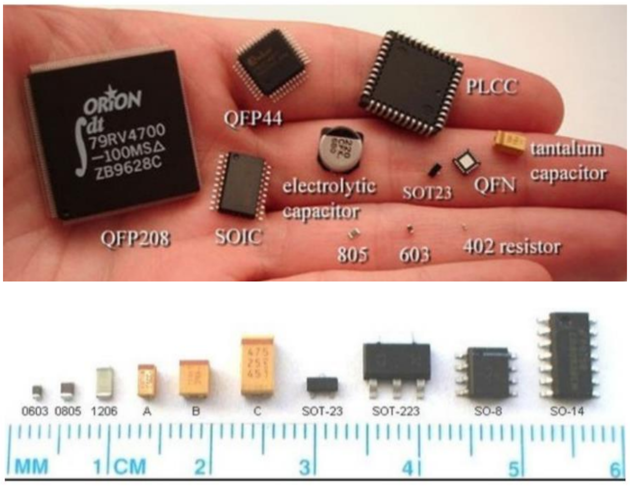

Fig. 1. Components used in PCB production using surface-mount technology [11]

The lack of reliability and repeatability of manual controls required a more thorough approach using automated systems. Equipment based on AOI tests such parameters as shape detection, and the presence of the required components. Top face coplanarity, component width, length, and height, angles, component polarity, component surface text, solder volume and height, bearing and solder deficit are checked. The height of the arms and the feet of the legs, and the short circuit between the solder joints are also tested.

2. Development of technical solutions

Today, many companies offer AOI equipment that provides comprehensive proof test coverage and minimizes false calls [29]. There are many design solutions available to provide the user with the best possible assistance in the quality control process in terms of the adopted budget [25]. The technological development of AOI-based equipment continues. The hardware development started with an inspection system using a two-dimensional machine to detect solder defects after brazing [32]. These include solder bridges and missing components. This could improve electronics productivity and create assembly lines. Further advances in surface mount technology created a need for more precise ways of controlling component placement and assessing soldering quality [33]. Initially, an inspection system based on two-dimensional vision defined the future direction of changes in plate quality control.

Automated optical 3D inspection systems provide a precise metrology system, eliminating shadows, image cropping and distortion, providing reliable data and high-resolution 3D visualization for even the most complex product geometries [34].

2.1. Hardware design

The passage of time and the desire to obtain an accurate method of welding boards forced the development of such equipment. As surface mount technology advances, greater defect detection is being introduced to the processes to meet stringent requirements. Efficiency and quality indicators are also important.

The most commonly used automated inspection methods are based on vision, infrared (IR) [31] and X-rays [14]. The constructed structures allowed for the detection of defects at the surface level, determination of the mass of solder present, and determination of linear and angular alignment. X-ray inspection was used to obtain pictures of the soldered joints.

There have even been online inspections of surface mount components using vision and infrared sensors [6]. The use of vision and infrared sensors allowed for the separation of solder joint defects. The vision sensor used in the construction provided information about defects at the surface level. On the other hand, the infrared sensor informed about a defect of solder paste. Diagonal and flat lighting techniques were used. 2D grayscale images of the plaques were obtained and further processed to uncover the corresponding defects. The limitations of the automated systems resulted from the range of the individual sensors in classification of the known defect range.

Paper [27] presents a technique of controlling the solder paste by means of directional LED lighting obtained from a camera mounted from the top. The use of lighting allows 2D images to be obtained. This is a quick method that shows the defects of a lack of solder. To better illustrate other defects, directional side lighting was used in the construction to obtain 2.5D images.

During the testing, a sequence of three images is collected. Image processing is then performed to detect geometric defects in the solder paste. The proposed method also detected other defects, previously invisible by using only light from above.

An example of a vision system was also presented in [4]. The upper vision module was mounted on a gantry that was attached to a movable cart. The location of the upper CMOS camera can be precisely adjusted along the Y and Z directions for positioning. The overhead vision module consisted of an ImagingSource DMK41BUC02, a metal oxide semi–con–ductor (CMOS) camera combined with a Moritex MML1-ST65 telecentric lens and a horizontal backlight illuminator – Figure 2a. As shown in Figure 2b, the side vision module consisted of a CMOS DMK41BUC02 imaging source camera (side CMOS camera) in combination with a Moritex MML1-ST65 telecentric lens, ring illuminator, and vertical illuminator. The ring illuminator was installed on the lens barrel. The illuminator was installed on the side plate of the module.

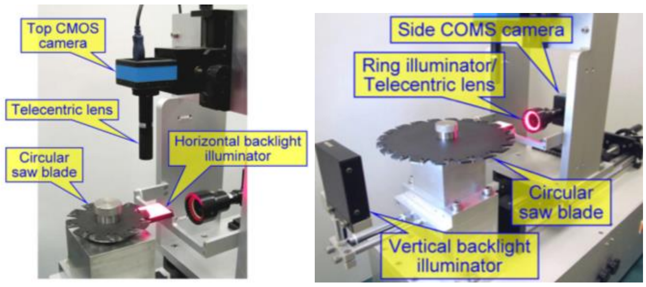

Fig. 2. The constructed AOI system: a) setup of the AOI system for radial runout inspection; b) setup of the AOI system for axial runout inspection [4]

In [24], an illuminator was used for the automatic optical inspection system. The structure of the designed illuminator consisted of three arrays of light emitting diodes (LEDs). The diodes used have different colors and radiation angles. The resulting new model of illuminator radiation and solder joint irradiance was tested, with promising results. The optimized dimensions of the illuminator, based on the irradiation intensity model, gave rise to a new research project.

Modern inspection systems provide comprehensive checks of the body of the element and the solder joint by combining a 2D texture with a 3D inspection. Additionally, they detect and prevent misplaced components. Figure 3 shows the components of the AOI measuring head. It includes: laser, high-resolution camera, telecentric optics, angular cameras, and LED lighting.

The device, equipped with many features, ensures efficient and reliable control. The design of the AOI equipment enables precise vision setup, although it is important to position individual boards. The ability to search for an element by name is useful for repairs, and it has an optimized user interface that signals both successful operation and errors via colors.

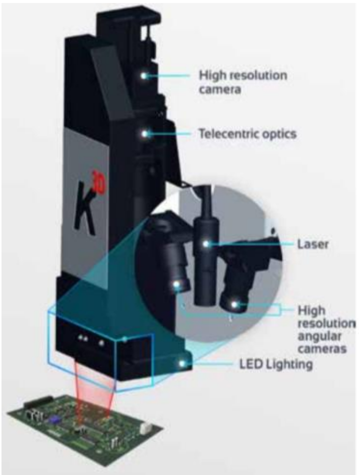

Fig. 3. Diagram of the AOI measuring head [12]

2.2. AOI systems

Fully integrated control of the tile production process would not be possible without the creation of software that allows you to measure its components. Even the best audit data requires intelligent information management. The software packages available on the market today provide a data source for solder paste inspection (SPI) and automatic optical inspection (AOI) data. Another important tool is the advanced image library tools with algorithmic help [8]. They contain industry-certified images in data libraries, so you can view the process in real time, and quickly drill down into the details in the picture and take corrective action. This saves time correlating databases, and more time getting to the root cause of the fault.

In [18], an optimal design of an automatic inspection system for processing light-emitting diode (LED) chips was discussed. The system is based on a support vector machine (SVM). To effectively design a defect classification system based on an SVM, many qualitative parameters need to be designed [2]. Figure 4 shows the procedure for using the system from [18]. It is based on two types of classification, experiment planning, component analysis, and defect classification result verification. The process enables micro-defect breakdown and quick classification, high accuracy and stability. It is applicable to high-precision LED detection, and can be used to accurately inspect mass production LEDs to effectively replace visual inspection, saving labor costs.

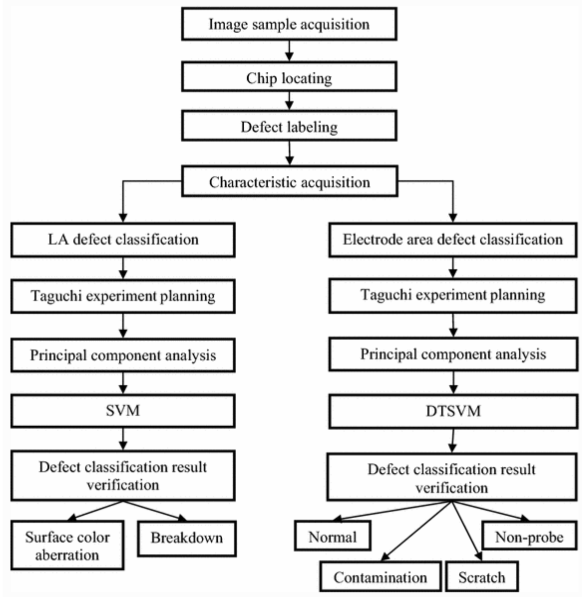

Fig. 4. Defect inspection system – flow chart [18]

Based on the development of the process of controlling micro-defects of the surface of LED chips, the application of an intelligent algorithm in industrial automation for the inspection and division of LED defects will be discussed. After image acquisition, chip localization and characteristic defect acquisition, planning of the image characteristic value and classifier design takes place (Taguchi method combined with PCA). An SVM is used to distinguish between surface color aberrations. A DTSVM helps to distinguish between normal, debris, scratch and missing probe. By comparing this against traditional DT, NN (Nearest Neighbour Algorithm) and LIBSVM (A Library for Support Vector Machines) [2], it has been verified that the established classifier has better accuracy and reliability for industrial automation control.

Equipment based on AOI tests such parameters as: shape detection, the presence of the required components, the coplanarity of the upper surface, the width, length, and height of the component, the angles, and the component polarity. It also checks the text on the component surface, the soldering volume and height, bearing and soldering deficit, the height of the arms and the feet of the legs, and a short circuit between soldering. The software ensuresmissed unmounted elements, skipping damaged boards, and parameterization of patterns [4].

Additionally, the import and export of pick & place files via the built-in converter is very functional [26]. The systems also provides the export of data supporting cost estimation, editing of component housings with the possibility of creating new types, and support for individual stages of work on the project. One of the latest features of inspection machines is that they can be networked to allow immediate feedback to the previous machine to enable automatic adjustments [22]. With the introduction of 3D technology, this process became more reliable; 3D inspection allows for more accurate measurements and provides a more stable inspection process [13].

The combination of software and stable production makes it possible to continuously improve the product in the production process. Human interaction will always be involved when solving technological problems. This is because product quality is related to the quality of the material, the product design and the manufacturing process [5]. Improving product quality affects people, machinery and materials. It is also important to implement a process-oriented overall quality control system.

2.3. Processing of images received by AOI

Many methods were used to process the images obtained with AOI. They include a number of automatic methods [16, 30] and integrated systems [1, 3, 21]. Article [7] discusses the quality control of inserts using one of these technologies: a component twist or pin defect. At the beginning of the development of the field, binarization techniques, torsional angle estimation methods and various techniques of morphological image processing were compared.

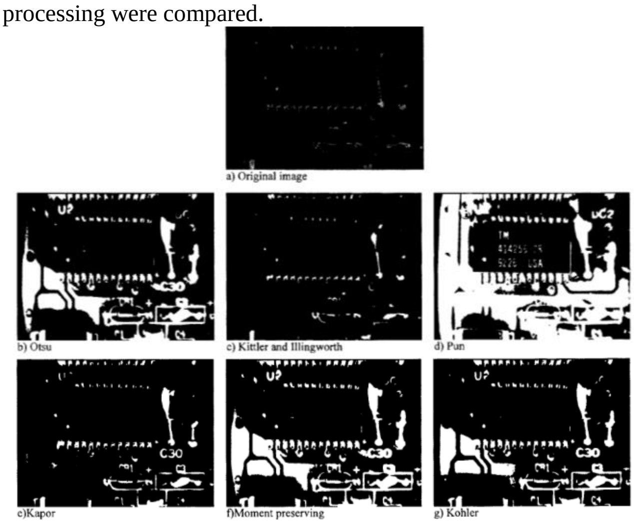

Fig. 5. Results of the thresholding methods [7]

Figure 5 shows the effects after thresholding the original image with different 6 methods. Pun and Otsu thresholding have been found to be beneficial for this particular application. Morphological methods provide robust tools for detecting missing pins and un-drilled washers.

A very important process is to assess the quality of small elements on the board surface. One of them is a light emitting diode (SMD-LED). Visual inspection may result in misdiagnosis due to different recognition standards. An automatic SMD-LED defect detection system was developed in [11]. Non-contact control and defect recognition standardization were used here. The developed software detects common and important defects of the elements of the LED package, including missing element, no chip, wire offset and foreign material [8]. The diagram of the procedure is presented in Figure 6. Image processing starts with ROI selection, then texture anomaly is detected by multi-scale adaptive Fourier analysis (MAFA). The segmentation threshold is selected based on the entropy information to successfully segment the weld line. Figure 7 shows the program window, where the user can choose from the ROI image and provide the selected element for analysis. The result proves that the proposed method can correctly and efficiently segment the defect, in comparison to phase transform (PHOT) and multi-scale phase transform (MPHOT), and can be used in other fields of texture anomaly detection. The overall recognition rate of this system is 98.25%.

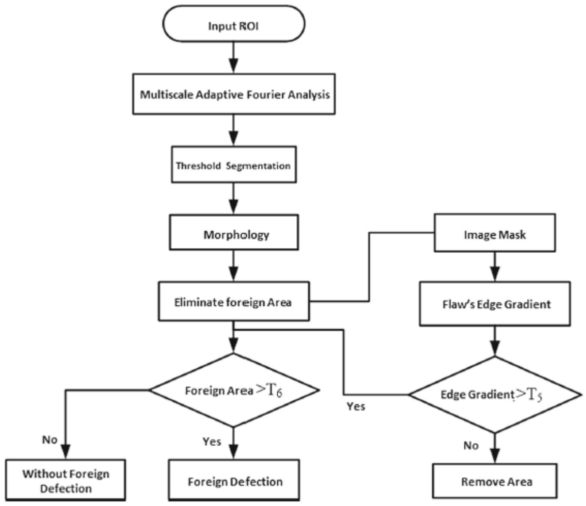

Fig. 6. Overall foreign material defect detection process from [8]

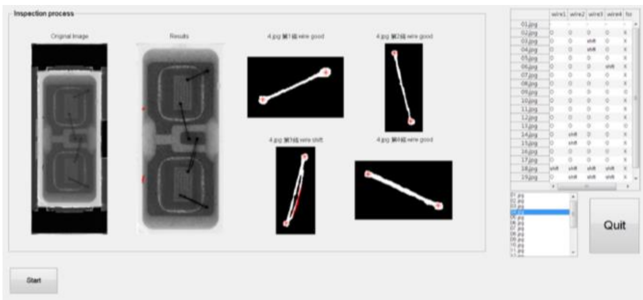

Fig. 7. View of program window from [8]

Article [9] presents an innovative approach to examining the defects of BGA components – the spherical grid system. These are high-density components with large-scale integration. The image transformation processes begin with adaptive thresholding in combination with a modified (ε, δ) segmentation of components. A grayscale image of the solder beads is obtained. The next step is to use the line-based grouping method to recognize the ball array. Due to the mentioned actions, the exact position and orientation of the BGA is obtained. The final step is to extract the ball element to diagnose any potential defects. The proposed procedure is satisfactory for most BGA systems with different spherical arrays.

3. Summary

The use of surface mounted devices (SMDs) creates the need to reduce costs while maintaining quality, reliability, process continuity and the possibility of their continuous modification. The complexity of the tests performed requires the continuous development of automated sequences used for quality control. However, for smaller productions, a combination of automatic optical inspection and electrical testing is used. The effectiveness of both of these activities is determined on the basis of the measurement accuracy and consistency of the measurements [19].

The advantages of surface-mount technology include automatization, miniaturization, high density of component placement, and the possibility of placing components on both sides of the printed circuit board. Low connection impedance improves properties at high frequencies. An additional advantage is the good mechanical properties under shock and vibration conditions resulting from the lower weight of the components. Surface mounting ensures quick assembly, the possibility of combining machines into a production line, and low production costs. All design, system and image processing solutions are part of the efforts to help increase the efficiency, quality and repeatability of plate inspection.

References

[1] Celik T., Tjahjadi T.: Contextual and variational contrast enhancement. IEEE Transactions on Image Processing 20(12), 2011, 3431–3441.
[2] Chang C. C., Lin C. J.: LIBSVM: A library for support vector machines. ACM Transactions on Intelligent Systems and Technology 2(3), 2011, 1–27.
[3] Chang K. H.: Development of optical inspection system for surface mount device light emitting diodes – master thesis. National Sun Yat-sen University, Taiwan 2012.
[4] Chang W., Su C., Guo D.: Automated optical inspection for the runout tolerance of circular saw blades. Int. J. Adv. Manuf. Technol. 66, 2013, 565–582.
[5] Colledani M., Tolio T.: Impact of Quality Control on Production System Performance. CIRP Annals - Manufacturing Technology 55(1), 2006, 453–456, [http://doi.org/10.1016/S0007-8506(07)60457-0].
[6] Dar M., Newman K. E., Vachtsevanos G.: On-line inspection of surface mount devices using vision and infrared sensors. Conference Record Autotestcon'95. Systems Readiness: Test Technology for the 21st Century 1995, 376–384, [http://doi.org/10.1109/AUTEST.1995.522699].
[7] Demir D., Birecik S., Kurugollu F., Sezgin M., Bucak I.O., Sankur B., Anarim E.: Quality inspection in PCBs and SMDs using computer vision techniques. 20th Annual Conference of IEEE Industrial Electronics 1994, 857–861 [http://doi.org/10.1109/IECON.1994.397899].
[8] Fang Y. C., Tzeng Y. F., Wu K. Y.: A study of integrated optical design and optimization for LED backlight module with prism patterns. Journal of Display Technology 10(10), 2014, 812–818.
[9] Gao H., Jin W., Yang X., Kaynak O.: A Line-Based-Clustering Approach for Ball Grid Array Component Inspection in Surface-Mount Technology. IEEE Transactions on Industrial Electronics 64(4), 2017, 3030–3038.
[10] Garakani A., Michael D. J., Koljonen J.: Automated optical inspection apparatus. US Patent 5, 640, 199, 1997.
[11] http://www.surfacemountprocess.com/#Circuit layout
[12] https://www.cherbsloeh.pl/attachments/category/327/Brochure-K3D-Series_EN_Rev06-2017-12.pdf
[13] Inman R. R., Blumenfeld D. E., Huang N., Li J.: Designing production systems for quality: Research opportunities from an automotive industry perspective. International Journal of Production Research 41(9), 2003, 1953–1971 [http://doi.org/10.1080/0020754031000077293].
[14] Juha M.: X-ray Machine Vision for Circuit Board Inspection. Conf. of SME, Proc. Vision 86, 1986, 341–355.
[15] Kim S. E., Jeon J. J., Eom I. K.: Image contrast enhancement using entropy scaling in wavelet domain. Signal Processing 127, 2016, 1–11.
[16] Kuo C. F. J., Hsu C. T. M., Liu Z. X., Wu H. C.: Automatic inspection system of LED chip using two-stages back-propagation neural network. Journal of Intelligent Manufacturing 25(6), 2015, 1235–1243.
[17] Kuo C. J., Fang T., Lee C.: Automated optical inspection system for surface mount device light emitting diodes. J. Intell. Manuf. 30, 2019, 641–655.
[18] Kuo C. J., Tung C., Weng W: Applying the support vector machine with optimal parameter design into an automatic inspection system for classifying micro-defects on surfaces of light-emitting diode chips. J. Intell. Manuf. 30, 2019, 727–741 [http://doi.org/https://doi.org/10.1007/s10845-016-1275-1].
[19] Langley F. J., Boatright R. R., Crosby L.: Composite electro-optical testing of surface-mount device boards-one manufacturer's experience, Proceedings: Meeting the Tests of Time, International Test Conference 1989, 686–691 [http://doi.org/10.1109/TEST.1989.82356].
[20] Li Q., Ren S.: A visual detection system for rail surface defects. IEEE Transactions on Systems Man and Cybernetics Part C-Applications and Review 42(6), 2012, 1531–1542.
[21] Li Q., Ren S.: A visual detection system for rail surface defects. IEEE Transactions on Systems Man and Cybernetics Part C-Applications and Review, 42(6), 2012, 1531–1542.
[22] Lin, H. D.: Automated defect inspection of light-emitting diode chips using neural network and statistical approaches. Expert Systems With Applications 36(1), 2009, 219–226.
[23] Ling-Yau C., Lawrence Wing-Tung L.: Total quality control for a surface mount technology process for the manufacture of printed circuit board assemblies, Quality and Reliability Engineering International 11(5), 1995, 325–331 [https://doi.org/10.1002/qre.4680110503].
[24] Lu S., Zhang X., Kuang Y.: Optimal illuminator design for automatic optical inspection systems. International Journal of Computer Applications in Technology 37(2), 2010.
[25] Mahon J., Harris N., Vernon D.: Automated visual inspection of solder paste deposition on surface mount technology PCBs. Elsevier – Computers in Industry, 1989.
[26] Nandi G., Datta S., Bandyopadhyay A., Pal P.K.: Application of PCA-based hybrid Taguchi method for correlated multicriteria optimization of submerged arc weld: A case study. International Journal of Advanced Manufacturing Technology 45(3–4), 2009, 276–286.
[27] Pang G. K. H, Chu M.: Automated optical inspection of solder paste based on 2.5D visual images. 2009 International Conference on Mechatronics and Automation, Changchun, 2009, 982–987 [http://doi.org/10.1109/ICMA.2009.5246351].
[28] Perng D. B., Liu H. W., Chen S. H.: A vision-based LED defect auto-recognition system. Nondestructive Testing and Evaluation 29(4), 2014, 315–331.
[29] Savage R. M., Park H. S., Fan M. S.: Automated inspection of solder joints for surface mount technology. NASA Technical Memorandum 104580, 1993 [http://doi.org/https://ntrs.nasa.gov/citations/19930016948].
[30] Tsai D. M., Huang T. Y.: Automated surface inspection for statistical textures. Image and Vision Computing 21(4), 2003, 307–323.
[31] Vanzetti R., Traub A. C.: Combining Soldering with Inspection. IEEE Control Systems Magazine 8(5), 1988, 29–32.
[32] Watanabe Y.: Automated optical inspection of surface mount components using 2D machine vision. 15th Annual Conference of IEEE Industrial Electronics 3, 1989, 584–589 [http://doi.org/10.1109/IECON.1989.69697].
[33] Wu H. H., Zhang X. M., Kuang Y. C., Lu S. L.: A real-time machine vision system for solder paste inspection. Proceeding of the 2008 IEEE/ASME International Conference on Advanced Intelligent Mechatronics, 205–210.
[34] Zhao H., Cheng J., Jin J.: NI vision based automatic optical inspection (AOI) for surface mount devices. Devices and method – 2009 International Conference on Applied Superconductivity and Electromagnetic Devices, 356–360 [http://doi.org/10.1109/ASEMD.2009.5306622].

M.Sc. Magdalena Michalska
e-mail: magdalena.michalska@pollub.edu.pl

Ph.D. student at the Department of Electronics and Information Technology, Lublin University of Technology. Recent graduate of Warsaw University of Technology. Her research field covers medical image processing, 3D modelling, optoelectronics, and spectrophotometry. Author of more than 10 publications.

https://orcid.org/0000-0002-0874-3285

otrzymano/received: 1.11.2020 *przyjęto do druku/accepted: 10.12.2020*

http://doi.org/10.35784/iapgos.2361

AN ELECTRICALLY-CONTROLLED AXIAL-FLUX PERMANENT MAGNET GENERATOR

Piotr Paplicki, Pawel Prajzendanc, Marcin Wardach
West Pomeranian University of Technology in Szczecin, Faculty of Electrical Engineering, Department of Power Systems and Electrical Drives, Szczecin, Poland

Abstract. *The paper presents a design of an axial-flux surface-mounted permanent-magnet generator with flux-regulation capability. Based on three-dimensional finite-element analysis (3D-FEA), the no-load air-gap magnetic flux density, flux-control characteristics, cogging torque and electromagnetic torque of the machine have been predicted. Simulation results of no-load back-EMF waveforms performed at different DC control coil excitations have been compared with experimental results.*

Keywords: axial-flux machine, PM generator, hybrid excitation, flux-control, voltage regulation

GENERATOR TARCZOWY Z MAGNESAMI TRWAŁYMI Z ELEKTRYCZNIE KONTROLOWANYM WZBUDZENIEM

Streszczenie. *W artykule przedstawiono projekt generatora tarczowego z powierzchniowo mocowanymi magnesami trwałymi z możliwością regulacji strumienia wzbudzenia. Na podstawie trójwymiarowej analizy polowej metodą elementów skończonych (3D-MES) wyznaczono rozkład indukcji magnetycznej w szczelinie powietrznej, charakterystykę regulacji strumienia, moment zaczepowy oraz moment elektromagnetyczny maszyny. Symulowany przebieg napięcia indukowanego w uzwojeniach stojana w funkcji prądu DC dodatkowego uzwojenia wzbudzeniu maszyny porównano z wynikami eksperymentalnymi.*

Słowa kluczowe: maszyna tarczowa, generator z magnesami trwałymi, wzbudzenie hybrydowe, regulacja strumienia, regulacja napięcia

Introduction

Nowadays, development in the field of unconventional permanent magnet (PM) synchronous generators with adjustable flux capabilities is clearly observed. They can effectively regulate terminal voltage with an inverter control technique or a hybrid-excitation technique with a flux-control (FC) capability, and they can be used in propulsion applications with frequent rotational speed variations such as generators in small wind turbines mounted at low altitudes.

In order to control the air-gap flux of a PM machine successfully, many different novel machine concepts have been recently designed [1–7, 9, 11–15]. This increased attention is mainly due to their wide speed-control range with flux-weakening (FW) or field-strengthening (FS) operation.

It should be noted that although PM machines have limits, e.g the risk of demagnetization of the PMs, they are still the most used type of machines in variable speed drive applications. Ensuring the effective air-gap flux control of the machine in FW operation is also a challenge.

The paper shows a design and the preliminary results of a Field-controlled Axial-flux PM machine (FCAFPM-machine) with the FC feature. A field control range (FCR) factor was introduced and used in the study as a measure of the effectiveness of the machine flux control. The FCR factor is calculated as the ratio of the linked flux Ψ_s of the machine, taken from the FS operation, occurring under a positive DC control coil current (I_{DC+}), to the FW operation, arising under the negative value of the DC control coil current (I_{DC-}).

1. Structure of FCAFPM-machine design

1.1. FCAFPM-machine topology description

The base model of the FCAFPM machine is a PM axial flux machine consisting of an inner double-wound stator and two outer rotors. Additional elements of the FCAFPM are a metal bushing (7) connecting the rotors and an additional DC control coil (5) fitted inside the stator, as shown in Figure 1. It should be pointed out that the presented machine design has been previously investigated and partially described in [8, 10].

The stator of the FCAFPM machine can be made of one or two toroidal cores (1), around which the phase windings (6) are wound. An additional DC coil (5) with 500 turns is mounted on the inner surface of the stator. The coil resistance is 4.8 Ω. The DC coil, as an additional excitation of the constant field together with the stator, is stationary, thanks to which there are no brushes and slip rings for it. The rotor's magnetic circuit consists of two disc yokes (2) and a connecting metal bushing (7). Six iron (4) and PM (3) poles are mounted alternately facing each other on each disc. All magnets are axially polarized in the same direction. The rotor disks (yokes), iron poles (IP) and the bushing are made of magnetic steel and rotate on a non-magnetic shaft (8).

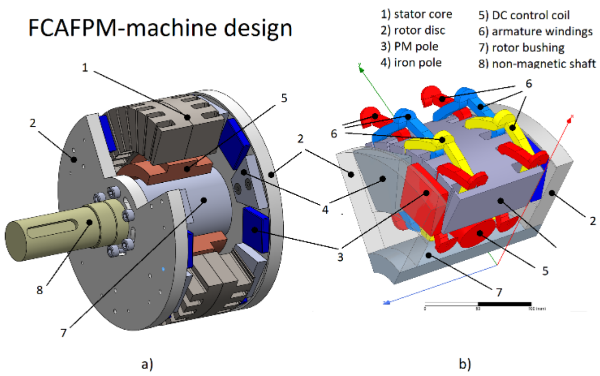

Fig. 1. Structural model (a) and 3D fine element method (FEM) model (b) of FCAFPM-machine

The selected dimensions of the proposed machine are listed in Table 1. Each disc has 6 pairs of poles, which gives a total of 12 pairs of poles. The machine does not have additional cooling, so it was assumed that the current density in the stator and DC coil windings would not exceed 5 A/mm^2. It should be noted that the presented machine design is not optimized yet, and is intended for low speed generator design.

Table 1. Dimensions of proposed FCAFPM-machine

Parameters	value
External radius of the stator	300 mm
Internal radius of the stator	180 mm
Thickness of the stator	100 mm
Number of stator slots	36 (double sided)
Axial length of the rotor disk	20 mm
Thickness of the IP	15 mm
Dimensions of the PM	50x50x12 mm
Height of the air gap above the IP	1 mm
External radius of the rotor bushing	50 mm

1.2. FCAFPM-machine prototype

Figure 2a shows a FCAFPM-machine prototype which has been developed and assembled for validation purposes. Figure 2b shows the stator and rotor components before machine assembly, where the PMs are protected against mechanical damage and centrifugal forces with special 3D-printed shields. The DC control coil is located between the front terminals of the stator coils and is sealed with epoxy resin.

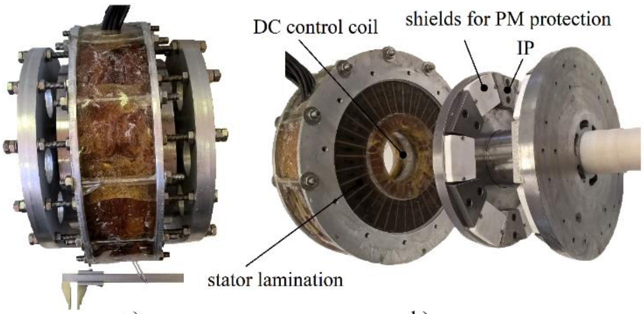

a) b)

Fig. 2. FCAFPM-machine prototype (a) and stator and rotor components before assembly (b)

Figure 3 shows the manufactured rotor disc with IPs already mounted, along with its main dimensions. The IP base has the shape of an isosceles trapezoid with arms inclined to each other at an angle of 45°. This IP shape was used to reduce the cogging torque of the PM machines. The primary excitation field of the generator is from the cuboid-shaped PMs that are mounted between the IPs. The PMs are made of N-38SH material with the following basic parameters: remanence = 1.23 T, coercivity = 907 kA/m at 20°C, and $(BH)_{max} \approx 300$ kJ/m^3. Both the IPs and PMs are mounted on the rotor in a special groove with a depth of 1 mm. The IPs are bolted to the rotor yoke with screws, while the PMs are glued and surrounded by a 3D-printed shield. The thickness of each PM is 12 mm and the thickness of each IP is 15 mm, which results in an air gap above the magnets of 4 mm, and over IPs of 1 mm.

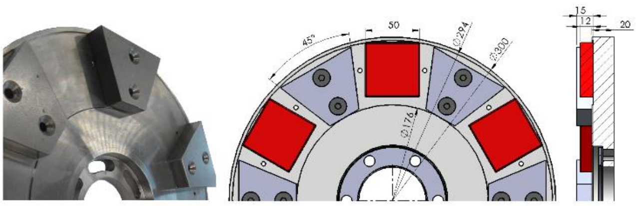

a) b)

Fig. 3. Design of disc type rotor yoke with IPs

2. Results of FEM simulation and experimental tests

This part of the article presents the 3D-FEA results including magnetic flux density distribution, air-gap flux density, no-load flux linkage, cogging torque, phase winding back-EMF waveforms, and experimental validation.

2.1. Magnetic field test results

The magnetic flux from the PMs and the additional constant magnetic field generated by the DC coil current (I_{DC}) together constitute the total flux of the machine Φ_{tot}. Air-gap flux regulation is achieved by increasing the current I_{DC}. In other words, magnetic flux generated by the DC excitation windings Φ_{DC} interacts with the magnetic flux excited by the PMs (Φ_{PM}). In the FW operation, the magnetic flux produced by the DC excitation coil reduces the total air-gap flux. When the DC current reverses its direction, the total air-gap flux is increased.

This relation can be express by the following equations:

$$\phi_{tot} = \phi_{tot/PM} + \phi_{tot/DC} \quad (1)$$

$$\phi_{tot/PM} = \phi_{PM/PM} + \phi_{IP/PM} \quad (2)$$

$$\phi_{tot/DC} = \phi_{PM/DC} + \phi_{IP/DC} \quad (3)$$

where: ϕ_{tot} – total air-gap flux; $\phi_{tot/PM}$ – air-gap flux component created by a PM over one pole; $\phi_{tot/DC}$ – air-gap flux component created by the DC excitation field over one pole; $\phi_{PM/PM}$ – air-gap flux component created by a PM in front of the PM pole; $\phi_{IP/PM}$ – air-gap flux component created by a PM in front of the IP; $\phi_{PM/DC}$ – air-gap flux component created by the DC excitation field in front of the PM pole; and $\phi_{IP/DC}$ – air-gap flux component created by the DC excitation field in front of the IP.

In order to evaluate the performance and air-gap flux control of the machine concept, a simulation study was carried out. The simulation study was performed by using 3D finite element analysis (3D-FEA) at various levels of magnetomotive force (MMF) excited by the DC control coil. In this study, the MMF, expressed as ampere-turns (AT), is defined as the product of the DC control coil current I_{DC} and the number of turns of the coil.

Figure 4 shows the no-load magnetic flux density distribution on the rotor and stator cores of the machine (left) and the magnetic flux density in the middle of the air-gap (right). The 3D-FEA model of the FCAFPM machine was developed in the ANSYS software package and was limited to one sixth of the whole machine.

Figure 5 shows the air-gap flux distribution under three different MMFs, for comparison, meaning under no-load ($I_{DC} = 0$) and $I_{DC} = \pm 5$A (MMF ±2500 AT) loading conditions.

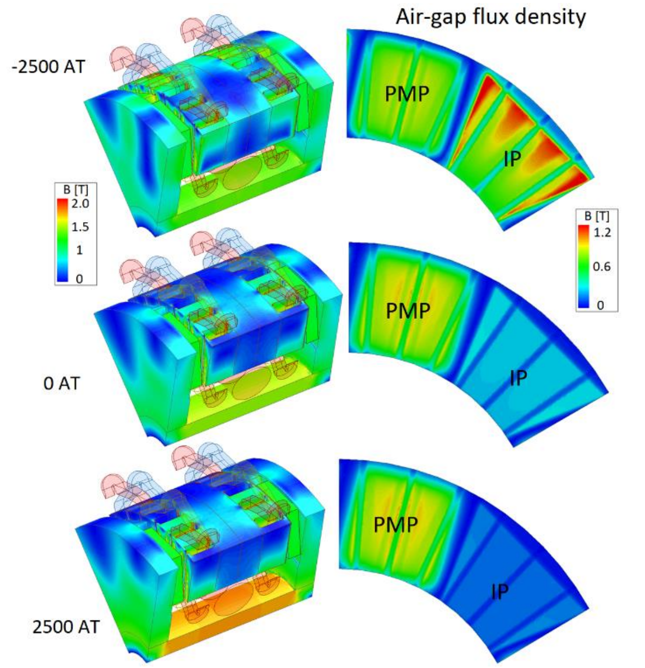

Fig. 4. Magnetic field distribution in the machine (left) and the two-dimensional air-gap flux density distribution over one pole pair under different MMF excitations – 0 and ±2500 AT (right).

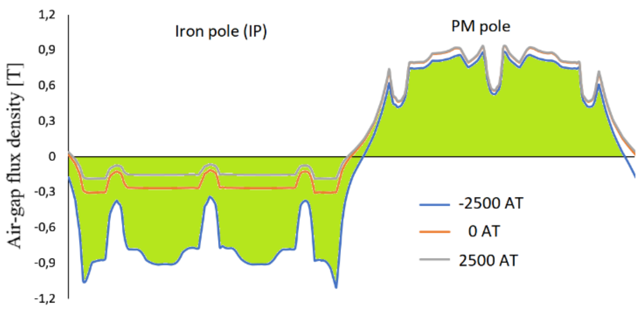

Fig. 5. Air-gap flux density distribution over one pole pair under different MMF excitations – 0 and ±2500 AT

In order to predict the no-load FC characteristics of the machine, 3D-FEA investigations were carried out.

Figure 6 shows phase magnetic flux linkage waveforms produced by the rotor permanent magnets, and the DC excitation field for three different MMFs.

The results in Figures 4 and 5 show that the MMF generated by the DC in the extra coil changes the air-gap flux distribution, and consequently, the stator flux linkage (Ψ_s) is effectively changed. The result can be seen in Figure 6, where the maximum values of flux linkage Ψ_{sm} under different MMF excitation levels operations are changed (under FS-operation, it is 780 mWb, no-load = 232 mWb, and FW-operation = 114 mWb). The results confirmed that controlling the DC field excitation successfully changes the stator flux linkage. The results also show that the FW operation is less effective than the FS operation, under the same MMF condition.

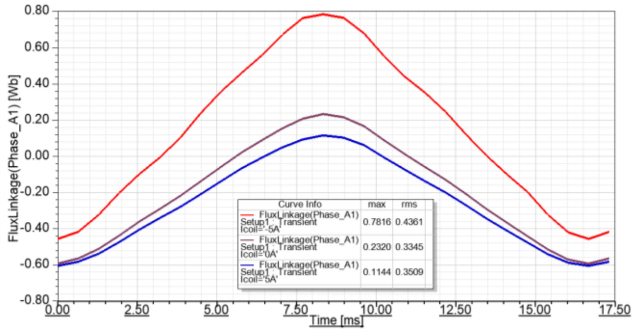

Fig. 6. 3D-FEA effect of no-load stator flux linkage (Ψ_s) waveforms at different MMF excitation levels

2.2. Electromagnetic torque test results

Low torque ripple is mostly required in generators to reduce acoustic noise and mechanical vibration. The effect of the shapes of the IP and PM poles on the cogging torque of the machine was investigated by a 3D-FEA time-stepping analysis.

The cogging torque simulation results are shown in Figure 7, where it can be seen that the maximum value of cogging torque is approximately 2.2 Nm, and this is observed during FS operation. During FW operation, the cogging torque waveform is slightly different from the waveform obtained under the no-load DC excitation field.

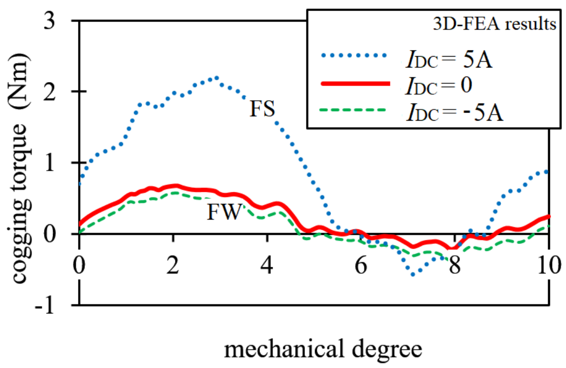

Fig. 7. 3D-FEA predictions of cogging torque waveforms at three different values of DC control coil current

The results show that the maximum value of cogging torque is significantly increasing during FS operation, and it should be reduced, e.g. by considering the skewed stator or rotor method.

In order to analyse the influence of the DC excitation field on the optimum current phase angle for the purposes of maximum torque determination, the electromagnetic torque versus angle rotor position characteristics were calculated and are shown in Figure 8. The electromagnetic torque waveforms including cogging torque were analysed for three different MMF conditions and at a constant DC armature current (I_s) of 100 A for phase A and 50 A for phases B and C.

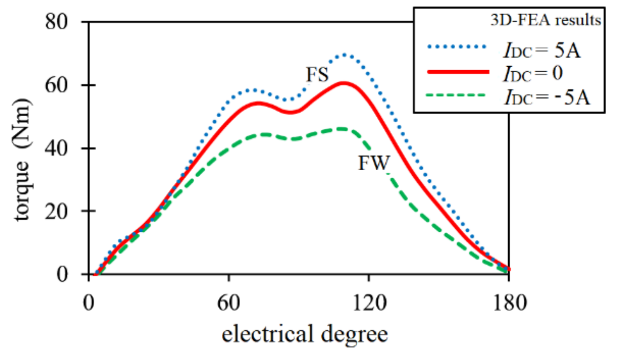

Fig. 8. 3D-FEA results of torque angle characteristics at three different values of the DC control coil currents

The maximum steady torque of the machine is 69.3 Nm (for FS operation), 60.4 Nm (no-load MMF) and 46.0 Nm (for FW operation).

3. Experimental validation

This section compares the simulation and experimental results of the back-EMF waveforms obtained under three different MMFs.

3.1. Experimental setup

To verify the FCR of the machine, an experimental setup for the proposed FCAFPM-machine as a generator was built and is shown in Figure 9. The machine prototype is mechanically connected to a 10-kW PMSM machine. In order to control current I_{DC} of the DC control coil, a controllable AC/DC power supply unit was used.

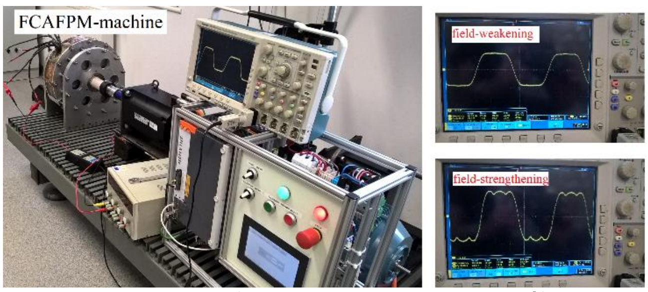

a) b)

Fig. 9. Experimental setup (a) and oscilloscope screen showing back-EMF waveforms (b) for the FCAFPM-machine at a rotor speed of 200 rpm measured at two MMF excitations under FW (upper) and FS operation

3.2. No-load back-EMF control validation

No-load tests were performed using the PMSM drive machine. The tests were carried out at a rotor speed of 200 rpm, under different DC excitation fields, where the current I_{DC} was varied between positive and negative values. Figure 9 shows the terminal voltage achieved at two different MMF excitation levels of ±2500 AT. As seen on the oscilloscope screen, the root-mean-square (RMS) value of the terminal voltage increased from 15.0 V to 22.5 V as the excitation of the MMF increased from 0 AT to 2500 AT (by I_{DC} = ±5.0 A).

It can be seen that the FW operation does not affect the induced voltage waveform, which is trapezoidal. On the other hand, the field amplification operation caused the appearance of additional harmonics that distorted this waveform. Optimizing the geometry of the IPs can reduce or even eliminate this problem.

Figure 10 compares the no-load terminal voltage and the simulation of back-EMF. As can be seen in the figure, the measured results match the 3D-FEA predictions well.

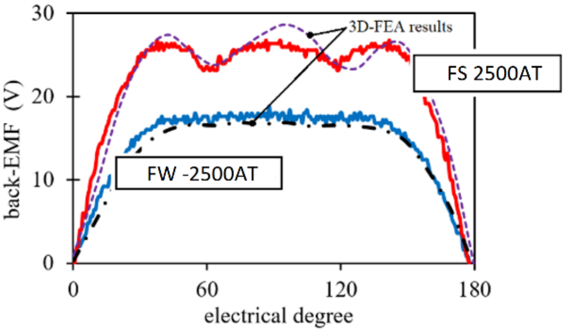

Fig. 10. Comparison of simulation and experimental results of no-load back-EMF waveforms of the FCAFPM-machine at a rotor speed of n = 200 rpm, at three different MMF excitation levels

Table 2 shows the effective values of the electromotive force induced in the stator windings at a rotor speed of 200 rpm for different magnetomotive forces in the DC coil. It can be seen that the results for both MMF = -2500 AT and MMF = 2500 AT are very similar, which confirms the correctness of the theoretical assumptions and the models.

Table 2. Phase-induced voltage

	Simulation	Experiment
MMF = 2500 AT	14.6 V	15.0 V
MMF = 0 AT	16.0 V	16.2 V
MMF = -2500 AT	23.5 V	22.5 V

4. Conclusion

Both the simulation and experimental results confirm that the FCAFPM-machine design concept can be effectively used as a generator with regulated output voltage.

Moreover, the developed FCAFPM-machine concept with air-gap flux boosting capability has an important feature that allows the control of the power energy for several electric machines and applications, for example in electric vehicles, where constant power operation across a wide range of speeds is required. In the same way, the output power of a wind turbine varies in a way which is highly correlated to wind speed. It is a challenging task to generate the required output power regardless of the wind conditions, within a certain range of wind speeds.

The presented machine prototype can be used as a low-speed 3 kW power generator with hybrid excitation to overcome the variation of output power on wind speed in the range of 50%.

The full experimental results for both load and fault conditions will be presented in future papers.

References

[1] Afinowi I. A. A., et al.: Hybrid-Excited Doubly Salient Synchronous Machine With Permanent Magnets Between Adjacent Salient Stator Poles. IEEE Transactions on Magnetics 51(10), 2015, 8107909, 1–9 [https://doi.org/10.1109/TMAG.2015.2446951].
[2] Aydin E., et al.: A hybrid-excited axial transverse flux permanent magnet generator. IEEE Energy Conversion Congress and Exposition (ECCE) – Milwaukee, 2016, 1–6 [https://doi.org/10.1109/ECCE.2016.7854701].
[3] Aydin M., Surong H., Lipo T.A.: Design, Analysis, and Control of a Hybrid Field-Controlled Axial-Flux Permanent-Magnet Motor. IEEE Transactions on Industrial Electronics 57(1), 2010, 78–87 [https://doi.org/10.1109/TIE.2009.2028294].
[4] Di Barba P., et al.: Hybrid excited synchronous machine with flux control possibility. International Journal of Applied Electromagnetics and Mechanics 52(3-4), 2016, 1615–1622 [https://doi.org/10.3233/JAE-162190].
[5] Dupas A., et al.: Investigation of a New Topology of Hybrid-Excited Flux-Switching Machine With Static Global Winding: Experiments and Modeling. IEEE Transactions on Industry Applications 52(2), 2016, 1413–1421 [https://doi.org/10.1109/TIA.2015.2497305].
[6] Hua H., Zhu Z. Q., Zhan H.: Novel Consequent-Pole Hybrid Excited Machine With Separated Excitation Stator. IEEE Transactions on Industrial Electronics 63(8), 2016, 4718–4728 [https://doi.org/10.1109/TIE.2016.2559447].
[7] Lee C. H. T., Liu C., Chau K. T.: A magnetless axial-flux machine for range-extended electric vehicle. Energies 7(3), 2014, 1483–1499, https://doi.org/10.3390/en7031483].
[8] Paplicki P., Prajzendanc P.: The Influence of Permanent Magnet Length and Magnet Type on Flux-control of Axial Flux Hybrid Excited Electrical Machine. 14th Selected Issues of Electrical Engineering and Electronics (WZEE), 2018 [https://doi.org/10.1109/WZEE.2018.8749015].
[9] Paplicki P.: A novel rotor design for a hybrid excited synchronous machine, Archives of Electrical Engineering 66(1), 2017, 29–40 [https://doi.org/10.1515/aee-2017-0003].
[10] Paplicki P.: Modified concept of axial-flux permanent magnet machine with field weakening capability. Archives of Electrical Engineering 63(2), 2014, 177–185 [https://doi.org/10.2478/aee-2014-0014].
[11] Tapia, J. A., Leonardi, F., Lipo, T. A.: Consequent-Pole Permanent-Magnet Machine with Extended Field-Weakening Capability. IEEE Transactions on Industry Applications 39(6), 2003, 1704–1709 [https://doi.org/10.1109/TIA.2003.818993].
[12] Wang Q., Niu S., Luo X.: A Novel Hybrid Dual-PM Machine Excited by AC With DC Bias for Electric Vehicle Propulsion. IEEE Transactions on Industrial Electronics 64(9), 2017, 6908–6919 [https://doi.org/10.1109/TIE.2017.2682778].
[13] Wardach M., et al.: Novel Hybrid Excited Machine with Flux Barriers in Rotor Structure. COMPEL – The international journal for computation and mathematics in electrical and electronic engineering 37(4), 2018, 1489–1499 [https://doi.org/10.1108/COMPEL-08-2017-0364].
[14] Wardach M., Paplicki P., Palka R.: A hybrid Excited Machine with Flux Barriers and Magnetic Bridges. Energies 11, 2018, 676 [https://doi.org/10.3390/en11030676].
[15] Zepp L. P., Medlin J. W.: Brushless permanent magnet motor or alternator with variable axial rotor/stator alignment to increase speed capability. US 6555941 B1, 2003.

D.Sc. Ph.D. Eng. Piotr Paplicki
e-mail: piotr.paplicki@zut.edu.pl

Piotr Paplicki was born in Pyrzyce, Poland in 1975. Graduated and received a Ph.D. degree from the Electrical Department, Szczecin University of Technology, Szczecin, Poland, in 2001 and 2006, respectively. Since 2017, he has been an Associate Professor with the Faculty of Electrical Engineering, West Pomeranian University of Technology, Szczecin, Poland. From 2016 until now, Vice-Dean for Student Affairs. His research interests include the design of electrical machines and drives.

http://orcid.org/0000-0003-0364-2028

M.Sc. Eng. Pawel Prajzendanc
e-mail: pawel.prajzendanc@zut.edu.pl

Pawel Prajzendanc was born in Pyrzyce, Poland in 1990. Received a B.S. degree in electrical engineering from West Pomeranian University of Technology, Szczecin, Poland in 2015 and an M.S. degree in 2017. He is currently pursuing a Ph.D. degree in electrical engineering at the Faculty of Electrical Engineering, West Pomeranian University of Technology, Szczecin, Poland. His awards and honors include a scholarship of Prime Minister of Poland. His research interests include the design of electrical machines and drives.

http://orcid.org/0000-0002-1662-4390

D.Sc. Ph.D. Eng. Marcin Wardach
e-mail: marcin.wardach@zut.edu.pl

Marcin Wardach was born in Barlinek, Poland in 1980. He graduated and received a Ph.D. degree from the Electrical Department, Szczecin University of Technology, Szczecin, Poland, in 2006 and 2011, respectively. From 2020 until now, he has been an Associate Professor with the Faculty of Electrical Engineering, West Pomeranian University of Technology, Szczecin. His research interests include the design of electrical machines and drives.

http://orcid.org/0000-0002-1017-9054

otrzymano/received: 14.10.2020 *przyjęto do druku/accepted: 10.12.2020*

http://doi.org/10.35784/iapgos.2103

METHOD OF DETERMINING THE COP COEFFICIENT FOR A COOLING SYSTEM

Mariusz R. Rząsa[1], Sławomir Pochwała[2], Sławomir Szymaniec[1]
[1]Opole University of Technology, Institute of Computer Science, Opole, Poland, [2]Opole University of Technology, Department of Mechanical Engineering, Opole, Poland

Abstract. *The basic metrological problem analyzed in this article is the experimental determination of the COP coefficient for a refrigerating system working in a stationary cooling chamber. This issue is because manufacturers of chillers provide the value of this coefficient in device technical data. In practice, after installing the refrigeration unit, the COP is often lower. The paper presents a method of balancing cooling energy for a complete refrigeration system.*

Keywords: coefficient of performance, cooling system, inverter compressor

SPOSÓB WYZNACZENIE WSPÓŁCZYNNIKA COP DLA UKŁADU CHŁODNICZEGO

Streszczenie. *Podstawowym problemem metrologicznym, który autorzy pragną przedstawić jest eksperymentalne wyznaczenie współczynnika COP dla układu chłodniczego, pracującego w stacjonarnej komorze chłodniczej. Zagadnienie to jest istotne, ponieważ producenci agregatów chłodniczych najczęściej podają współczynnik COP dla agregatu chłodniczego. W praktyce po zamontowaniu agregatu chłodniczego w komorze chłodniczej współczynnik COP jest niejednokrotnie niższy. Trudność z wyznaczeniem współczynnika COP w układzie chłodniczym polega na konieczności zbilansowania mocy chłodniczej dla całego układu wraz z komorą chłodniczą. W pracy przedstawiono sposób bilansowania energii chłodniczej dla kompletnego układu chłodniczego oraz opisano budowę stanowiska do wyznaczania współczynnika COP.*

Słowa kluczowe: współczynnik COP, układ chłodniczy, sprężarka inwertorowa

Introduction

The currently manufactured refrigeration systems commonly apply inverter compressors [2]. This solution is applied in systems with direct heat transfer of the cooled air (condensing chillers), as well as in systems comprising intermediate liquid (refrigerant aggregates) [1]. In practice, various types of compressor units are used, in which the heat of condensation can be transmitted to the environment or applied for generation of useful energy [3].

The principle of operation of a typical refrigeration system is shown in Figure 1. The refrigeration system consists of two heat exchangers (evaporator and condenser), an inverter compressor, and an expansion valve.

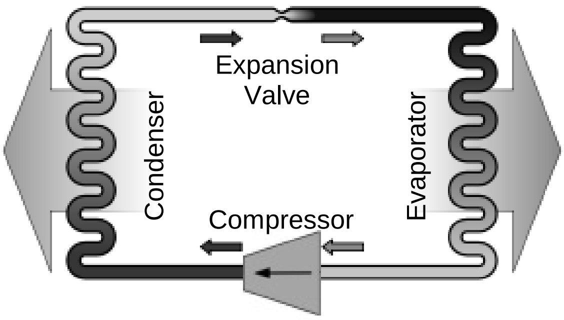

Fig. 1. Principle of operation of a typical refrigeration system

The main element in the operation of a refrigerator is a fluid, called a refrigerant or, occasionally, a working fluid. In a refrigerator, the refrigerant forms the "circuit" that allows heat transfer from the cooler region to the warmer region.

A compressor, using energy from the wall outlet, compresses the gas adiabatically. This raises its temperature and forces it into the condenser. As the compressed gas moves into the condenser coils, its temperature is higher than that of the surrounding air. Thus, heat is transferred out of the refrigerant and is taken away by the air. The refrigerant is condensed during this process, so it is in its liquid state as it moves on to the next stage. The condensed liquid is forced back into the refrigerator through an expansion valve. The active cooling agent is forced into evaporator coils where a sharp drop in pressure causes the refrigerant to revert to a gaseous state. During this process, the refrigerant absorbs a significant amount of ambient heat. This causes the cooling of the chamber with the evaporator. Finally, the "circuit" is closed; the refrigerant enters the compressor again.

The efficiency of the cooling units is greatly influenced by the selection of its individual components. The efficiency of the refrigeration unit is defined in terms of the COP (Coefficient of Performance). It is usually determined for several temperatures corresponding to the operating cycles of the compressor unit. Its value is the ratio of heating capacity (transferred in the condenser) to the use of electricity by the compressor:

$$\mathrm{COP} = \frac{Q_k}{P} \tag{1}$$

where: Q_k – heating efficiency of the condenser [W], P – the electrical power needed to achieve cooling capacity Q_k [W].

The use of a cooling capacity control system forms an indispensable element in refrigeration systems, the duration of products at a specified temperature is defined on its basis [4]. This is a necessary element of a refrigeration system [5], although it leads to the decrease of the value of COP. The paper presents an approach taken to determine the COP coefficient for a refrigeration system coupled with a dedicated control system. This solution provides a tool capable of determining the COP coefficient for the cooling system and not only for the chiller itself. This value more precisely corresponds to the actual cost of operating a refrigeration system.

1. Experimental setup

An experimental setup (Fig. 2) was developed and built for the purposes of the present study, the main element of which comprised a chiller manufactured by the Polish company FRIGIPOL, fed with an inverter compressor with a capacity of 480 W, and powered by 48V dc. As a result of implementing such a solution, it was possible to adjust the compressor capacity by varying the value of the input voltage. The experimental setup applied in the study also included a measuring chamber ($V = 12.41\ m^3$), which was in the form of an industrial container.

The container was placed in an empty space outdoors, as the present study envisaged an investigation of the performance of the investigated chiller in conditions similar to its natural operation. A tank filled with 0.75m3 of water was placed inside the container. This water tank acted as a thermal energy accumulator, as it simulated the material subjected to cooling. The setup was equipped with a data acquisition system that was developed in the LabView environment, which provided constant monitoring and recording of a number of physical parameters during the research.

In order to verify the correct operation of the laboratory stand, tests were carried out to cool the chamber interior under changing environmental conditions. For this purpose, several test cycles of cooling the inside of the chamber were carried out. Each time, the tests were started with a tank filled with water at a temperature of about 6°C. An example of the temperature measurement results for a compressor rotational speed of 3750 rpm is shown in Figure 3. The presented characteristics omit the results obtained from the T2 sensor placed inside the chamber, because the air temperature inside the chamber only slightly differed from the water temperature in the tank.

T4 temperature changes on the outside of the chamber are caused by the daily temperature changes that prevailed during the experiment. Along with these changes, the T1 temperature on the inner wall of chamber also changed. This proves that during the measurement, a significant part of the energy of the refrigeration system was lost due to conduction through the walls of the chamber. Uniform cooling (T3) of the water in the tank proves a properly selected capacity, which guarantees the stability of the process. As it results from the conducted research, the fluctuations in the outside temperature do not significantly affect the drop in water temperature. However, energy losses due to conduction through the chamber walls should be included in the power balance when calculating the COP.

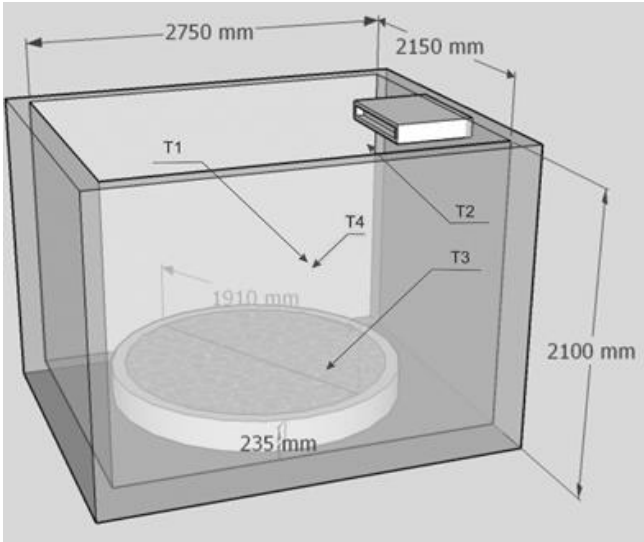

Fig. 2. Test stand

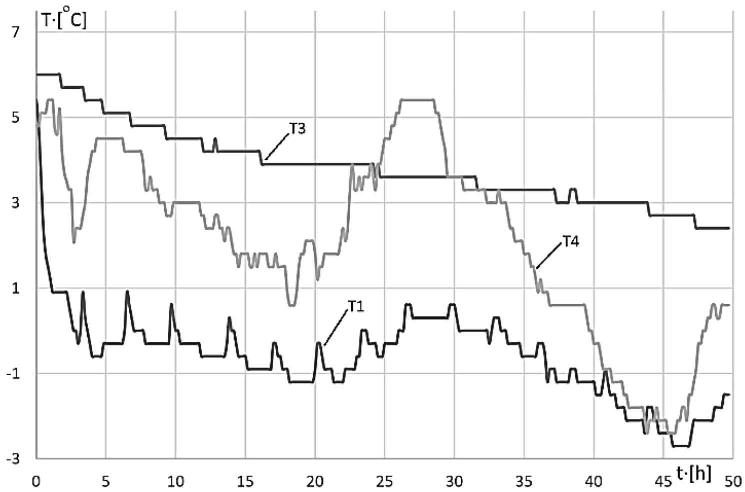

Fig. 3. Temperature characteristics of the cooling process

2. Laboratory determination of COP

For the purposes of determining the COP of a cooling system, it is necessary to know the power P_a that has been input from the refrigeration system. For this purpose, the power balance of the system was developed. The basic power sources are: thermal power delivered from the water tank P_w and thermal power received from the air inside the measuring chamber P_p. The heat conducted through the walls of the container cannot be underestimated Q. On this basis, the power balance equation was derived in the form:

$$P_a = P_w + P_p + Q \quad (2)$$

The values of power delivered from the water tank and the power derived from the air inside the chamber are calculated on the basis of the measurements from the relations in (4) and (5). The power transmitted through the walls of the cooling chamber is calculated on the basis of the conduction law on the basis of equation (6). The formula in (6) accounts for a heat transfer coefficient whose precise determination poses some difficulties. This is due to the design of the cooling chamber as insulation (thermal bridges) is not homogeneous on the entire surface of the chamber.

In addition, the heat supply by convection to the outer surface of the chamber is not the same in all cases. Further, variable weather conditions result in some differences in the heat transmission to the container surface, which results in a non-isotropic temperature distribution over the surface of the container. Curve T3 in Figure 4 represents the variation in water temperature during the cooling process. On the basis of this characteristic, it is possible to derive water cooling gradients for selected time intervals. The characteristics of changes in the temperature difference between sensors T1 and T4 forms the basis for calculating the heat transfer coefficient. Since the calculation of the power conducted by the walls of a chamber poses some difficulties and would normally require the application of a considerably more complex measurement system, the decision was made to calculate an averaged value of the heat transfer coefficient. A series of tests were carried out involving the determination of similar characteristics for various capacities of cooling by controlling the rotational speed of the compressor in the range from 3000 to 4400 rpm. On the basis of several characteristics, four time ranges were identified corresponding to occurrence of stable conditions.

In the case of compressors driven by DC inverters, the electrical power consumed by the compressor strongly depends on the rotational speed, which affects the cooling efficiency. The dependence of the consumed power on the rotational speed for the compressor used is shown in Figure 5.

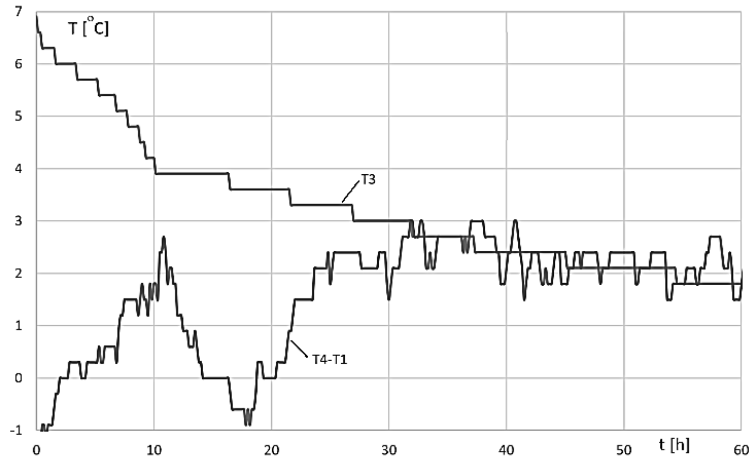

Fig. 4. Temperature characteristic of the cooling system

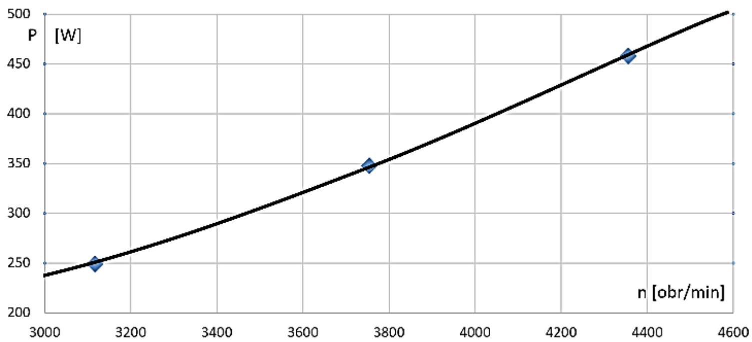

Fig. 5. Characteristics of changes in electric power consumption depending on the rotational speed of a compressor driven by a DC inverter motor

Table 1. Plunger material characteristics

Measurement range	Time	ΔT	P_W	P_p
	h	°C	W	W
1	42–55	2.1	0.52	0.16
2	30–35	8.1	1.2	0.94
3	14–20	2.4	0.3	0.02
4	41–46	0.3	0.3	0.24

The stabilization of the process is evidenced by the fact that the temperature intervals measured on the wall of the chamber do not change significantly for a few hours even in the conditions when an instant drop in the temperature of the cooled water occurs. As a result, temperature gradients for the cooled water were determined and the mean value of the differential temperature on the wall of the measuring chamber was recorded for these ranges. Consequently, on the basis of the water temperature gradients, the power delivered from both the water and air inside the chamber could be derived. A summary with the results of measurements and calculations is found in Tab. 1

In order to determine the averaged value of the heat transfer coefficient, in this study, it was assumed that the thermal heat transfer coefficient is constant and does not vary depending on the method of cooling. On the basis of this assumption, the following power balance equation can be developed:

$$P_{w1} + P_{p1} + Q_1 = P_{w2} + P_{p2} + Q_2 \quad (3)$$

Subscripts 1 and 2 relate respectively to selected time intervals. Using the data summarized in Table 1, it is possible to develop six independent equations, which can be applied to calculate six values of the heat transfer coefficient by transforming the equation in (3).

The power that was extracted from the water and air could be calculated using the following formulae:

$$P_w = V_w \cdot \rho_w \cdot c_w \cdot \frac{dT_w}{dt} \quad (4)$$

$$P_p = V_p \cdot \rho_p \cdot c_p \cdot \frac{dT_p}{dt} \quad (5)$$

where: V_w, V_p – water and air density [m^3], ρ_w, ρ_p – water and air density [kg/m^3], c_w, c_p – specific heat of water and air [J/(kg·K)], T_w, T_p – water and air temperature [K], t – time [h].

Since the temperatures outside and inside the chamber were considerably different, it was necessary to determine the energy that is transferred through the chamber walls. The energy transferred through the chamber walls was derived on the basis of the Fourier law:

$$Q = \lambda \cdot A \cdot \Delta T_s \quad (6)$$

where: A – surface area of the container wall, λ – heat transfer coefficient [W/(m^{2}K)], ΔT_s – temperature difference along the inside and outside interfacial surface of the container measured by the T1 and T4 sensors. The formula representing the heat transfer coefficient assumes the following form:

$$P_w = V_w \cdot \rho_w \cdot c_w \cdot \frac{dT_w}{dt} \quad (7)$$

The results of calculations for various combinations of the measurement points are presented in Fig. 3. The majority of the results are found in the range that is close to λ = 0.89 W/(m^{2}K). The values corresponding to points 5 and 6 are not taken into account in the further calculations due to the fact that they were considered to be considerable errors. The reasons for their occurrence are associated with the small differences in the values of powers and temperatures adopted during the calculations of the heat transfer coefficient.

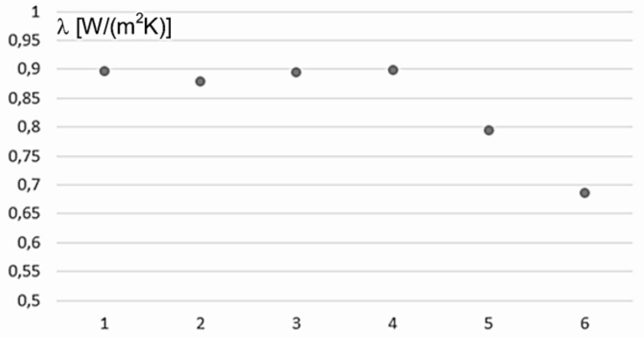

Fig. 6. Six values of heat transfer coefficient

The standard uncertainty was derived on the basis of the formula:

$$U_{\lambda} = \sqrt{\frac{(\bar{\lambda} - \lambda_i)^2}{N(n-1)}} \tag{8}$$

where: $\bar{\lambda}$ – the arithmetic mean derived from the value of the heat transfer coefficient, and λ_i – its particular component terms. The level of uncertainty after the results are extended to include the confidence level $p = 95\%$ was equal to $U_{\lambda} = 0.098$ W/(m^{2}K). This result can be considered as satisfactory and adequate for engineering applications.

The examples of the calculated results of COP for the refrigeration system used are given in Table 2. As we can see from these calculations, the COP coefficient for the entire analysed refrigeration system is slightly higher than one. In comparison to the values of this coefficient for refrigeration units given by manufacturers, the calculated value is about two times lower. The basic reason is associated with the process of determining COP in which manufacturers of chillers do not take into account the characteristics of the cooling system and only determine the thermal power of the condenser, which leads to a significant overestimation of the results.

Table 2. Results of calculated power

Compressor speed	Electric power input	Cooling power	COP
pmr	W	W	-
4356	458.2	617.6	1.35
3753	338.1	447.9	1.32
3118	249.6	333.5	1.34
4356	458.2	617.6	1.35

3. Conclusions

The work discusses the manner in which the COP coefficient of a refrigeration system can be feasibly determined. As was shown, the values of COP for the cooling system are significantly lower than the values of this coefficient determined for the chiller. The presented approach provides the means to assess the cooling parameters of a refrigeration system, and can offer much better insight in terms of assessing the efficiency of cooling equipment than just a comparison of the COP coefficients in commonly applied chillers. The use of some simplifications in determining the mean heat transfer coefficient does not lead to a significant level of error, which can be evidenced by the uncertainty level of 10% of the value calculated in the present study. Thus, the solution discussed in this paper can be applied in the study of complex refrigeration systems and in assessing the power consumption of these systems.

References

[1] Anweiler S., Masiukiewicz M.: Experimental based determination of SCOP coefficient for ground-water heat pump. 10th Conference on Interdisciplinary Problems in Environmental Protection and Engineering EKO-DOK 2018, Polanica-Zdrój 2018, 16–18.

[2] Kang S. M., Yang E. S., Shin J. U., Park J. H., Lee S. D., Ha J. H., Son Y. B., Lee B. C.: Development of High Speed Inverter Rotary Compressor for the Air-conditioning System. 9th International Conference on Compressors and their System, IOP Conf. Series: Materials Science and Engineering 90, 2015 [http://doi.org/10.1088/1757-899X/90/1/012038].

[3] Mu B., Li Y., House J.M., Salsbury T.: Real-time optimization of a chilled water plant with parallel chillers based on extremum seeking control. Applied Energy 208, 2017, 766–781 [http://doi.org/10.1016/j.apenergy.2017.09.072].

[4] Park Y. S., Jeong J. H., Ahn B. H.: Heat pump control method based on direct measurement of evaporation pressure to improve energy efficiency and indoor air temperature stability at a low cooling load condition. Applied Energy 132, 2014, 99–107 [http://doi.org/10.1016/j.apenergy.2014.07.011].

[5] Wang B., Liu X., Shi W.: Performance improvement of air source heat pump using gas-injected rotary compressor through port on blade. International Journal of Refrigeration 73, 2017, 91–98 [http://doi.org/10.1016/j.ijrefrig.2016.09.017].

D.Sc. Eng. Mariusz R. Rzasa
e-mail: m.rzasa@po.edu.pl

Graduated from the Faculty of Electrical Engineering, Automatic Control and Informatics at Opole University of Technology, specializing in automation and electrical metrology. Employed in the Department of Thermal Engineering and Industrial Facilities at Opole University of Technology. Received a Ph.D. degree with the specialization in the Construction and Operation of Machines. Habilitation obtained at the Faculty of Mechanical Engineering and Computer Science, Częstochowa University of Technology. Scientific work in the field of two-phase flow measurement.

http://orcid.org/0000-0002-3461-2131

Ph.D. Eng. Slawomir Pochwala
e-mail: s.pochwala@po.edu.pl

Graduated from the Faculty of Mechanical Engineering at Opole University of Technology, specializing in industrial metrology. The subject of his main scientific research is the evaluation of the influence of typical flow-disturbing components on the indications of flow meters. For the last five years, he has been dealing with the use of unmanned aircraft applications for thermographic, air quality, and electromagnetic field measurements under industrial conditions. Employed in the Department of Thermal Engineering and Industrial Facilities at Opole University of Technology. Scientific work on the influence of disturbances on flowmeters.

http://orcid.org/0000-0002-8128-5495

Prof. D.Sc. Eng. Sławomir Szymaniec
e-mail: s.szymaniec@po.edu.pl

Prof. dr. eng. (born 1949 in Opole) is analog electronics engineer, expert in diagnostics, appraiser of electrical machines; Head of Department. In 2010, 1st place winner of the 15th edition of the competition for the research prize of the Siemens company for outstanding achievements in technology and research. He was the inspiration for the research team of Diagnostics of Electrical Machines and Drives, well-known in Poland and abroad. Together with his team, he deals with the operation and diagnostics of electrical machines. Together with his team, he deals with the operation and diagnostics of electrical machines. His work in the department has resulted in the publications of 42 scientific works research and implemented in industry, and 1,400 technical works for industry.

http://orcid.org/0000-0002-7642-1456

otrzymano/received: 02.08.2020 *przyjęto do druku/accepted: 10.12.2020*

http://doi.org/10.35784/iapgos.2377

THE IMPACT OF DIGITAL PHOTOGRAPHY PROCESSING IN MOBILE APPLICATIONS ON THE QUALITY OF REACH IN SOCIAL MEDIA

Magdalena Paśnikowska-Łukaszuk, Arkadiusz Urzędowski
Lublin University of Technology, Faculty of Fundamentals, Lublin, Poland

Abstract. *Modern technologies allow for quick processing of digital images. In the era of the Internet, there are many mobile applications supporting the digital processing of photos used on social media. The algorithms of many popular social networks focus on many factors, however, the photography that is placed on a given portal is of great importance. Social media allows you to reach many sources and people. With the help of a good photo, we can get high post reach that contain additional information. The use of mobile applications helps to achieve very good results. This paper presents the results obtained in the process of comparing posts using digital photo processing with those in which the photos were used without processing in a graphics program.*

Keywords: mobile communication, digital communication, social media, multimedia communication

WPŁYW CYFROWEGO PRZETWARZANIA FOTOGRAFII W MOBILNYCH APLIKACJACH NA ZWIĘKSZANIE ZASIĘGU W MEDIACH SPOŁECZNOŚCIOWYCH

Streszczenie. *Nowoczesne technologie pozwalają na szybkie przetwarzanie obrazów cyfrowych. W dobie rozwoju Internetu pojawia się wiele aplikacji mobilnych wspomagających proces obróbki cyfrowej zdjęć używanych w mediach społecznościowych. Algorytm wielu popularnych portali społecznościowych skupia się na wielu czynnikach, jednakże duże znaczenie ma fotografia, która zostaje umieszczona na danym portalu. Media społecznościowe pozwalają dotrzeć do wielu źródeł i osób. Za pomocą dobrego zdjęcia można uzyskać wysokie zasięgi postów, w których zawarte są dodatkowe informacje. Wykorzystanie aplikacji mobilnych pomaga uzyskać bardzo dobre efekty. W niniejszej pracy zostaną przedstawione wyniki uzyskane w procesie porównywania postów wykorzystujących obróbkę cyfrową zdjęć oraz tych, w których fotografie były użyte bez przetworzenia w programie graficznym.*

Słowa kluczowe: komunikacja mobilna, komunikacja cyfrowa, media społecznościowe, komunikacja multimedialna

Introduction

Currently, the development of technology is conducive to the appearance of more and more new solutions in the field of computer graphics. The pace of the appearance of smartphones, tablets and other mobile devices on the market has led to more and more people becoming interested in mobile applications. The usefulness of these devices means that on many operating systems, applications which were meant to facilitate everyday functioning and work in many areas of life and science began to develop very quickly [1]. In addition, this development contributed to the popularization of social media, which to a large extent was to serve primarily interpersonal contacts. Over time, they were also used to promote many products, and then these media began to replace traditional websites in favor of profiles on social networks. The most popular of them are Facebook and Instagram [2]. A few years ago, the Internet community also used portals in the form of mobile applications such as Snapchat, which was used to transfer content in the form of photos and videos, but over time, its popularity was replaced by the aforementioned Instagram, which operates on the basis of an algorithm.

Most of the posts that appear on social media are based on a photo and then a description. However, it is the photo that is designed to attract attention and then make the user want to read the rest of the post. Today, more and more programs popping up to adapt their editing tools for social media. Figure 1 present the most popular social media platforms in 2020.

One of these programs is the Canva application, which can be used on both mobile devices and computers. The templates used in this application allow you to prepare appropriate graphics that can be used to post information on social networks. It is worth adding, however, that the most popular applications are those that help to obtain the appropriate reach. Due to the fact that currently every potential recipient is focused on the quick reception of content, the person who prepares this content must be sure that the material prepared by them will get noticed. Therefore, mobile application manufacturers offer a number of tools to facilitate this task.

1. Popular mobile applications for processing digital images

The Android system and IOS offer a number of applications supporting the digital processing process. Currently, the most popular are Adobe Lightroom Mobile version and Snapseed. The first mentioned program is popular among computer graphic designers in the traditional version used on computers. Currently, this application has been disseminated by using so-called Presets. These are tool settings that allow you to quickly obtain a digitally processed photo without spending a lot of time, and this effect also allows you to obtain photos which are similar in color. Its modern design and friendly interface allow the user to obtain a satisfactory digital photo processing effect.

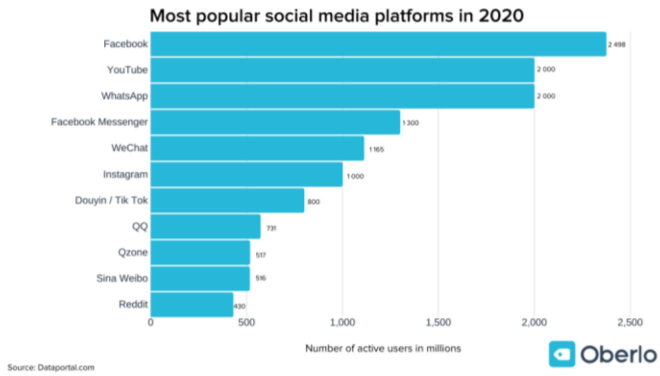

Fig. 1. Most popular social media platforms in 2020 [9]

An example of editing a photo in Adobe Lightroom Mobile is shown in Figures 2 and 3. It can be seen that the second photo catches the eye with its unusual colors and reflects a modern effect. In addition, this application allows you to enhance the edges, which is useful when the photo was moved during recording.

Fig. 2. Photo before digital processing in Adobe Lightroom

Fig. 3. Photo after digital processing in Adobe Lightroom

The Snapseed mobile application is a combination of many tools that create a fast and very useful program that helps to achieve an effect similar to if you were using Adobe Photoshop. Together with changing the colors and focus settings, the application also offers photo retouching and photomontage tools. In addition, the user can obtain a background blur effect, which can be created by using appropriate photographic equipment, while here, it is enough to use one tool. The application offers a number of filters to facilitate the process of high-speed digital processing. In addition, Snapseed and Adobe Lightroom allow you to share files directly to your social accounts. With the Android overlay, we can also enjoy direct file sending between users. An example of editing a photo in Snapseed is shown in Figures 4 and 5.

There are more and more new applications for digital photo processing in mobile application stores, but practically all of them are based on the same tools as Adobe Lightroom or Snapseed discussed in this chapter. Some are even confusingly similar. However, it is worth choosing one that will help you achieve the right end results.

Fig. 4. Photo before digital processing in Snapseed mobile application

Fig. 5. Photo after digital processing in Snapseed mobile application

2. Social media in the era of Internet development

Currently, Facebook is the most popular portal on the market. It is a huge platform that has changed to a business tool from a profile intended for interpersonal contacts. Today, most Facebook users have to deal with other people's advertising and business profiles [3, 5, 7]. We can reach multiple audiences with business settings. The Facebook and Instagram algorithm (which will be discussed later in the article) are based on the user's interests. Non-interest posts tend to have fewer views. The more views of a given post, the greater the reach. Most people ask themselves how to increase the reach of a given post. The basic tool that is supposed to increase the displays is photography. This is the main point that will encourage the users to read the content at a later stage. A good photo equals a good reception. Since Facebook is built as a scrolled page, the mobile version of the application should also be adapted to the format of the page and the application [4, 8]. Therefore, we may notice an increase in views if the image is vertical rather than horizontal, hence the length of the recipient's focus. Vertical photos are meant to "draw" the users' attention. Vertical photos take up more screen real estate on the device. It is similar with the Instagram application. Unlike Facebook, users here focus more on content transmitted primarily in the form of graphics or videos. It should be added that video posts have also been available on Facebook for some time. Figures 6 and 7 show statistics on how many views were generated on pages that used vertical photos and horizontal photos.

Fig. 6. Stats for a page using horizontal photos

Fig, 7. Stats for a page using vertical photos

We can see an over two-fold increase in the response to published content. Many factors contributed to this result. In order to check the additional effectiveness of photo editing, a study was conducted involving the publication of photos using digital processing in a mobile application. The results will be discussed in the next section. Instagram also generates views by using tools such as hashtags. However, nowadays, filtered photos are an effective way to attract attention. The Instagram application itself offers a number of filters to help achieve the effect of a digitally processed photo. The interface is shown in Figure 8.

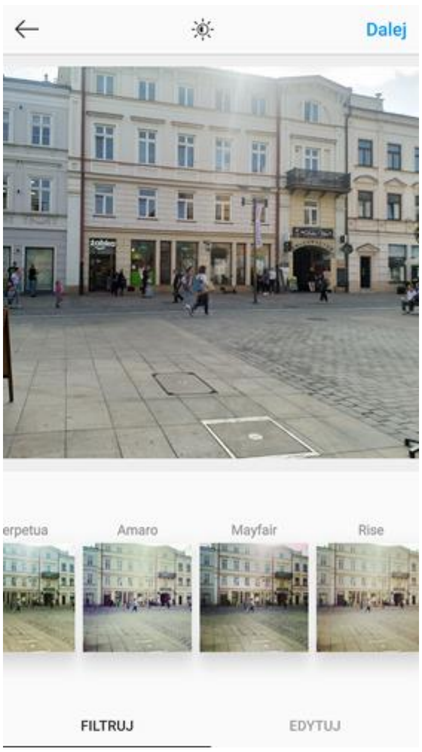

Fig. 8. Interface of Instagram editor

The editor in the Instagram application also allows you to properly crop the photo in order to cover as much vertical real estate as possible. To check the statistics of published photos, the user has to switch a private account to a business account [6]. Then they have a complete preview of how their content is received.

3. Researching the reach of posts using photography

In order to obtain the data, several posts on Instagram were published using photography without digital processing and one that was edited with presets in the Adobe Lightroom Mobile application. The ranges resulting from the display of the post were monitored. Figure 9 shows an example of a statistic from a post in which a digitally processed photo was published.

Fig. 9. Instagram statistics

Tables 1–4 show the results of 20 digitally processed posts and 20 posts where the photos were published without processing.

Table 1. Results of published post with photography without post processing

Number of post	Follows	Reach	Impressions
1	2	500	861
2	1	550	932
3	0	460	785
4	1	450	461
5	2	434	788
6	2	456	772
7	2	468	755
8	2	493	774
9	1	575	685
10	0	515	604

Table 2. Results of published post with photography without post processing

Number of post	Follows	Reach	Impressions
11	0	572	664
12	1	692	794
13	2	575	670
14	2	612	706
15	0	645	741
16	0	669	778
17	1	611	713
18	1	599	700
19	1	502	597
20	3	440	514

Table 3. Results of published post with photography with post processing

Number of post	Follows	Reach	Impressions
1	2	728	1201
2	2	603	1005
3	4	535	900
4	2	488	865
5	4	539	909
6	4	504	842
7	5	512	855
8	4	609	942
9	3	683	849
10	4	689	805

Table 4. Results of published post with photography with post processing

Number of post	Follows	Reach	Impressions
11	4	798	917
12	2	843	967
13	4	1345	1502
14	3	770	886
15	4	996	1089
16	4	1018	1124
17	3	1068	1197
18	3	901	993
19	3	829	967
20	5	1054	1102

The comparison of the results is presented in the diagram (Figure 10). You can see a significant increase in interaction in the case of publishing photos that were processed in the Adobe Lightroom application. The modern design of the photography caught the attention of followers as well as new users. The trend line is upward. The same hashtags were used in the posts to exclude the influence of other factors. However, it should be added here that properly selected hashtags also boost views, but they must be matched to the content and the photo that is published. In addition to impressions and increased range, we should see an increase in new followers. These are small numbers, but still representing an upward trend. Summing up, using presets in Adobe Lightroom has a positive effect on the increase in statistical factors in the Instagram application when publishing content.

4. Conclusions

Digital processing has a huge impact on the viewing of posts by users. At the same time, it contributes to the growth of observers on social media. Photos with bright colors in warm tones had more views than photos with sharp colors. Posts with photos processed in the mobile application had more comments and reactions from observers. In addition, the posts encouraged users to read the rest of the content. It can therefore be concluded that the processing of digital images is conducive to building ranges and relationships between users, and the use of additional tools such as hashtags or marking locations strengthens these ranges. Through the desire to gain coverage in social media, users also develop their skills in using graphics programs, and this also increases market demand for the production of mobile applications for digital photo processing. Manufacturers can also reach a new audience in this way. To sum up, if the user wants to achieve very good results in the form of an increase in reach and display of published content, they should use an image and photography processing application.

References

[1] Bevilaqua M.: Guide to image editing and production of figures for scientific publications with an emphasis on taxonomy. Zoosystematics and Evolution 96(1), 2020, 139–158.

[2] Davies T., Lorne C., Salley-Huggins L.: Instagram photography and the geography field course: snapshots from Berlin. Journal of Geography in Higher Education 43(3), 2019, 362–383 [http://doi.org/ 10.1080/03098265.2019.1608428].

[3] Hemesley J., Jacobson J., Gruzd A., Mai P.: Social Media for Social Good or Evil: An Introduction. Sage Journals 4(3), 2018 [http://doi.org/10.1177/2056305118786719].

[4] Hochman N.: The social media image. Sage Journals 1(2), 2014 [http://doi.org/10.1177/2053951714546645].

[5] Korga S., Płecha A., Szulżyk-Cieplak A.: Media społecznościowe w dobie społeczeństwa informatycznego. Poszerzamy horyzonty 5, 2017, 158–166.

[6] Perrin A.: Social Media Usage: 2005–2015. Pew Research Center, October, 2015.

[7] Skowron S., Skrzetuski R.: Media społecznościowe jako narzędzie komunikacji firmy z klientem. Handel Wewnętrzny 359(6), 2015, 162–172.

[8] Szulżyk-Cieplak J., Puchtel A., Płecha A.: Media społecznościowe jako narzędzia reklamy internetowej. Edukacja – Technika – Informatyka 20(2), 2017, 290–295.

[9] https://www.oberlo.com/statistics/most-popular-social-media-platforms (accessed: 26.09.2020).

M.Sc. Eng. Magdalena Paśnikowska-Łukaszuk
e-mail: m.pasnikowska-lukaszuk@.pollub.pl

Graduate of Fundamentals of Technology Faculty at Lublin University of Technology. Author of 24 scientific works. Her research interests are environmental engineering, power engineering, and IT and telecommunications.

https://orcid.org/0000-0002-3479-6188

M.Sc. Eng. Arkadiusz Urzędowski

Postgraduate student of the department of Civil Engineering and Architecture Faculty, Fundamentals of Technology Faculty and Electrical Engineering and Computer Science Faculty at Lublin University of Technology. Author of 24 scientific works. His research interests are heat transport phenomena in microstructures of building materials, computer-aided design, and building information modeling.

https://orcid.org/0000-0002-0440-3013

otrzymano/received: 30.10.2020 *przyjęto do druku/accepted: 10.12.2020*

http://doi.org/10.35784/iapgos.2398

USE OF WEB 2.0 TOOLS BY POLISH HEALTH PORTALS

Magdalena Czerwinska
Lublin University of Technology, Department of Economics and Economic Management, Lublin, Poland

Abstract. *The Internet, as a global, universal communication network, has become an important channel of information distribution. Currently, it has a very social character, thanks to the dissemination of Web 2.0 sites, which allow users to create and publish their own multimedia content. Web 2.0 technologies make it easier for users to communicate, create, collaborate and share information. They are widely available and are characterized by low costs of use. The article presents the results of research on the most popular Polish health websites. It was examined whether health services meet the requirements of Web 2.0 sites. The analysis is focused on the technological and social aspects. The COVID-19 pandemic lockdown in March and April 2020 in Poland was observed as having an influence on users and views of heath websites. The obtained results confirm the use of elements (both technological and social) by health services selected for research. However the usage of Web 2.0 technologies among websites varies.*

Keywords: health information, health websites, Web 2.0, Health 2.0

WYKORZYSTANIE NARZĘDZI WEB 2.0 PRZEZ POLSKIE PORTALE POŚWIĘCONE ZDROWIU

Streszczenie. *Internet, jako globalna, uniwersalna sieć komunikacyjna, stał się ważnym kanałem dystrybucji informacji. Obecnie ma bardzo społeczny charakter, dzięki upowszechnieniu serwisów Web 2.0, które umożliwiają użytkownikom tworzenie i publikowanie własnych treści multimedialnych. Technologie Web 2.0 ułatwiają użytkownikom komunikację, tworzenie, współpracę i udostępnianie informacji. Są powszechnie dostępne i charakteryzują się niskimi kosztami użytkowania. W artykule przedstawiono wyniki badań najpopularniejszych polskich serwisów poświęconych zdrowiu. Zbadano, czy usługi zdrowotne spełniają wymagania witryn Web 2.0. Analiza koncentruje się na aspektach technologicznych i społecznych. Zaobserwowano, że zamknięcie gospodarki wskutek pandemii COVID-19 w marcu i kwietniu 2020 r. w Polsce znacząco wpłynęło na użytkowników i oglądalność witryn o tematyce zdrowotnej. Uzyskane wyniki potwierdzają wykorzystanie wybranych do badań elementów (zarówno technologicznych, jak i społecznych). Jednak wykorzystanie technologii Web 2.0 na poszczególnych witrynach internetowych jest zróżnicowane.*

Słowa kluczowe: informacja zdrowotna, strony internetowe poświęcone zdrowiu, Web 2.0, Health 2.0

Introduction

The popularity of the Internet has increased at a galloping rate in recent years. It is present in all areas of human life and activity. It is displacing traditional media such as television, radio and newspapers. According to the annual "Digital In 2020" report of the We Are Social website, regarding the use of the Internet, mobile devices and social media, there are currently 4.54 billion Internet users around the world, 5.19 billion mobile phone users and 3.8 billion active social media users (as of January 2020) [18].

The most dynamically developing group are users of social media – their number increased within one year (from January 2019) by 9.2% (by 321 million people). The second area of significant growth was recorded in the group of Internet users (by 7%, or 298 million people) [18]. Such growth trends in the world have been occurring for several years. According to these global trends, the number of Internet users is also systematically increasing in Poland. In 2019, in Poland, 78.3% of people aged 16–74 regularly (at least once a week) used the Internet (as compared to 72.7% in 2017). About 49% of people aged 16–74 used social networking sites, that is, 65.9% of all Internet users, and 54.3% of those aged 16–74 used mobile devices [8].

The Internet is increasingly used in the area of health issues. According to Statistics Poland (pol. GUS) data, in 2017, 47.4% of Poles aged 16–74 search the Internet for health information (during the year, this rate increased by 2.4 percentage points – in 2018 it was 45%) [7]. Patients are also increasingly active on health-related blogs and Internet forums. The Internet has also become a platform for the exchange of information between patients and medical staff, and for the latter, it is also a source of professional knowledge. In general, any manifestation of the use of the Internet or ICT in healthcare is called e-health.

E-health is a broad concept that goes beyond just using information. Newer applications (so-called Health 2.0 applications) offer all types of interactive technologies that help people communicate on health issues. Internet users communicate with other patients and health care professionals, e.g. through forums or e-consultations, to independently monitor their health (e.g. through patient portals) and even obtain assistance via the Internet [17].

1. Web 2.0 technologies

E-health activities were strengthened by Web 2.0 services that appeared at the beginning of the 21st century. The Internet has become more social, giving users the opportunity to create and publish their own multimedia content. Web 2.0 is not a new information technology, but is a different way of creating websites, giving users autonomy in co-creating content on the web. Web 2.0 technologies emphasise interactivity, allow you to create groups and networks of friends, post information on the web, search it and evaluate it. These technologies are focused on the involvement of participants in creating the content of websites [13].

Formerly, websites were created by one person (author), who was the only one able to change their content. Web 2.0 focuses on users who cease to be passive recipients of the media – they can comment, add, delete, share knowledge and resources, and give their opinions on the content [11].

On the one hand, these technologies result in socializing in communication and creating content and knowledge, while on the other hand, it causes a huge increase in information and the need to support the user in the search for and access to good quality information.

Web 2.0 technologies have a social and technological dimension. The technological dimension involves the use of specific technologies, the Wiki mechanism, weblogs, providing XML interfaces that allow other websites and programs to use Web 2.0 data (mainly by ATOM and RSS).

The social dimension of these technologies focus on: the creation and modification of content by users, the emergence of communities associated with particular websites, the use of collective intelligence, open licenses (e.g. Creative Commons) and the use of folksonomy. The main features of Web 2.0 sites are [5, 19]:

1) Interactivity – allows the user to create content and interact with other users – possible by using tools such as: AJAX, XHTML, SOAP, XUL, RDF, Ruby on Rails (RoR);
2) Wiki – software enabling the cooperation of many users in creating web content, often without the need for authorization, with public access to editing the content of a certain website;
3) Opportunity for users to make contacts, create groups and social links;

4) Co-creation and sharing – active participation (making comments and assessments), ease of exchanging and sharing information with other users;
5) Staying in beta – websites are still in the development phase;
6) Breaking existing rules – websites give users new value, breaking methodologies that have been functioning on the market so far;
7) The choice of content and time of access to them – the user decides what information and when he/she uses it (e.g. through ATOM technologies or RSS feeds enabling aggregation of content from multiple sources in one place);
8) Speed of website creation – thanks to easy-to-use technologies and relatively low start-up costs;
9) Mortality of websites – disappearance of websites caused by a high level of market competitiveness.

E-health systems use a range of tools to search for information and gain knowledge about health. These include Web 2.0 tools, such as: Internet forums, discussion groups, blogs, specialist medical portals, health information websites, online encyclopaedias, on-line video consultations with doctors, doctors' consultations via the Internet, websites evaluating medical professionals, online pharmacies and drug price comparison websites. The development of information systems based on Web 2.0 solutions has opened new possibilities to improve the management of medical knowledge and has become the basis for building the Health 2.0 model and the concept of assessing the usability of these systems from the users' point of view [12, 20].

2. Health 2.0 – application of Web 2.0 technologies in e-health

The use of Web 2.0 technologies in e-health has led to the creation of the new concept called Health 2.0 or Medicine 2.0. It was presumed that the expected beneficial aspect of these projects would be the improvement of the quality and effectiveness of health care. Health 2.0 actively engages consumers in the health care system. Health 2.0 technologies assume that patients will actively contribute to their own care process. Along with the e-health concept and postulates of the use of ICT in the health care sector, a new type of patient has appeared – an e-patient (a person, who uses health care services using ICT regardless of whether they are healthy or ill) [12]. The concept of Health 2.0 also includes the concepts of "patient empowerment" [3] and the "smart patient" [2], characterized by active participation of the citizen in his or her health and care pathway with the interactive use of Information and Communication Technologies [1]. Health 2.0 serves to strengthen the position of the patient in the health care system and make it easier for him to be an active subject deciding his or her health choices.

Various concepts on the definition of Health 2.0 and Medicine 2.0 are presented in the literature. Some authors differentiate them (claiming that Health 2.0 is a broader concept regarding healthcare in general, whereas Medicine 2.0 focuses on the patient-medical staff relationship), some consider them as substitutional terms of the same concept [16]. The specificity of Health 2.0 is manifested in the fact that:
1) The creators of health content are the stakeholders themselves (mainly potential patients and medical staff) who create knowledge themselves, and disseminate it using tools such as blog, RSS, wikis, and discussion lists.
2) Patients are open to co-creating content. When a patient has a lack of knowledge, they ask questions, and expect support from others (this leads to sharing knowledge and experiences with others).
3) New resources of health content are created, which are based on blogs, and content aggregated in RSS readers. These resources coexist in parallel with specialist knowledge coming from scientific studies and from medical professionals. The catalogue of sources of content about health issues is broadened and entities have easier access to knowledge and information co-created by many authors.
4) Health 2.0 allows you to integrate existing online resources through the use of various sources, specialist studies, databases and thematic portals.
5) It is inseparably connected with the creation of social networking sites, which enable establishing contacts between their users, and participation (sharing and exchange of information) through activity on the website. Passive participants of the website (being only the recipients of information) obtain wide autonomy by the possibility of choosing the time and manner of using the shared content and the freedom of their evaluation and commenting.
6) It stimulates the creativity of Internet users who can appear on health portals in any way.
7) Folksonomy appears. This is the process of using digital content tags for categorization or annotation. It allows users to classify websites, pictures, documents and other forms of data so that the content may be easily categorized and located by users.

There is no doubt that the use of Web 2.0 elements on health portals extends the possibilities of using the Internet for health purposes. Thanks to the Web 2.0 components, websites dedicated to health can become an interactive, social portals that can be used in health care in its broadest sense.

3. Empirical studies

The selected elements of Web 2.0 were characterized in the paper. Their occurrence on the most popular Polish health portals was examined.

The 17 selected websites dedicated to health were analysed. The selection criterion was the popularity of websites measured by the number of users and page views in the Gemius/PBI study conducted in October 2016 [15]. The study concerned the popularity of health services on the Polish Internet. The results of this research are presented in Table 1.

Table 1. The most popular Internet health services, Source: Internet health websites. Research report Gemius/PBI, October 2016 [15]

Name of the website	Users	Views	Range among Internet users
poradnikzdrowie.pl	6,312,531	25,072,438	24.20%
abczdrowie.pl	4,629,965	18,929,211	17.75%
medonet.pl	2,598,347	7,817,034	9.96%
doz.pl	2,584,246	8,574,655	9.91%
mp.pl	2,342,430	8,808,737	8.98%
znanylekarz.pl	2,086,220	12,261,082	8.00%
wylecz.to	1,205,069	2,247,686	4.62%
infozdrowie24.pl	1,055,584	2,510,763	4.05%
medicreporters.com	751,315	1,316,326	2.88%
sluzbazdrowia.pl	699,221	2,119,371	2.68%
medbiz.pl	627,856	2,072,714	2.41%
gurbacka.pl	456,041	1,596,327	1.75%
kardiolo.pl	452,251	1,306,545	1.73%
rankinglekarzy.pl	449,722	1,372,503	1.72%
echirurgia.pl	408,579	1,450,914	1.57%
krokdozdrowia.pl	386,354	2,186,544	1.48%
forumginekologiczne.pl	370,945	1,169,285	1.42%

Table 2. The most popular Internet health services, Source: Internet health websites. Research report Gemius/PBI, April 2020 [15]

Name of the website	Users	Views	Range among Internet users
medonet.pl	10,178,220	74,802,872	36.1%
abczdrowie.pl	7,140,724	54,420,319	25.3%
poradnikzdrowie.pl	5,636,660	18,641,809	20.0%
wprost.pl – health	4,660,044	24,762,386	16.5%
mp.pl	4,309,647	19,954,174	15.3%
doz.pl	3,325,061	45,754,443	11.8%
radiozet.pl – health	3,144,023	11,244,523	11.1%
gazeta.pl – health	2,129,848	4,973,666	7.6%
znanylekarz.pl	2,028,816	8,166,511	7.2%
stronazdrowia.pl	1,712,531	5,703,310	6.1%

Table 3. The most popular Internet health services, Source: Internet health websites. Research report Gemius/PBI, September 2020 [15]

Name of the website	Users	Views	Range among Internet users
medonet.pl	7,518,176	35,406,446	27.2%
abczdrowie.pl	7,079,869	41,887,075	25.6%
poradnikzdrowie.pl	5,719,816	18,263,198	20.7%
mp.pl	3,964,794	16,614,012	14.3%
znanylekarz.pl	3,633,459	15,379,126	13.1%
pacjenci.pl	2,408,993	10,261,491	8.7%
medme.pl	2,005,145	4,420,167	7.2%
gdziepolek.pl	1,667,143	5,403,370	6.0%
radiozet.pl – health	1,425,574	3,855,354	5.2%
wprost.pl – health	1,234,259	4,429,739	4.5%

Table 4. The most popular Internet health services, in COVID-19 lockdown in Poland March 2020, Source: Internet health websites. Research report Gemius/PBI, April 2020 [15]

Name of the website	Avg. from 3 February to 1 March		Avg. from 9 March to 15 March	
	Users	Views	Users	Views
medonet.pl	3,593,083	8,763,874	7,093,586	28,028,363
wprost.pl – health,and,medicine	1,097,228	3,254,172	3,309,496	12,388,862
abczdrowie.pl	2,698,893	9,424,187	2,896,457	9,847,263
naszemiasto.pl – health and medicine	306,466	1,106,645	2,309,246	6,816,082
mp.pl	1,812,059	5,386,155	2,044,729	6,079,361
doz.pl – health and medicine	1,404,870	4189,107	1,922,292	9,155,806
poradnikzdrowie.pl	2,023,176	4,640,066	1,644,465	3,795,742
gazetawroclawska.pl – health and medicine	177,069	446,001	1,558,314	8,089,741
radiozet.pl – health and medicine	662,255	1,496,179	1,526,632	4,040,743
gazetakrakowska.pl – health and medicine	156,377	421,218	1,429,505	5,138,351

Table 5. The most popular Internet health services, year-by-year, Source: Internet health websites. Research report Gemius/PBI, April 2020 [15]

Name of the website	April 2019		April 2020	
	Users	Views	Users	Views
medonet.pl	5,524,137	16,350,263	10,178,220	74,802,872
abczdrowie.pl	6,201,037	48,322,801	7,140,724	54,420,319
poradnikzdrowie.pl	5,151,397	16,031,816	5,636,660	18,641,809
wprost.pl – health	-	-	4,660,044	24,762,386
mp.pl	3,551,511	15,444,085	4,309,647	19,954,174
doz.pl	3,574,259	15,325,441	3,325,061	45,754,443
radiozet.pl – health	1,577,524	3,252,380	3,144,023	11,244,523
gazeta.pl – health	1,974,414	4,009,987	2,129,848	4,973,666
znanylekarz.pl	2,680,444	14,166,146	2,028,816	8,166,511
stronazdrowia.pl	-	-	1,712,531	5,703,310

Table 6. The most popular Internet health services, year by year, Source: Internet health websites. Research report Gemius/PBI, September 2020 [15]

Name of the website	September 2019		September 2020	
	Users	Views	Users	Views
medonet.pl	5,297,265	17,124,102	7,518,176	35,406,446
abczdrowie.pl	4,736,841	30,584,460	7,079,869	41,887,075
poradnikzdrowie.pl	4,910,167	15,591,492	5,719,816	18,263,198
mp.pl	4,743,056	18,723,567	3,964,794	16,614,012
znanylekarz.pl	3,266,206	12,307,123	3,633,459	15,379,126
pacjenci.pl	-	-	2,408,993	10,261,491
medme.pl	2,435,998	5,332,692	2,005,145	4,420,167
gdziepolek.pl	-	-	1,667,143	5,403,370
radiozet.pl – health	680,206	2,231,309	1,425,574	3,855,354
wprost.pl – health	-	-	1,234,259	4,429,739

We can notice that there is a big change in the most popular Internet health services since October 2016 (Table 1–3). In October 2016, only the *poradnikzdrowie.pl* and *abczdrowie.pl* were popular among Internet users in Poland. In September 2020, we have three websites competing with each other, i.e.: *medonet.pl*, *abczdrowie.pl*, *poradnikzdrowie.pl*, whose range among Internet users is greater than 20%. Two others have a range of 13–14% (*mp.pl* and *znanylekarz.pl*).

An interesting situation can be observed in the period of COVID-19 lockdown in Poland (Table 3 to 6). The number of users and views of medical sites rapidly increased in April 2020. In the case of views of the top site, *medonet.pl*, this was 3 times more compared month-to-month. However one can notice that in September 2020, the number of users and views decreased in the case of the two top health websites.

3.1. Empirical research – technological aspects

The article presents the specificity of selected Web 2.0 technologies based on ready-made, functioning solutions that operate in the area of health services. As part of the technology area, the following web technologies have been searched: Wiki, blogs, RSS, ATOM, Ajax, and Ruby. In the social area, whether the websites offer such functionalities as a forum and newsletter was examined, and whether the websites are available on Facebook, Twitter, Google+ and Instagram. The emergence of these technologies was analysed with the help of online tools BuiltWith (https://builtwith.com/) and W3Techs – World Wide Web Technology Surveys (https://w3techs.com/), and with the Wappalyzer plugin [6].

One of the Web 2.0 technologies is Wiki technology. Pages created using this technology allow users to quickly add and modify content contained in the web browser. Wiki pages are linked by URL addresses that allow quick navigation [14]. The most popular example of these is Wikipedia – a multilingual online encyclopaedia. A Wiki is a good platform for exchanging information and materials, creating and storing them, as well as for group discussions on selected topics. It allows multiple users to work together. It allows users to document the results of their work and comment on and evaluate the work of others. It can thus broaden and enrich access to information resources, including those related to health.

The use of a Wiki in e-health may also have negative effects. Without control over the quality of content added by different users, it is not possible to verify the information. Promoting false, bad or incomplete information on the Internet can have fatal consequences for the health and lives of patients. The obtained research results confirmed that there were no Wiki technologies in use on the analysed websites.

The next Web 2.0 technology is RSS (RDF Site Summary). Thanks to RSS, websites that often update their content, publish them in an easy way, informing users about it. RSS has become an important contents distribution channel for blogs. It is the most popular standard of the so-called web feed, that is, a data format used to inform and deliver contents to users. RSS enables aggregation of content from multiple sources in one place. It gives us the opportunity to check from one place, what's new that has been published on our favourite websites and blogs.

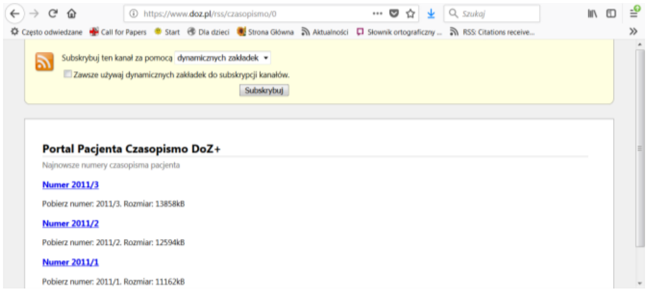

Fig. 1. RSS feeds – access to subscribed messages

ATOM is a more modern protocol than RSS. It is the standard of information channels, and was designed to replace RSS. It was created in response to problems related to the existence of parallel RSS standards (Really Simple Syndication / Rich Site Summary and RDF Site Summary) and errors of these specifications. ATOM avoids ambiguity in RSS specifications, improves compliance with XML and other standards, and adds elements that were missing from RSS.

Among the examined websites, two had an RSS feed – *doz.pl* and *gurbacka.pl* – while ATOM wasn't found on any of them. Figure 1 shows the RSS channel at *www.doz.pl*.

Another Web 2.0 tool is blogs. A blog is a kind of website, where the author places content dated in chronological order from the newest. It is a constantly updated electronic publication online. It is a kind of Internet diary, it has a very personal character, it presents the subjective assessments, comments, thoughts etc.

of the author. It can also be used as a portal dedicated to a specific topic, marketing or e-learning tool. Blogs can be run by individual authors, informal or formal groups of people, companies and institutions, authorities, local governments, and non-governmental organizations. They can be closed (intended for a specific group of readers) and open (public and available to all). On the Internet, due to the great interest in health issues, there is a large number of blogs thematically related to health care, which are run by private individuals dealing with health issues professionally (doctors, midwives, dieticians, etc.) and those for whom the health problem is just a subject of interest (hobby). In the group of analysed health services, only one (*www.znanylekarz.pl*) offered functionality in the form of blogs (separately for patients and doctors) (Figure 2).

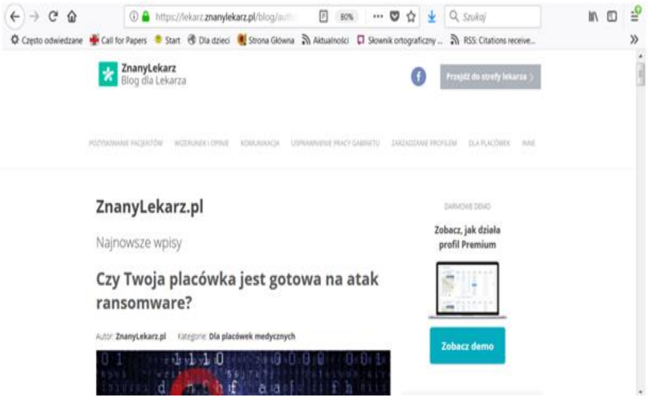

Fig. 2. Blog – an example of application in health care

The next technological element of Web 2.0 is AJAX (Asynchronous JavaScript and XML) – a technique for creating web applications. It allows downloading and sending part of the data without the need to reload the entire website, and thus it simplifies the use of the websites. It is not a new, independent technology, but only a new way of thinking about web applications using existing solutions: XML, CSS, JavaScript, and DOM. The results show that AJAX was used by all of the analyzed websites.

The last element of Web 2.0 included in the website analysis is Ruby on Rails – a framework for building applications written in the Ruby programming language. Since its public release in 1995, the popularity of this programming language has been consistently increasing. Ruby is ranked among the top ten on most indexes measuring the growth and popularity of programming languages in the world (such as the TIOBE index). Ruby owes much of this growth to the popularity of software written using it, especially the Ruby on Rails framework. Ruby is completely free (this applies to the using, copying, modifying and distributing this language). The results show that none of the examined websites is based on the use of this language.

Summing up the technological aspects of Web 2.0, it should be noted that the analysed websites still have a lot of potential for using Web 2.0 technologies. A number of them do not use the technological solutions related to Web 2.0 in a wide scope. The complete list is presented in Figure 3.

The most significant change in the years 2018 and 2020 can be observed in the use of Wiki and Ruby technologies. That means that health portals in Poland have started to use content management systems (CMS) and are paying attention to tagging their information.

At the same time, there are questions that may be the subject of further research in this area. Does this state of affairs affect the functioning of these websites and their popularity? Or will their introduction only constitute an additional workload and additional costs without being translated into possible benefits? Or maybe technological progress is so fast that the technologies mentioned in the literature (e.g. RSS or ATOM) are already outdated and it is worth looking for new solutions in this area?

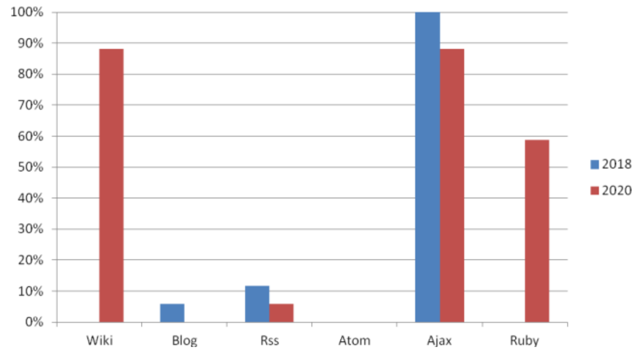

Fig. 3. The structure of the use of Web 2.0 technologies by Polish health services in 2018 and 2020 (source: own study)

3.2. Empirical research – social aspects

The social area of health services was also analysed. It was checked whether they offer forum and newsletter functionalities and whether they appear on social media (Facebook, Twitter, Google+, Instagram). The results obtained are shown in Figure 4. An interesting fact is that the social elements on the health web pages decreased in 2020 compared to 2018.

In the social area, there was greater involvement of the examined websites than in the field of using Web 2.0 technologies. This confirms the incredible power of social media's influence and their expansion in the modern world.

Social media is an attractive information channel with, among other things, many educational advantages. It is also an alternative form of education and upbringing in the field of promoting a healthy lifestyle. The essence of social media and its potential in the field of health education is primarily associated with its huge reach, which is very important for the spread of health education. It enables immediate access to specific social groups that are online. On social networks, there is the phenomenon of creating support groups, ties, building and developing interpersonal relations around topics discussed on the Internet (including those regarding health and life protection). This channel is also very attractive for marketing, so it often happens that educational content is a camouflaged form of advertising. The flood of information, often contradictory and controversial, can also harm health education.

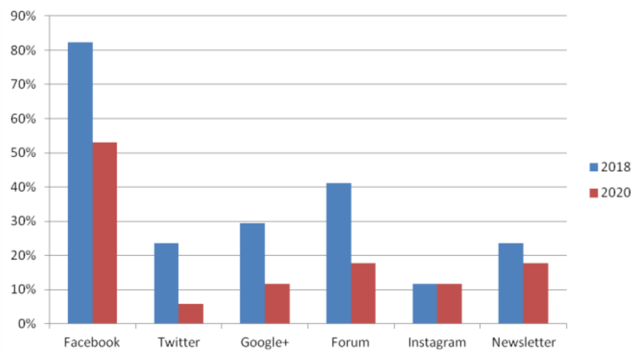

Fig. 4. Structure of the occurrence of social elements in Polish health services in 2018 and 2020 (source: own study)

Social media are distinguished by the free flow of information from their participants. In social media, the information spreads in a viral way (quickly and uncontrollably). The big advantage is multitooling – it's easy to create and publish information not only in the form of text, but also other attractive files. Multi-channelling allows the systematization of incoming information from various sources in the network. Activity on social media is measurable – numerous statistics motivate to action, and determine the level of support for the creator of the information provided and its attractiveness [10].

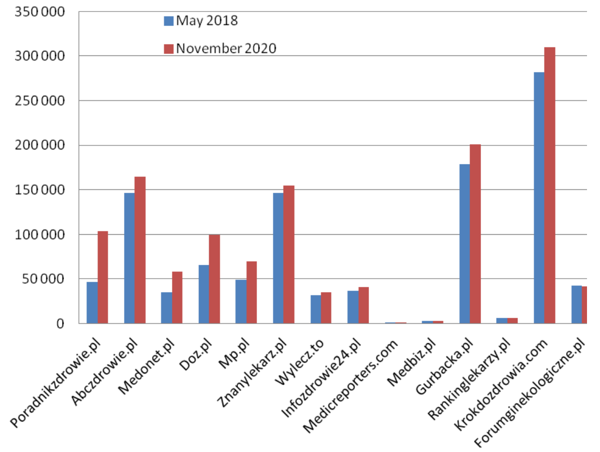

Fig. 5. Number of Facebook fans of chosen health portals in the May 2018 and November 2020 (source: own study)

Figure 5 presents the number of Facebook fans for chosen health services in May 2018 and November 2020. The leader in the ranking is *krokdozdrowia.pl* with the number being over 300,000 fans. *Gurbacka.pl* is in second place (about 200,000 fans). *Abczdrowie.pl* and the *znanylekarz.pl* have over 160,000 fans each. For the other websites, the number of fans does not exceed 110,000.

The next graph (Figure 6) shows the percentage change in the number of fans of chosen health services over a period of 2 years (from May 2018 to November 2020). The dynamics of the changes is wide and ranges from +120% (*poradnikzdrowie.pl*) to -5% (*medbiz.pl*).

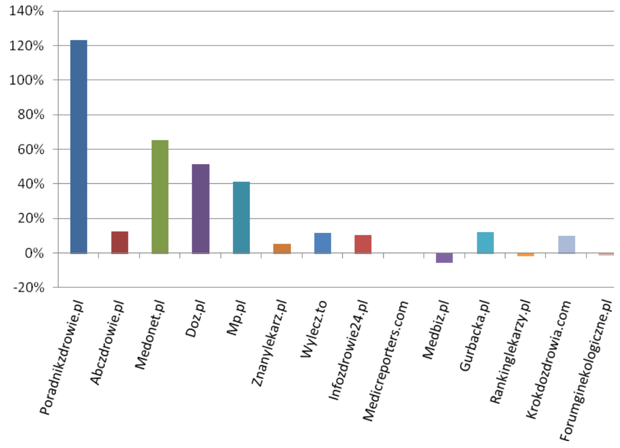

Fig. 6. Change in fans over the period of May 2018 to November 2020 (source: own study)

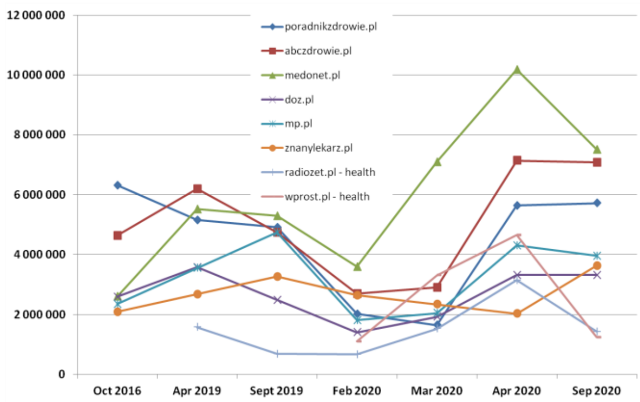

Fig. 7. Change in users over the period of October 2016 to September 2020 in chosen health services (source: own study)

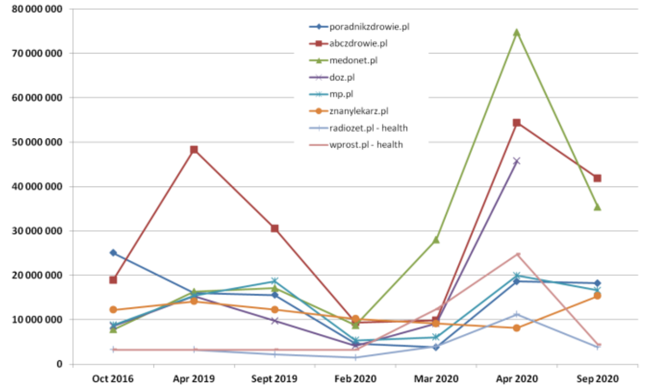

Fig. 8. Change in views over the period of October 2016 to September 2020 in chosen health services (source: own study)

Figures 7 and 8 present the change of the users and the views of the health web sites in the period of time starting from October 2016 until September 2020. This summary was prepared on the basis of the data from Tables 1–6. One can notice that *medonet.pl* and *abczdrowie.pl* are the top two health services in Poland.

The allocation of medical knowledge on forums, blogs, and information portals, using Web 2.0 technologies is a reaction to the growing needs of Internet users as prosumers in the area of health protection. On the other hand, the more common use of social media results in changes in attitudes and behaviors, and also forces the modification of functions and capabilities of information systems. According to Web 2.0, even end users (consumers, patients) can be seen as experts, and their collective wisdom can and should be used (a health care professional is an expert in diagnosing the disease and the patient is an expert in its experience) [4].

The cyclical research conducted in 2013–2019 indicates the fact that the most frequently used ICT tools are Internet forums and discussion groups (about 70% of respondents), specialist medical portals and information websites dedicated to health and Internet encyclopaedias (e.g. Wikipedia) [9].

Social media gives everyone who wants it, the opportunity to share knowledge and information. This is a very positive solution. They also shape the skills of searching and using various sources of knowledge. Users participating in online communities gain the opportunity to self-fulfil, develop interests and use information provided by other Internet users.

Unfortunately, misuse of social media causes threats. The poor quality of content entered by users may reduce the credibility of websites. Users do not take responsibility for the quality of their content. Information appears in the web in a chaotic and distracting way. There are no mechanisms to control and verify the quality of this information. Quantitative data (statistics of visits, likes and shares) often stand in for the value of information. Content creators do not guarantee that the content they provide will be valuable and reliable. There are examples of low-quality substantive information. Such information misleads their recipients. The evaluation of the quality of online sources of health information is a very important issue that is of interest to specialists in medicine, information technology and knowledge and information management.

4. Conclusions

The main conclusion that can be drawn from the study is that the most popular Polish health websites have the character of Web 2.0 websites.

They use technological and social elements of Web 2.0. They use social elements to a greater degree (forum functionalities and newsletter as well as the presence of their profiles on Facebook, Twitter, Google+ and Instagram) than technological ones (Wiki, blogs, RSS, ATOM, Ajax, Ruby).

An interesting behavior of the Internet users can be noticed while comparing the popularity of the websites from Tables 1 to 6 and the number of Facebook fans from Figure 5. The popularity of websites does not reflect the number of Facebook users following the website's profile. The following health portals (in descending order): *krokdozdrowia.pl*, *gurbacka.pl*, *abczdrowie.pl*, *znanylekarz.pl*, have the highest number of Facebook fans (above 140,000). The portal *krokdozdrowia.pl*, which is moderately popular, has the highest number of Facebook fans (over 300,000).

One can notice that the number of Facebook fans of health sites in Poland in the years 2018 and 2020 mostly increases (Figure 5), however the number of registered users of the health sites changes rapidly in the years 2016 and 2020 (Figure 7).

The obtained results confirm the impact of social media. Users in many cases are more likely to visit the profiles of specific pages on Facebook than their web counterparts. In the case of the COVID-19 lockdown in Poland (April 2020), one can observe that users are more willing to register on the websites than to be Facebook fans (Figures 7 and 8). On the other hand, after unfreezing the economy in the summer, a change is noticeable and in September 2020, leading heath sites recorded declines in users and views.

References

[1] Bos L, Marsh A, Carroll D, Gupta S, Rees M.: Patient 2.0 Empowerment. SWWS 97(4), 2008, 164–168.

[2] Czerwinska M.: Specificity of the e-patients' behaviours on the Internet. Collegium of Economic Analysis Annals 38, 2015, 343–352.

[3] Czerwinska M.: The Influence of the Digitalisation of Health-Related Information on Internauts' Behaviour. Collegium of Economic Analysis Annals 46, 2017, 39–49.

[4] Davison K. P., Pennebaker J. W.: Virtual narratives: Illness representations in online support groups. Petrie K. J., Weinman J. A. (Ed.): Perceptions of health and illness: Current research and applications. Harwood Academic Publishers. Amsterdam 1997.

[5] Gümüş H., Bal V.: Analysis of the Effect of Quality Components of Web 2.0 Enabled E-Commerce Websites on Electronic Word-of-Mouth Marketing (EWOM) and on Customer Loyalty. Annals of the University of Oradea – Economic Science 25(1), 2016, 979–986.

[6] Identify technologies on websites, https://www.wappalyzer.com/ (accessed: 11.10.2020).

[7] Information society in Poland. How do we use the Internet? 2019. https://stat.gov.pl, (available: October 2020).

[8] Information society in Poland. Results of statistical surveys in the years 2015–2019. https://stat.gov.pl (available: 12. 2019).

[9] Júnior S. H. D. L., Silva F. Í. C., Albuquerque G. S. G., de Medeiros, F. P. A., Lira H. B.: Enterprise Architecture in Healthcare Systems: A systematic literature review. 2020 arXiv preprint arXiv:2007.06767.

[10] Kotsenas A. L., Arce M., Aase L., Timimi F. K., Young C., Wald, J. T.: The strategic imperative for the use of social media in health care. Journal of the American College of Radiology 15(1), 2018, 155–161.

[11] Krouska A., Troussas C., Virvou M.: A literature review of Social Networking-based Learning Systems using a novel ISO-based framework. Intelligent Decision Technologies 13(1), 2019, 23–39.

[12] Laurenza E., Quintano M., Schiavone F., Vrontis, D.: The effect of digital technologies adoption in healthcare industry: a case based analysis. Business Process Management Journal 24(5), 2018, 1124–1144.

[13] Maheshwari B., Sarrion M., Motiani, M., O'Sullivan, S., Chandwani, R.: Exploration of factors affecting the use of Web 2.0 for knowledge sharing among healthcare professionals: an Indian perspective. Journal of Knowledge Management, 2020 [https://doi.org/10.1108/JKM-02-2020-0105].

[14] Musto C., Semeraro G., de Gemmis M., Lops P.: Learning word embeddings from wikipedia for content-based recommender systems. European Conference on Information Retrieval. Springer, Cham. 2016.

[15] Research Gemius/PBI company. Report: Internet health websites (in Polish), http://pbi.org.pl (accessed: 11.10.2020).

[16] Van der Belt T.H., Engelen L.J., Berben S.A., Schoonhoven L.: Definition of Health 2.0 and Medicine 2.0: A Systematic Review. Journal of Medical Internet Research 12(2), 2010, e18 [http://doi.org/10.2196/jmir.1350].

[17] Van der Vaart R., Drossaert C.: Development of the Digital Health Literacy Instrument: Measuring a Broad Spectrum of Health 1.0 and Health 2.0 Skills. Journal of Medical Internet Research 19(1), 2017, e27 [http://doi.org/10.2196/jmir.6709].

[18] We are social, Global Digital Report 2020, https://wearesocial.com/digital-2020, (2020).

[19] Web 2.0: https://en.wikipedia.org/wiki/Web_2.0 (accessed: 10.2020).

[20] Yusif S., Hafeez-Baig A., Soar J.: e-Health readiness assessment factors and measuring tools: A systematic review. International Journal of Medical Informatics 107, 2017, 56–64.

Ph.D. Magdalena Czerwinska
e-mail: m.czerwinska@pollub.pl

Assistant professor at the Faculty of Management, Lublin University of Technology, head of the Department of Economics and Economic Management. She has been researcher since 1996 and is the author of over 40 papers. Her scientific interests include: knowledge management, ehealth, information technology acceptance models, health information, and IT technology acceptance. She is active member of scientific societies (Polish Economic Society, Scientific Society of Economic Informatics, Scientific Society of Organization and Management).

http://orcid.org/0000-0002-7945-1044

otrzymano/received: 19.11.2020 *przyjęto do druku/accepted: 10.12.2020*

LIST OF REVIEWERS COOPERATING WITH THE JOURNAL IN 2020

LISTA RECENZENTÓW WSPÓŁPRACUJĄCYCH Z CZASOPISMEM W ROKU 2020

Prof.	Barabahs	Oleg	State University of Telecommunications (Kyiv, Ukraine)
Ph.D.	Bober	Dariusz	University of Rzeszow (Rzeszow, Poland)
Ph.D.	Boyko	Oksana	Danylo Halytsky Lviv National Medical University (Lviv, Ukraine)
Ph.D.	Cechowicz	Radosław	Lublin University of Technology (Lublin, Poland)
Ph.D.	Chepurna	Oksana	Shenzhen University (Shenzhen, China)
Prof.	Cięszczyk	Sławomir	Lublin University of Technology (Lublin, Poland)
Ph.D.	Falkowski-Gilski	Przemysław	Gdansk University of Technology (Gdansk, Poland)
Ph.D.	Golubeva	Ekaterina	Taras Shevchenko National University of Kyiv (Kyiv, Ukraine)
Ph.D.	Holuk	Mariusz	State School of Higher Education Chelm (Chelm, Poland)
Prof.	Hotra	Zenon	Lviv Polytechnic National University (Lviv, Ukraine)
Ph.D.	Ilarionov	Oleg	Taras Shevchenko National University of Kyiv (Kyiv, Ukraine)
Prof.	Jackowska-Strumiłło	Lidia	Lodz University of Technology (Lodz, Poland)
Ph.D.	Kalizhanova	Aliya	Institute of Information and Computational Technologies SR MES RK (Almaty, Kazakhstan), Al-Farabi Kazakh National University (Almaty, Kazakhstan)
Ph.D.	Karczemska	Anna	Lodz University of Technology (Lodz, Poland)
Prof.	Kisała	Piotr	Lublin University of Technology (Lublin, Poland)
Prof.	Klymash	Mykhailo	Lviv Polytechnic National University (Lviv, Ukraine)
Prof.	Knyazeva	Nina	Odessa National Academy of Food Technologies (Odessa, Ukraine)
Prof.	Koltunowicz	Tomasz	Lublin University of Technology (Lublin, Poland)
Prof.	Komarov	Fadey	Belarusian State University (Minsk, Belarus)
Prof.	Kotyra	Andrzej	Lublin University of Technology (Lublin, Poland)
Prof.	Kovalyuk	Zakhar	Institute for Problems of Material Science I.M. Frantsevich National Academy of Science (Kyiv, Ukraine)
Prof.	Kudrya	Volodymyr	Odessa National Polytechnic University (Odessa, Ukraine)
Prof.	Kułażyński	Marek	Wroclaw University of Technology (Wroclaw, Poland)
Prof.	Liubchyk	Vitalii	Khmelnytskyi National University (Khmelnytskyi, Ukraine)
Ph.D.	Ławicki	Tomasz	Lublin University of Technology (Lublin, Poland)
Ph.D.	Łukasik	Edyta	Lublin University of Technology (Lublin, Poland)
Prof.	Lytvynenko	Volodymyr	Kherson National Technical University (Kherson, Ukraine)
Ph.D.	Małek	Arkadiusz	University of Economics and Innovation in Lublin (Lublin, Poland)
Prof.	Miaskowski	Arkadiusz	University of Life Sciences in Lublin (Lublin, Poland)
Prof.	Mosorov	Volodymyr	Lodz University of Technology (Lodz, Poland)
Prof.	Mudry	Stepan	Ivan Franko National University of Lviv (Lviv, Ukraine)
Ph.D.	Naumchuk	Oleksandr	National University of Water and Environmental Engineering (Rivne, Ukraine)
Prof.	Olszewski	Serge	Taras Shevchenko National University of Kyiv (Kyiv, Ukraine)
Ph.D.	Omiotek	Zbigniew	Lublin University of Technology (Lublin, Poland)
Prof.	Pavlov	Sergey	Vinnytsia National Technical University (Vinnytsia, Ukraine)
Ph.D.	Pecyna	Anna	University of Life Sciences in Lublin (Lublin, Poland)
Prof.	Piotrowski	Robert	Gdansk University of Technology (Gdansk, Poland)
Ph.D.	Polakowski	Krzysztof	Warsaw University of Technology (Warsaw, Poland)
Ph.D.	Politans'kyy	Ruslan	Lviv Polytechnic National University (Lviv, Ukraine)
Prof.	Potencki	Jerzy	Rzeszow University of Technology (Rzeszow, Poland)
Ph.D.	Romanyk	Igor	Quartz Plant LLC (Chernivtsi, Ukraine)
Prof.	Rozorinov	Heorgiy	National Technical University of Ukraine "Igor Sikorsky Kyiv Polytechnic Institute" (Kyiv, Ukraine)
Prof.	Semenov	Andriy	Vinnytsia National Technical University (Vinnytsia, Ukraine)
Prof.	Sikora	Jan	Research & Development Centre Netrix SA (Lublin, Poland)
Ph.D.	Smailova	Saule	D. Serikbayev East Kazakhstan State Technical University (Ust-Kamenogorsk, Kazakhstan)
Prof.	Smolarz	Andrzej	Lublin University of Technology (Lublin, Poland)
Prof.	Sokolovsky	Alexander	Oles Honchar Dnipro National University (Dnipro, Ukraine)
Prof.	Sorokatyi	Ruslan	Khmelnytskyi National University (Khmelnytskyi, Ukraine)
Ph.D.	Stój	Jacek	Silesian University of Technology (Gliwice, Poland)
Prof.	Sulemenov	Batyrbek	Kazakh National Research Technical University after K.I.Satpayev (Almaty, Kazakhstan)
Ph.D.	Telejko	Marek	Kielce University of Technology (Kielce, Poland)
Prof.	Toliupa	Serhii	Taras Shevchenko National University of Kyiv (Kyiv, Ukraine)